



BINDING SERVICES

Tel +44 (0)29 2087 4949

Fax +44 (0)29 20371921

e-mail bindery@cardiff.ac.uk

**PERFORMANCE OF CONCRETE STRUCTURES
RETROFITED WITH CARDIFRC[®] AFTER THERMAL
CYCLING**

by

FARHAT AGRIBI FARHAT
M.Phil. (NEWCASTLE UPON TYNE)

Thesis submitted to Cardiff University
in candidature for the degree
of Doctor of Philosophy

September, 2004

School of Engineering
Cardiff University
Wales

UMI Number: U584659

All rights reserved

INFORMATION TO ALL USERS

The quality of this reproduction is dependent upon the quality of the copy submitted.

In the unlikely event that the author did not send a complete manuscript and there are missing pages, these will be noted. Also, if material had to be removed, a note will indicate the deletion.



UMI U584659

Published by ProQuest LLC 2013. Copyright in the Dissertation held by the Author.
Microform Edition © ProQuest LLC.

All rights reserved. This work is protected against
unauthorized copying under Title 17, United States Code.



ProQuest LLC
789 East Eisenhower Parkway
P.O. Box 1346
Ann Arbor, MI 48106-1346

In the name of God

the compassionate and the merciful

ACKNOWLEDGEMENT

First of all, I would like to thank my supervisor Professor B. L. Karihaloo for his invaluable guidance, support, encouragement and patience as well as his friendship during the investigation and preparation of this thesis.

I would also like to thank my colleagues Dr. Q. Z. Xiao, Dr Terry Bennett, Dr. Farshid Alaei, Dr. Hassan Abdalla, Mr. Demetris Nicolaidis, Mr. Antonios Kanellopoulos, and Mr. Christopher Joseph, for their support and encouragement throughout the period of my study.

My thanks also go to the technical staff, in particular Mr. D. M. S. Sanford, Mr. K. S. Lyall, Mr. B. Hooper, Mr. Len Czekaj, Mr. Carl Wadsworth and Mr. Andrew Sweeney for their valuable help during the time of the study.

Special thanks must be reserved for my wife for her encouragement and support and also the courage of my lovely children Dania, Wisal and Agribi. I am also indebted to my parents for their love, understanding, encouragement and support throughout the duration of this study.

Thanks are due to my loved country Libya for its continuous financial support provided throughout the duration of the study.

Synopsis

A new retrofitting technique using CARDIFRC[®], a material compatible with concrete, has recently been developed at Cardiff University. It overcomes some of the problems associated with the current techniques based on externally bonded steel plates and FRP (fibre-reinforced polymer), which are due to the mismatch of their tensile strength and stiffness with that of concrete structure being retrofitted.

This study investigates the effect of thermal cycles on the performance of reinforced concrete control and retrofitted beams. The concrete beams were heated to a maximum temperature of 90°C from the room temperature of about 25° C. The number of thermal cycles varied from 0 to 90 cycles. After the requisite number of thermal cycles, the beams were tested at room temperature in four-point bending.

The tests indicate that the retrofitted beams are stronger, stiffer and more importantly failed in flexure. No visual deterioration or bond degradation was observed after thermal cycling of the retrofitted beams (the bond between the repair material and the concrete substrate remained intact) attesting to the good thermal compatibility between the concrete and CARDIFRC[®]. Therefore, this type of retrofit material can be successfully used in hot climates.

The study also evaluates the performance of normal and high strength concretes repaired with CARDIFRC[®] using the wedge splitting test (WST). The main factors that could affect the bond between the repair material and concrete such as the surface roughness and thermal cycling are also investigated. It is shown that surface roughness plays a significant role in the overall bonding system, and no visual deterioration is observed after thermal cycling.

Two analytical/computational models for predicting the ultimate moment capacity and the complete load–deflection behaviour of the retrofitted beams were applied. Both models predict very well the ultimate moment capacity of the retrofitted beams.

LIST OF CONTENTS

Declaration	i
Acknowledgement	ii
Synopsis	iii
List of Contents	iv
List of Figures	ix
List of Tables	xvi
List of Plates	xviii

Chapter 1 Introduction

1.1 Introduction	1
1.1.1 Retrofitted concrete	2
1.2 Objectives of the Thesis	4
1.3 Outline of the Thesis	4

Chapter 2 Retrofitting of Concrete Structures

2.1 Introduction	7
2.2 Externally bonded steel plates	8
2.2.1 Flexural strengthening	8
2.2.1.1 Failure modes	9
2.2.2 Shear strengthening	10
2.3 Fibre reinforced plastic FRP	13
2.3.1 Flexural strengthening	14
2.3.1.1 Modes of failure	15
2.3.2 Shear strengthening	17
2.3.3 Environmental effects	19
2.3.3.1 The effect Fire exposure	21
2.3.3.2 The effect of freeze and freeze-thaw	22
2.4 High performance fibre reinforced cementitious composites HPFRCCs	23
2.4.1 Engineered cementitious composite ECC	23
2.4.2 Retrofitting with CARDIFRC [®]	27
2.4.2.1 Flexural strengthening	29
2.4.2.2 Flexural and Shear strengthening	29

Chapter 3 Fracture Mechanics of Concrete

3.1 Introduction	32
3.2 Linear Elastic Fracture Mechanics (LEFM)	33
3.2.1 Griffith Theory of Brittle Fracture	33
3.2.2 Irwin Theory of Brittle Fracture	35
3.2.2.1 Irwin Theory and Local Energy Considerations	39
3.2.3 Barenblatt's Cohesive crack model	41
3.3 Is LEFM Applicable to Concrete?	42
3.4 Nonlinear Fracture Theory of Concrete	44
3.4.1 Fictitious Crack Model (FCM)	44
3.4.2 Crack Band Model (CBM)	46
3.5 Determination of fracture energy G_f	48
3.6 Size-Independent specific fracture energy G_F	51
3.7 Fracture behaviour of bimaterial systems	55

3.7.1 Experimental evaluation	56
3.7.2 Characterisation of cracks at bimaterial interfaces	57
3.8 Application of fracture mechanics to reinforced concrete	59
3.8.1 Calculation of the plastic moment of a cracked beam element	60

Chapter 4 High Performance Fibre-Reinforced Cementitious Composites. HPFRCC- An overview

4.1 Introduction	63
4.2 Normal strength concrete (NSC)	64
4.3 High strength concrete (HSC)	64
4.4 High performance concrete (HPC)	65
4.5 Fibre reinforced concrete (FRC)	65
4.6 HPFRCCs	66
4.6.1 Bridging action of the fibres	67
4.6.2 Constitutive Model	71
4.6.2.1 Linear elastic behaviour	72
4.6.2.2 Strain-hardening behaviour	73
4.6.2.3 Tensile Strength	76
4.6.2.4 Tension softening behaviour	76
4.6.2.4.1 Fracture energy G_f	78
4.6.3 Types of HPFRCC	79
4.6.3.1 Macro-Defect-Free Cement (MDF)	79
4.6.3.2 Slurry Infiltrated Fibre Concrete (SIFCON)	79
4.6.3.3 Engineered Cementitious Composites (ECC)	80
4.6.3.4 Reactive Powder Concrete (RPC)	80
4.6.3.5 DSP Cementitious Materials	81
4.6.3.6 CARDIFRC [®]	81
4.6.3.6.1 The effect of high temperature Curing conditions	83
4.6.3.6.2 The effect of silica fume	84
4.6.3.6.3 The effect of dispersing agent (Superplasticizer)	87
4.6.3.6.4 The effect of steel fibres	88
4.6.3.6.4.1 Fibre distribution	88
4.6.3.6.4.2 Volume fraction of fibre	89
4.6.3.6.4.3 Aspect ratio of fibre (l/d)	89
4.6.3.6.5 Constitutive description of CARDIFRC [®]	90
4.7 Conclusion	91

Chapter 5 Performance of NSC Bonded to CARDIFRC[®] after Thermal Cycling

5.1 Introduction	93
5.2. Mixing and casting procedure of CARDIFRC [®]	94
5.2.2 Curing regime	95
5.3 Mixing and casting of NSC specimens	96
5.4 Preparation of WS bonded specimens	96
5.5 Adhesive bonding	97
5.6 Thermal cycling	98
5.7 Mechanical tests	99
5.7.1 Compressive strength	99
5.7.2 Splitting strength	101
5.7.3 Modulus of rupture MOR	102
5.7.4 Modulus of Elasticity	104
5.8 Fracture tests	105
5.8.1 Test procedure	105

5.8.2 Control NSC specimens	108
5.8.2.1 Measured fracture energy	109
5.8.2.2 Size-independent specific fracture energy	111
5.8.2.3 Brittleness	113
5.8.3 CARDIFRC [®] /NSC bonded system	114
5.8.3.1 Direct wet casting	115
5.8.3.2 Adhesive bonding	116
5.8.3.2.1 Influence of surface preparation	117
5.8.3.2.1.1 Repair material (CARDIFRC [®])	117
5.8.3.2.1.2 Parent concrete	117
5.8.3.2.1.3 Surface improvement	119
5.8.3.2.2 Effect of thermal cycling	122
5.8.3.2.3 Size-independent specific fracture energy	124
5.9 Comparison of the results	125
5.9.1 Specimens exposed to 0 thermal cycles	125
5.9.2 Specimens exposed to 30 thermal cycles	126
5.9.3 Specimens exposed to 90 thermal cycles	129
5.10 Conclusion	131

Chapter 6 Performance of HSC Bonded to CARDIFRC[®] after Thermal Cycling

6.1 Introduction	133
6.2 Control specimens	133
6.2.1 Mix proportion of HSC	133
6.2.2 Mechanical properties	134
6.2.2.1 Compressive strength f_c	134
6.2.2.2 Splitting strength f_t	135
6.2.2.3 Modulus of rupture (MOR)	136
6.2.2.4 Modulus of elasticity	136
6.2.3 Fracture properties	137
6.2.3.1 Measured fracture energy G_f	137
6.2.3.2 Size independent fracture energy G_F	140
6.2.3.3 Brittleness	141
6.3 CARDIFRC [®] bonded specimens	141
6.3.1 Direct wet casting	142
6.3.2 Adhesive bonding	144
6.3.2.1 Influence of surface preparation	144
6.3.2.1.1 Parent concrete (HSC)	144
6.3.2.1.2 Surface improvement	147
6.3.2.2 Influence of notch size	150
6.3.2.3 Influence of thermal cycling	150
6.3.2.3.1 Size- independent specific fracture energy G_F	152
6.4 General Conclusions	154

Chapter 7 Retrofitting of Reinforced Concrete Beams with CARDIFRC after thermal cycling

7.1 Introduction	156
7.2 Test Beams	159
7.3 Test Procedure	159
7.4 CARDIFRC [®] strips	160
7.5 Mechanical degradation (Pre-cracking)	161
7.6 Retrofitting Procedure	161
7.7 Thermal cycling	162

7.8 Results	162
7.8.1 Control beams	163
7.8.1.1 Beams without shear reinforcement	163
7.8.1.2 Beams with sufficient shear reinforcement	167
7.8.2 Retrofitted beams	170
7.8.2.1 Pre-cracking	170
7.8.2.2 Beams without shear reinforcement	171
7.8.2.2.1 Beams retrofitted with one strip on the tension face	171
7.8.2.2.2 Beams retrofitted with three long and four short strips	177
7.8.2.3 Beams with sufficient shear reinforcement	180
7.8.2.3.1 Beams retrofitted with one strip on the tension face	182
7.8.2.3.2 Beams retrofitted with three long and four short strips	184
7.9 Discussion	188
7.10 Conclusions	194

Chapter 8 Analysis of the Reinforced Concrete Beams Retrofitted with CARDIFRC[®]

8.1 Introduction	196
8.2 Constitutive relations	196
8.2.1 Concrete	196
8.2.2 Steel reinforcement	200
8.2.3 CARDIFRC [®]	200
8.3 First analytical model (Classical theory)	201
8.3.1 Model assumptions	202
8.3.2 Calculation procedure	204
8.3.3 Moment-curvature relationship	205
8.3.4 Model results	208
8.4 Second analytical model (Fracture mechanics method)	215
8.4.1 Sequence of crack growth	216
8.4.2 Modelling of dominant flexural crack	219
8.4.3 The condition of smooth closure of crack faces	221
8.4.3.1 Stress Intensity factor due to the applied moment K_{IM}	222
8.4.3.2 Stress Intensity factor due to the steel force	222
8.4.3.3 Stress intensity factor due to the residual tensile stress of concrete K_{Iconc}	223
8.4.3.4 Stress intensity factor due to the closure force of tension strip $K_{I(t-strip)}$	224
8.4.3.5 Stress intensity factor due to the closure force of side strip $K_{I(s-strip)}$	225
8.4.4 Crack opening compatibility equation	226
8.4.4.1 Compliance coefficient due to a unit moment λ_{SM}	227
8.4.4.2 Compliance coefficient due to a unit steel force λ_{SS}	227
8.4.4.3 Compliance coefficient due to a unit tensile force in concrete λ_{Sconc}	228
8.4.4.4 Compliance coefficient due to a unit force in retrofit tension strip $\lambda_{S-(t-strip)}$	228
8.4.4.5 Compliance coefficient due to a unit force in retrofit	

side strips $\lambda_{S-(s-strip)}$	229
8.4.5 Bridging force exerted by steel F_S	230
8.4.5.1 Carpinteri's approximation	230
8.4.5.2 Kaar's formula	231
8.4.5.3 Modified Kaar's formula	232
8.4.6 Evaluation of moment resistance of the beams	232
8.4.7 Model results	233
8.5 Conclusions	235
Chapter 9 Conclusions and Recommendations for Future work	
9.1 Conclusions	236
9.2 Recommendations for Future work	238
List of References	240
Appendices	

Figure	List of Figures	Page
2.1	Sudden shear failures of plated beams. Failure by: (a) ripping off of the concrete cover, (b) Plate debonding (After Ziraba et al., 1994)	10
2.2	Repair schemes: (a) full encasement of the shear zone by jacket plate, (b) U- strips on the shear zone, (c) flat strips at the shear zone, and (d) flat plates on the sides of the beams (After Sharif et al., 1995)	11
2.3	Shear strengthening of RC beam using horizontal steel plate (After Adhikary et al., 2000)	11
2.4	Common failure modes for FRP retrofitted beams	16
2.5	Three GFRP shear strengthening schemes (a) shear strips, (b) shear wings, and (c) U-Jacket. (After Al-Sulaimani et al., 1994)	18
2.6	(a) Trapping mechanism in a bimaterial interface system, (b) fibre bridging in a kinked crack (After Lim and Li 1997) (Reproduced from Alaei, 2002)	25
2.7	Configurations of retrofitting. Beams retrofitted with: (a) one strip on the tension face, (b) one strip on the tension and two strips on sides, (C) one strip on the tension face and four rectangular strips on sides, (d) one strip on the tension and four trapezoidal strips on sides, (e) one strip on the tension, (f) one strip on the tension and four short strips on sides covering supports and ends of tension strip, and (g) one strip on the tension and four short and two continuous strips on sides, fully covering supports and tension strip sides (After Karihaloo et al., 2003b)	28
3.1	The principle of superposition (a) the plate is under external tension (b) uncracked plate under σ (c) plate without external σ but with equal and opposite stress applied to the crack to create a stress-free crack (After Karihaloo, 1995).	34
3.2	Modes of crack propagation	36
3.3	An infinite elastic body with a sharp crack of length $2a$ under mode I.	37
3.4	Shapes of traction-free crack tip zones and distribution of normal stress, σ_{yy} in front of the crack tip for $K_I > 0$, $K_I < 0$ and $K_I = 0$ (From Karihaloo, 1995).	38
3.5	Barenblatt's cohesive crack model in mode I. Note $c \ll a$.	41

3.6	Typical load-deformation response of a quasi-brittle material in tension/flexure (a) and the fracture process zone ahead of the real traction-free crack (b) (After Karihaloo, 1995).	43
3.7	(a) A real traction-free crack of length a_0 terminating in a fictitious crack of length l_p whose faces close smoothly near its tip ($K_I=0$). The material ahead of the fictitious crack tip is assumed to be linear (b), but the material within the fracture process zone is softening; the area under softening curve equals fracture energy G_F (c) (After Karihaloo, 1995).	45
3.8	Crack band model for fracture of concrete (a) a microcrack band fracture and (b) stress-strain curve for the microcrack band (From Shah et al., 1995).	47
3.9.	Testing configuration and geometry of specimen. P = load, L = specimen length, S = specimen loading span, W = beam depth. B = beam thickness and a = initial notched depth.	48
3.10.	Principle of wedge splitting test: (a) a test specimen on a linear support, (b) placing of two load devices with roller bearing, (c) pressing a wedge between bearings, and (d) forces acting on the wedge. (After Rossi et al., 1991)	50
3.11	The FPZ and discrete bridging stresses. The FPZ is divided into the inner softening zone and the outer micro - fracture zone. w_c is related to the width of the inner softening zone w_{sf} (Hu and Wittmann, 1992).	52
3.12	g_f decreases monotonically along the ligament, so that G_f has to be dependent on the a/W ratio, as observed in many experiments (Hu and Wittmann, 1992).	53
3.13	A notched test specimen of depth W and notch depth a (a) showing the distribution of fracture energy (G_f and g_f) along the un-notched ligament, $W-a$ (b).	54
3.14	Different composite geometry to determine the load-deformation curve for bimaterial.	57
3.15	Geometry of a bi-material system with an interface crack	57
3.16	A small beam segment with a crack showing the bending moment M and steel force P (After Bosco and Carpinteri, 1992)	60
4.1	(a) A single fibre pull-out without snubbing ($\phi = 0$) and (b) with snubbing ($\phi \neq 0, \phi = \varphi$) (After Karihaloo and Wang, 2000)	68
4.2	A linearised bridging law describing the relation between the bridging force and the crack opening displacement (Karihaloo and Wang, 1997)	69

4.3	Idealised interfacial matrix-fibre shear stress (τ) vs. half crack mouth opening for single fibre (dashed line) and multiple fibre (solid line) pull-out (After Lange-Kornbak, 1997)	69
4.4	Complete pre- and post-peak tensile response of two short fibre-reinforced cementitious composites (After Karihaloo and Wang, 2000).	71
4.5	(a) Representative unit volume of the matrix containing one microcrack of length $2a$ (note that the volume V of this unit = $W*H*1$ and the surface area of the crack $S = 2a*1$); (b) an enlarged view of the crack opening (After Benson, 2003).	75
4.6	(a) Crack configuration prior to coalescence of crack (b) after coalescence of cracks during tension softening of fibre-reinforced quasi-brittle materials (After Karihaloo and Wang, 2000).	75
4.7	(a) Flocculated particles in ordinary cement paste. (b) densely packed cement grains and microsilica in DSP paste	86
4.8	(a) Flocculated particles in cement paste. (b) superplasticised cement particles.	87
4.9	Complete pre- and post peak tensile curve for CARDIFRC [®] .	91
5.1	Configurations of specimens shapes and bonding techniques: (a) roughened and grooved surface of concrete half cube and (b) adhesive bonding procedure.	97
5.2	Schematic representation of thermal cycling	99
5.3	Configurations of WS test: (a) specimen shape, (b). loading arrangements, (c) the points of application of wedge force and (d) location of clip gauge for measuring CMOD.	107
5.4	The influence of notch size on the load-CMOD curves after: (a) zero thermal cycling (b) 30 thermal cycling and (C) 90 thermal cycling	110
5.5	The effect of thermal cycling on measured and size-independent fracture energy of NSC.	113
5.6	Configuration of bonded specimens: (a) Loading arrangements and (b) wedge splitting specimen of bonded system.	115
5.7	Direct casting technique	116
5.8	Load-CMOD curve for bonded NSC (direct casting)	116
5.9	Load- CMOD curves for CARDDIFRC [®] adhesively bonded to NSC with and without cement paste film.	121
5.10	Load- CMOD curves for bonded and control NSC specimens, $\alpha = 0.30$	121
5.11	The influence of notch size on the load-CMOD curves of bonded NSC specimens after: (a) zero thermal cycling, (b) 30 thermal cycling and (c) 90 thermal cycling	123

5.12	The effect of thermal cycling on measured and size-independent fracture energy of CARDIFRC [®] /NSC bonded system	125
5.13	Load-CMOD curves for control and bonded NSC specimens with $\alpha=0.20$ after: (a) zero thermal cycles, (b) 30 thermal cycles and (c) 90 thermal cycles.	127
5.14	Load-CMOD curves for control and bonded NSC specimens with $\alpha=0.50$ after: (a) zero thermal cycles, (b) 30 thermal cycles and (c) 90 thermal cycles.	128
6.1	Load-CMOD curves for high and normal WS concrete specimens, with notch to depth ratio of 0.20.	137
6.2	The effect of thermal cycling on measured and size-independent fracture energy of HSC.	141
6.3	Load-CMOD curves of directly bonded CARDIFRC [®] to HSC half cube with $\alpha= 0.30$ (horizontal casting)	143
6.4	Load-CMOD curve of directly bonded HSC to CARDIFRC [®] half cube with $\alpha= 0.30$ (vertical casting)	143
6.5	The effect of cement paste film of HSC on the bonded HSC/CARDIFRC [®] specimen with $\alpha = 0.30$.	146
6.6	Load -CMOD curves for control and CARDIFRC [®] bonded to HSC specimens	146
6.7	Schematic representation of pre-existing crack initiated between the adhesive and CARDIFRC [®]	149
6.8	Schematic representation for tested CARDIFRC [®] /HSC: (a) $\alpha(0.20)$ with diagonal shear failure, (b) $\alpha(0.25)$ crack propagation through the HSC.	149
6.9	The effect of thermal cycling on measured and size-independent fracture energy of CARDIFRC [®] /HSC bonded system.	153
6.10	The effect of thermal cycling on m size-independent fracture energy of control and CARDIFRC [®] /HSC bonded specimens..	153
7.1	Beam details and arrangement of transducers: (a) beam dimensions, internal reinforcement, and load arrangement for beam without shear reinforcement, (b) beam with sufficient shear reinforcement and (c) arrangement of transducers	157
7.2	Configurations of retrofitting: (a) beam retrofitted with one strip on the tension face, (b) beam retrofitted with one strip on the tension face, two long and four short strips on the sides and (c) beam retrofitted with one strip on the tension face, two long and four short strips on the sides	158
7.3	Steel moulds for casting two retrofit strips	160
7.4	Roughened and grooved surface of damaged beams: (a) side face, (b) tension face.	161

7.5	Load-Deflection responses of control beams without shear reinforcement after: (a) 0 thermal cycles, (b) 30 thermal cycles, and (c) 90 thermal cycles.	165
7.6	Load-Deflection responses of control beams with shear reinforcement after: (a) 0 thermal cycles, (b) 30 thermal cycles, and (c) 90 thermal cycles.	168
7.7	Load-Deflection response of beams during pre-loading and unloading.	171
7.8	Load-Deflection responses of beams without shear reinforcement retrofitted with one strip on the tension face after: (a) 0 thermal cycles, (b) 30 thermal cycles, and (c) 90 thermal cycles.	174
7.9	Load-Deflection responses of beams retrofitted with three long and four short strips strip after: (a) 0 thermal cycles, (b) 30 thermal cycles, and (c) 90 thermal cycles.	178
7.10	Load-Deflection responses of beams retrofitted with one strip on the tension face after: (a) 0 thermal cycles, (b) 30 thermal cycles and (c) 90 thermal cycles.	183
7.11	Load-Deflection responses of beams retrofitted with one strip on the tension face and two strips on the sides after: (a) 0 thermal cycles, (b) 30 thermal cycles, and (c) 90 thermal cycles.	185
7.12	Typical deflection of control beams without shear reinforcement after 0, 30 and 90 thermal cycles.	189
7.13	Typical deflection of beams without shear reinforcement retrofitted with one plate on the tension face and three continues and four short plates compared with that of control beams at 20 kN after: (a) 0 thermal cycles, (b) 30 thermal cycles, and (c) 90 thermal cycles	190
7.14	Typical deflections of control beams with sufficient shear reinforcement after 0, 30 and 90 thermal cycles.	191
7.15	Typical deflection of beams with sufficient shear reinforcement retrofitted with one plate on the tension face and three continues and four short plates compared with that of control beams at 20 kN after: (a) 0 thermal cycling, (b) 30 thermal cycles and (c) 90 thermal cycles	193
8.1	Stress-strain diagram for concrete in compression	197
8.2	Stress-strain and stress-crack opening diagrams for concrete in tension: (a) pre-cracking region and (b) post-cracking region.	198
8.3	Stress-strain diagram for steel	200
8.4	Complete pre- and post peak tensile curve for CARDIFRC [®] (After Benson, 2004)	201
8.5	Beam strengthened with one strip on the tension face, two continuous and four short strips on the sides	203

8.6	Modelling of the flexural crack in the middle of the beam strengthened with one strip on the tension face, two continuous and four short strips on the sides (After Alaei, 2002)	203
8.7	Effective length of strip for calculation of crack opening	203
8.8	Relation between moment resistance of sections and curvature.	206
8.9	Moment and curvature diagrams of the beams retrofitted with: (a) one strip under four-point bending, (b) three continuous and four short strips on the sides	207
8.10	Comparison of the moment resistance of beams tested after 0 thermal cycles with that predicted by the model	209
8.11	Comparison of the moment resistance of beams tested after 30 thermal cycles with that predicted by the model.	209
8.12	Comparison of the moment resistance of beams tested after 90 thermal cycles with that predicted by the model.	209
8.13	Comparison of the load-deflection response of the control beam predicted by the model with test results when the tensile capacity of concrete is completely ignored.	210
8.14	Comparison of the load-deflection response of control beams with that of the model predictions after zero thermal cycles, when the complete tensile response is included.	210
8.15	Comparison of the load-deflection response of control beams with that of the model predictions after 30 thermal cycles.	211
8.16	Comparison of the load-deflection response of control beams with that of the model predictions after 90 thermal cycles.	211
8.17	Comparison of the load-deflection response of beams retrofitted with one plate on the tension face with that of the model predictions after zero thermal cycles.	213
8.18	Comparison of the load-deflection response of beams retrofitted with one plate on the tension face with that of the model predictions after 30 thermal cycles.	213
8.19	Comparison of the load-deflection response of beams retrofitted with one plate on the tension face with that of the model predictions after 90 thermal cycles.	213
8.20	Comparison of the load-deflection response of beams retrofitted with one plate on the tension face, two continuous and short strips on the sides with that of the model predictions after zero thermal cycles.	214
8.21	Comparison of the load-deflection response of beams retrofitted with one plate on the tension face, two continuous and short strips on the sides with that of the model predictions after 30 thermal cycles.	214

8.22	Comparison of the load-deflection response of beams retrofitted with one plate on the tension face, two continuous and short strips on the sides with that of the model predictions after 90 thermal cycles.	214
8.23	Sequence of crack growth in the middle part of the beams retrofitted with one strip: (a) existing crack in the pre-damaged beam, (b) reopening of the existing crack in the pre-damaged beam, (c) propagation and penetration of the dominant crack into the tension strip, (d) opening of the dominant crack, and (e) load levels corresponding to the observed crack growth sequence (After Alae and Karihaloo, 2003b)	217
8.24	Cracking in middle part of beams retrofitted with three strips: (a) when pre-existing crack penetrated into tension strip. For clarity side strip is not shown. Note that stages (a) and (b) of Figure 8.23 are obscured by side strips; (b) at maximum load, and (c) load levels corresponding to stages (a) and (b). (After Alae and Karihaloo, 2003b)	218
8.25	Free body diagram of dominant flexural crack in retrofitted beams. Beams retrofitted with (a) one tension strip, and (b) one tension strip and two side strips. (After Alae and Karihaloo, 2003b)	220
8.26	Smooth closure of crack faces. (After Alae and Karihaloo, 2003)	220
8.27	Towards the discretisation of the bridging stresses in concrete (After Alae and Karihaloo, 2003b)	223
8.28	Cracking of a reinforced concrete member under flexure (After Park and Paulay 1975)	231
8.29	Comparison of the moment resistance of retrofitted beams with the prediction of the model after: (a) 0 thermal cycles, (b) 30 thermal cycles and (c) 90 thermal cycles.	234

Table	List of Tables	Page
4.1.	Mix proportions for CARDIFRC® Mix I and Mix II (per m ³) (Karihaloo et al., 2001)	83
4.2	Typical material properties of CARDIFRC® Mix I and Mix II,	83
5.1.	Mix proportions for CARDIFRC® Mix I (per m ³) (Karihaloo et al., 2002)	94
5.2	Cube crushing strength of NSC and CARDIFRC® after 0, 30 and 90 thermal cycling.	100
5.3	Splitting strength results of NSC and CARDIFRC® after 0, 30 and 90 thermal cycling	102
5.4	Flexural test results of NSC and CARDIFRC® after 0, 30 and 90 thermal cycling	103
5.5	f_c, f_i and f_r after different environmental conditions and age.	104
5.6	The effect of thermal cycling on the modulus of elasticity of NSC and CARDIFRC®	104
5.7	WS results of NSC after 0 thermal cycling	111
5.8	WS results of NSC after 30 thermal cycling.	111
5.9	WS results of NSC after 90 thermal cycling.	111
5.10	Size-independent fracture energy after 0, 30 and 90 thermal cycles.	112
5.11	Characteristic length l_{ch} of NSC after 0, 30 and 90 thermal cycles.	114
5.12	NSC repaired with CARDIFRC® (direct casting) $\alpha = 0.50$	116
5.13	WS results of CARDIFRC® adhesively bonded to NSC ($\alpha = 0.30$)	121
5.14	WS results of CARDIFRC®/NSC after 0 TC	122
5.15	WS results of CARDIFRC®/NSC after 30 TC	122
5.16	WS results of CARDIFRC®/NSC after 90 TC	122
5.17	Size-independent fracture energy of bonded NSC specimens	124
5.18	The effect of thermal cycling on failure load of repaired and control NSC specimens	129
6.1	Mix proportions for HSC	134
6.2	Cube crushing test of HSC after different thermal cycling.	135
6.3	Splitting test of HSC after different thermal cycling.	135
6.4	Flexural strength test of HSC after different thermal cycling.	136
6.5	f_c, f_i and f_r after different environmental conditions	136
6.6	The effect of thermal cycles on the Modulus of elasticity of concrete	137
6.7	WS results of control HSC after 0 TC.	139
6.8	WS results of control HSC after 30 TC.	139
6.9	WS results of control HSC after 90 TC.	140
6.10	Size-independent specific fracture energy after different thermal cycles.	140
6.11	The effect of thermal cycles on l_{ch} for concrete	141
6.12	Trial WS results of CARDIFRC®/HSC with $\alpha=0.30$ (adhesive bonding)	147
6.13	WS results of CARDIFRC®/HSC after 0 TC.	151
6.14	WS results of CARDIFRC®/HSC after 30 TC.	151

6.15	WS results of CARDIFRC [®] /HSC after 90 TC.	151
6.16	Size-independent specific fracture energy after different thermal cycles.	152
7.1	Compression and splitting strength results for ordinary concrete	163
7.2	Four-point test results of control beams after thermal cycling.	166
7.3	Four-point test results of control and retrofitted beams without shear reinforcement after different thermal cycles	172
7.4	Four-point test results of control and retrofitted beams with sufficient shear reinforcement after different thermal cycles	181
8.1	Assumed parameters for modelling the compressive strength behaviour of concrete	197
8.2	Assumed parameters for modelling the tensile strength behaviour of concrete	199
8.3	Tensile test results of steel reinforcing bar	200
8.4	Comparison of the test results of beams with only flexural reinforcement with the analytical model prediction.	208
8.5	Crack opening w_F , crack depth a_F and the moment resistance M_F of the beams at the maximum load predicted by the model after 0, 30 and 90 thermal cycles.	233

Plate	List of Plates	Page
5.1	Wedge splitting test, showing the wedge mounted between two roller bearing at each side of the specimen.	108
5.2	Wedge splitting test for bi-material system CARDIFRC [®] /NSC)	108
5.3	The effect of cement paste film on the failure mode of CARDIFRC [®] /NSC, (a) before, (b) after removal of film.	118
5.4	The effect of cement paste film on the fractured surface of CARDIFRC [®] /NSC: (a) before, (b) after removal of film.	118
6.1	The effect of cement paste film on the failure mode of CARDIFRC [®] /HSC, (a) before, (b) after the removal of film.	145
6.2	The effect of cement paste film on the fractured surface of CARDIFRC [®] /HSC, (a) before, (b) after the removal of film.	145
6.3	The effect of pre-existing crack on the fracture surfaces of bonded specimens.	149
7.1	Typical shear failure in control beams reinforced only in flexure.	169
7.2	Typical flexural failures in control beams reinforced in shear and flexure.	169
7.3	Typical shear failure in beams retrofitted with one strip on the tension Face.	175
7.4	Debonding at the end of the strip.	175
7.5	Shear failure of beams retrofitted with three plates only	179
7.6	Typical flexural failure of beams retrofitted with three long and four short strips	179
7.7	Typical flexural failure of beams reinforced in shear and flexure and retrofitted with one strip on the tension face.	182
7.8	Typical flexural failure of beams reinforced in shear and flexure and retrofitted with three long and four short strips..	186
7.9	Bridging action of steel fibres	186

Chapter 1

Introduction

1.1 Introduction

Concrete has been used in construction for more than a century as a main construction material owing to its significant resistance in compression. Much attention has been paid to the mechanical and fracture properties of concrete at room temperature (under 50° C), including strength, stiffness, toughness, brittleness and fracture energy. Detailed information can be found in textbooks (e.g. Neville, 1995; Karihaloo, 1995; Shah et al., 1995; Van Mier, 1997).

Hot dry climate is characterised by high daytime temperature (40-50°C), very low relative humidity, intense solar radiation, and high diurnal temperature variation, of about 16°C. Moreover, it has been revealed that the surface temperature of exposed concrete reaches around 60°C to 65°C when the ambient temperature is only about 30°C to 33°C. In some places where the temperature goes beyond 40°C, the surface temperature of an exposed concrete element reaches somewhere between 80°C to 90°C during the day. On the other hand, it may fall to 5-10°C lower than the ambient temperature at night-time (Soroka and Jaigerman, 1984). Therefore, a concrete element that is situated in such climatic conditions may be said to undergo a thermal cycle every 24 hrs.

Although some of the material properties at elevated temperature (above 100 °C) have been studied (i.e. strength and stiffness) (e.g. Castillo and Durrani, 1990; Saad et al., 1996; Bertero and Polivka, 1972; Berwanger and Sarkar, 1973 and Schneider, 1976), little information is available on the fracture properties like toughness, brittleness and fracture energy (e.g. Zhang et al., 2000 and 2002; Baker 1996; Bazant and Part, 1988 and Prokoski, 1995). Moreover, very limited research has been conducted to study the properties of concrete in hot dry climatic environments and when it is exposed to daily or annual temperature fluctuations (thermal cycling) (Rostasy and Budelmann, 1986; Abdel-Fattah and Hamoush, 1997)

With regard to the studies related to the fracture properties mentioned above accounting for temperature effect, only size-dependent fracture energy has been considered. However, size-independent fracture energy is required in practical applications. Recently it has been demonstrated that the size-independent fracture

energy can be determined based on the concept of boundary effect model proposed by Duan et al (2001), and its additional verifications by Abdalla and Karihaloo (2003).

1.1.1 Retrofitted concrete

Concrete structures can deteriorate and therefore need repair after long periods in service. To accommodate for a load carrying capacity higher than the original design value, members may need to be strengthened through retrofitting. A common repair and strengthening technique for concrete beams is to bond a steel plate to the tension side of the beam. However, several problems have been encountered with this technique, including the occurrence of undesirable shear failures, difficulty in handling heavy steel plates, corrosion of steel that can cause deterioration of the bond at a glued steel-concrete interface, and the need for butt joint systems as a result of limited workable lengths (Jones et al., 1988; Ziraba et al., 1994).

Recently, attention has been directed towards the use of fibre-reinforced plastic (FRP) plates, which offer a higher strength/weight ratio and improved durability over their steel counterparts (Meier et al., 1992; Meier, 1997). Retrofitting using FRP is also vulnerable to undesirable brittle failures due to a large mismatch in the tensile strength and stiffness with that of concrete. Another problem, which has also been observed with this technique, is the effect of long exposure to temperature variations (Sen et al., 2000; Zhen and Chung, 2000; Toutanji and Gomez, 1997).

It is important to note that exposure to a variety of environmental conditions can dramatically change failure modes of the FRP composites, even in cases where performance levels remain unchanged. Exposures can result in the weakening of the interface between FRP composites and concrete, causing a change in the failure mechanism and sometimes a change in performance (Karbhari, 1998). A daily temperature variation of about 40°C can cause significant thermal strains at the repair interface due to differences in the coefficients of thermal expansion of the repair materials and the parent concrete. This thermal incompatibility at the repair interface may significantly damage the quality of adhesion/bond between the repair material and the parent concrete. As far as the compatibility between the repair material and

concrete is concerned, it must be pointed out that one of the essential parameters that will determine the success or failure of a repair is the effective bonding of repair material to the old concrete. This implies concerns about surface preparation as well as the quality of adhesion and the compatibility of the bonding material with the parent concrete. The last factor is of particular importance in hot climate conditions such as countries situated at the tropic of cancer, where fluctuations of temperature on concrete surfaces may range from 25° C to 75° C on a typical summer day. Over a period of time these thermal cycles may cause debonding of the repair material and parent concrete at the repair joint due to thermal incompatibility of the parent concrete and the repair material.

In harsh climatic conditions there is an acute need for a durable repair that can withstand the climatic influences that are caused by large changes in temperature or humidity and their subsequent affects. A durable repair can be defined as a material that will bond firmly to the existing concrete for the total length of the expected surface life of the repair and will not develop cracks that will reduce the expected level of protection.

A new retrofitting technique using CARDIFRC[®], a material compatible with concrete, has recently been developed at Cardiff University. It overcomes some of the problems associated with the current techniques based on externally bonded steel plates and FRP (fibre-reinforced polymer) which are due to the mismatch of their tensile strength, stiffness and coefficient of linear thermal expansion with that of the concrete structure being retrofitted (Karihaloo et al., 2002).

The results of Karihaloo et al. (2002) showed that retrofitting of flexural RC members using CARDIFRC[®] plates on the tension face improves the flexural load carrying capacity and also decreases the crack width and the deflection. Moreover, when the RC beams were retrofitted with three strips (one strip on the tension face and two strips on the sides), the damaged beams were strengthened not only in flexure, but also showed improved shear capacity.

This thesis investigates the feasibility of using CARDIFRC[®] as a retrofitting material in hot climatic conditions

1.2 Objectives of the Thesis

The main objectives of this thesis are;

- To investigate the performance of reinforced concrete beams retrofitted with CARDIFRC[®] and subjected to thermal cycles between 25°C and 90°C. Each thermal cycle consists of a temperature rise period of 20min in which the temperature is raised from 25°C to 90°C, a dwell period of 8 hours at 90°C and a cooling period of 16 hours in which the temperature is reduced from 90°C to 25°C;
- To evaluate the effect of thermal cycling on the mechanical and fracture properties of normal and high strength concrete;
- To evaluate the role of the interface when normal and high strength concretes are repaired with CARDIFRC[®], concentrating particularly on the main aspect that might affect the repair system such as thermal cycling and surface preparation.

1.3 Outline of the Thesis

Including this introductory chapter, this thesis is divided into nine chapters. The layout of the chapters is as follows:

Chapter-1 presents a general introduction to the study as well as the objectives and an outline of the thesis.

Chapter-2 discusses the different methods for retrofitting concrete structures such as steel plates, fibre reinforced plastics FRP and High Performance Fibre Reinforced Cementitious Composites (HPFRCCs) such as Engineered Cementitious Composites (ECC) and CARDIFRC[®]. A description of each method is presented.

Chapter-3 provides a concise review of the basic concepts of the fracture mechanics approach (FM). It describes those fracture mechanics aspects which will be useful in the subsequent chapters. Firstly, linear elastic fracture mechanics (LEFM) for brittle materials is discussed. Then it is argued that LEFM is not applicable to concrete. Therefore, the concepts of non-linear fracture theories for concrete are explained. Secondly, the fracture behaviour of repaired systems is discussed. Finally, an application of fracture mechanics to reinforced concrete structures is demonstrated on a longitudinally reinforced cracked beam.

In Chapter 4, the behaviour of normal strength concrete (NSC), high strength concrete (HSC), high performance concrete (HPC) and fibre reinforced concrete (FRC) is briefly reviewed. High Performance Fibre Reinforced Cementitious Composites (HPFRCCs) with a particular reference to CARDIFRC[®] is reviewed in depth including, types, constitutive relations and fracture properties.

Chapters 5 and 6 evaluate the performance of NSC and HSC specimens repaired with CARDIFRC[®] using the wedge splitting test (WST) (Tschegg, 1991). The main factors that could affect the bond between the repair material and concrete such as the surface roughness and thermal cycling are also investigated. It is shown that surface roughness plays a significant role in the overall bonding system and no visual deterioration is observed after thermal cycling. In this chapter the mechanical and fracture properties of NSC and HSC under thermal cycling are investigated experimentally. It is shown that these properties are influenced by thermal cycling.

The application of CARDIFRC[®] to retrofitting pre-damaged reinforced concrete beams (with and without shear reinforcement), after thermal cycles, is investigated in Chapter 7. It is shown that the retrofitted beams are stronger, stiffer and more importantly fail through flexure rather than shear. It was also observed that thermal exposure does not cause any degradation to the retrofitted beam strength. CARDIFRC[®] is therefore a very promising material for repair and retrofit in high temperature environments.

Chapter 8 is devoted to the prediction of the moment resistance and the load–deflection behaviour of the retrofitted beams using two analytical models. The first model is based on the classical theory, but takes into account the complete tensile contributions (i.e. pre and post-crack response) from concrete and CARDIFRC[®]. The second model takes a purely fracture mechanics approach and follows the initiation and growth of the flexural crack which eventually leads to the failure of the retrofitted beams. The predictions of both models are in good agreement with the experimental test results

Chapter 9 finally provides some general conclusions and recommendations for future work in this field of study.

Chapter 2

Retrofitting of concrete structures

2.1 Introduction

The deterioration of concrete structure may be caused by many different factors such as accidental loading, chemical reactions, corrosion of embedded steel, freezing and thawing, large temperature variations, fire damage and inadequate construction or design. The replacement and rebuilding of most deteriorated structures is not always feasible. Therefore, all of these forms of deterioration necessitate repair of the structure.

In general, there are four repair-related terms that have often been used interchangeably in the construction maintenance industry. These are; repair, strengthening, retrofitting, and rehabilitation, and defined as follows:

- **Repair:** to improve the deteriorated structural performance of damaged structures back to their original level;
- **Strengthening:** this is the process of enhancing the structural performance over and above the originally specified levels, usually by means of adding extra structural components.
- **Retrofitting:** this term is more often used in North America. It implies additional structural components after initial construction and has been used synonymously with both rehabilitation and strengthening.
- **Rehabilitation:** this is a generic term indicating any aspect of repair and strengthening. Moreover, the rehabilitation work is not necessarily limited to structural sense, any non structural or decorative alterations to the appearance of a structure, for example, can also be termed as rehabilitation.

The common techniques for retrofitting concrete structure are by bonding steel or fibre reinforced plastic FRP plates to the tension side of the beam. However, several problems have been encountered with these techniques, e.g. corrosion of steel, which adversely affects the bond at the steel concrete interface, and premature debonding of FRP.

High performance fibre reinforced cementitious composites HPFRCCs are currently found to be reliable and effective materials for retrofitting (Li et al., 1995; Lim and

Li, 1997; Karihaloo et al., 2000; Karihaloo et al., 2001). The main advantage of these materials is their compatibility with concrete. Among these are Engineered Cementitious Composites (ECC) and CARDIFRC®.

This chapter provides a brief overview of the methods for retrofitting concrete structure using steel plates, FRP laminates, ECC and CARDIFRC®. Advantages and disadvantages of each method are evaluated.

2.2 Externally bonded steel plates

The method of strengthening existing reinforced concrete structures by external steel plate bonding using a structural adhesive system is a major strengthening technique. This technique has been used worldwide for over 30 years. Advantages of this method as described by Barnes et al. (2001) are

- Possible increase in the beam ductility;
- It may be possible to strengthen the structure whilst it is still in use;
- Provides an increase to both the serviceability and the ultimate load capacity of the section;
- Accessibility for inspection and maintenance.

2.2.1 Flexural strengthening

Strengthening and repair of reinforced concrete members by steel plates externally bonded to the tension face of the members is one technique that has been studied by many researchers (e.g. Jones et al., 1988; Swamy et al., 1987; Jones et al., 1980). These investigations show that the bonding of steel plates to the surface of concrete beam can lead to a significant improvement in structural performance under both service and ultimate load conditions. Jones et al. (1980) studied the behaviour of plain and reinforced concrete beams strengthened with steel plates bonded to the tension face of the beams. They used two different types of adhesive and two grades of steel plate. The effects of adhesive thickness, plate lapping, multiple plates, and of pre-cracking prior to bonding were investigated. They concluded that epoxy bonded steel plates resulted in enhancement of elastic range, reduction in tensile stresses, increase in strength and stiffness, and improvement in ductility at flexural failure.

Another study by Macdonald and Calder (1982) reported the results of rectangular beams strengthened with epoxy bonded steel plates. Their results showed significant improvements in the ultimate strength of the strengthened beams. Furthermore, exposure tests were also carried out on reinforced concrete beams with steel plates bonded on the tension face. Results showed a smaller ultimate strength. This reduction in the ultimate strength was attributed to corrosion at the interface of steel and epoxy.

2.2.1.1 Failure modes

Ziraba et al. (1994) classified the common failure modes of reinforced concrete beams strengthened with steel plates on the tension face into

- Flexural failure;
- Interface separation;
- Plate peel-off.

Interface separation occurs when the adhesive is weak or gluing is not properly executed and can be avoided by proper quality control. Plate peel-off is considered as a premature failure which happens if the allowable strength values of the interface are exceeded. If the bonding adhesive is weak, this type of failure may be characterized by plate debonding initially emanating from the plate curtailment. As the plate debonding proceeds a way from the support and the effective plate length is reduced, the peak peeling stresses progressively increase to a value where a shear critical crack develops, leading to sudden failure (Figure 2.1a).

If gluing is strong enough to prevent plate debonding, cracking emanates from the location of plate curtailment. The existence of peak peeling and shear stresses at the plate curtailment zone, in addition to the bonding stress, results in a biaxial tensile stress state, forcing the crack to move in an essentially horizontal direction just below the level of internal reinforcement where the section is weakest. Failure ensues when the horizontal crack propagates, culminating in a steep vertical ascent toward the point of loading (Figure 2.1b).

Researchers have tried to avoid plate peeling failure by anchoring the ends of the plates using bolts. However, much work remains to be done before such anchoring technique may safely be used in practice (Raof et al., 2000). Nevertheless, a fairly common technique for preventing this type of failure involves using normal (or, lately, prestressed) bolts to provide additional anchorage at the end of the plate: by virtue of the prestressed bolts, experimental work reported by Jansze et al. (1996) demonstrates that the mechanism of plate separation changes from brittle concrete cover peel-off to a more ductile type of failure between the concrete and the epoxy glue. Munawar (1992) emphasised that using external shear reinforcement in the shear span region prevents peel-off failure and ensures flexural failure with accompanying crushing of concrete in the compression zone. Oehlers et al. (1998) presented an experimental study in which steel plates are glued to the sides of RC beams specially to inhibit tension face plates from debonding. Their results show that adhesively bonded plates to the sides of RC beams can prevent such premature debonding.

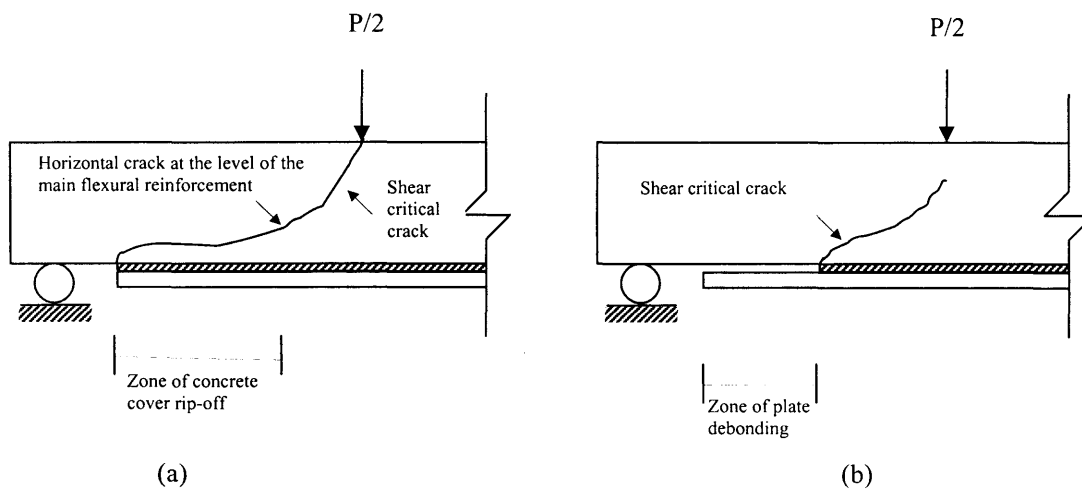


Figure 2.1 Sudden shear failures of plated beams. Failure by: (a) ripping off of the concrete cover, (b) Plate debonding (After Ziraba et al., 1994)

2.2.2 Shear strengthening

Shear failure of concrete structures always occurs in a catastrophic manner due to its brittle nature and the fact that it gives no advance warning prior to failure. Various laboratory studies for rehabilitation of shear-deficient structures using different methods such as resin injection, post tensioning in shear and stitching of shear cracks

have been reported (Hewlett and Morgan, 1982; Collins and Roper, 1990). The most common method to enhance the shear capacity of damaged beams is to bond steel

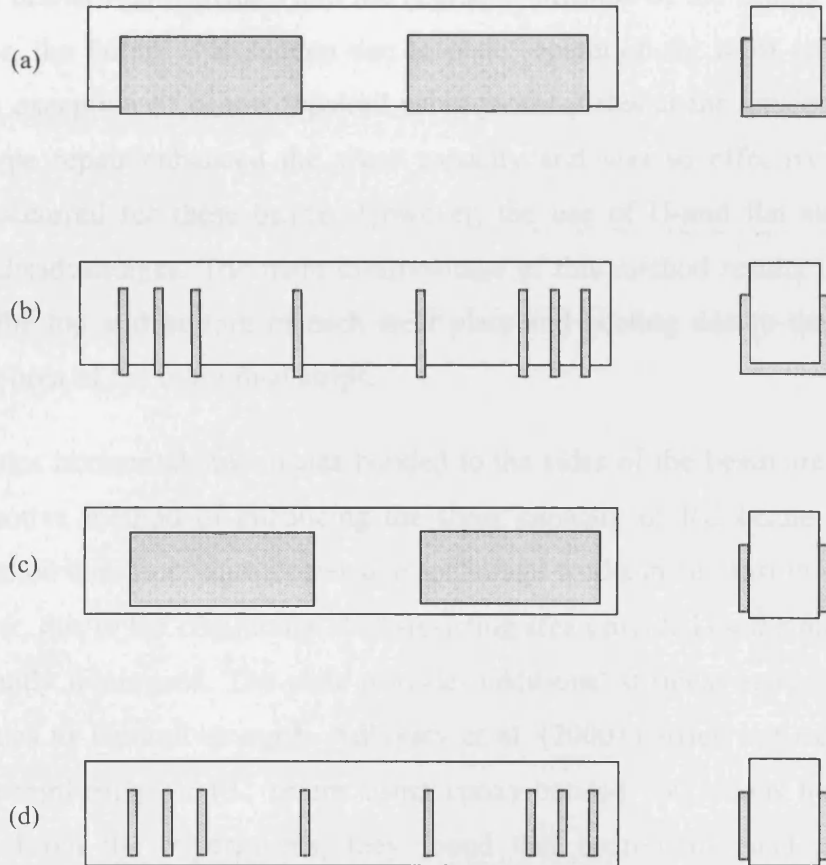


Figure 2.2. Repair schemes: (a) full encasement of the shear zone by jacket plate, (b) U- strips on the shear zone, (c) flat strips at the shear zone, and (d) flat plates on the sides of the beams (After Sharif et al. 1995)

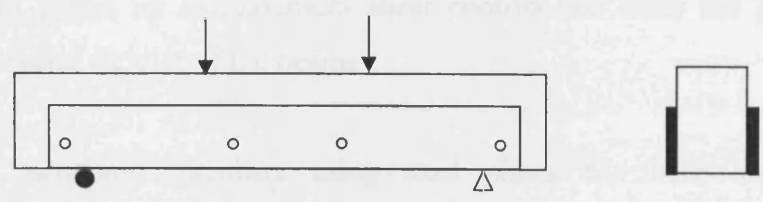


Figure 2.3 Shear strengthening of RC beam using horizontal steel plate (After Adhikary et al., 2000)

plates to the sides of the beam. Sharif et al. (1995) used different arrangements of steel plates bonded on the sides of the beams in order to eliminate shear failure and develop ductile behaviour (Figure 2.2). They observed that the strength of all repaired beams was increased and the degraded stiffness of the beams was restored. However, the failure was sudden due to plate separation for most repaired beams, with the exception of beams repaired using jacket plates at the tension zone. Such jacket-type repair enhanced the shear capacity and was so effective that flexural failure occurred for these beams. However, the use of U-and flat steel strips has several disadvantages. The main disadvantage of this method results in the need to anchor the top and bottom of each steel plate and peeling due to the small shear-resisting area of the individual strips.

Continuous horizontal steel plates bonded to the sides of the beam are a convenient and effective method of enhancing the shear capacity of RC beams (Figure 2.3). This method does not require extensive anchorage works in contrast to vertical strips. Moreover, due to the continuous shear-resisting area provided by the plate, peeling is significantly minimised. The plate provides additional stiffness against bending and contributes to flexural strength. Adhikary et al. (2000) carried out experiments for shear strengthening of RC beams using epoxy-bonded continuous horizontal steel plates. From the experiments, they found that continuous steel plates bonded externally on the sides are effective for the shear strengthening of RC beams. The shear strength of the beams increases with increasing plate thickness and plate depth. A maximum 84 per cent increase in shear strength was observed over that of the control beam without steel plate. Moreover, they observed that beams should be reinforced with plates up to maximum shear contribution from the plate and to improve the flexural rigidity of the beams.

Strengthening structural members using steel plates has been shown to be satisfactory technique in the past, but its applications have declined in recent decades. This is owing to perceived disadvantages regarding the use of steel, due to

- Transportation and handling;
- Installation of heavy plates;

- The need for having a substantial working cradle of falsework;
- Limitation in supplying plates of appropriate lengths and forming satisfactory joints;
- Uncertainty regarding adhesive bond durability;
- The need for careful surface preparation of steel prior to bonding;
- Metal corrosion.

The greatest concern in steel plate bonding is the problem of corrosion of steel plates. Since the plates are bonded externally, they are even more susceptible than the internal steel reinforcement in RC structures to potential and prolonged environmental attack even though coating or other form of encasement may be applied.

In recent years, researchers are focusing their attention on using non-metallic composite materials instead of steel plates to overcome some of the shortcomings of this strengthening technique.

2.3 Fibre reinforced plastic (FRP)

The introduction of fibre reinforced plastic (FRP) offers unique advantages for tackling many civil engineering problems in areas where conventional materials fail to provide satisfactory service life. FRP materials consist of strong and stiff fibres embedded in a matrix resin. They exhibit superior properties, such as high tensile strength and stiffness (between 1000 - 2000 MPa), lightweight (SG 1.3 - 1.5), relatively high stiffness (75 – 150 GPa), outstanding corrosion resistance and excellent fatigue performance. These properties make them suitable for rehabilitation. Externally bonded FRP composites are a relatively new repair technology that is attractive because of its ease and speed of installation in the rehabilitation of deteriorating civil engineering structures. As the externally bonded FRP sheets are applied to tension face of concrete beams, it is possible to increase the ultimate strength and stiffness of the repaired members.

The main material types used in the construction industry are glass, carbon and aramid fibres (He et al., 1997; Jones and Swamy, 1995). Commercially available

fibres vary widely in their ability to meet particular design needs. For example, many categories of glass fibres tend to degrade in the presence of alkaline and humid environment, but they have considerable toughness. Carbon fibres can have high stiffness and resistance to chemical attack, but they tend to also have low toughness and impact resistance. Aramid fibres have toughness similar to that of glass fibres, but in comparison to carbon are less dense, and have a lower Young's modulus. In the selection of fibres some factors have to be considered such as electrical conductivity, coefficient of thermal expansion, use in elevated temperature ranges, radiation resistance, time dependent degradation and overall cost of installation and maintenance (Tann, 2001)

Strengthening with FRP composites can be applied to various types of structural members including beams, columns, slabs, and walls. Depending on the member type, the objective of strengthening may be one or a combination of several of the following;

- To increase axial, flexural, or shear load composites;
- To increase ductility for improved seismic performance;
- To increase stiffness for reduced deflections under service and design loads;
- To increase the remaining fatigue life;
- To increase durability against environmental effects.

2.3.1 Flexural strengthening

Flexural strengthening of reinforced concrete elements using FRP composites can be provided by epoxy bonding the materials to portions of the element in tension, with fibres parallel to the principal stress direction. Well-established strengthening procedures for RC structures may be followed, provided that special attention is paid to issues related to the linear-elastic nature of FRP materials and the bond between the substrate and FRP (Bakis et al., 2002). As the externally bonded FRP composites are applied to tension face of concrete beams, it is possible to increase the ultimate strength and stiffness of the repaired members. This have been verified by several researchers (e.g. Teng et al., 2002; Triantafillou and Plevris, 1992; Saadatmanesh

and Ehsani, 1991; Hutchinson and Rahimi, 1993; Meier and Kaiser, 1991; Rahimi and Hutchinson, 2001).

2.3.1.1 Modes of failure

Failure of FRP strengthened members may take place through several mechanisms depending on the beam and strengthening parameters. In general, the main failure modes are (ACI, 2001; Buyukozturk and Hearing, 1998):

1. Steel yielding followed by FRP rupture;
2. Concrete compressive crushing;
3. Shear failure;
4. Concrete peel-off (ripping off of the concrete cover);
5. FRP debonding (delamination of FRP plate).

Of the above, modes one and two are the most desirable modes, since they happen in a ductile manner. Sections with smaller amounts of reinforcement fail by FRP tensile rupture, while larger amounts of reinforcement result in failure by crushing of the compressive zone concrete prior to the attainment of ultimate tensile strain in the outermost layer of FRP (Bakis et al., 2002). Mode three occurs when the shear capacity of the section is exceeded prior to the load level reaching the flexural strength. It has been found that the most common failure modes are associated with concrete peel-off and delamination of FRP strip from the concrete surface (Buyukozturk and Hearing, 1998; Wu et al., 1997). These failure modes are undesirable because the FRP plate would not be fully utilized. The former failure mode is initiated by stress concentration at the plate end, which leads to the formation and upward propagation of an inclined crack. Once the crack grows significantly beyond the steel reinforcement, load transfer to the concrete cover will occur mainly through shear and normal stresses at the level of reinforcements. Under increased loading, a horizontal crack may form and its propagation will cause the concrete cover to peel-off with the FRP plate. Moreover, failure by ripping-off occurred when the shear and tensile stresses in the reinforcing bars bottom level exceeded the strength of the concrete reinforcing bars interface at the plate-end region.

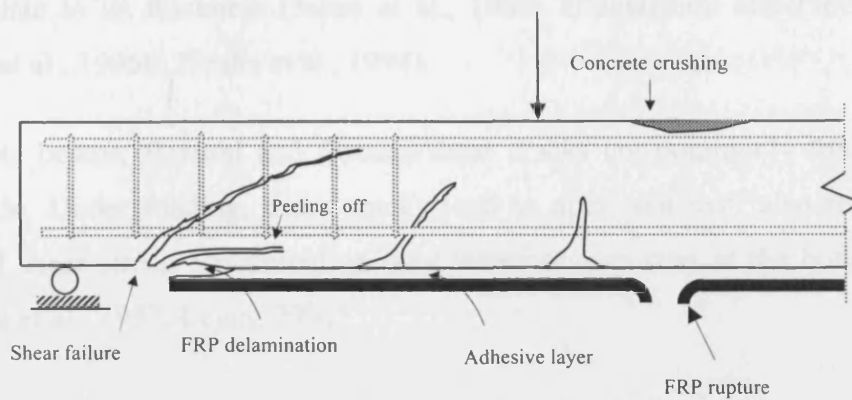


Figure 2.4 Common failure modes for FRP retrofitted beams

Triantafyllou and Plevris (1992) tested eight small RC beams. One beam was used as a control while the other seven were strengthened by CFRP sheets. The percentages of CFRP reinforcement for the seven beams varied from 0.1 to 1.26. The results show that the failure loads of the CFRP strengthened beams increased from 53% to 335 % over the unplated control beam, while the mid span deflections at failure were shown to be typically halved compared to the conventionally reinforced control beam. Of the eight beams tested to ultimate failure, the control beam failed by tension reinforcement yielding, the two beams with the two lowest CFRP reinforcement failed by steel yielding first followed by CFRP rupture. All other beams failed either by ripping off of the concrete cover or FRP delamination. The study confirmed that concrete cracking had an important role in the FRP delamination failure. It concluded that the FRP delamination was related to the thickness of the CFRP composites; there appeared to be a critical thickness, beyond which brittle failure occurs without CFRP material's flexural strength being fully utilized, and as a result the ductility of the beam was adversely affected.

Delamination of FRP plate commonly occurs at the end of the plate. From flexural tests and modified beam tests on composite-to-concrete joints, it was concluded that plate delamination was due to high local interfacial bond stresses and peeling forces at the ends of the plates (Oehlers and Moran, 1990; Quantrill et al., 1996a). These stresses were found to depend on the tensile strength of the concrete, the flexural rigidity of the cracked plated section, the concrete surface preparation, the strength and thickness of the adhesive, and, to a lesser extent, on the ratio of the width of the

bonded plate to its thickness (Jones et al., 1980; Triantafillou and Plevris, 1992; Quantrill et al., 1996b; Ziraba et al., 1994).

In concrete beams, flexural and flexural/shear cracks are commonly found on the tensile side. Under loading, these cracks tend to open and may also reduce high interfacial shear stress. Delamination may therefore also start at the bottom of the beam (Wu et al., 1997; Leung 2001)

FRP debonding can also occur in different manner (Wu et al., 1997; Rahimi and Hutchinson, 2001) in a way that the separation occurs within the concrete at a small distance from the concrete/adhesive interface plate. This is evidenced from the thin layer of concrete (of about several millimetres) attached to the FRP plate after debonding failure occurs. In this case, debonding is initiated at the bottom of a flexural or shear/flexural crack along the concrete beam.

The occurrence of debonding at a distance from the concrete/adhesive interface can be explained as follows. Firstly, penetration of adhesive into the concrete may increase the strength of a thin layer of material right next to the interface. Secondly, high shear stress acting along the concrete/adhesive interface will produce microcracks that tend to propagate away from the interface at a certain angle. The interaction and coalescence of these inclined cracks will produce the final debonding surface inside the concrete (Leung, 2001).

Several methods for eliminating such premature failures have been investigated. These include plate curtailment, the use of end anchorage plates, and the addition of side plates at the soffits. Tests by Jones et al. (1988) showed that the use of glued anchor plates at the end of the strengthened plate was the most effective way to prevent peeling failure.

2.3.2 Shear strengthening

As mentioned earlier, shear failure is catastrophic and occurs with no advance warning of distress. Many of the existing RC beams have been found to be deficient in shear and in need of strengthening. Deficiencies occur owing to several reasons such as insufficient shear reinforcement or reduction in steel area due to corrosion,

increased service load, construction defects. In these situations, it has been shown that externally bonded FRP reinforcement can increase the shear capacity.

Different methods have been used to bond FRP plates/sheets for shear strengthening of RC beams. These include bonding FRPs on the sides of a beam only (Chaallal et al., 1998a; Li et al., 2001), bonding U jackets to cover both sides and the soffit (Chaallal et al., 1998b) and wrapping FRPs around the cross section (Tajsten and Teknik, 2001; Winistoerfer et al., 2001).

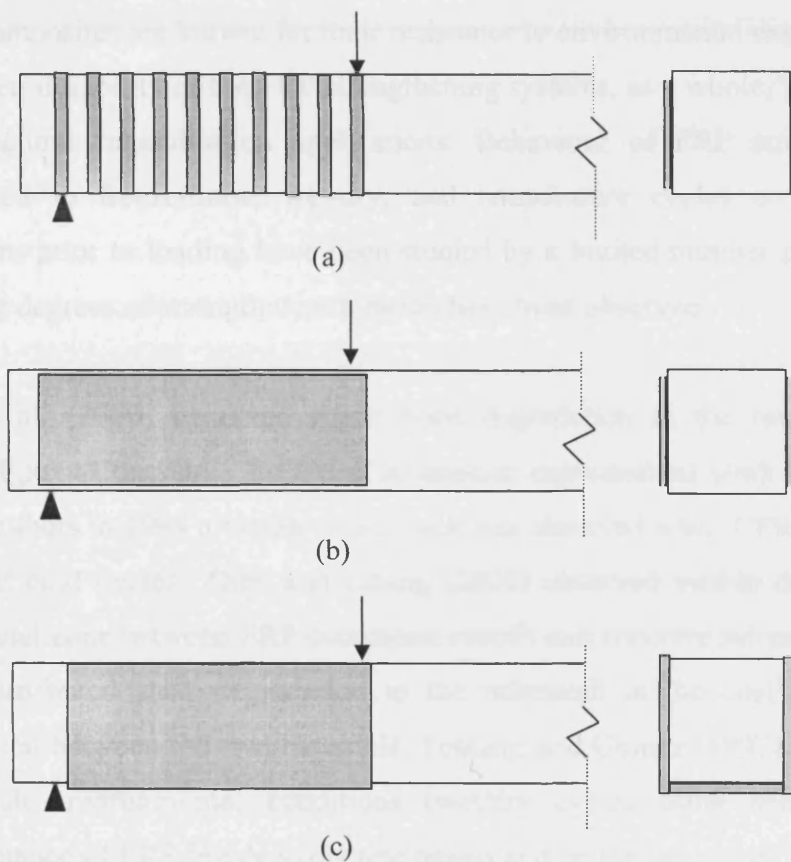


Figure 2.5 Three GFRP shear strengthening schemes (a) shear strips, (b) shear wings, and (c) U-Jacket. (After Al-Sulaimani et al., 1994)

Al-Sulaimani et al. (1994) tested sixteen low internal reinforcement beams strengthened with GFRP. Three different repair configurations were used for external shear strengthening as shown in Figure 2.5. Test results indicate that using external bonded GFRP plates for shear strengthening was potentially a feasible technique. The use of GFRP shear strips and shear wings resulted in similar increase in beams shear capacity. The failure of shear strips and wings by GFRP plate delamination

when the maximum shear stress at the bottom of the strips or wings reaches the interface shear strength, this behaviour was noted to be similar to that associated with flexural strengthening. They concluded that all three shear repair schemes restored the stiffness of the beam, which was degraded during the preloading stage. It was found that shear repair by the U-jacket method was the most effective one. No plate debonding was observed in these beams and the increase in shear capacities were significant which resulted in flexure failure of the beams

2.3.3 Environmental effects

FRP composites are known for their resistance to environmental exposure conditions, however, durability of the FRP strengthening systems, as a whole, is a major concern in structural rehabilitation applications. Behaviour of FRP strengthened beams subjected to freeze-thaw, wet-dry, and temperature cycles or various aqueous solutions prior to loading have been studied by a limited number of researchers and varying degrees of strength deterioration have been observed.

Sen et al. (2000) observed slight bond degradation in the interfacial phase of CFRP/Epoxy/Concrete. Referring to another experimental work conducted by the same authors in 1999 a visible bond crack was observed when CFRP was exposed to hot and cold cycles. Zhen and Chung (2000) observed visible degradation in the interfacial zone between FRP composite retrofit and concrete substrate upon heating. They attributed such degradation to the mismatch in the coefficient of thermal expansion between the two materials. Toutanji and Gomez (1997) studied the effect of harsh environmental conditions (wet/dry cycles using salt water) on the performance of FRP-bonded concrete beams and on the interfacial bond between the fibre and the concrete. Their results showed that the specimens subjected to wet/dry conditions showed less improvements in flexural strength than those kept at room temperature. The reduction in the strength may be attributed to the degradation of the epoxy, which led to the weakening of the bond between the concrete specimens and the FRP sheets. Chajes et al. (1995b) studied the durability of concrete-epoxy fabric system under severe environments. They performed flexural tests on 48 small-scale RC beams exposed to freeze and thaw or wet and dry in a calcium chloride solution, and 12 beams were left in a control environment. The tests indicate that chloride

exposure in both wet and dry and freeze and thaw environments cause degradation to the beam strength.

It is important to note that exposure to a variety of environmental conditions can dramatically change failure modes of the FRP composites, even in cases where performance levels remain unchanged. Exposures can result in the weakening of the interface between FRP composites and concrete causing a change in the failure mechanism and sometimes a change in performance (Karbhari, 1998). The daily temperature variation of about 40° C can cause significant thermal strains at the repair interface due to differences in the coefficients of thermal expansions of the repair materials and the parent concrete. This thermal incompatibility at the repair interface may significantly damage the quality of adhesion/bond between the repair material and the parent concrete.

As far as the compatibility between the repair material and concrete is concern, it must be pointed out that one of the essential parameters that will determine the success or failure of a repair is the effective bonding of repair material to old concrete. This implies concerns about surface preparation as well as the quality of adhesion and the compatibility of the bonding material with the parent concrete. The last factor is of particular importance in hot climate conditions such as these in countries situated at the tropic of cancer, where fluctuations of temperature on concrete surfaces may range from 25° C to 75° C on a typical summer day. Over a period of time these thermal cycles may cause debonding of the repair material from parent concrete at the repair joint due to thermal incompatibility of the parent concrete and the repair material

The successful application of FRP plate bonding, to a large degree, depends on the effectiveness of the bond line. The adhesive layer bonds the concrete and the FRP to develop composite action, so that the tensile stresses can be transferred from the concrete and the internal reinforcement to the external FRP plate. There are incompatibilities among the three component materials, for example, the coefficient of linear thermal expansion of the epoxy based adhesives is in the range of $44-120 \times 10^{-6} /^{\circ}\text{C}$ (Hancox and Mayer, 1994); this value for concrete is expected to be from 6

to $13 \times 10^{-6} / ^\circ\text{C}$; while for CFRP in the direction of fibre it is between -0.2 and $-1.3 \times 10^{-6} / ^\circ\text{C}$ (Tann, 2001).

2.3.3.1 The effect of fire exposure

Exposure of a concrete structure to fire can lead to yielding of the reinforcement and subsequent reduction of load bearing capacity. Given such circumstances, strength loss can be returned by incorporating external plate bonding into the overall repair package, assuming that satisfactory, structurally sound concrete repairs are carried out.

The performance of the composites at elevated temperatures depends solely on their constituents: the fibres, the matrix, the proportion of fibres to matrix, and the relative stiffness of each. Carbon fibres, alone, are capable of resisting temperatures well in excess of 1000°C without serious strength loss (ACI, 2001). The epoxy matrix, however, is the critical component governing fire behaviour of the overall composite (Williams et al., 2003)

When FRP is exposed to fire it is susceptible to combustion because of the flammable nature of the matrix. Upon approaching and surpassing the glass transition temperature of the matrix, it becomes viscous and rubbery (Bank, 1993). This change is accompanied by degradation in strength properties by a factor of 10 to 100 (Blontrock et al., 1999). Stiffness is lost, leading to excessive deflection of the FRP. Eventually, the matrix may ignite, supporting flame spread and toxic smoke (Apicella and Imbrogno, 1999). Though smoke from the resins is toxic, FRP is usually used in open spaces and is found in relatively small quantities, hence toxic effects are minimal (Ballinger et al, 1993). However, the volatile fragments produced by decomposition of the matrix react with available oxygen creating more heat, and furthering the fire's destructive capability (Nelson, 1995). Once a fire is over, FRP has suffered charring, melting, delamination, cracking and buckling (Milke and Vizzini, 1993), and its structural integrity is questionable. In short, the major areas of concern with respect to epoxies are the potential for ignition, flame spread and toxic by-products, and the assured loss of strength and stiffness with increasing temperature.

2.3.3.2 The effect of freeze and freeze-thaw

The effects of cold region environments, especially those related to freeze-thaw cycling are of some concern because it is possible that in addition to changes in materials response caused by cold temperatures, the absorption of moisture into the composite followed by subsequent freezing could lead to increased microcracking and further degradation caused by the cyclic process (Karbhari, 2002). As it has been pointed out earlier environmental exposure to conditions such as freeze-thaw will potentially affect not just the composite material but also the concrete and the bond between them.

Howie (1995) exposed carbon/epoxy concrete cylinders to freeze-thaw cycles between 20° C to -18° C for a period of 45 days and reported a decrease in compressive strength of about 5% and significant reduction in overall stiffness. Soudki and Green (1997) exposed a very limited number of carbon/epoxy wrapped concrete cylinders to 50 freeze-thaw cycles and concluded that the exposure caused a more catastrophic failure, with specimens showing evidence of microcracking.

Karbhari et al. (2000) cycled carbon/epoxy confined concrete cylinders between 22.5°C and -20°C 201 times without prior moisture exposure and noted there was insignificant change in levels of ultimate strength, although a decrease in hoop strain levels was seen. It was noted, however, that “dry” freeze-thaw cycling did result in substantial matrix microcracking that in the presence of moisture, could result in significantly accelerated degradation in overall response under ambient conditions rather than under conditions of exposure.

Although FRP composites can have strength levels significantly higher than those of steel, and can be formed of constituents such as carbon fibres that have moduli equal to or greater than the modulus of steel, it is important to note that the limit of use is often dictated by strain limitations. FRP composites in general behave in linear elastic manner to failure, without any significant yielding or plastic deformation induced ductility as seen in steel or reinforced concrete. Additionally, it should be noted that unlike reinforcing steel, some fibres, such as carbon fibres, are anisotropic, having different properties in the longitudinal and transverse directions. This

anisotropy is also apparent in thermal expansion in the longitudinal and transverse directions. The difference in strength and coefficients of thermal expansion can result in bond deterioration. Moreover, these can cause lateral stresses and low cycle shear fatigue under repeated thermal cycling (Karbhari, 2001).

2.4 High performance fibre reinforced cementitious composites (HPFRCCs)

In recent years, rapid advances have been made in the development of high performance fibre reinforced cementitious composites (HPFRCCs). These materials are characterized by tensile strain-hardening after first cracking. Even though many of these materials are targeted for structures with high load or high deformation demands, it is proposed that the large ductility of certain HPFRCCs should make them excellent materials for retrofitting (Hammil, 1999; Karihaloo et al., 2001; Li et al., 1995), and for seismic retrofitting (Parra-Montesinos, 2003; Krstulovic-Opara et al., 2000; Billington 2004). Naturally, the repair material must be durable under expected service conditions, including environmental and mechanical loads. Thus, some HPFRCC material may meet many of these demands for high performance repair.

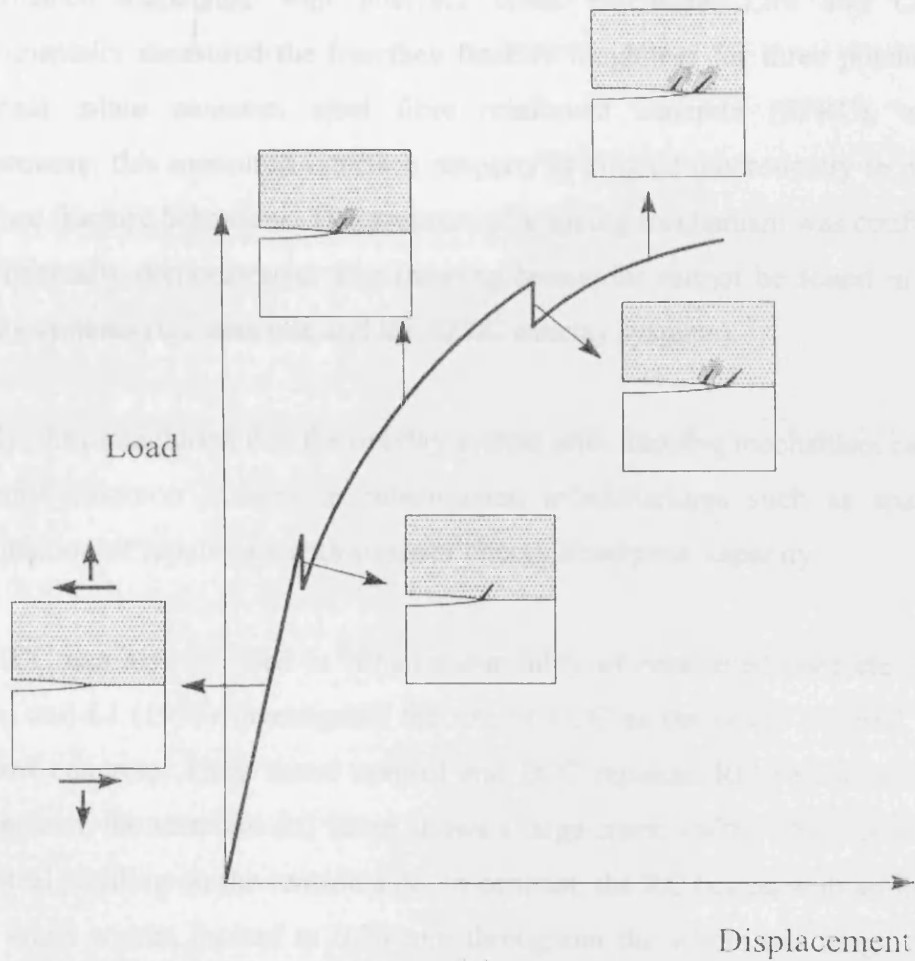
2.4.1 Engineered cementitious composite (ECC)

The ECC is a class of high performance fibre reinforced composite that exhibits pseudo strain-hardening behaviour accompanied by multiple cracking (Li, 1998). The use of ECC for concrete repair was proposed by Li et al. (1995), and Lim and Li (1997). In these experiments, specimens representative of an actual repair system-bonded overlay of a concrete pavement above a joint, were used. It was shown that the common failure modes of spalling or delamination in repaired concrete systems were eliminated by means of a kink-crack trapping mechanism (Figure 2.6). The concept of kink crack mechanism as experimentally observed by Lim and Li (1997) is as follows: as the load increases, the initial interface crack is trapped by the ECC so that further load increase forces crack extension into the interface. The kinking-trapping process then repeats itself, resulting in a succession of kink cracks in the ECC. However, spalling of the ECC was not observed since the kink crack does not propagate to the specimen surface. Delamination of the interface was also eliminated since the interface crack tip repeatedly kink into the ECC.

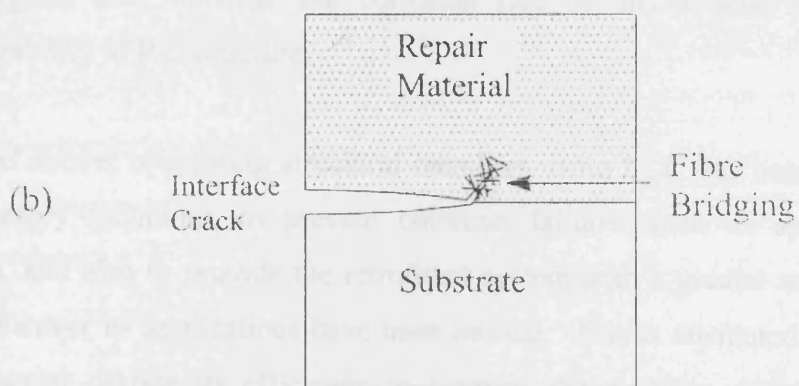
In standard concrete repair, surface preparation of the substrate concrete is considered essential in achieving a durable repair (Cusson and Malivaganam, 1996). In the study of Lim and Li (1997), the ECC is cast onto a diamond saw cut surface of the concrete. Hence the concrete surface is smooth and is expected as a result to produce a low toughness interface. Higher interface roughness has been associated with higher interface toughness in bi-material systems (Evans and Hutchinson, 1989).

Kamada and Li (2000) further investigated the effect of surface preparation on the kink-crack trapping mechanism of ECC/concrete repair system. Three different substrate surfaces were investigated. The first surface was obtained as cut surface by using a diamond saw (smooth surface). The second one was obtained by applying a lubricant on the smooth surface of the concrete to decrease the bond between the base concrete and the repair material. The third surface was prepared with a portable scarifier to produce a roughened surface. In their experiment, the smooth surface system showed more desirable behaviour in the crack pattern and the crack widths than the rough surface system. As claimed by the authors, the special phenomenon of kink-crack trapping which prevents the typical failure modes of delamination or spalling in repaired systems is best revealed when the substrate concrete is prepared to have a smooth surface prior to repair.

The interface between repair material and substrate plays a very important role in durable repair system. The interface property is considered an important parameter for such a repaired system. Lim and Li (1997) used interface fracture mechanics as an analytical approach for predicting whether an interface (delamination) crack will propagate along the interface or kink out from the interface, as well as for predicting the load magnitude necessary to drive the force.



(a)



(b)

Figure 2.6 (a) Trapping mechanism in a bimaterial interface system, (b) fibre bridging in a kinked crack (After Lim and Li 1997) (Reproduced from Alaei, 2002)

They believe that interface fracture toughness is capable of predicting repair system performance associated with interface crack extension. Lim and Li (1997) experimentally measured the interface fracture toughness for three potential repair materials; plain concrete, steel fibre reinforced concrete (SFRC), and ECC. Furthermore, this measured interface property is utilized theoretically to predict the interface fracture behaviour. The presence of trapping mechanism was confirmed and experimentally demonstrated. The trapping behaviour cannot be found in the other overlay systems (the concrete and the SFRC overlay systems).

Finally, they concluded that the overlay system with trapping mechanism can prevent the most common failures in rehabilitated infrastructures such as spalling and delamination of repair part with superior energy absorption capacity.

The ECC can also be used to enhance durability of reinforced concrete structures. Maalej and Li (1995) investigated the use of ECC as the cover material replacing standard concrete. They tested control and ECC repaired RC beams in four-point bending test, the standard RC beam shows a large crack width which grows rapidly after steel yielding on the tension side. In contrast, the RC beams with an ECC cover show crack widths limited to 0.20 mm throughout the whole test range. Since the permeability of cracked concrete has been shown to scale with the cube of the crack width, the restriction of the crack width is expected to slow down the migration of aggressive agents and therefore the corrosion rate of the re-bars, resulting in enhanced durability of RC structure.

As mentioned above, retrofitting structural members using ECC has been shown to be a satisfactory technique to prevent common failures such as spalling and delamination, and also to provide the retrofitted system with a greater and superior ductility. However its applications have been limited. This is attributed to the fact that this material despite its efficiency to increase the ductility cannot improve significantly the load carrying capacity.

2.4.2 Retrofitting with CARDIFRC[®]

CARDIFRC[®] is a high performance fibre reinforced cementitious composite which is characterised by a high tensile/flexural strength and a high energy absorption capacity. The special characteristics of CARDIFRC[®] make it particularly suitable for retrofitting of existing concrete structures. The key advantage of CARDIFRC[®] mixes for retrofitting is that unlike steel and FRP, their tensile strength, stiffness and coefficient of linear thermal expansion are comparable to that of the material of the parent member (Karihaloo et al., 2001). The CARDIFRC[®] constitutive behaviour will be further explained in Chapter 4.

Strengthening of RC beams using CARDIFRC[®] may be performed by two techniques; direct casting or adhesive bonding. The preliminary results of Alaei (2002) showed that the former can be effectively used for improving the flexural capacity of damaged beams. However, great care is required to ensure that the retrofit material adheres securely to concrete. Moreover, the need of special formwork is likely to limit the application of this technique in practice. The use of adhesive bonding technique does not suffer from these drawbacks and can be used for retrofitting damaged RC members

CARDIFRC[®] therefore, can be used as a new material for retrofitting damaged and/or understrength reinforced concrete beams (Karihaloo et al., 2002, 2000; Alaei et al., 2001). In this technique thin, pre-cast of CARDIFRC[®] strips are adhesively bonded to the tension and/or the side faces of RC beam for flexural and shear strengthening, respectively. The technique ensures that the ultimate failure of the retrofitted beams will occur in the gradual, flexural mode. It therefore overcomes some of the problems associated with the existing retrofitting techniques, based on bonded steel plates and FRP laminates.

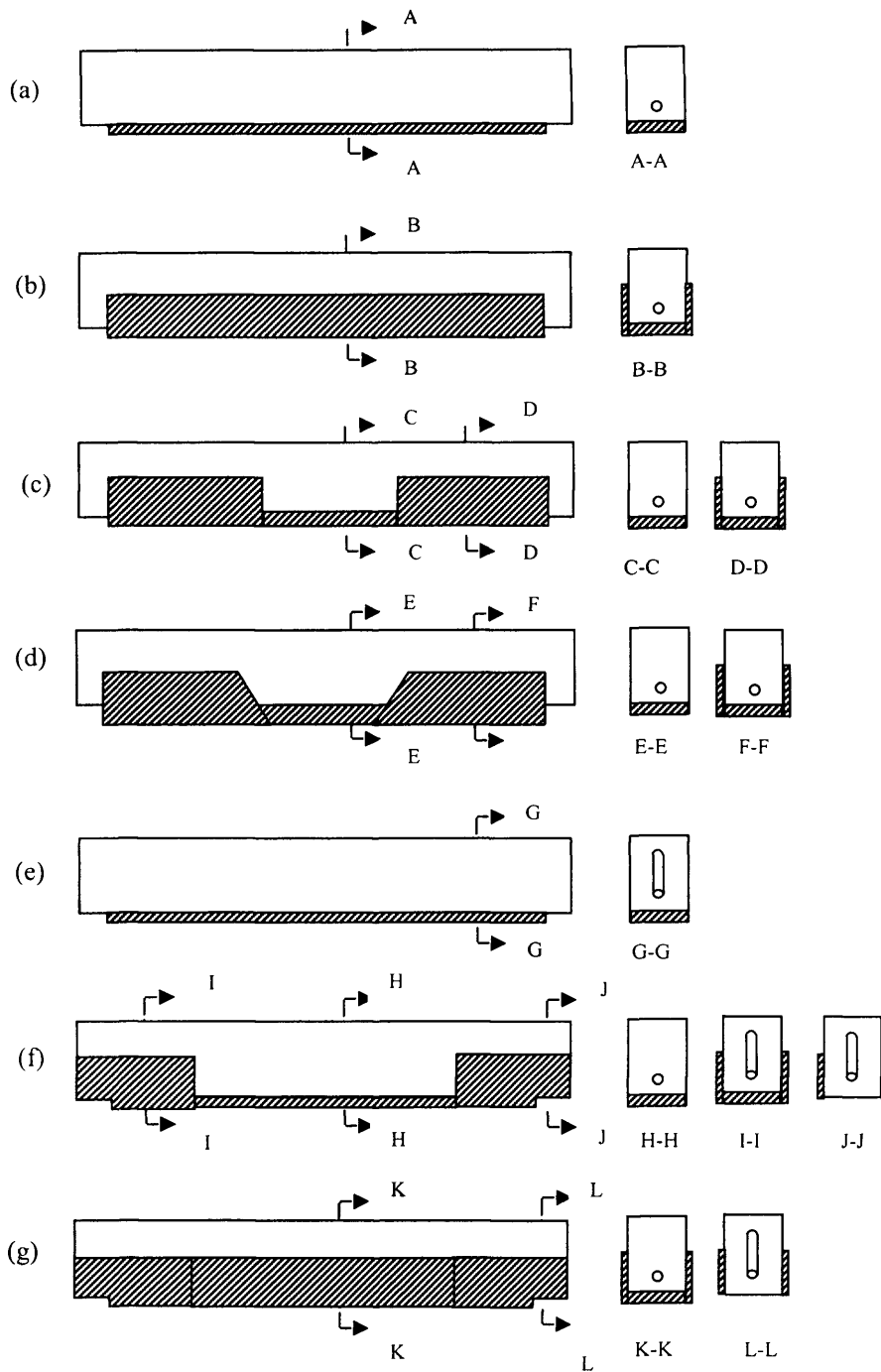


Figure 2.7 Configurations of retrofitting. Beams retrofitted with: (a) one strip on the tension face, (b) one strip on the tension and two strips on sides, (c) one strip on the tension face and four rectangular strips on sides, (d) one strip on the tension and four trapezoidal strips on sides, (e) one strip on the tension, (f) one strip on the tension and four short strips on sides covering supports and ends of tension strip, and (g) one strip on the tension and four short and two continuous strips on sides, fully covering supports and tension strip sides (After Karihaloo et al, 2003).

2.4.2.1 Flexural strengthening

Flexural strengthening of damaged beams can be achieved by bonding CARDIFRC[®] strips on the prepared surface of the beam. Karihaloo et al. (2003) conducted an extensive experimental program, using damaged beams retrofitted with CARDIFRC[®] strips bonded on the tension face. Two types of beams were investigated: beams without shear reinforcement, which were designed to fail either in flexure or in shear, and beams with sufficient shear reinforcement (Figure 2.7a and e). The retrofitted beams were loaded to failure, and their behaviours were compared to control beams. The test results showed that the adhesive bonding of pre-cast CARDIFRC[®] strips on the tension face with inherent unstable failure mode cannot change the failure mode to a stable flexural one. Regarding beams with adequate shear reinforcement, the technique may introduce shear cracking at the ends of the strip. However, it can improve the load carrying capacity and the serviceability (i.e. reduce crack opening) of the beam. From the results of Karihaloo et al (2001) it is obvious that in such a system of retrofitting the beam is strengthened in flexure but the retrofit strip along the bottom of the beam cannot significantly add to the shear strength of the section. Therefore, the probability of shear failure is even higher than that of control beams.

2.4.2.2 Flexural and shear strengthening

The beams retrofitted for flexural and shear, were similar to those only retrofitted on the tension face (i.e. with and without shear reinforcement). To prevent shear failure for beams without internal shear reinforcement (stirrups), CARDIFRC[®] strips was bonded on the sides, as well as the tension face of the beams (Figure 2.7b). Such a system of retrofitting greatly improves the load carrying capacity and serviceability of the beams. Moreover, to prevent flexural over-strengthening of the beams retrofitted by side and tension strips, the middle part of the beams may be left without retrofit strips (Figure 2.7c-d). This system also improves the load carrying capacity and ensures ductile failure.

To prevent shear cracking for beams with sufficient shear reinforcement and retrofitted with only one strip on the tension face, Alaei (2002) bonded short retrofit strips on the sides (Figure 2.7f). This method was found to be very effective. However, it does not improve the load carrying capacity of the beams. To achieve a

very high load carrying capacity and stiffness without any shear distress in the beams retrofitted with only one retrofit strip, the sides of the beams may be fully covered by retrofit strips. The results of Karihaloo et al. (2002) showed that by adopting this method the failure load can be increased up to 87 percent compared to that of control beams.

To predict the moment resistance and the load-deflection behaviour of the retrofitted beams Alaei and Karihaloo (2003a) developed an analytical model which is based on the classical theory, but takes into account fully the tensile contributions (i.e. pre-crack and post-crack) from concrete and retrofit strips. Alaei and Karihaloo (2003b) also developed a second analytical model which takes a purely fracture mechanics approach and follows the initiation and growth of the flexural crack which eventually leads to the failure of the retrofitted beams. The results of both analytical models were found to be in very good agreement with the test results. These models are modified and used in Chapter 8. Analytical details of the models are given in the same Chapter.

The study of Alaei (2002) showed that CARDIFRC[®] strip bonding system is a promising method for improving the flexural and shear behaviour of damaged concrete beams. It does not suffer from the drawbacks of the existing techniques. The major advantages of CARDIFRC[®] in retrofitting of concrete structures are:

- Ensuring gradual failure without delamination;
- Improving serviceability considerably by reducing deflections and crack widths;
- Ensuring compatibility with the material of structure being retrofitted;
- The same material without fibres can be first used to make any necessary repairs to the structure (e.g. filling of cracks, replacement of spalled concrete).

The behaviour of CARDIFRC[®] as a bonded material will be examined in Chapter 5, using wedge splitting tests, with emphasis on the elimination of the interfacial delamination of the bonded materials.

CARDIFRC[®] retrofit material can also be used when there is a need to improve the durability of existing concrete structures, as the material is very durable because of its highly dense microstructure. The durability (thermal cycling) of CARDIFRC[®] retrofitted beams will be investigated thoroughly in Chapter 7.

Chapter 3

Fracture mechanics of concrete

3.1 Introduction

The mechanical behaviour of structures is greatly influenced by the materials used in their construction. Based on their tensile stress-deformation response, most engineering materials can be categorized into; brittle: stress suddenly drops to zero when a brittle material fractures, ductile: stress remains constant or increases when a ductile material yields, and quasi-brittle: stress gradually decreases after the peak stress.

Plain and reinforced concrete structures contain inherent flaws, such as water filled pores, air voids, shrinkage cracks, even prior to the application of load. These flaws, and especially the small cracks (microcracks), grow stably under external loading, coalesce with existing or newly-formed microcracks until large fracture are formed which cause the collapse of the structure. To date these structures are designed without regard to either the propagation of large cracking zones through them or an energy failure criterion. Fracture mechanics provides an energy based failure theory that could be used in designing cement-based structures against the consequences of crack initiation and propagation (Karihaloo, 1995).

This chapter provides a brief outline of fracture mechanics theories which will be useful for subsequent chapters. Comprehensive literature on this vast topic can be found in (e.g. Karihaloo, 1995; Shah et al., 1995; Van Mier, 1997; Broek, 1978 and 1989; Ewalds and Wanhill, 1985; Knott, 1973). First, an introduction into the linear elastic fracture mechanics (LEFM) for brittle materials is given. Then it is shown that LEFM is not applicable to concrete. Therefore, the concepts of non-linear fracture theories for concrete are explained. Second, the fracture behaviour of repaired systems is discussed. Finally, an application of fracture mechanics to reinforced concrete structures is demonstrated on a longitudinally reinforced cracked beam.

3.2 Linear Elastic Fracture Mechanics

3.2.1 Griffith Theory of Brittle Fracture

Griffith (1920) explained that the large discrepancy between the theoretically predicted and real tensile strengths of hard brittle materials is due to the presence of small cracks and other crack-like defects in these materials. The theory is based on the assumption that the fracture initiates at the cracks as a result of very high tensile stress concentrations, which are induced around the crack tips when the load is applied (Anthony and Newman 1965).

Consider a large plate of unit thickness containing a crack of length $2a$ subjected to a uniform far-field tensile stress (Figure 3.1a). From Inglis's (1913) solution for a slit-like cut the vertical displacement of the upper face of the cut is

$$v(x) = \frac{2\sigma}{E} \sqrt{a^2 - x^2}, \quad 0 \leq |x| \leq a \quad (3.1)$$

where E is Young's modulus.

With reference to Figure 3.1, it is clearly seen that the elastic plate with the slit-like cut of length $2a$ can be considered as the superposition of an elastic plate without a cut under external stress σ and the same plate without external σ but with equal and opposite stresses (i.e. $-\sigma$) applied gradually to the faces of the intended cut. Hence the stress σ on each of the two faces is displaced by the amount $v(x)$ of equation (3.1), so that the work done is given by:

$$W = 2 \left(-\frac{\sigma}{2} \int_{-a}^a v(x) dx \right) = -\frac{\pi a^2 \sigma^2}{E} \quad (3.2)$$

The negative sign in equation (3.2) indicates the stress and displacement are of the opposite sign, and the factor $1/2$ appears because the stress gradually increases from 0 to σ .

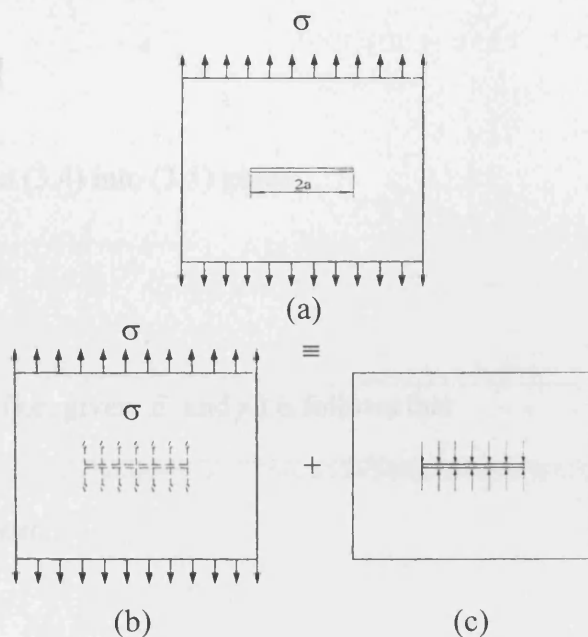


Figure 3.1. The principle of superposition (a) the plate is under external tension (b) uncracked plate under σ (c) plate without external σ but with equal and opposite stress applied to the crack to create a stress-free crack (After Karihaloo, 1995).

If the loaded boundaries of the panel are free to move, then the elastic strain energy U of the body increases during the crack process, and the change in W is equal to the change in the potential energy Π of the system.

3.1.2 Irwin's Theory of Elastic Fracture

If the crack growth is stable, then

$$dW = -d\Gamma \quad (3.3)$$

where

$$\Gamma = 4a\gamma \quad (3.4)$$

Γ is the surface energy consumed in the creation of the crack, and γ is the surface energy density, that is the energy required to create a unit crack surface.

The principle of minimum potential energy is applied for a stable crack, and it may be rewritten as:

$$\frac{\partial}{\partial a}(W + \Gamma) = 0 \quad (3.5)$$

Substituting (3.2) and (3.4) into (3.5) gives

$$\sigma^2 = \frac{2E\gamma}{\pi a} \quad (3.6)$$

For a given material (i.e. given E and γ) it follows that

$$\sigma\sqrt{\pi a} = \sqrt{2E\gamma} = \text{const.} \quad (3.7)$$

According to the Griffith fracture criterion or the global energy criterion a brittle material will fracture when the stress σ reaches the value σ_c that satisfies equation (3.7). It shows that the strength of a brittle material σ_c is dependent on physical parameters such as the Young modulus, the surface energy density, and the length of crack.

3.2.2 Irwin Theory of Brittle Fracture

Griffith's work was significant; however it did not include ductile materials in its consideration. Irwin (1957) began to see how the theory would apply to ductile materials. He determined that there was also a certain energy from plastic deformation that had to be added to the strain energy originally considered by Griffith in order for the theory to work for ductile materials as well, creating what is known as the strain energy release rate. If the energy used in the plastic deformation is included in equation (3.7), it becomes,

$$\sigma = \sqrt{\frac{2E(\gamma + \gamma_p)}{\pi a}} \quad (3.8)$$

where, γ_p is the energy used in the plastic deformation associated with the crack extension.

Generally, there are three possible modes of deformation at a crack tip (Figure 3.2):

- Mode I – opening or tensile mode, where the crack surfaces move directly apart (Figure 3.2a).
- Mode II – sliding or in-plane shear mode, where the crack surfaces slide over one another in a direction perpendicular to the leading edge of the crack (Figure 3.2b).
- Mode III – tearing or antiplane shear mode, where the crack surfaces move relative to one another and parallel to the leading edge of the crack (Figure 3.2c).

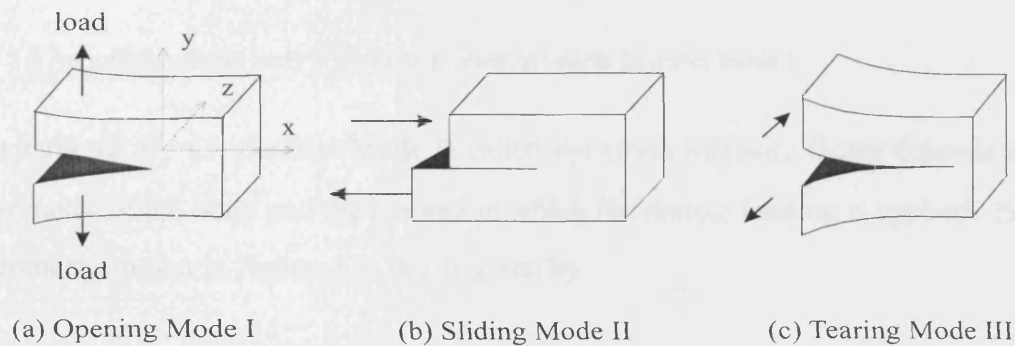


Figure 3.2. Modes of crack propagation

The most severe mode from the point of view of fracture is Mode I, as the propagation of a crack in real material under pure Mode II and III conditions needs a great amount of energy, due to friction between the crack faces.

Now, consider a two dimensional (plane) body of infinite extent subjected to a uniform stress remote from the crack, which induces an opening mode of stress at the crack tips (Figure 3.3). The stress and displacement components of a point in the vicinity of the crack tip can be written as:

$$\sigma_{ij} = \frac{K_I}{\sqrt{2\pi r}} f_{ij}(\theta) + \dots \quad i, j \in \{x, y\} \quad (3.9)$$

$$u_i = \frac{K_I(1+\nu)}{E} \sqrt{\frac{2r}{\pi}} g_i(\theta) + \dots \quad i \in \{x, y\} \quad (3.10)$$

where r and θ are the polar co-ordinates of the point with respect to the crack tip. E and ν are the Young modulus and the Poisson ratio of the material, respectively.

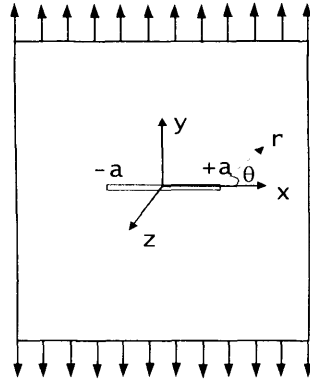


Figure 3.3 An infinite elastic body with a sharp crack of length $2a$ under mode I.

The parameter K_I (I denotes Mode I) called the stress intensity factor depends on the geometry of the body and the manner in which the remote loading is applied. For the geometry shown in Figure 3.3, K_I is given by

$$K_I = \sigma \sqrt{\pi a} \quad (3.11)$$

Generally, K_I is finite and positive. There can be situations when K_I vanishes, but it can never be negative. The shapes of the crack tip zones and the stress distributions ahead of the tips are shown in Figure 3.4 for $K_I > 0$, $K_I < 0$ and $K_I = 0$. When $K_I = 0$ (Figure 3.4c), the crack faces close smoothly and the stresses ahead of the crack tip are finite. It should be mentioned that the constant term or terms which depend on r and thus vanish as $r \rightarrow 0$, have been omitted from equations (3.9) and (3.10).

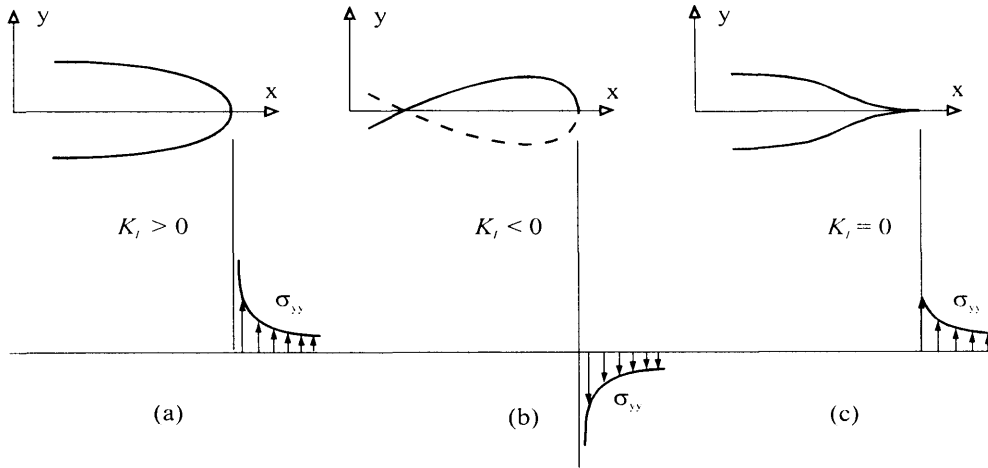


Figure 3.4. Shapes of traction-free crack tip zones and distribution of normal stress, σ_{yy} in front of the crack tip for $K_I > 0$, $K_I < 0$ and $K_I = 0$ (From Karihaloo, 1995).

According to the Irwin fracture criterion, a sharp crack in a brittle material will propagate when the stress intensity factor K_I reaches a critical value, denoted K_{Ic} . This critical value is a material constant and is called the fracture toughness of the material. The distinction between K_{Ic} and K_I is important, and is similar to the distinction between strength and stress. In other words, K_{Ic} is related to the stress intensity factor K_I for the opening mode crack in the same way that a material's tensile strength is related to the stress in a tensile specimen (Brown and Srawley, 1966). For the geometry and mode I loading of Figure 3.3, Irwin's criterion gives

$$\sigma_c \sqrt{\pi a} = K_{Ic} \quad (3.12)$$

According to this relation, when the external stress reaches the value σ_c the crack will propagate.

Comparing equation (3.12) with (3.7) indicates that the Irwin local stress criterion at the crack tip where the fracture process is taking place, is exactly identical to the Griffith global energy criterion. The constant in the right hand side of equation (3.7) can be identified with K_{Ic} , i.e.

$$\sqrt{2E\gamma} = K_{Ic} \quad (3.13)$$

or

$$K_{Ic}^2 = EG_c \quad (3.14)$$

where, G_c is the critical Griffith surface energy density or the critical energy release rate, with $G_c = 2\gamma$.

Today, Irwin's fracture theory is more widely used than Griffith's because it is much easier to determine directly the fracture toughness K_{Ic} than it is to determine the surface energy density γ (Karihaloo, 1995)

The fracture toughness of a material can be determined from a pre-cracked specimen. The most commonly used specimen shape for the determination of K_{Ic} is a notched beam loaded in three-point bending. The specimen is loaded gradually until the sharp notch begins to propagate. The corresponding maximum load is noted to calculate the bending moment at mid-span (M_{max}). The critical stress intensity factor K_{Ic} is then calculated using the formula (Karihaloo, 1995)

$$K_{Ic} = \frac{6YM_{max}\sqrt{a}}{BW^2} \quad (3.15)$$

where Y is a function of a/W (i.e. the ratio of the depth of notch to the height of the specimen), B and W are the width and height of the beam, respectively.

3.2.2.1 Irwin Theory and Local Energy Considerations

Consider a crack of length $2a$ in an infinite body of unit thickness under mixed mode loading (Figure 3.3) and calculate the change in its potential energy when the crack grows by an infinitesimal amount Δa at each end. Using the superposition approach, we need only to eliminate the stress σ_{yy} due to the remote mode I loading at the location of the crack by applying equal stress of opposite sign and calculate the work

done by this stress when the crack faces open up. As mentioned earlier, this work done equals the change in the potential energy of the body, $\Delta\Pi$

$$\Delta\Pi = -2 \int_0^{\Delta a} \sigma_{yy} u_y dx \quad (3.16)$$

The negative sign in front of the integral indicates that the displacement and corresponding stress have opposite signs, and the factor 2 allows for the symmetric growth of the two crack tips. The stress and displacement components (i.e. σ_{yy} and u_y) are chosen from equations (3.9) and (3.10), respectively, corresponding to $\theta = 0$ (i.e. in the direction of crack advance). After integrating equation (3.16), we obtain

$$\Delta\Pi = -\frac{2K_I^2}{E} \Delta a \quad (3.17)$$

On the other hand, the energy required to extend the crack by an amount Δa is $\Delta\Gamma = 4\gamma\Delta a$. Noting that $-\Delta\Pi = \Delta\Gamma$, the relation between γ and stress intensity factor in the loading mode I can be written as

$$\frac{2K_I^2}{E} = 4\gamma \quad (3.18)$$

At the critical instant of crack propagation, this relation would take the form $K_{Ic}^2 = 2E\gamma = EG_c$, which is identical to equation (3.14). Therefore, the important relationship between Griffith and Irwin criteria of fracture from energy consideration alone is re-obtained.

Now, from equation (3.17) the rate of change in the potential energy for growing a crack tip in a brittle material under mode I loading can be derived as

$$-\frac{d\Pi}{da} \equiv G = \frac{K_I^2}{E} \quad (3.19)$$

where G is the energy release rate.

3.2.3 Barenblatt's Cohesive Crack Model

The main features of LEFM described above are:

- (i) The description of brittle fracture involves only one additional material parameter, besides the usual two constants E and f_t . This parameter may be related to the energy of the body (material toughness) G_{Ic} or to the stress field near the crack tip present in the fracture toughness K_{Ic} .
- (ii) The stresses and strains in the vicinity of a crack tip are very large (at the tip itself they tend to infinity).
- (iii) During the fracture process the entire body remains elastic, the energy is only dissipated at a crack tip.

Griffith (1920) had observed the inconsistency between the linear elastic fracture model and the real physical situation prevailing at the crack tip. He therefore, proposed that the crack faces should be allowed to close smoothly (Figure 3.4c) under the influence of large cohesive forces.

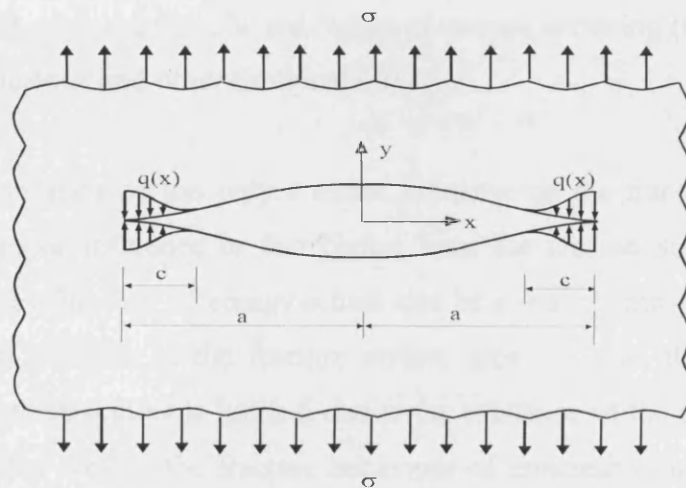


Figure 3.5. Barenblatt's cohesive crack model in mode I. Note $c \ll a$.

Barenblatt (1959) gave the first fracture mechanics analysis based on the concept of a crack-tip cohesive zone in which he assumed that there were large cohesive forces $q(x)$ (see Figure 3.5) acting over a small zone of length c ($c \ll a$) near the crack tip

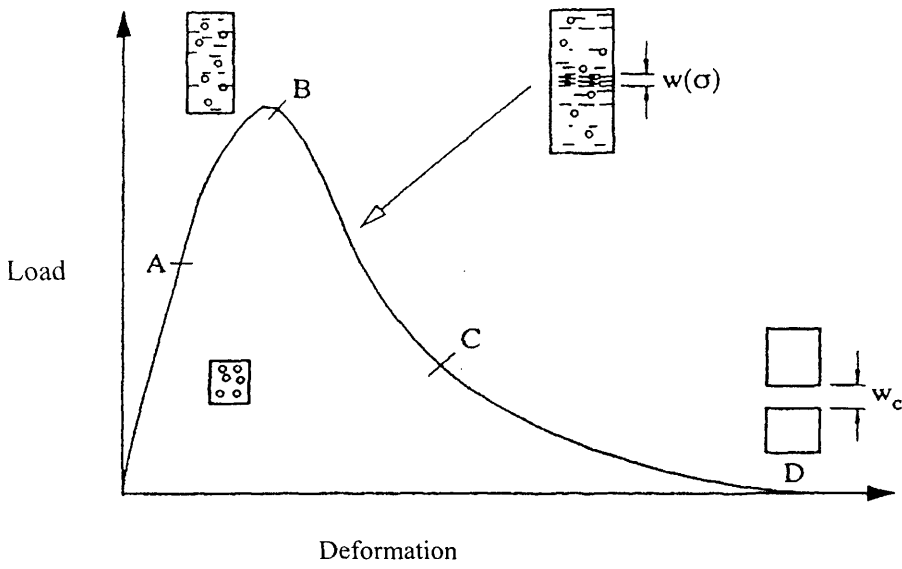
and that the crack faces close smoothly. The distribution of these cohesive forces is generally unknown and due to the presence of other defects it is difficult to ascertain.

Dugdale (1960) and Bilby et al. (1963) used a similar cohesive zone model to describe the behaviour of the elastic-plastic materials but they considered the cohesive stress to be constant and invariant with the crack opening. In fact, a plastic zone will form at each crack tip and extend as far as is necessary to satisfy the yield condition ($\sigma_{yy} \leq \sigma_y$). Therefore, the closing stress over the plastic zone will be constant and equal to the yield stress of the material (σ_y).

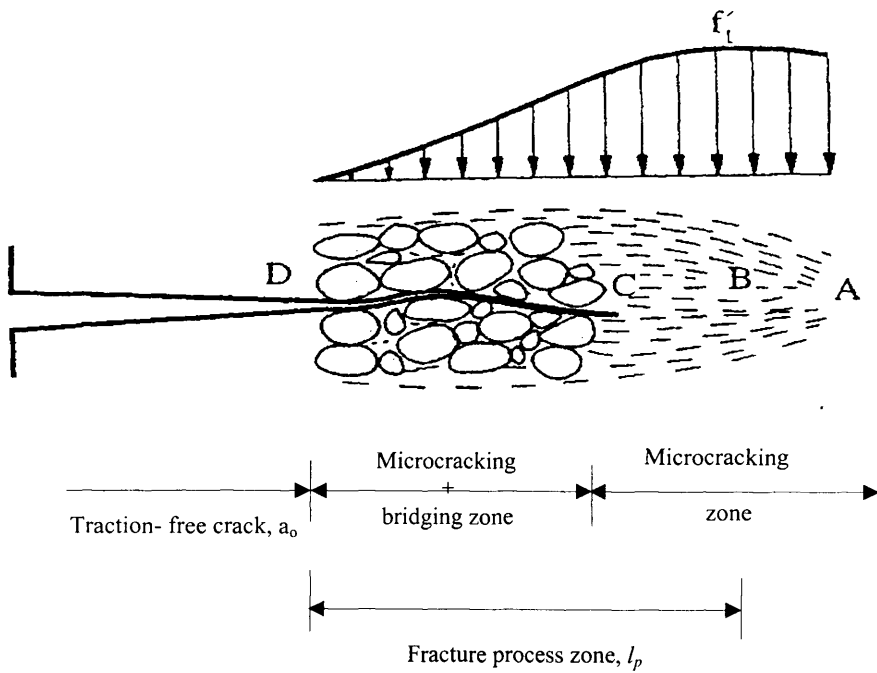
3.3 Is LEFM Applicable to Concrete?

Attempts were made to apply LEFM to concrete, which was thought to be a brittle material, but these proved unsuccessful. Intense research in this field revealed that all the cement-based materials that were traditionally regarded to be brittle exhibit in reality a different response. Figure 3.6a shows the load-deformation response of these materials in tension/flexure. It can be seen that a substantial non-linearity exists before the maximum stress is reached (AB) and there is a region of tension softening after the attainment of the maximum load (BC). These are primarily a result of randomly formed microcracks. The tail region of tension softening (CD) is caused by the aggregate interlock and other frictional effects.

The pre-peak non-linearity has only a minor influence on the fracture behaviour of concrete. The major influence in fact comes from the tension softening response because it reduces the flux of energy which can be released into the crack tip and thus leads to an increase in the fracture surface area. Hence, the application of LEFM to concrete structures is limited, due to the existence of the tension softening response. In other words, the fracture behaviour of concrete is influenced by the formation of an extensive fracture process zone ahead of the pre-existing notch/crack, as illustrated in Figure 3.6b.



(a)



(b)

Figure 3.6. Typical load-deformation response of a quasi-brittle material in tension/flexure (a) and the fracture process zone ahead of the real traction-free crack (b) (After Karihaloo, 1995).

3.4 Nonlinear Fracture Theory of Concrete (NLFM)

In the previous section it was argued that the LEFM is not applicable to concrete due to the existence of the inelastic toughening mechanisms (i.e. fracture process zone) that appear around a crack when it propagates. Therefore, a fracture theory capable to describe the material softening process that takes place in the fracture process zone must be a non-linear fracture theory.

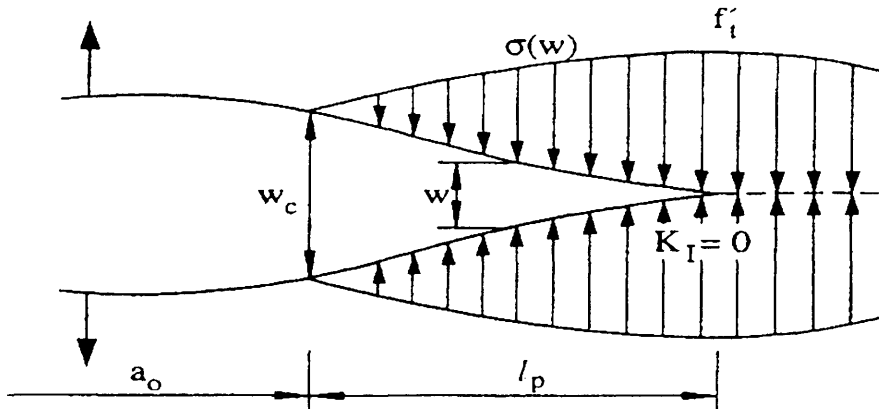
3.4.1 Fictitious Crack Model (FCM)

The first non-linear theory of fracture mechanics for concrete was proposed by Hillerborg et al. (1976). It includes the tension softening fracture process zone through a fictitious crack ahead of the pre-existing crack whose faces are acted upon by a certain closing stress (Figure 3.7). This model, which is known by the name of Fictitious Crack Model (FCM), is applicable to cracks whose faces close smoothly.

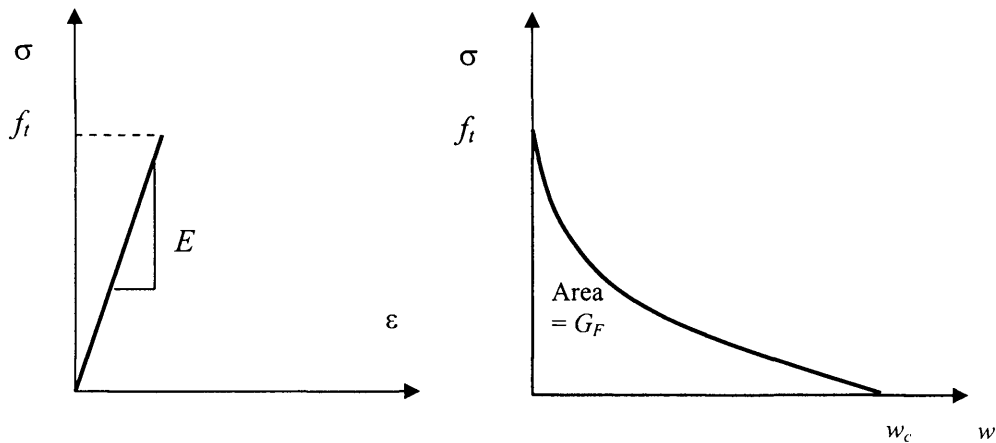
The FCM is similar in some points to the Barenblatt and Dugdale models, mentioned above. Like these models, the FCM assumes that the fracture process zone is of negligible thickness and the crack tip faces close smoothly ($K_I = 0$, see Figure 3.4c). However, the closing stresses in the FCM are not constant, as they are in the Dugdale model. They increase from zero at the tip of the pre-existing stress-free crack to the tensile strength of the material, f_t , at the tip of the fictitious crack (Figure 3.7a). In fact, the distribution of the cohesive stresses, $\sigma(w)$, along the fracture process zone depends on the opening of the fictitious crack faces, w . The size of the fracture process zone (l_p in Figure 3.7a) in the FCM may also be long compared with that of the pre-existing crack, so the FCM also differs from the Barenblatt model.

In contrast to LEFM which needs a single parameter to describe a brittle material (e.g. K_{Ic} in Irwin's theory), in the FCM it is necessary to have two material parameters.

- The shape of stress-deformation relation $\sigma(w)$ in the softening zone;



(a)



(b)

(c)

Figure 3.7. (a) A real traction-free crack of length a_0 terminating in a fictitious crack of length l_p , whose faces close smoothly near its tip ($K_I=0$). The material ahead of the fictitious crack tip is assumed to be linear (b), but the material within the fracture process zone is softening; the area under softening curve equals fracture energy G_F (c) (After Karihaloo, 1995).

- The area under the tension softening curve which is the specific fracture energy G_F (Figure 3.7c)

$$G_F = \int_0^{w_c} \sigma(w)dw \quad (3.20)$$

where, w_c is the critical crack opening at which the closing stress is equal to zero.

There is also another material parameter which can be obtained from the above information, namely the characteristic length of the material

$$l_{ch} = \frac{EG_F}{f_t^2}. \quad (3.21)$$

The characteristic length, l_{ch} , is related to the heterogeneity in the material microstructure, giving an indication of its brittleness. It has a value proportional to the length of the fracture process zone. The bigger the characteristic length of the material is, the more ductile will be the material (i.e. less brittle). This is attributed to the fact that a bigger value of characteristic length is an indication of more inelastic toughening mechanisms getting involved around a crack when it propagates, resulting in increased energy absorption. The characteristic length has a value for mortar and concrete in the range of 100 to 200 mm and 150 to 500 mm, respectively (Karihaloo, 1995).

3.4.2 Crack Band Model (CBM)

According to the fictitious crack model, the fracture process zone (FPZ) is assumed to be line crack with negligible width. Bazant and Oh (1983) developed a similar model called a crack band model (CBM), in which the fracture process zone was modelled by a band of uniformly and continuously distributed (smeared) microcracks of width h_b (Figure 3.8a). Stable crack propagation is assumed by progressive microcracking within this band, which is described by a stress-strain relationship (Figure 3.8b).

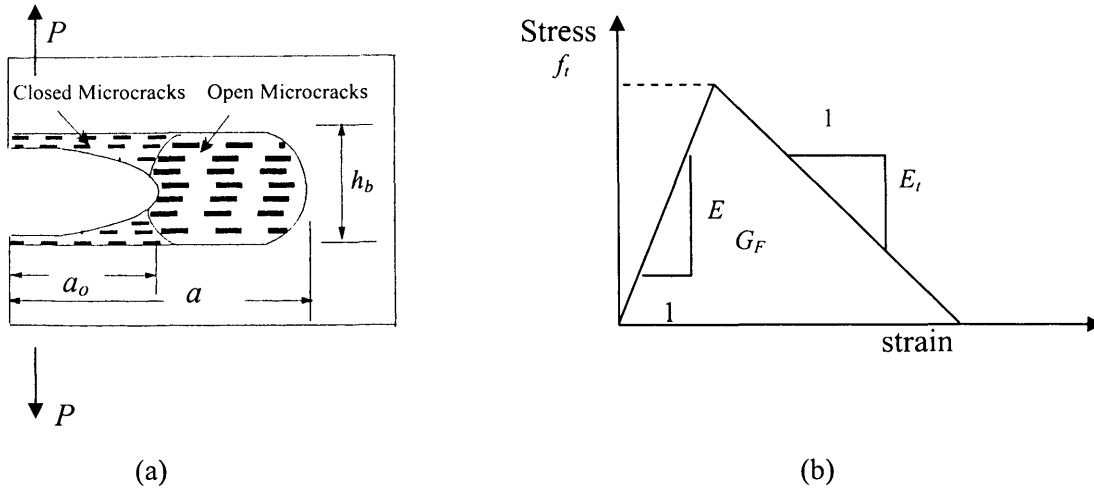


Figure 3.8 Crack band model for fracture of concrete (a) a microcrack band fracture and (b) stress-strain curve for the microcrack band (From Shah et al., 1995).

The crack opening displacement w is equal to the product of the strain and the width of the crack band, h_b .

Based on the assumption that the energy produced by the applied load is completely balanced by the cohesive pressure $\sigma(w)$ in the fictitious crack approach, the energy consumed due to the crack growth per unit area of the crack band, G_F , is the product of the area under the stress-strain curve in Figure 3.8b, and the width of the crack band, h_b . This leads to

$$G_F = h_b \left(1 + \frac{E}{E_t} \right) \cdot \frac{f_t^2}{2E} \quad (3.22)$$

where E is the modulus of elasticity,
 E_t is the strain-softening modulus, and
 f_t is the tensile strength of the material.

The values of E and E_t are defined as positive. It may be seen that in addition of E the crack band model requires two additional material parameters, namely h_b and E_t . An approximate function $h_b = n_a d_a$ has been proposed to calculate the h_b value, where d_a is the maximum aggregate size in concrete and n_a is a constant, which is equal to 3 for concrete.

It should be noted that the main difference between the two mentioned non-linear models (FCM and CBM) is the thickness of the fracture process zone. As the band width h_b in the CBM tends to zero, the two models will merge.

The CBM is generally used when the cracks are diffuse and numerous. That is why it is also called the smeared crack model. The FCM, on the other hand, is used when the cracks are few and isolated. That is why it is also called the discrete crack model.

3.5 Determination of fracture energy G_F

According to the RILEM recommendation (RILEM, 1985), the specific fracture energy (G_F) is the average energy given by dividing the total work of fracture with the projected fracture area. This parameter can be measured using a pre-cracked (notched) specimen. As for the determination of K_{Ic} , a commonly used specimen shape for the determination of G_F is a notched beam loaded in three-point bending (Figure 3.9). The specimen is loaded gradually and the variation of the load (P) is plotted against the mid-span deflection. The specific fracture energy (G_F) is then calculated using the formula

$$G_F = \frac{1}{(W - a)B} \int Pd\delta \quad (3.23)$$

where W , B and a are the specimen depth, width and the notch length, respectively. The weight of the specimen can be considered, if necessary (i.e. large specimens).

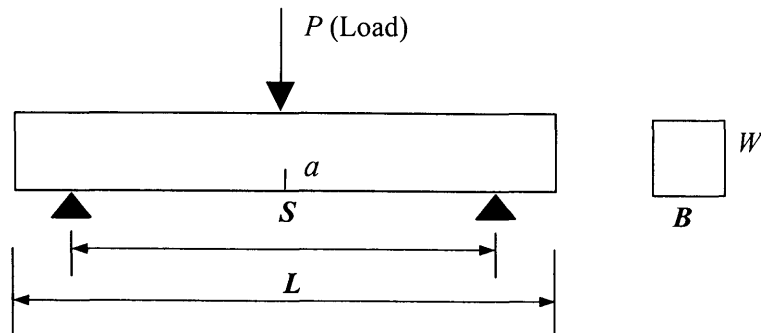


Figure 3.9. Testing configuration and geometry of specimen. P = load, L = specimen length, S = specimen loading span, W = beam depth. B = beam thickness and a = initial notched depth.

However, most researchers have found that there exist size effects to a certain extent when TPB is used to determine the specific fracture energy of concrete. As a material parameter, fracture energy should be a constant and independent of specimen size. Therefore, some researchers have doubted the validity of G_F obtained using TPB

Because of the testing simplicity, TPB recommended by RILEM Committee FMC-50 is widely used for the determination of fracture energy. However, most experiments are performed on relatively small beams, and therefore the self-weight compared to the fracture area of the TPB beams is large. Hence, the effect of self-weight on fracture properties must be carefully considered in TPB. To overcome this situation, RILEM set up a committee (Rossi et al., 1991) charged with the task of proposing a test method based on compact specimens. The specimen is provided with a groove and starter notch. The fracture parameters are determined by wedging open the starter notch; hence it is called the wedge splitting (WS) test. The principle of the WST (Brühwiler and Wittmann, 1990) is schematically presented in Figure 3.10.

A cubic specimen with an initial rectangular groove carries two-load transmission pieces (Figure 3.10). The loading of the wedge implies a defined horizontal-force F_H application to the specimen, which causes crack propagation. The load is applied gradually and the crack mouth opening displacement (CMOD) is monitored with a clip gauge and used as a feed back signal.

The splitting force, F_H is calculated from the vertical force F_M on the bearings and wedge angle, taking into account frictional effects.

$$F_H = \frac{F_M (1 - \mu \tan \alpha)}{2 \tan \alpha (1 + \mu \cot \alpha)} \approx \frac{F_M}{(1 + \mu \cot \alpha)(2 \tan \alpha)} \quad (3.24)$$

where μ is the coefficient of friction. The manufacturers of roller bearings quote μ between 0.1 and 0.5%. For $\alpha = 15^\circ$, the contribution of $\mu \cot \alpha$ in the previous

expression is therefore between 0.40 and 1.9%. Therefore, in the WST, F_H may be expressed by

$$F_H \approx \frac{F_M}{2 \tan \alpha} \quad (3.25)$$

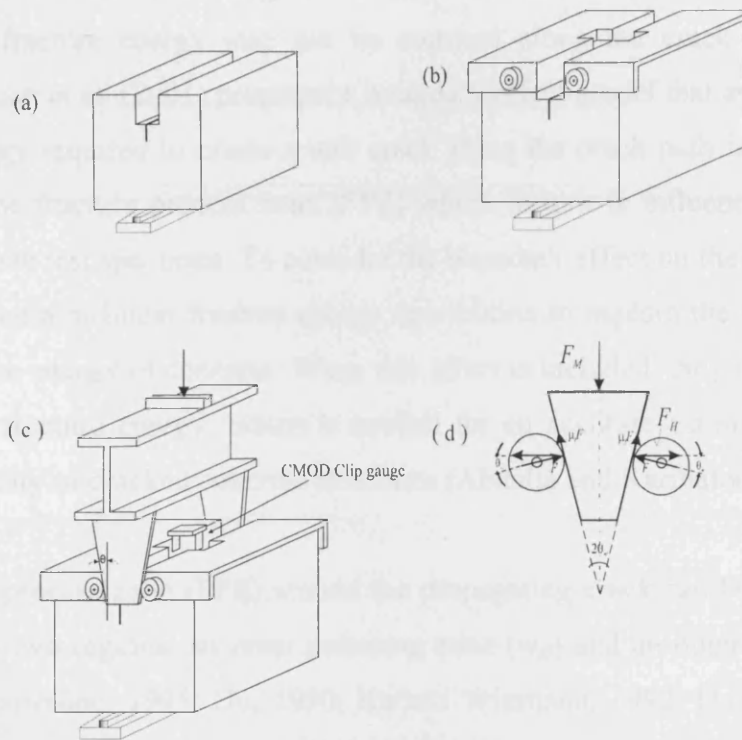


Figure 3.10. Principle of wedge-splitting test: (a) a test specimen on a linear support, (b) placing of two load devices with roller bearing, (c) pressing a wedge between bearings, and (d) forces acting on the wedge. (After Rossi et al., 1991)

The area under load-CMOD curve corresponds to the work done which is required to separate the specimens. Dividing this work by the fracture area or ligament area that was intact before the test began yields the measured specific energy G_f . This value characterises the crack propagation resistance of the tested material and can be simply calculated as follows:

$$G_f = \frac{1}{A_{lig}} \int_0^{CMOD_{max}} F_H d(CMOD) \quad (3.26)$$

3.6 Size-Independent Specific Fracture Energy G_F

The specific fracture energy G_F is the most useful material parameter in the fracture analysis of concrete structures (Karihaloo, 1995). The method of experimental determination of the fracture energy, G_F , and even its definition has been a subject of debate among researchers because of its variability with the size and shape of the test specimen (Abdalla and Karihaloo, 2003). Hu and Wittmann (1992) have shown that the specific fracture energy may not be constant along the crack path in a test specimen. Duan et al. (2001) proposed a boundary effect model that assumes that the fracture energy required to create a unit crack along the crack path is influenced by the size of the fracture process zone (FPZ) which in turn is influenced by the free boundary of the test specimen. To consider the boundary effect on the propagation of FPZ, they used a bi-linear fracture energy distribution to explain the ligament effect on the fracture energy of concrete. When this effect is included, they obtained a size-independent fracture energy, which is needed for an accurate estimate of the load bearing capacity of cracked concrete structures (Abdalla and Karihaloo, 2003)

The fracture process zone (FPZ) around the propagating crack can be considered as consisting of two regions, an inner softening zone (w_{sf}) and an outer micro-fracture zone (w_f) (Karihaloo, 1995; Hu, 1990; Hu and Wittmann, 1992; Duan et al., 2001) (Figure 3.11). The inner softening zone w_{sf} contains interconnected cracks along the aggregate and mortar interfaces. The main open crack plus a few large crack branches along the interfaces can be formed within the softening zone. The formation and complete separation of the softening zone controls the $\sigma(w)$ relationship. The outer micro-fracture zone contains isolated micro-cracks that are not interconnected. These do not contribute to the concrete softening. The fracture energy consumed in the outer micro-fracture zone is small, and equations (3.20) and (3.23) should in principle determine the same specific fracture energy (Duan et al., 2001).

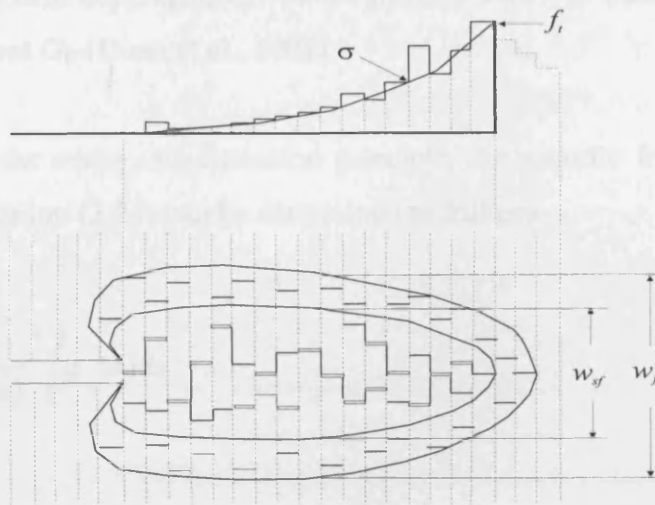


Figure 3.11 The FPZ and discrete bridging stresses. The FPZ is divided into the inner softening zone and the outer micro - fracture zone. w_c is related to the width of the inner softening zone w_{sf} (Hu and Wittmann, 1992).

However, during crack propagation the inner and the outer zone widths w_{sf} and w_f may vary according to the crack tip stress field. Obviously the critical crack opening w_c is limited by the inner and the outer zone widths. This limit becomes more obvious when a FPZ approaches the free boundary of a specimen. Therefore, a smaller w_c and a smaller fracture energy are found if equation (3.20) is used. These variations in w_{sf} , w_f and w_c lead to the conclusion that the fracture energy G_F defined by equation (3.23) can be dependent on the location of FPZ in relation to the free boundary of the specimen. To distinguish the fracture energy G_f defined by equation (3.23) from that defined by equation (3.20), Duan et al. (2001) use the symbol g_f for the local fracture energy defined by equation (3.20) (Abdalla and Karihaloo, 2003). Hu (1990) and Hu and Wittmann (1992) have made the following assumptions

$$\begin{aligned}
 w_{sf}(x) &\propto w_f(x) \\
 w_c(x) &\propto w_{sf}(x) \\
 g_f(x) &\propto w_c(x)
 \end{aligned}
 \tag{3.27}$$

where x denotes a position along a fracture ligament in the FPZ and $g_f(x)$ represents the local fracture energy. The fracture energy defined by equation (3.23) which may

be size or ligament dependent is denoted through $G_f(a)$, to differentiate it from the size-independent G_F (Duan et al., 2001)

According to the energy conservation principle, the specific fracture energy $G_f(a)$ defined by equation (3.23) can be determined as follows:

$$G_f(a) = \frac{1}{(W-a)} \int_0^{W-a} g_f(x) dx \quad (3.28)$$

Differentiating equation (3.28) with respect to the crack length gives the local fracture energy $g_f(x)$ at the crack tip

$$g_f(x) = G_f(a) - (W-a) \frac{dG_f(a)}{da} \quad (3.29)$$

Equations (3.28) and (3.29) above imply that $G_f(a) = \text{constant} = G_F$, if $g_f(x) = \text{constant}$. If $g_f(x) \neq \text{constant}$, $G_f(a) \neq \text{constant}$, i.e. size or ligament effects are observed. Figure 3.12 shows schematically that if $g_f(x)$ decreases when approaching the boundary of the specimen at later stages of fracture, $G_f(x)$ is indeed dependent on the ligament or initial crack length (Duan et al., 2001).

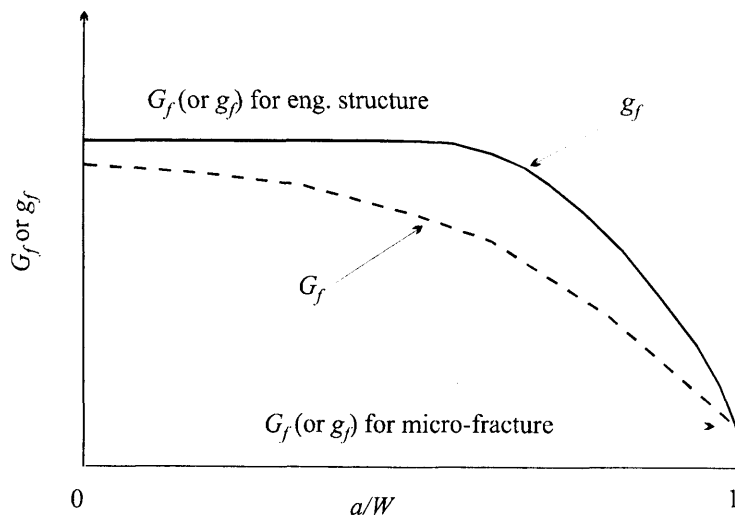


Figure 3.12 g_f decreases monotonically along the ligament, so that G_f has to be dependent on the a/W ratio, as observed in many experiments (Hu and Wittmann, 1992).

To simplify the previous local fracture energy analysis (Hu, 1990; Hu and Wittmann, 1992), $g_f(x)$ is assumed to vary in a bi-linear manner, as shown in Figure 3.13. Figure 3.13a displays a specimen of depth W and an initial crack of size a . The bi-linear function consists of a horizontal line with the value of G_F and a descending branch that reduces to zero at the back surface of the specimen. The intersection of these two straight lines is defined as the *transition ligament size* a_l or the crack reference length (Hu and Wittmann, 2000). The transition ligament size a_l is a parameter depending on both the material properties and specimen geometry.

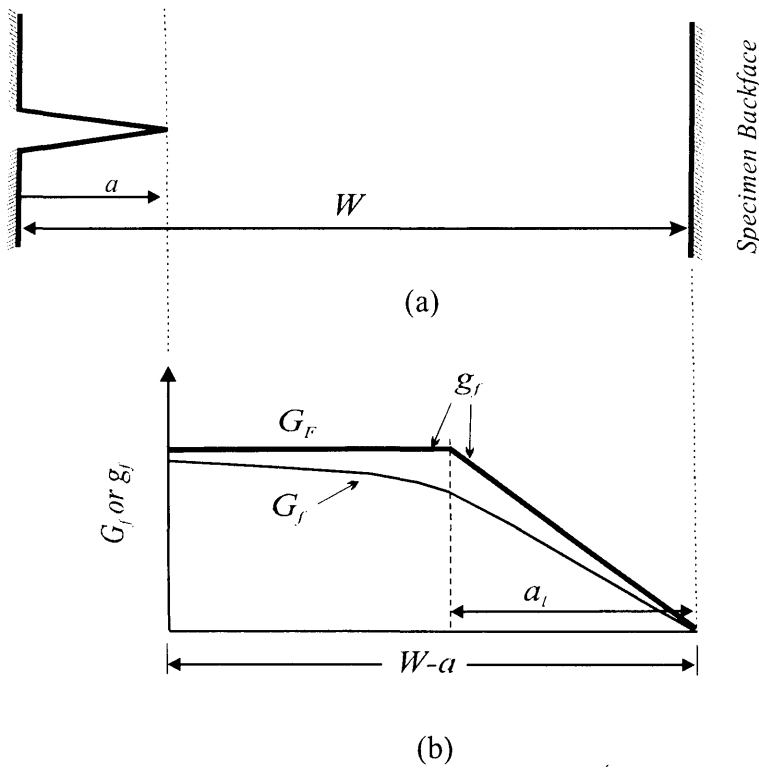


Figure 3.13 A notched test specimen of depth W and notch depth a (a) showing the distribution of fracture energy (G_f and g_f) along the un-notched ligament, $W-a$ (b).

For a specimen with a ligament size ($W-a$) larger than the transition ligament size a_l , $g_f(x)$ is given by (Hu and Wittmann, 2000)

$$g_f(x) = \begin{cases} G_F & x < W - a - a_l \\ G_F \left[1 - \frac{x - (W - a - a_l)}{a_l} \right] & x \geq W - a - a_l \end{cases} \quad (3.30)$$

If $(W-a)$ is smaller than the ligament transition length a_l , the first function in equation 3.26 disappears. Substituting equation (3.30) into (3.28) and introducing the a/W ratio, the size dependent fracture energy G_F is obtained (Duan et al., 2001).

$$G_f(a/W, W) = \begin{cases} G_F \left[1 - \frac{a_l/W}{2(1-a/W)} \right] & ; \quad 1 - a/W > a_l/W \\ G_F \cdot \frac{(1-a/W)}{2(a_l/W)} & ; \quad 1 - a/W \leq a_l/W \end{cases} \quad (3.31)$$

As shown in Figure 3.13, when the initial crack length grows from a to W , the $G_f(a, W)$ or $G_f(a/W, W)$ curve is obtained, showing the ligament effect on the fracture energy. The upper limit of $G_f(a/W, W)$ is the size-independent fracture energy G_F . It can also be seen from Figure 3.13 that it is not necessary to test a very large concrete specimen, because G_F can be back calculated from the size-dependent fracture energy $G_f(a/W, W)$, as long as $(W-a) > a_l$ (Duan et al., 2001)

Abdalla and Karihaloo (2003) further verified the work of Duan et al. (2001) using TPB and wedge splitting (WS) tests on normal (NSC) and high strength (HSC) concretes. For the WS test, they tested specimens of different notch to depth ratios 0.2, 0.3, 0.4 and 0.50. From the load-CMOD diagrams the fracture energy $G_f(a)$ was calculated. These set results were substituted into equation (3.31) in order to determine the size independent specific fracture energy G_F . This experimental work provides further verification of the assumption that $G_f(a)$ is dependent on both the a/W ratio and the specimen size. Furthermore, Karihaloo et al. (2003) simplified the determination of size independent specific fracture energy, G_F by testing a single size specimen with only two notch to depth ratios, provided they are well separated ($a/W = 0.20$ and 0.50 in WS) The selection of the specimen dimensions is dependent on the maximum size of aggregate used in the mix.

3.7 Fracture behaviour of bimaterial systems

A bimaterial is by definition two materials which are perfectly bonded. For example, a substrate/repair system can be considered a bimaterial. Application of any repair material results in bimaterial interface between the repair material and the existing material of the repaired structure. The bonding at the interface is important for safety

and durability. Failure of repaired system relates to cracking along the interface or kinking out of the interface. In the interface cracking case, the interface is relatively weaker than the bordering materials, meaning that the interface crack will propagate exclusively along the least resistance path, i.e. the interface. In the crack kinking case, the interface is relatively stronger than at least one of two adjoining materials. Quantitative evaluation of whether an interface crack will advance straight ahead or kink-out of the interface requires the knowledge of interfacial fracture toughness to be measured (Li et al., 1995).

3.7.1 Experimental Evaluation

To assess the performance of interfaces, several standardized bond strength tests are currently used. Tensile or shear bond strength is usually accepted as an interface property in practice accompanied by a variety of test techniques (Emmons, 1994). However, tensile or shear bond strength give essentially only a maximum value of the stress. It is very difficult to tell from such technique if de-cohesion or separation is obtained in a brittle or ductile manner. Moreover, there is no information about the amount of energy (fracture energy) needed for the separation of the materials. Therefore, the bond strength as such may be useful for ranking of repair materials, but is not expected to have field performance predictive capability due to size and geometric effects. It is important to evaluate the bond properties after the maximum load in order to understand the failure process.

In fracture mechanics, the load-deformation curve contains all information that characterises fracturing of concrete. It is one of the fracture mechanics parameters and is suitable to evaluate the bond failure after the maximum load (Kunieda et al., 2000). To obtain the load deformation curve for a repaired structure, three-point bending and wedge splitting test can be used (Figure 3.14). To date, there are only a few researchers who have used the WS test for evaluating the performance of repaired system, such as Tschegg and Stanzel (1991) (old concrete-new concrete), Tschegg et al. (1995) (Aggregate-cement matrix), Tschegg (1997) (bituminous and layer bonds), Irhouma et al. (1998) (concrete-concrete) and Harmuth (1995) (concrete-polymer modified cement).

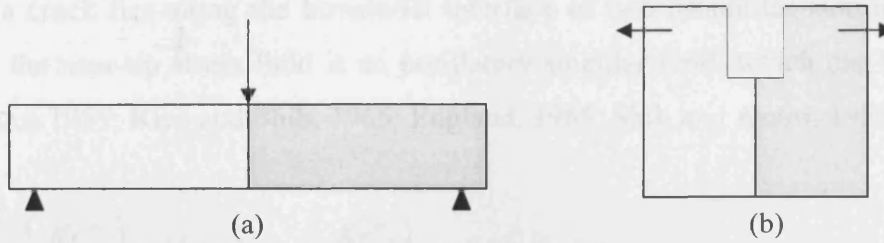


Figure 3.14 Different composite geometry to determine the load-deformation curve for bimaterial.

3.7.2 Characterisation of Cracks at Bimaterial Interfaces

The characterisation of cracks at bimaterial interfaces substantially differs from that of homogenous materials. Unlike homogeneous materials, bimaterial exhibits a coupling of tensile and shear effects. In addition the singular stresses are oscillatory in the vicinity of the interface crack tip. The stress field is characterized by a complex stress intensity factor, K , together with the bimaterial constant ε relating to the elastic properties of the two materials. An alternative characterization of the near tip stress field involves the energy release rate G , together with the mode mixity χ . The mode mixity is a quantity measuring the ratio between the shear stress and the normal stress at the interface in front of the crack tip.

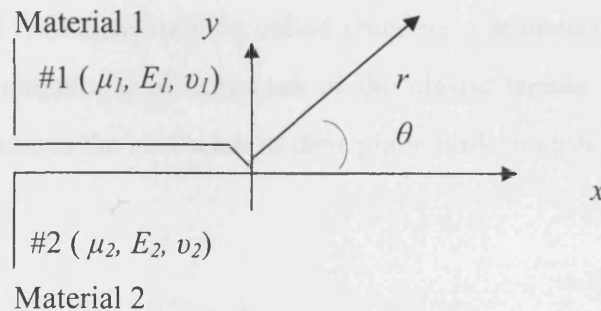


Figure 3.15 Geometry of a bi-material system with an interface crack

Assume two isotropic elastic solids joined along the x -axis (Figure 3.15). Let E_j , ν_j denote the Young modulus and the Poisson ratio of the j th material ($j = 1, 2$), respectively. The corresponding shear modulus, is obtained through

$$\mu_j = \frac{E_j}{2(1 + \nu_j)} \quad (3.32)$$

When a crack lies along the bimaterial interface of two dissimilar isotropic elastic media, the near-tip stress field is an oscillatory singular field, which can be written (Williams 1959; Rice and Shih, 1965; England, 1965; Shih and Asaro, 1988) as

$$\sigma_{ij} = \operatorname{Re} \left\{ \frac{K r^{i\varepsilon}}{\sqrt{2\pi r}} \right\} \sigma_{ij}^{-I}(\theta, \varepsilon) + \operatorname{Im} \left\{ \frac{K r^{i\varepsilon}}{\sqrt{2\pi r}} \right\} \sigma_{ij}^{-II}(\theta, \varepsilon) \quad (3.33)$$

Here r and θ are the polar coordinates; Re and Im denote real and imaginary parts; K is the stress intensity factor; σ_{ij}^{-I} and σ_{ij}^{-II} are the dimensionless angular functions of θ and ε (Shih and Asaro, 1988), and the bimaterial constant ε is defined by

$$\varepsilon = \frac{1}{2\pi} \ln \left(\frac{k_1/\mu_1 + 1/\mu_2}{k_2/\mu_2 + 1/\mu_1} \right) \quad (3.34)$$

where k and μ are Lamé constants and subscripts 1 and 2 refer to the materials 1 and 2, respectively. The quantity ε vanishes when the two materials are identical. The solution of elastic plane problems for bimaterial depends only on two non-dimensional combinations of the elastic moduli, called Dunders' parameters α and β . Physically, α measures the magnitude of mismatch of the elastic tensile moduli of the two bimaterial and β measures the mismatch in their plane bulk moduli

$$\alpha = \frac{\mu_1(k_2 + 1) - \mu_2(k_1 + 1)}{\mu_1(k_2 + 1) + \mu_2(k_1 + 1)} \quad (3.35)$$

$$\beta = \frac{\mu_1(k_2 - 1) - \mu_2(k_1 - 1)}{\mu_1(k_2 + 1) + \mu_2(k_1 + 1)} \quad (3.36)$$

Therefore, the parameter ε can be rewritten as

$$\varepsilon = \frac{1}{2\pi} \ln \left(\frac{1 - \beta}{1 + \beta} \right) \quad (3.37)$$

The energy release rate G is related to K by

$$G = \frac{(1 - \beta^2)}{E^*} (K_1^2 + K_2^2) = \frac{(1 - \beta^2)}{E^*} |K|^2 \quad (3.38)$$

Where $|K|$ is the modulus of K and the effective $E^* = 2E_1' E_2' / (E_1' + E_2')$, in which $E' = E / (1 - \nu^2)$ for plane strain problems and $E' = E$ for plain stress problems and ν is the Poisson ratio. Using the asymptotic field equation (3.33), the tractions at a distance r ahead of the crack-tip along the interface ($\theta = 0$) can be expressed according to Hutchinson et al. (1987) as

$$(\sigma_{22} + i\sigma_{12})_{\theta=0} = \frac{Kr^{i\epsilon}}{(2\pi)^{1/2}} \quad (3.39)$$

According to dimensional analyses (Rice, 1998), the modulus of K has the dimension

$$|K| = [stress][length]^{(1/2)-i\epsilon} \quad (3.40)$$

Obviously, the dimension of the modulus K is quite different from that of homogeneous materials.

The equations of the above paragraph are going to be used in Chapter 5.

3.8 Application of Fracture Mechanics to Reinforced Concrete

The application of the theory of fracture mechanics to reinforced concrete elements is relatively new. Nevertheless, the importance of the results obtained is increasingly recognised since this approach has provided new ways of understanding, and often the only possibility of interpreting, the real structural behaviour which shows failure modes depending upon the size of the structure and the amount of reinforcement. Recently, it has been proved experimentally that even the minimum percentage of reinforcement that enables the element to prevent brittle failure, depends on the size of the element (Bosco et al., 1990a, b and Bosco and Carpinteri, 1992). This

approach was used by Alaei and Karihaloo (2003b) to predict the moment resistance of pre-cracked reinforced concrete beams retrofitted with CARDIFRC[®] and the results found to be in agreement with the test results. The calculation of the plastic moment of a cracked beam element will be briefly explained in the next section.

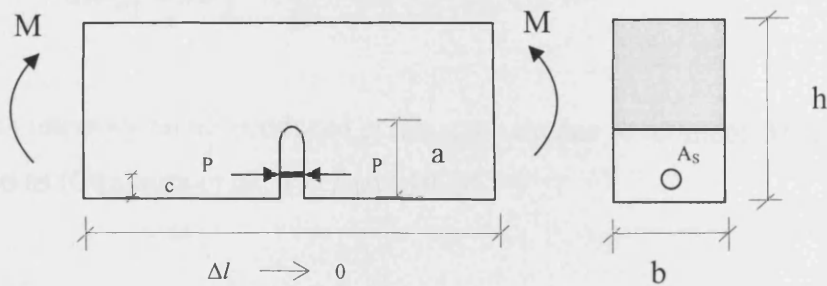
3.8.1 Calculation of the Plastic Moment of a Cracked Beam Element

A cracked section of reinforced concrete beam is shown in Figure 3.16. The section is subjected to a bending moment M and the closing force P applied on the crack surfaces by reinforcement. We can evaluate the angular deformation $\Delta\varphi_{MP}$ produced by the forces P , together with the crack opening displacement $\Delta\delta_{PP}$, at the point where the forces P are applied, and, at the same time, the crack opening displacement $\Delta\delta_{PM}$ caused by the bending moment M , together with the angular deformation $\Delta\varphi_{MM}$. By linear superposition, the total crack opening $\Delta\delta$ and the total relative rotation of the crack faces $\Delta\varphi$ can be written as

$$\Delta\delta = \Delta\delta_{PM} + \Delta\delta_{PP} = \lambda_{PM}M - \lambda_{PP}P \quad (3.41)$$

$$\Delta\varphi = \Delta\varphi_{MM} + \Delta\varphi_{MP} = \lambda_{MM}M - \lambda_{MP}P \quad (3.42)$$

where λ_{MM} , λ_{PM} , λ_{MP} , λ_{PP} , are the compliances of the member due to the existence of the crack. These factors can be derived from energy principles considering the moment M acting simultaneously with the forces P .



3.16 A small beam segment with a crack showing the bending moment M and steel force P (After Bosco and Carpinteri, 1992)

Denoting by K_{IM} and K_{IP} the stress intensity factors due to M and P , respectively, the change in the potential energy, when the crack is gradually introduced, can be

calculated from the integration of (3.19). It should be noted that P does not influence the crack until it has crossed the reinforcing bar

$$\Delta W = \int_0^c \frac{K_{IM}^2}{E} b dx + \int_c^a \frac{(K_{IM} + K_{IP})^2}{E} b dx \quad (3.43)$$

$$\Delta W = b \int_0^a \frac{K_{IM}^2}{E} dx + b \int_c^a \frac{K_{IP}^2}{E} dx + 2b \int_c^a \frac{K_{IM} K_{IP}}{E} dx \quad (3.44)$$

Note that the first term from the second integral has been combined with the first integral with an appropriate change in limits of integration. Using Clapeyron's Theorem, we also have

$$\Delta W = \frac{1}{2} M \cdot \Delta \varphi_{MM} + \frac{1}{2} P \cdot \Delta \delta_{PP} + \frac{1}{2} (P \cdot \Delta \delta_{PM} + M \cdot \Delta \varphi_{MP}) \quad (3.45)$$

Comparing equations (3.45) and (3.44) and recalling Betti's reciprocal theorem ($P \cdot \Delta \delta_{PM} = M \cdot \Delta \varphi_{MP}$), we obtain

$$\frac{1}{2} M \cdot \Delta \varphi_{MM} = b \int_0^a \frac{K_{IM}^2}{E} dx \quad (3.46)$$

$$\frac{1}{2} P \cdot \Delta \delta_{PP} = b \int_c^a \frac{K_{IP}^2}{E} dx \quad (3.47)$$

$$P \cdot \Delta \delta_{PM} = M \cdot \Delta \varphi_{MP} = 2b \int_c^a \frac{K_{IM} K_{IP}}{E} dx \quad (3.48)$$

The stress intensity factor produced at the crack tip due to moment M can be expressed as (Okamura et al., 1973 and 1975)

$$K_{IM} = \frac{M}{h^{3/2} b} Y_M(\xi) \quad (3.49)$$

where ξ is the ratio of the depth of crack to the height of the beam (a/h). Similarly, the stress intensity factor produced by the forces P acting at the level of reinforcement is (Tada et al., 1985)

$$K_{IP} = \frac{P}{h^{1/2}b} Y_P(\beta, \xi) \quad (3.50)$$

where $\beta = c/h$. Substitution of (3.49) and (3.50) into (3.46)-(3.48) gives the compliance coefficients

$$\lambda_{MM} = \frac{2}{h^2 b E} \int_0^\xi Y_M^2(x) dx \quad (3.51)$$

$$\lambda_{PP} = \frac{2}{b E} \int_{c/h}^\xi Y_P^2(\beta, x) dx \quad (3.52)$$

$$\lambda_{PM} = \lambda_{MP} = \frac{2}{h b E} \int_{c/h}^\xi Y_M(x) \cdot Y_P(\beta, x) dx \quad (3.53)$$

The compliance functions $Y_M(x)$ and $Y_P(\beta, x)$ will be given in Chapter 8.

Next, if it is assumed that the crack faces do not open (i.e. the net relative displacement $\Delta\delta$ is zero in (3.41)) up to the moment of yielding or slippage of the reinforcement, then the moment at plastic flow or slippage of steel can be computed from (3.41) as

$$M_p = P_p h \frac{\int_{c/h}^\xi Y_P^2(\beta, x) dx}{\int_{c/h}^\xi Y_M(x) \cdot Y_P(\beta, x) dx} \quad (3.54)$$

where $P_p = A_s f_y$ indicates the yielding force in the reinforcement.

As mentioned before, this application will be further discussed and expanded in Chapter 8 and the consequences of the assumption that $\Delta\delta = 0$ when P reaches P_p examined.

Chapter 4

High Performance Fibre Reinforced Cementitious Composites (HPFRCCs)

4.1 Introduction

Concrete as a structural material has undergone several important stages of development. In the early 1900s and around 1940s, steel reinforced concrete and prestressed concrete established themselves as viable alternatives to steel as major construction materials. High strength concrete became commercialised around 1970s with the arrival of silica fume and superplasticizer as chemical additives. The development of high strength concrete (HSC) continues to impact the design of taller, longer and bigger infrastructures. Fibre reinforced concrete (FRC) began its broader acceptance by the practicing community in the 1980s, although mostly limited to non-structural use.

Cementitious materials have proven their versatility in many construction applications worldwide. However, they have inherently low strain capacity in tension and consequently low fracture energy. The addition of fibres to such materials leads to improvement in all their material properties.

High Performance Fibre Reinforced Cement Composites (HPFRCCs) represent a class of cement composites whose stress-strain response in tension undergoes strain hardening behaviour accompanied by multiple cracking, leading to a high failure strain capacity. HPFRCCs result from the inclusion of a large amount of fibres in the cement based matrix without affecting the workability of the mix. These advances are based on the use of silica fume and surfacants which reduce water demand and densify the matrix, thereby improving the fibre-matrix interfacial bond (e.g. Morin et al., 2001; Yogendran et al., 1987; Roa, 2001; Bache, 1981)

A new class of HPFRCC materials has been recently developed at Cardiff University, designated CARDIFRC[®]. It is characterised by high tensile/flexural strength and high-energy absorption capacity (Karihaloo et al., 2001). This chapter will focus on the behaviour of this class of material, as well as other HPFRCCs that have been presented to the industry so far.

4.2 Normal strength concrete (NSC)

Plain concrete, which is known as normal strength concrete (NSC), consists of cement, water and aggregate (coarse and fine) and exhibits relatively good compressive strength up to 40 MPa, low tensile strength and low strain at fracture. Due to its heterogeneity and the characteristics of its basic materials, it is difficult to obtain better mechanical properties unless additives are incorporated in the original mix.

Plain concrete has two major deficiencies; a low tensile strength and a low strain at fracture. The tensile strength of concrete is very low because plain concrete contains numerous microcracks. It is the rapid propagation of these microcracks under applied stress that is responsible for the low tensile strength of the material (Ramakrishnan 1995). The mechanical behaviour of concrete is governed by the initiation and propagation of the pre-existing microcracks when subjected to loads. Under loading, these microcracks remain stable up to approximately 30 % of peak load. With increasing load, the randomly distributed microcrack networks begin to increase in length, width and number; this stage is known as slow crack propagation (Neville, 1995). Hence, there is a substantial non-linearity even before maximum load. As the load approaches 70% to 90% of peak load, the microcracks coalesce and localisation occurs; this is known as the fast crack propagation stage (Ansari, 1989; Neville, 1995). After peak load, softening behaviour occurs under steady-state crack propagation.

The propagation of cracks in NSC is due to the bond failure at the aggregate-paste interface, which is partially a result of stress concentration caused by the incompatibility of the elastic moduli of cement paste and the aggregate (Newman, 1965). Cracks normally run around aggregates through the cement aggregate bonds (Bentur and Mindess, 1986), thus, the main factor limiting strength development is the aggregate-matrix interface (Struble et al., 1980).

4.3 High strength concrete (HSC)

In order to meet some specific needs and requirements, concrete properties have to be improved. As far as the strength is concerned, Neville and Aitcin (1998) stated that the strength can be required at a very early age in order to put the structure into

service. However, high strength concrete tends to be brittle when loaded to failure. This is due to the lack of plastic deformation that is typical of low strength concrete.

The microstructure of HSC is more homogeneous and the size of the inherent flaws is smaller and more uniform. Moreover, the difference between the modulus of elasticity of the concrete matrix and aggregate for HSC is smaller than for NSC, resulting in lower stress concentrations at the transition zone (Neville, 1997). Cracks in HSC are relatively uniform in size and are activated approximately simultaneously under loading resulting in a more linear stress-strain relation and increased brittleness (Reinhardt, 1995). They usually travel through the aggregate (Tasdemir and Tasdemir, 1995) resulting in a relatively smooth fracture surface.

4.4 High performance concrete (HPC)

High performance concrete contains, in general, the following ingredients: good quality aggregate, ordinary portland cement (at high content, about 450-550 kg/m³), silica fume (about 5-15% by volume) and superplasticizers. Moreover, it has been mentioned that some other cementitious materials, such as fly ash or ground granulated blastfurnace slag (ggbfs) may be used depending on the application.

Domone and Soutsos (1995), and Sabir (1995) reported that high strength concrete could be considered as a particular case of high performance concrete (HPF). This is because the high performance concrete has other enhanced properties such as stiffness, abrasion resistance and durability. However, Neville and Aitcin (1998) stated that high performance concrete is not the same as high strength concrete. The emphasis has moved from very high strength to other properties desirable under some circumstances. These are a high modulus of elasticity, high density, low permeability and resistance to some forms of chemical attack. Despite the superior characteristics of HPC, some problems seem not to have been overcome. As mentioned earlier, low tensile strength and low strain have yet to be improved.

4.5 Fibre reinforced concrete (FRC)

In order to reduce the brittleness of concrete, which means increasing its ductility and energy absorption capacity as well as improving the overall durability, it is

necessary to incorporate fibres in the original mix. Said and Mandel (1989) stated that the problems of low tensile strength and impact resistance of concrete could be overcome by incorporating steel, glass, polymeric or other types of fibre in the mix.

The idea of using fibres as reinforcement in building materials is not new. The use of straw in clay bricks, horsehair in plaster and asbestos in cement is well known (Dunstan, 1987). The primary role of the fibres in hardened concrete at low volume fractions is to modify the cracking mechanism. Ramakrishnan (1995) reported that, by modifying the cracking mechanism the macro-cracking becomes micro-cracking and therefore smaller cracks reduce the permeability and enhance the ultimate strain. Furthermore, one of the major contributions of fibres is to bridge across the matrix cracks that develop as concrete is loaded and as a result, improve the toughness or apparent ductility of the concrete.

As stated by Ramakrishnan et al. (1987), because of the flexibility in method of fabrication, fibre reinforced concrete (FRC) is an economical and useful construction material. FRC specimens, unlike plain concrete specimens that fail at the point of ultimate flexural strength or the first crack, do not fail immediately after the initiation of the first crack. After the first crack the load is transferred from the concrete matrix to the fibres.

Although some concrete properties might be dramatically enhanced by using steel fibres, some problems could still occur. Firstly, corrosion of steel fibres in concrete with a high water to cement ratio may cause deterioration and secondly, the problem of ensuring adequate workability (flowability and compactability). Narayanan and Kareem (1982) reported that, one of the most common problems in the application of FRC is the lack of adequate workability. The workability is influenced by the water/cement ratio, aggregate/cement ratio, the size and shape of aggregate and the length of fibre.

4.6 HPFRCCs

Fibre reinforced cementitious composites can be classified into three groups. FRC employing low fibre volume fractions (< 1%) utilize the fibre for reducing shrinkage

cracking (Balaguru and Shah 1992). FRC with moderate fibre volume fractions (between 1% and 2%) exhibit improved mechanical properties including modulus of rupture (MOR), fracture toughness, and impact resistance. In the last decade, a third class of FRCs, generally labelled as high performance FRC, or simply HPFRCC, has been introduced. HPFRCC exhibits apparent strain-hardening behaviour by employing high fibre contents

FRCs can be categorised into two classes according to their tensile response: conventional FRC and high performance FRC (HPFRCC). Conventional FRC exhibits an increase in ductility over that of plain concrete, whereas HPFRCCs exhibit a substantial strain-hardening response, leading to a large improvement in both strength and toughness compared with the plain concrete (Shah et al., 1999).

HPFRCCs include materials such as SIFCON (Slurry Infiltrated Fibre Concrete), MDF (Macro Defect Free), ECC (Engineered Cementitious Composites) Fibre reinforced DSP (Densified Small Particle Systems), CRC (Compact Reinforced Composite), RPC (Reactive Powder Concrete) and CARDIFRC[®]. These materials have been shown to develop outstanding combinations of strength and ductility as well as long-term durability (Reinhardt, 1991; Karihaloo et al., 2001; Li and Kanda, 1998; Lankard 1985; and Bache, 1981).

HPFRCCs can be designed systematically, based on the knowledge of how crack-like defects in the composite grow and the influence of fibre bridging on the mode of composite failure. Fracture mechanics plays a significant role in the development of composite design strategy (Bache 1989; Li 1993).

4.6.1 Bridging action of the fibres

Extensive research has shown that the most fundamental property of a fibre reinforced cementitious material is the fibre bridging across a matrix crack (Li, 1992; Li et al., 1991; Lin and Li 1997).

Incorporation of fibres in HPFRCCs is a vital factor for increasing the tensile strength of the composite and for improving the ductility (turns brittle material into a

very ductile one). When the composite is first loaded, the load-displacement response is approximately linear and the fibres act as a crack arrester, thus increasing the required energy for crack propagation. The response starts to become non-linear just before the matrix first crack (Mobasher et al., 1990). The region after the initiation of first crack is called the multiple cracking region in which the stress-strain curve deviates from linearity. The first crack strength depends primarily on the matrix properties and is only minimally dependent on the fibre parameters (Johnston and Skarendahl, 1992). This mechanism at the material level results in an increase of strength, with the magnitude of this increase primarily dependent upon the fibre content (Rossi and Chanvillard, 1992). As the load is further increased, some microcracks will emerge. These microcracks will be bridged by fibres. Very high shear stresses are developed between the fibres and the matrix where the fibres emerge from the crack face (Gray, 1984). The shear stress values attained depend on the difference on the elastic modulus between the fibres and the matrix and on the fibre volume fraction. This shear stress helps transfer some of the load to the fibres. According to Balaguru and Shah (1992) when the matrix cracks, the fibre transmits the load across the crack.

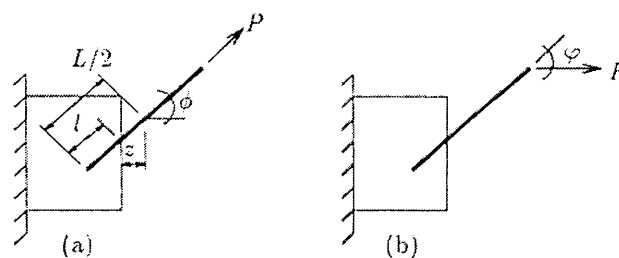


Figure 4.1 (a) A single fibre pull-out without snubbing ($\phi = 0$) and (b) with snubbing ($\phi \neq 0, \phi = \phi$) (After Karihaloo and Wang, 2000)

Since fibres are randomly dispersed throughout the matrix, their orientations relative to the direction of the applied load are an important factor. In a matrix containing randomly distributed fibres, few fibres align in the direction of applied load, instead almost all fibres are oriented at different angles to the load direction (Figure 4.1). When a fibre is pulled out from the cementitious matrix, the snubbing friction at the fibre exit point can increase the pull-out resistance, and contributes to the overall

composite action. Experimental observations showed that inclined fibres can sustain a greater load as they bend. This is known as dowel action. Naaman and Shah (1976) reported that after matrix cracking, the load and energy required to pull a steel fibre out from the matrix can be higher for fibres inclined to the load direction.

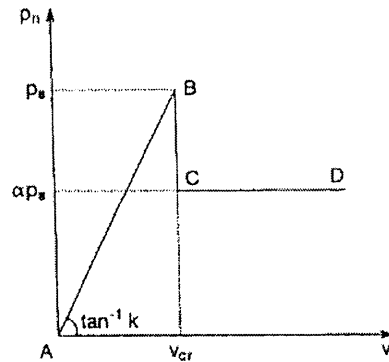


Figure 4.2 A linearised bridging law describing the relation between the bridging force and the crack opening displacement (Karihaloo and Wang, 1997)

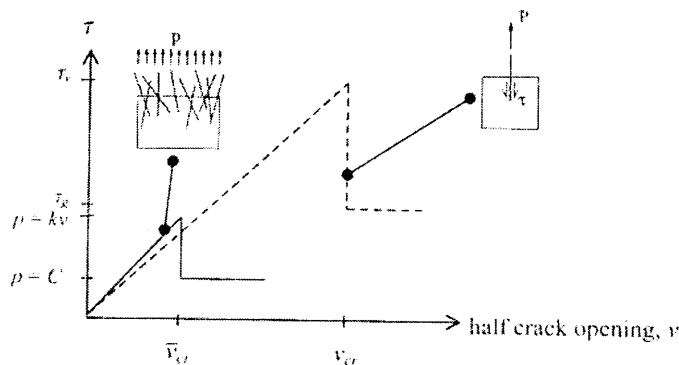


Figure 4.3 Idealised interfacial matrix-fibre shear stress (τ) vs. half crack mouth opening for single fibre (dashed line) and multiple fibre (solid line) pull-out (After Lange-Kornbak, 1997)

It is assumed that when the crack opening displacement reaches a critical value v_{cr} , some of the fibres bridging the crack will debond from the matrix, resulting in a sudden drop in the bridging force (BC), whereafter these fibres will exert a reduced closure force by frictional pull-out (CD) (see Figure 4.2). This is based on single pull-out tests. From this single fibre relationship, the average closure force on crack faces bridged by many fibres is obtained through an approximation to the fibre distribution function (Figure 4.3). The slope of the elastic part of this averaged pullout diagram gives directly the parameter k in equation (4.2) below.

When the crack opening exceeds the critical value \bar{v}_{cr} , the bridging stress $p(v)=kv$ drops to the constant frictional pull-out value, the parameter C in equation (4.3) below.

The bridging stress for multiple fibre bridging is expressed in terms of single fibre properties τ_v , the adhesive bond strength of the fibre and the matrix, and τ_g the frictional pull-out strength of fibre. This is achieved by introducing the ratio

$$\zeta = \frac{\bar{v}_{cr}}{v_{cr}} \quad (4.1)$$

where \bar{v}_{cr} follows from the multiple crack model, since it assumes that slip is initiated immediately after reaching the ultimate tensile load, whereby the corresponding maximum half opening of the crack equals \bar{v}_{cr} (Lange-Kornback and Karihaloo, 1997). The bridging forces are

$$p(v) \approx 2V_f \frac{\tau_v}{\tau_g} E_f \frac{h}{L} v \equiv kv \quad v < \bar{v}_{cr} \quad (4.2)$$

$$p(v) \approx \frac{1}{2} V_f \tau_g \frac{L}{d} h \frac{\bar{v}_{cr}}{v_{cr}} \equiv C \quad v \geq \bar{v}_{cr} \quad (4.3)$$

where V_f is the volume fraction of fibre, L the length of the fibre, d the diameter of the fibre, and h is the snubbing factor (defined by Karihaloo and Wang, 2000) as

$$h = \frac{2}{(4 + f^2)} (e^{f\pi/2} + 1) \quad (4.4)$$

where f is the snubbing friction coefficient.

4.6.2 Constitutive Model

The constitutive model describes the stress-strain behaviour of short fibre-reinforced cementitious in tension/flexure. The similarities and differences in the constitutive behaviour of two types of FRC (conventional FRC and high-performance FRC), as described by Karihaloo and Wang (2000) follow.

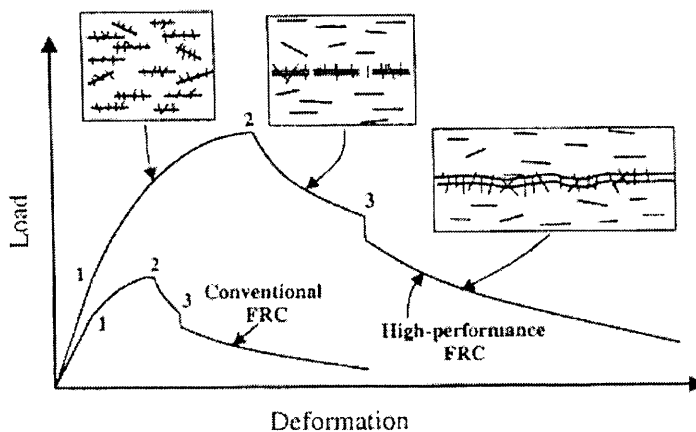


Figure 4.4 Complete pre- and post-peak tensile response of two short fibre-reinforced cementitious composites (After Karihaloo and Wang, 2000).

Figure 4.4 illustrates the load-deformation response of conventional and high performance FRC to tensile/flexural loading. As can be seen, the total tensile strain and load carrying capacity of HPFRCC are higher than for the conventional FRC, and the amount of stored energy represented by the area under the curve in HPFRCC is much higher than that of conventional FRC. The deformation is generally expressed in terms of strain up to the peak load (point 2) and through crack opening displacement thereafter. Both materials exhibit the following responses (Karihaloo and Wang 2000)

- Linear elastic behaviour up to 1
- Strain hardening behaviour between 1 and 2.
- Tension softening due to localisation of damage in the form of unconnected macrocracks 2 and 3.
- Continued tension softening due to localisation of damage in the form of a through crack until complete rupture.

The complete constitutive relation will be briefly outlined in the following.

4.6.2.1 Linear elastic behaviour

As can be seen in Figure 4.4 both materials exhibit linear elastic behaviour up to point 1 at which the transition between linear elastic and strain hardening behaviour takes place. This is only governed by the tensile strength of the matrix but is mostly unaffected by the fibres parameters (i.e. fibre aspect ratio, volume fraction and bond strength). Due to the fact the HPFRCC contains no coarse aggregate it is extremely brittle, therefore the stress at transition point 1, is uniquely related to the matrix fracture toughness

$$K_{IC,m} = f(w/c, g, V_a) \quad (4.5)$$

where $K_{IC,m}$ is the fracture toughness of the matrix (where I denotes mode I cracking), w/c is the water to cement ratio, g is the maximum size of aggregate and V_a is the volume fraction of fine aggregate. For the calculation of Young's modulus of fibre reinforced concrete Karihaloo and Lange-Kornbak (2001) used the following equation for a two-phase system based on the work of Nielsen (1992)

$$E = E_m \frac{n + \Theta + V\Theta(n-1)}{n + \Theta - V(n-1)} \quad (4.6)$$

where V is the volume fraction of discrete phase, Θ is the geometry function accounting for the configuration (aspect ratio) of the discrete phase and n is the ratio of the modulus of elasticity of the discrete phase to that of continuous phase E_m (i.e. of matrix). The Young's modulus for HPFRCC mix can be obtained by applying equation (4.6) twice (Benson, 2003). First to a two-phase system in which the continuous phase is the cement-silica binder paste and the discrete phase is the fine aggregate, and then to a system in which the cement-silica-fine aggregate mortar is the continuous phase and the fibres the discrete phase. The values of n , V , E_m and Θ are different in the two steps.

4.6.2.2 Strain-hardening behaviour

As can be seen in Figure 4.4, the strain hardening region is located between point 1 and 2. This is known to be a result of the bridging action of fibres on microcracks which prevents their growth and coalescence (Mobasher et al., 1990; Tjiptobroto and Hansen, 1993). This region, which is inelastic strain region due to micro-cracking (also called multiple cracking region), is a unique property of HPFRCCs (Tjiptobroto and Hansen, 1993). Multiple cracking is a property of the bulk material, since no strain localisation occurs. The density of microcracks increases with increasing tensile/flexural loading until it reaches a saturation level (point 2). The extent of strain hardening is determined by the microstructure of the cementitious matrix, the volume fraction of fibres and the bond strength of the fibres.

The occurrence of multiple cracking was explained in an analytical approach developed by Tjiptobroto and Hansen (1993) assuming that the first crack is also the failure crack (observed from failure tests). If the energy needed to form new microcracks is smaller than the energy needed to open the first microcrack (i.e. the onset of failure) then multiple cracking takes place. The model predicts that the existence of a multiple cracking process depends on the fibre properties (fibre length and fibre diameter), interface and matrix properties (debonding energy, interface frictional stress, matrix strength, and water-cement ratio). Moreover, their analyses predict that the major energy term determining the behaviour of multiple cracking is the fibre debonding energy.

Bridging of the multiple cracks by short fibres is a significant mechanism for increasing the strength and toughness of the composite and for preventing a sudden loss of the overall stiffness when the microcracks coalesce into large bands (Wang and Karihaloo, 2000). The role of fibres in the composite matrix was explained by Balaguru and Shah (1992) and Karihaloo et al. (1996).

When the matrix is loaded, part of the load is transferred to the fibres along its surface. As mentioned earlier due to the difference in stiffness of fibre and matrix, shear stresses develop along the surface of the fibre. This shear stress helps transfer some of the load to the fibre. When the matrix cracks, the fibre transmits the load

across the crack. Fibres added to concrete arrest cracks and distribute imposed deformation into many microcracks.

These microcracks are arbitrarily orientated. Because of this reason modelling of the constitutive behaviour of a material with microcracks is a difficult and complicated problem. One simplified way to model a microcracked solid from a fracture mechanics point of view is to assume that the cracks are arranged in a regular pattern, among which the simplest form is the doubly periodically arranged array (Karihaloo et al., 1996). Karihaloo et al. (1996) solved the problem of doubly periodic arrays of cracks when the cracks are free of traction and when they are subjected to a closure pressure. They showed that the stiffness decreases in the strain hardening region between 1 and 2 according to the following formula

$$\frac{E_y}{E} = \left[1 - \eta \frac{\omega}{\pi \Omega^2} \ln \left(\cos \frac{\pi}{2} \Omega \right) \right]^{-1} \quad (4.7)$$

where (E_y/E) is the normalised instantaneous modulus in the direction of loading, $\omega = a^2/(WH)$ is the crack density and $\Omega = 2a/W$. W and H are the horizontal and vertical crack spacing, respectively (Figure 4.5). The coefficient

$$\eta = \frac{1}{1 + \alpha + \beta} \quad (4.8)$$

and

$$\alpha = 4 \sin^2 \frac{\pi a}{W} e^{-2 \frac{H}{W} \pi} \left[\frac{1}{1 - e^{-2 \frac{H}{W} \pi}} + \frac{2 \frac{H}{W} \pi}{\left(1 - e^{-2 \frac{H}{W} \pi} \right)^2} \right] \quad (4.9)$$

$$\beta = -\frac{kW^2}{\pi a E} \ln \left(\cos \frac{\pi a}{W} \right) \quad (4.10)$$

Note that k is the bridging stiffness (equation 4.4) and for unbridged cracks $\beta = 0$.

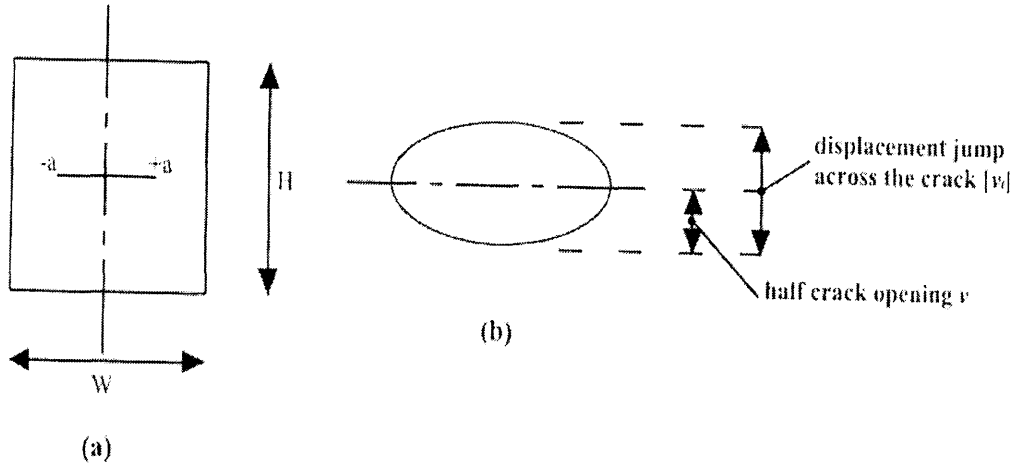


Figure 4.5 (a) Representative unit volume of the matrix containing one microcrack of length $2a$ (note that the volume V of this unit $= W*H*1$ and the surface area of the crack $S = 2a*1$); (b) an enlarged view of the crack opening (After Benson, 2003).

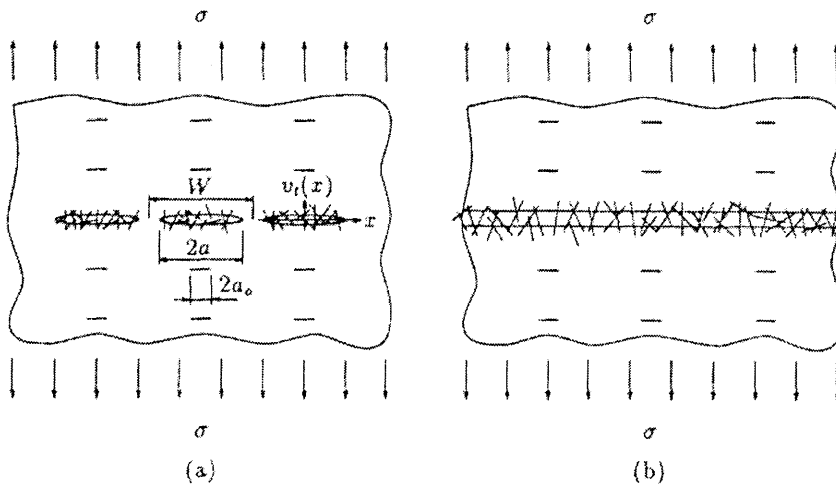


Figure 4.6 (a) Crack configuration prior to coalescence (b) after coalescence of cracks during tension softening of fibre-reinforced quasi-brittle materials (After Karihaloo and Wang, 2000).

4.6.2.3 Tensile Strength (f'_t)

The uniaxial tensile strength of the composite f'_t is the effective stress at the onset of localisation of deformation along the eventual failure plane. At this stage, the cracks in the localisation zone are still unconnected, so that the force is transmitted across the localisation zone partly by fibres (P_f) and partly by the unbroken matrix ligaments (P_b) (Karihaloo and Lange-Kornbak, 2001)

$$f'_t = \frac{P_b + P_f}{W^2} \quad (4.11)$$

where W is the centre-to-centre distance between the unconnected crack segments (Figure 4.5). The contribution of the unbroken matrix ligaments (P_b / W^2) and the contribution P_f / W^2 to f'_t can be evaluated. Lange-Kornbak and Karihaloo (1997) have shown that the rigorous estimate of f'_t given by this method is very close to that given by the rule of mixtures

$$f'_t = \beta_1 \frac{\eta K_{Ic,p}}{\sqrt{\pi a_0}} (1 - V_f) + \beta_2 \tau_v V_f \frac{L}{d} \quad (4.12)$$

where $\beta_1 \approx 1, \beta_2 \approx 0.5, \tau_v$ is the average bond stress at the fibre-matrix interface at the attainment of f'_t . a_0 is the half-length of each crack segment in the array at peak load and $\eta (>1)$ is a factor that depends on the volume fraction of the fine aggregate V_a . L and d are the length and diameter of fibres, respectively.

4.6.2.4 Tension softening behaviour

This is due to localisation of damage in the form of unconnected crack fragments between points 2 and 3 (Figure 4.4). When the strain hardening capacity has been exhausted (i.e. the tensile/flexural strength of the composite has been reached), some of the fibres begin to debond from the matrix, resulting in the localisation of deformation along the eventual failure plane. The localisation manifests itself in the opening of cracks along this plane, but without their actual coalescence. The strain level away from this localised zone usually decreases first and then remains almost

unchanged. The increased deformation is due to the progressive debonding of the fibre under decreased applied loading which results in the opening of fragmented cracks and their growth (region between 2 and 3).

The fraction of fibres that remains elastically bonded to the matrix progressively decreases from 2 to 3 until at 3 (Figure 4.4) all the fibres debond, resulting in an instantaneous drop in the residual load carrying capacity and in the coalescence of crack fragments to form a through crack. Thereafter, the residual tensile carrying capacity is determined entirely by the frictional contact between the fibres and the matrix until the fibres are completely pulled out of the matrix, and failure occurs.

The tension softening response of short-fibre-reinforced cementitious composites (SFRCC) which exhibit extensive matrix cracking was modelled by Karihaloo et al. (1996) and Li et al. (1991). Karihaloo et al. (1996) model is suitable to describe the initial softening behaviour (prior to coalescence of the cracks). It is akin to that used by Horii et al. (1989) and Ortiz (1988) for the tension-softening of un-reinforced quasi-brittle materials. However, it differs from that used by Li et al. (1991) who assumed that the localized damage has resulted in a through crack. Thus, this model is more appropriate for describing the extensive tail region of this response when the crack fragments have coalesced and their faces are held together by frictional forces only (Karihaloo et al., 1996). The multiple crack model of Karihaloo et al. (1996) and the through crack model of Li et al. (1991) were combined to yield the complete tension softening behaviour of fibre reinforced composites (Lange-Kornbak and Karihaloo, 1997).

Karihaloo et al. (1996) modelled the tension softening response of SFRCC using a collinear array (row) of cracks subjected to bilinear bridging forces. They proposed that the initial tension softening curve (i.e. point 2 to 3 in Figure 4.4) was the result of the growth of discontinuous crack fragments in the localisation zone into the unbroken material (Figure 4.6a). The fibres in this zone are progressively pulled out beginning from the centre of each crack where the opening is largest, so that the crack can grow towards its neighbours. Eventually, when the neighbouring cracks have linked up, a through crack forms which is under the action of the residual

frictional fibre bridging force (Figure 4.6b). Finally, at point 3 in Figure 4.4 only a few fibres remain elastically bonded to the matrix, hence an sudden drop in the stress is anticipated when the crack fragments link up to form a through crack (Lange-Kornbak and Karihaloo, 1997).

4.6.2.4.1 Fracture energy G_f

As mentioned in § 3.4.1 the measured specific fracture energy G_f is the area under the post peak deformation curve per unit crack surface created by fracture. According to Lange-Kornbak (1997) for composites that contain long fibres and not too low a volume fraction, the energy expended on the growth of discrete bridged cracks until the formation of a through bridged crack is a very small proportion of the total specific fracture energy, and it can be neglected. In fact, considerable amount of energy is consumed in the progress pull-out of fibres from a through crack until most of the fibres are pulled out and the load carrying capacity drops to nothing. For a through crack under the frictional action of fibres Karihaloo and Lange-kornbak (1998) showed that the relation between the crack opening w and the stress transmitted across it is

$$\sigma(w) \approx 2hLV_f\alpha\eta K_{IC,m} \sqrt{\frac{1}{d} \frac{E_f}{E_b}} \left\{ \frac{1}{8} - \frac{1}{2L} w + \frac{1}{2L^2} w^2 \right\} \quad (4.13)$$

Using the above relation they obtained the specific fracture energy as

$$G_f = \int_{w=0}^{L/2} \sigma(w)dw \approx \frac{h}{24} L^2 V_f \alpha \eta K_{IC,m} \sqrt{\frac{1}{d} \frac{E_f}{E_b}} \quad (4.14)$$

where E_f , E_b are the Young modulus of the fibre and the unreinforced and uncracked matrix, respectively, α is a parameter which is controlled by η (Karihaloo and Lange-Kornbak, 2001)

4.6.3 Types of HPFRCC

4.6.3.1 Macro-Defect-Free Cement (MDF)

The MDF cementitious materials (also called new inorganic materials, NIMs or chemically bonded ceramics, CBCs) are composites combining portland or high-alumina cement with a water-soluble polymer of high molecular mass (e.g. polyvinyl alcohol, PVA, hydroxypropyl methyl cellulose, HPMC). The latter acts as a rheological aid, reduces the inter-particle friction coefficient and reacts with the hydration products. It prevents flocculation of cement particles, increases the viscosity of the mix at low water to solids ratio, thus permitting the use of intensive-high shear mixing processes without inducing cavitation (Birchall et al., 1981; Shah and Young, 1990).

The MDF pastes have very high tensile strength (150 MPa or more) particularly when mixed with alumina cement. They are prepared under high shear, by mixing inorganic cement with a water-soluble polymer in the presence of limited amounts of water. The final product has very high bend strength, greater than 200 MPa, together with a high modulus of elasticity and relatively high fracture energy (Jennings, 1991). However, the material may display some drawbacks like a high sensitivity to water (Lewis and Kriven 1993). Moreover, the use of fibres in MDF cements is restricted (only long fibres may be used).

4.6.3.2 Slurry Infiltrated Fibre Concrete (SIFCON)

It is a high performance fibre reinforced concrete with a very high fibre content, up to 20 percent by volume depending on the type of fibres used and manufacturing method (Lankard and Newell 1984)

The matrix of this material has no coarse aggregate but a high cementitious content; however, it may contain fine sand and additives such as fly ash, microsilica, and latex emulsion (Naaman 1991). Furthermore, steel fibres are primary candidates for this type of materials. Balaguru and Kendzulak (1986) and Lankard (1985) have shown that in SIFCON the fibres are pre-placed in a mould to its full capacity and the corresponding fibre network is then infiltrated by cement-based slurry. The presence of fibres in SIFCON leads to an enhancement of ductility, as well as a

reduction in crack width. The use of a SIFCON matrix in over reinforced concrete beams can lead to ductility factors three to five times larger than control beams made from a plain concrete matrix (Naaman et al., 1990). They also observed that the use of such materials helps reduce crack widths in the tensile zone at least by one order of magnitude, and contributes to the spread of the zone of plasticity in the compression zone prior to failure.

4.6.3.3 Engineered Cementitious Composites (ECC)

Engineered Cementitious Composites are high performance fibre-reinforced cement based composite materials designed with micromechanical principles (Li, 1998). Micromechanical parameters associated with fibre, matrix and interface are combined to satisfy a pair of criteria, the first crack stress criterion and steady state cracking criterion to achieve the strain hardening behaviour (Li, 1993). ECC has a tensile strain capacity of up to 6% and exhibits pseudo-strain hardening behaviour accompanied by multiple cracking. It also has high ultimate tensile strength (5-10 MPa), modulus of rupture (8-25 MPa), fracture toughness (25-30 kJ/m²) and compressive strength (up to 80 MPa) and strain (0.6%). Due to its superior properties, the material was described above as a durable repair material.

4.6.3.4 Reactive Powder Concrete (RPC)

Reactive Powder Concrete RPC has been developed by the Scientific Division of Bouygues, SA, an international construction company with headquarters at St Quentin en Yvelines in France. The material is characterised by high silica fume content and very low water to cement ratio. It exhibits very high mechanical and durability properties (Richard and Cheyrezy 1994). Compared to conventional concrete, the ductility estimated in terms of fracture energy is increased by one to two orders of magnitude, while the compressive strength values are in the range of 200 to 800 MPa. As reported by Richard and Cheyrezy (1995) the development of RPC was based on the following principles.

- Elimination of coarse aggregate significantly improves the homogeneity of the mix.

- Optimisation of the granular mixture. Microsilica improves the compacted density of the mix thereby reducing voids and defects.
- Incorporation of steel fibres results in a ductile material.
- Reduction of the water to cement ratio and inclusion of superplasticizer ensures a workable mix.

4.6.3.5 DSP Cementitious Materials

Densified cement ultra fine particle based materials DSP was developed by the Danish cement producer, Aalborg Portland-Cement. Production of this material is made possible by superplasticizers and silica fume to systems that can be densely packed in a low stress field and with a very low water content (Bache 1981). DSP belongs to a new class of materials formed from

- Densely packed particles of a size ranging from 0.5 to 100 μm ,
- Homogeneously arranged ultra fine particles ranging in size from about 50 \AA to 0.5 μm and arranged in the spaces between the larger particles.

Dense packing of the particles (sand, cement and ultra-fine silica) together with fibres is essential for achieving the desired mechanical properties. It is also the prime feature of HPFRCCs materials. Materials such as DSP combine very densely packed cement particles (5-10 μm) and ultra fine silica fume (0.1-0.2 μm) filled the spaces between the cement particles and, normally densely arranged fibres, Figure 4.6 (Bache, 1981; Bache, 1987).

Furthermore, the DSP matrix is a very strong and brittle material with a compressive strength of 150 MPa – 270 MPa. Due to its brittleness, it's difficult to utilize this material effectively without the incorporation of fine, strong and stiff fibres. The fibres improve the tensile properties of DSP based matrix such as Densit[®].

4.6.3.6 CARDIFRC[®]

Researchers at CARDIFF University (Karihaloo and De Vriese 1999; Sullivan 1999; Karihaloo et al., 2000) have attempted to reproduce RPC and Densit[®] with materials widely used by the UK concrete industry. The mechanical properties were found to

be inferior to those reported in the literature (Richard and Cheyrezy, 1995; Bache, 1981), and the workability of some mixes was poor. These attempts however provided valuable clues on how to improve the mixing and processing techniques in order to produce HPFRCCs similar to RPC and Densit[®] but whose mechanical performance even exceeds that of the original mixes. Another type of mix, a HPFRCC with 6 mm coarse aggregate, was also investigated (Benson, 1999). The workability of this mix was satisfactory but the mechanical properties were inferior to those achieved with mixes containing no coarse aggregate (i.e. Densit[®] and RPC) (Benson, 2003).

Further rheological studies were continued at Cardiff to optimise HPFRCC. The aim was to achieve good workable mixes with a very low water/binder ratio and a high volume fraction of steel fibre, in order that the resulting concrete, in its hardened state, was very ductile with a relatively high tensile strength. This was achieved by using large amounts (up to 8 % by volume) of short steel fibres (6-13 mm long, 0.16 mm diameter) in a cementitious matrix densified by the use of silica fume. The matrix contains only very fine quartz sands (up to 2mm), instead of ordinary river sand and coarse aggregates. By optimising the grading of fine sands, the water demand is considerably reduced without affecting the workability of the mix.

As a result of many trial mixes and testing, the mixes shown in Table 4.1 are the optimised ones. Two different mixes (designated CARDIFRC[®], Mix I and Mix II) of high-performance concrete differing mainly by the maximum size of quartz sand used in the mix have been developed using novel mixing procedures. These procedures are described in patent application GB 0109686.6.

CARDIFRC[®], differs in several respects from RPC and DSP mixes. First of all, are the two different types of fibres used in combination to the high volume fraction adopted. This rather innovative technique was found to be quite beneficial to the load deflection response of the matrix in terms of both strength and ductility. Investigations showed that the use of two grades of fine quartz sand (Table 4.1) substantially improved the performance of Mix I. Similarly, in Mix II in order to maximize the dry density of the mix three grades of fine quartz were used. This

optimisation of grading of quartz sands used, led to considerable reduction in the water demand without any loss in workability

As claimed by Karihaloo et al. (2001) the produced material (CARDIFRC[®]) in its hardened state is characterised by very high compressive strength (in excess of 200 MPa), tensile /flexural strength (up to 30 MPa), high energy-absorption capacity (up to 20,000 J/m²). Table 4.2 shows the material properties of CARDIFRC[®].

Table 4.1 Mix proportions for CARDIFRC[®] Mix I and Mix II (per m³) (Karihaloo et al., 2001)

Constituents (kg)	Mix I	Mix II
Cement	855	744
Microsilica	214	178
Quartz sand:		
9-300µm	470	166
250-600µm	470	-
212-1000µm	-	335
1-2 mm	-	672
Water	188	149
Superplasticizer	28	55
Fibres: -6 mm	390	351
-13 mm	78	117
Water/cement ratio	0.22	0.20
Water/binder ratio	0.18	0.16

Table 4.2 Typical material properties of CARDIFRC[®] Mix I and Mix II,

Material properties	Mix I	Mix II
Indirect tensile strength (MPa)	28.6	21.4
Fracture energy (J/m ²)	22909	17875
Compressive strength (MPa)	207.0	185.0

4.6.3.6.1-The effect of high temperature curing conditions

Curing conditions and curing temperature influence the properties of hardened concrete. Neville (1995) reported that, a rise in the curing temperature speeds up the chemical reactions of hydration and thus affects beneficially the early strength of concrete. Typically, the remarkable strength properties observed in HPFRCCs are obtained by increasing its curing it at 90°C. For example, compressive strength of CARDIFRC[®] reaches up to 200 MPa when the specimens are cured at high

temperature up to 90°C for only 7 days. At this temperature the microstructure of such materials changes and thus the following exist:

- A homogenous and cohesive interface between CSH paste and the sand.
- A dense CSH matrix.
- A fibril CSH nanostructure.

Zanni et al. (1996) investigated the effect of heat treatment on the hydration of RPC. The investigations showed that silica fume consumption was highly dependent on heat treatment temperature and duration. Moreover, crushed quartz reactivity was also proved to be dependent on heat treatment and duration.

Heat treatment accelerates the hydration process, activates the pozzolanic reaction of silica fume and reduces the curing time of concrete. Karihaloo and De Vriese (1999) showed that, the curing time of RPC specimens could be reduced from 28 to 16 days, when the specimens are cured under the following regime:

7 days	at	ambient temperature
3 days	at	90°C
7 days	at	ambient temperature

The curing time can be reduced further to seven days. Sullivan (1999) confirmed this by exposing RPC specimens to high temperature curing for the entire seven days at 90°C immediately after the moulds are stripped. Similarly, the strengths attained for CARDIFRC[®] specimens cured at 90° C for seven days have been found to be the equivalent of standard 28-day water curing at 20° C (Alaee 2002).

4.6.3.6.2 The effect of silica fume

Silica fume is an extremely fine powder whose particles are about 100 times smaller than cement. The particles of such material pack tightly against the surface of the aggregate and fit in-between the cement particles, thus greatly improving packing. Neville (1995) reported that because the extremely fine particles of silica fume reduce the size and volume of voids near the surface of the aggregate, the so-called

interface zone has improved properties with respect to microcracking and permeability. The bond between the aggregate and the cement paste is improved, allowing the aggregate to participate better in stress transfer.

The main functions of silica fume in HPFRCCs as reported by Richard and Cheyrezy (1995) are:

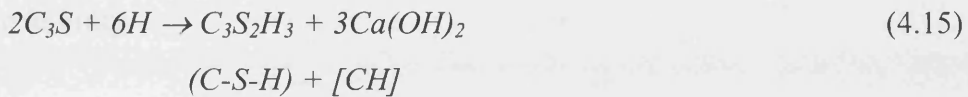
- Filling the voids between the next larger class particles [cement]
- Enhancement of rheological characteristics by the lubrication effect resulting from the perfect spherical shape of the basic particles.
- Production of secondary hydrates by pozzolanic reaction with the lime resulting from primary hydration.

One of the main advantages of using silica fume particles (particle size 0.1-0.2 μ m) with cement (particle size 5-10 μ m) is to fill the spaces between the cement particles and thus achieving very dense packing system. Bache (1981) attributed these to the following: a) the silica particles are smaller than even the finest cement we can produce by grinding and are therefore more conducive to dense packing into the spaces between the cement particles, b) the silica particles, being formed by condensation from gas phase, are spherical in shape (unlike crushed cement particles, which are angular) and this makes the silica particles even more suitable for dense packing than very fine cement, and finally c) the particles are chemically less reactive than cement, which eliminates the problem of too rapid hardening encountered with very fine cement; in addition, the silica is likely to ensure the formation of a coherent structural skeleton between the cement particles, resulting in a fine dense microstructure.

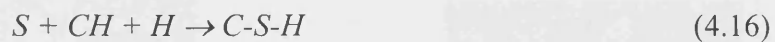
The use of microsilica in HPFRCCs can improve the bond by increasing the contact area between the fibre and the surrounding matrix. This introduction of fine microsilica particles will increase the density of the matrix, filling any pore spaces around the fibre. The increase in the surface contact area increases the pull-out force (Bache, 1981)

Another important property of microsilica is its pozzolanic behaviour. The material is extremely reactive, and hence can react with the surplus of calcium hydroxide, which in ordinary cement paste it will crystallize out as a separate and relatively weak phase. The reaction of microsilica with the remaining calcium hydroxide, from the primary cement water reaction, results in the production of an extra cement of C-S-H. The chemical representation of this process is shown below:

Primary reaction: Cement + Water



Secondary Reaction: Silica + Calcium Hydroxide + Water



The extra production of C-S-H results in a microstructure, which is very dense in the freshly mixed state and gets even denser during the succeeding hydration process. The effect of microsilica in the cement paste is shown in Figure 4.7.

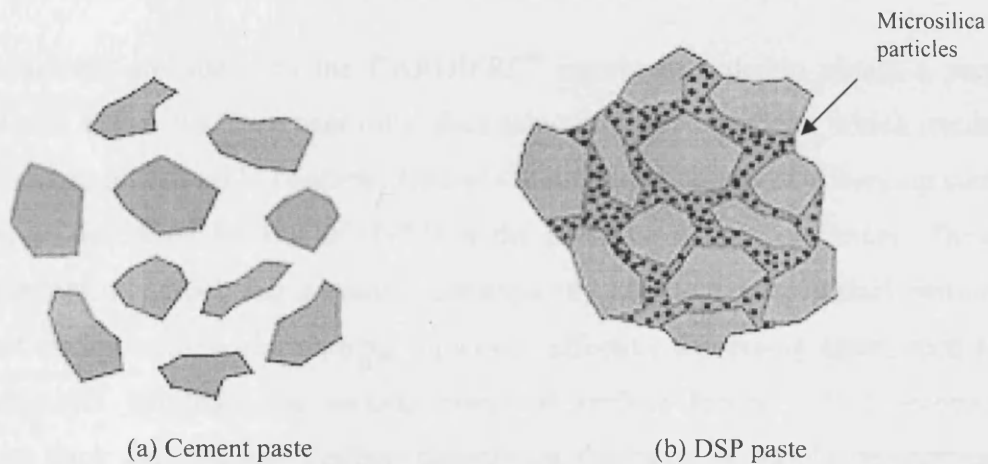


Figure 4.7 (a) Flocculated particles in ordinary cement paste. (b) densely packed cement grains and microsilica in DSP paste

4.6.3.6.3 The effect of dispersing agent (Superplasticizer)

As mentioned earlier, the silica fume (SF) is a finally ground materials and as such, generally increases the water requirement for a given degree of workability at low water/cement ratio. Thus, a high range water-reducing admixture is often introduced to promote the workability. Neville (1995) reported that, superplasticizers are long and heavy molecules, which wrap themselves around the cement particles and give them a highly negative electrical charge so that they repel each other. This results in deflocculation and dispersion of the cement particles (Figure 4.8) and therefore, in high workability.

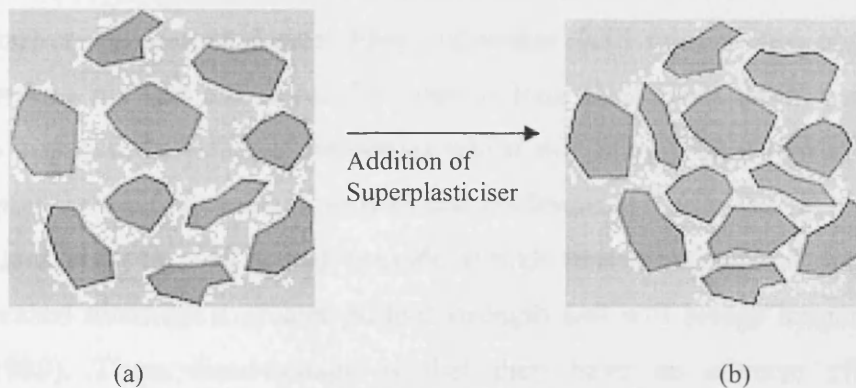


Figure 4.8 (a) Flocculated particles in cement paste. (b) superplasticised cement particles.

Superplasticizers are added to the CARDIFRC[®] matrix in order to obtain a very workable mix at low water/cement ratio, thus achieving dense packing which results in high strength and durable concrete. One of the main difficulties of achieving such a system, as described by Bache (1987) is the presence of surface forces. These forces interlock neighbouring particles, consequently counteracting mutual particle movement during mixing and shaping. However, effective dispersing agent, such as superplasticizers eliminate the locking effect of surface forces and it becomes possible to pack fine particle systems densely on the basis of purely geometrical principle.

The combination of superplasticizers with silica fume in the concrete mix results in high strength and/or high durability. Dugat et al. (1996) reported that by using superplasticizers with silica fume it is possible to reduce the water/cement ratio to less than 0.15. This helps reduce the total pore volume of the cement paste and the

average diameter of the pores, hence improving durability. Moreover, experience with RPC, DSP and CARDIFRC[®] showed remarkable strength properties when superplasticizers and silica fume are incorporated in the original mix.

The amount of superplasticizer used in both CARDIFRC[®] mixes is somewhat higher than that of the original RPC and DSP mixes. This causes the mixes to be very workable.

4.6.3.6.4 The effect of steel fibres

The incorporation of fibres in the CARDIFRC[®] matrix increases the tensile load-carrying capacity and turns an otherwise brittle material into a very ductile one. As mentioned earlier, brass-coated steel fibres (diameter 0.16 mm, 6 mm or 13 mm long) are used to prevent corrosion. The use of long and short fibres was found necessary to improve the material properties whilst minimising loss of workability. The short fibres prevent microcrack growth and coalescence (Mobasher et al., 1990; Tjiptobroto and Hansen, 1993) and provide a high tensile strength. Long fibres provide increased ductility, a greater pullout strength and will bridge longer cracks (Sullivan, 1999). Their disadvantage is that they have an adverse effect on workability.

4.6.3.6.4.1 Fibre distribution

Computerized Topography (CT) imaging and sectioning of specimens have confirmed that the novel mixing procedures used for the production CARDIFRC[®] ensures remarkably homogeneous mixes with a uniform distribution of up to 8 vol % of long and short fibres (Karihaloo and Jefferson, 2001).

To verify that the fibres are uniformly distributed in a CARDIFRC[®] mix, Benson (2003) employed non-destructive and destructive testing techniques. CT results show that the fibres are nearly uniformly distributed with random orientation in the mixes. Destructive testing also confirmed these findings and showed that the fibre distribution was generally uniform.

4.6.3.6.4.2 Volume fraction of fibre

The volume fraction of fibres in concrete affects both the fresh and hardened state. Hoy et al. (1999) reported that when higher volumes of steel fibre are added to concrete, there is a more significant loss of workability and greater chance that fibres will interlock. For these reasons, there is an optimum fibre content for any given fibre-matrix combination. Higher fibre contents will produce mixes which lack homogeneity and have poorer workability, while lower fibres contents will result in less efficient reinforcement. By a careful selection of mix proportions, the optimum fibre content can be increased with a resulting performance improvement.

Basically, as the volume fraction of fibre increases and as the fibres are more uniformly dispersed, the growth of microcracks is hindered, and the localisation of deformation is delayed with a consequent substantial increase in the tensile strength and strain capacities of the composite (Balaguru and Shah, 1992). Mobasher et al. (1990) carried out an experimental programme on the effect of fibre content on the fracture properties of concrete. They concluded that as the volume fraction of fibres increases the growth of microcracks was hindered through an arrest mechanism and the matrix fracture toughness was increased. The higher the volume fraction of fibres, the higher the peak load, and the higher the matrix contribution and the higher the acoustic emission (AE) rate. The higher AE event count means that there is a greater number of microcracks.

Karihaloo and Di Vriese, (1999) studied the affect of volume fraction of fibres on RPC mix. They found that increasing the volume fraction of steel fibres V_f led to major improvements in the properties of RPC, namely, specific fracture energy and indirect tensile strength. Furthermore, Shannag and Hansen (2000) showed that incorporating large volume fractions of short steel fibres (more than 2% by volume) in DSP composites results in a dramatic increase in matrix tensile strength (up to 100%).

4.6.3.6.4.3 Aspect ratio of fibre (l/d)

The physical shape of steel fibres is described by their aspect ratio (length/diameter). As a general rule, higher aspect ratio fibres perform better than lower aspect ones.

Fanella and Naaman (1985) and Gopalaratnam and Shah (1986) found a monotonic increase in compressive strength and ductility when the aspect ratio increased from 47 to 100. Sullivan (1999) also found that long fibres increased both the tensile strength and ductility of concrete. Karihaloo and De Vriese (1999) reported that an increase in fibre length – and consequently of aspect ratio- seems to be more effective than an increment only in volume fraction of fibres. The incorporation of long fibre (13 mm) in CARDIFRC[®] mixes was a primary cause of enhancing the ductility.

4.6.3.6.5 Constitutive description of CARDIFRC[®]

As mentioned by many researchers (Karihaloo et al., 1996; Wang et al., 2000; Karihaloo and Wang, 2000) the strain hardening of HPFRCC is due to the nucleation of microcracks under increased tensile/flexural stress. In the literature, assumptions have been made on their evolution but no experimental evidence is available to validate them. An experimental programme was implemented on CARDIFRC[®] specimens to quantify the increase in the crack density ω in equation (4.7) as a function of applied tensile stress σ and fibre parameters (Benson 2003). Their results show that the fracture process zone is not due to one dominant crack but is due to many cracks. In support of this, parallel cracks, crack branching, cracks linking-up and multiple cracking were all observed and recorded. Moreover, as the active crack opens, evidence of fibre bridging was confirmed. It was also noted that not all cracks continued to propagate; some cracks became dormant since the failure plane will occur along the path of least resistance.

Numerical expressions have been fitted to the test data to describe the behaviour of CARDIFRC in uniaxial tension. Figure 4.9 shows the three regions predicted by the equations. Laboratory test work shows clear evidence that the linear elastic region is larger than theoretically predicted (Karihaloo and Wang, 2000), a smaller strain hardening region with a distinct plateau at the peak load followed by a gradual decrease in the stress after the peak load.

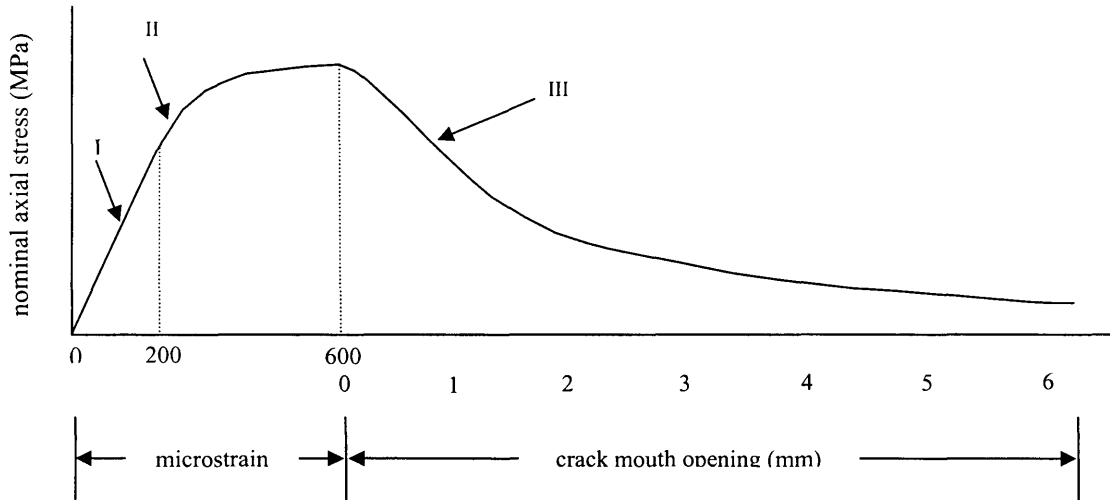


Figure 4.9 Complete pre- and post peak tensile curve for CARDIFRC®.

Stage I- Linear-elastic region

Applicable form 0 to 200 microstrain

$$\sigma_I = 0.046\varepsilon \quad (4.17)$$

Stage II- Strain hardening region

Applicable form 200 to 600 microstrain

$$\sigma = -4.34 \times 10^{-10} \varepsilon^4 + 8.32 \times 10^{-7} \varepsilon^3 - 6.03 \times 10^{-4} \varepsilon^2 - 0.199 \varepsilon - 12.62 \quad (4.18)$$

Stage III- Tension hardening region

Applicable From 0 to 6.5 mm

$$\sigma = 3.07 \times 10^{-3} w^7 - 0.08 w^6 + 0.82 w^5 - 4.42 w^4 + 12.80 w^3 - 18.11 w^2 + 5.73 w + 12.89 \quad (4.19)$$

4.7 Conclusion

From the foregoing literature review, HPFRCC materials have shown superior characteristics in terms of material properties. Their mechanical and fracture properties have been enhanced very substantially compared to other types of concrete. In fact, the brittleness of concrete is reduced by incorporating fibres. The incorporation of small amount of fibres is mostly apparent in the post-cracking

response. However, improvements in other properties such as first cracking strength, tensile strain capacity, and peak load are insignificant. With the advent of special processing methods (novel mixing procedure) and the use of high volume fraction of steel fibre, concretes of high compressive, tensile strength as well as high energy absorption have been reported. The produced material (CARDIFRC[®]) is characterized by strain hardening (multiple-cracking) and followed by tension softening due to localization of cracks.

CARDIFRC[®] is a new kind of high performance fibre reinforced cementitious composite (HPFRCC). It is an exciting durable material with great potential. It has many potential applications. This material can be used for retrofitting (Alaee et al 2001; Karihaloo et al., 2001; Karihaloo et al., 2002), for durable and reliable joining of pre-cast concrete elements, for the construction of structures for the containment and retention of hazardous materials and for the protection of valuable civilian and military assets, offshore and marine structures, overlays on ordinary concrete subjected to chemical attack, water and sewerage pipes, different climatic conditions, etc.

Chapter 5

*Performance of NSC bonded to
CARDIFRC[®] after thermal cycling*

5.1 Introduction

Concrete has been used for more than one hundred years ago as a main construction material owing to its significant resistance in compression. Much attention has been paid to the fracture properties of concrete at room temperature, including strength, stiffness, toughness and brittleness. Information about these properties under high temperature environment, however, is very useful for designing concrete structures subject to various high temperature environments.

So far, much attention has been paid to the study of concrete strength and stiffness (Castillo and Durrani 1990; Bertero and Polivka 1972; Berwanger and Sarkar 1973; Bairagi and Dubal 1996) for various heating scenarios (heating rate, maximum heating temperature, exposure period, heating rate, heating cycle). Some work has been done on concrete toughness (Abdel-Fattah and Hamoush 1997), and brittleness and fracture energy (Bazant and Part 1988; Baker, 1996; Zhang et al., 2000). Most of these studies have focused on concrete properties after fire. It was found that concrete exposed to elevated temperatures experiences severe deterioration. However, research on hardened concrete after the occurrence of climatic changes seems to be very limited.

As mentioned earlier in Chapter two, retrofitted concrete can also be affected by high temperature, particularly the daily and seasonal temperature fluctuations. The bonding at the interface between concrete and repair materials is most likely to be affected. For improved resistance of concrete structure against penetration of harmful materials, good bonding is required at concrete interfaces. Due to the effect of temperature on the interface, interface failure can limit the performance of the repaired system.

The aim of this chapter is to evaluate the performance of normal strength concrete specimens repaired with CARDIFRC[®] using the wedge splitting test (WST) (Tschegg, 1991), by investigating the interfacial fracture behaviour of CARDIFRC[®]/concrete repair system. Emphasis will be placed on the main factors that affect the bond between the repair material and concrete, such as the surface roughness and environmental conditions (thermal cycling). It is also intended to

provide information on the behaviour of control NSC under thermal cycling. The results of CARDIFRC[®]/concrete repair system will be compared with those of control NSC specimens exposed to the same environment.

5.2. Mixing and casting procedure of CARDIFRC[®]

The mix proportions of CARDIFRC[®] Mix I is shown in Table 5.1 and the mixing was performed according to the procedure outlined by Karihaloo et al. (2002). The mixing was done in a horizontal pan mixer. The coarsest constituent (250-600 μm sand) was initially mixed with the finest (microsilica) for two minutes. Sand grains are covered by a film of ultra fine microsilica particles. In fact, the rolling of the sand grains during the mixing makes nearly spherical shape particles, which can easily move past each other. The next coarsest constituent (9-300 μm sand) was added and mixed for two minutes until a uniformly distributed mixture was achieved. Following this, the next finest constituent (cement) was added and mixed for the same period. The fine sand and cement fill the gaps between the spherical particles of the coarsest sand.

Table 5.1. Mix proportions for CARDIFRC[®] Mix I (per m^3) (Karihaloo et al., 2002)

Constituents (kg)	Mix I
Cement	855
Microsilica	214
Quartz sand:	
9-300 μm	470
250-600 μm	470
Water	188
Superplasticizer	28
Fibres: -6 mm	390
-13 mm	78
Water/cement ratio	0.22
Water/binder ratio	0.18

In order to further strengthen the mix and enhance its energy absorption capacity, 13 mm and 6 mm brass coated steel fibres were added to the dry mixture. These fibres were added through appropriately sized vibrating aperture surfaces to achieve an even distribution of the fibres. The fibres were added as follows:

First, 25 percent of the shorter fibres (6 mm) were placed in a coarse sieve having an aperture size of 5 mm x 5 mm. The sieve was agitated to cause the fibres to fall into the mixture. It was found that the use of sieves helps to separate the fibres, thereby avoiding their clumping in the mixture. The fibres were mixed with the mixture for two minutes, before the next 25 percent of the fibres were added and mixed. This procedure was repeated until all the short fibres have been added. 13 mm long fibres were then added in a similar stepwise manner using a 12 mm sieve.

In the last stage a mixture of water and two-thirds of the total superplasticizer was added to the dry constituents according to the following sequence;

- One half of the mixture was added to the dry mix and mixed for two minutes.
- Half of the remaining mixture was added and mixed for the same duration.
- The process was repeated until the whole mixture has been added.
- Finally, the remaining one-third of the superplasticizer was added and mixed for approximately three minutes.

After mixing, the mix was placed into the WS specimen moulds and vibrated on an electric vibration table at 95 Hz. Thereafter, the moulds were left in environmental conditions for 24 hours before demoulding and placing the specimens in a hot curing tank.

5.2.2 Curing regime

As mentioned above, the demoulded specimens were placed in a steel temperature controlled-tank. The specimens were cured at a high temperature of 90° C for seven days. Sullivan (1999) found that curing HPFRCC mixes at high temperature can greatly improve their microstructure. This is due to the fact that the raised temperature activates the pozzolanic reaction between the calcium hydroxide formed during normal cement hydration and the silica fume contained in the mix. It has also been found that due to this elevated temperature curing regime, the total curing period can be reduced from 28 days to 7 days.

In order to avoid large thermal gradients, that will produce thermal shock, a gradual increase of temperature from ambient temperature to 90° C and vice versa was found



necessary. The specimens were left in the tank for 9 days. On the first day the temperature of the water was increased gradually from 20° C to 90° C and on the ninth day it was decreased (90-20° C).

5.3 Mixing and casting of NSC specimens

An extensive mix design for different grades of concrete has been conducted at Cardiff (Taylor et al., 1996) from which a NSC mix with the required compressive strength was selected. The mix used in this work, given by a cement: fine aggregate: coarse aggregate: water ratio of 1:2:2.5:0.56. The dry ingredients were weighed to the nearest 0.05 kg and kept in plastic buckets prior to mixing. The mixing was carried out in an electrical horizontal rotating pan with a maximum capacity of 0.05 m³. Cement, sand and aggregate were mixed and water added thereafter.

Immediately after the mixing process was completed, the fresh mix was transferred into the test specimens moulds. First, the test specimens needed to assess the mechanical properties of hardened concrete, i.e. compressive, tensile, flexural strengths and modulus of elasticity were cast. This group of specimens comprised of standard samples of 100x100 mm cubes, 100x200 mm cylinders and 100x100x500 mm beams. The second group of specimens is needed to assess the fracture properties of hardened concrete. This group of specimens comprised 200x200x200 mm cubes with a rectangular groove. These specimens were cast in specially manufactured steel moulds for WS test. The final group of specimens will play the role of parent concrete to which the repair material CARDIFRC® will be bonded. This group of specimens comprised of 200x200x98.5mm half cubes. These half cubes were produced using WS steel moulds partitioned with 3 mm sheet metal in the middle.

5.4 Preparation of WS bonded specimens

One day after casting, the half cubes of NSC were removed from the moulds and stored in water for twenty-eight days at 20° C. After curing, the mating surfaces of the half cubes were roughened by an angle grinder (Figure 5.1a). Half cubes of CARDIFRC® were also cast and then cured at 90° C for 9 days as described above. The half cubes of CARDIFRC® and NSC were now ready to be bonded together.

5.5 Adhesive bonding

In order to improve the bond between the repair material CARDIFRC® and the parent concrete, the contacting surface of NSC was carefully cleaned and roughened to create mechanical interlocking between the adhesive and the concrete. The latter was achieved by creating a grid of grooves with angle grinder. The grooves were approximately 3 mm deep at a spacing of 50 mm, (Figure 5.1b). The rough, irregular, and furrowed surface topography creates a structural morphology that allows the adhesive to penetrate into the irregularities, forming a strong interfacial layer

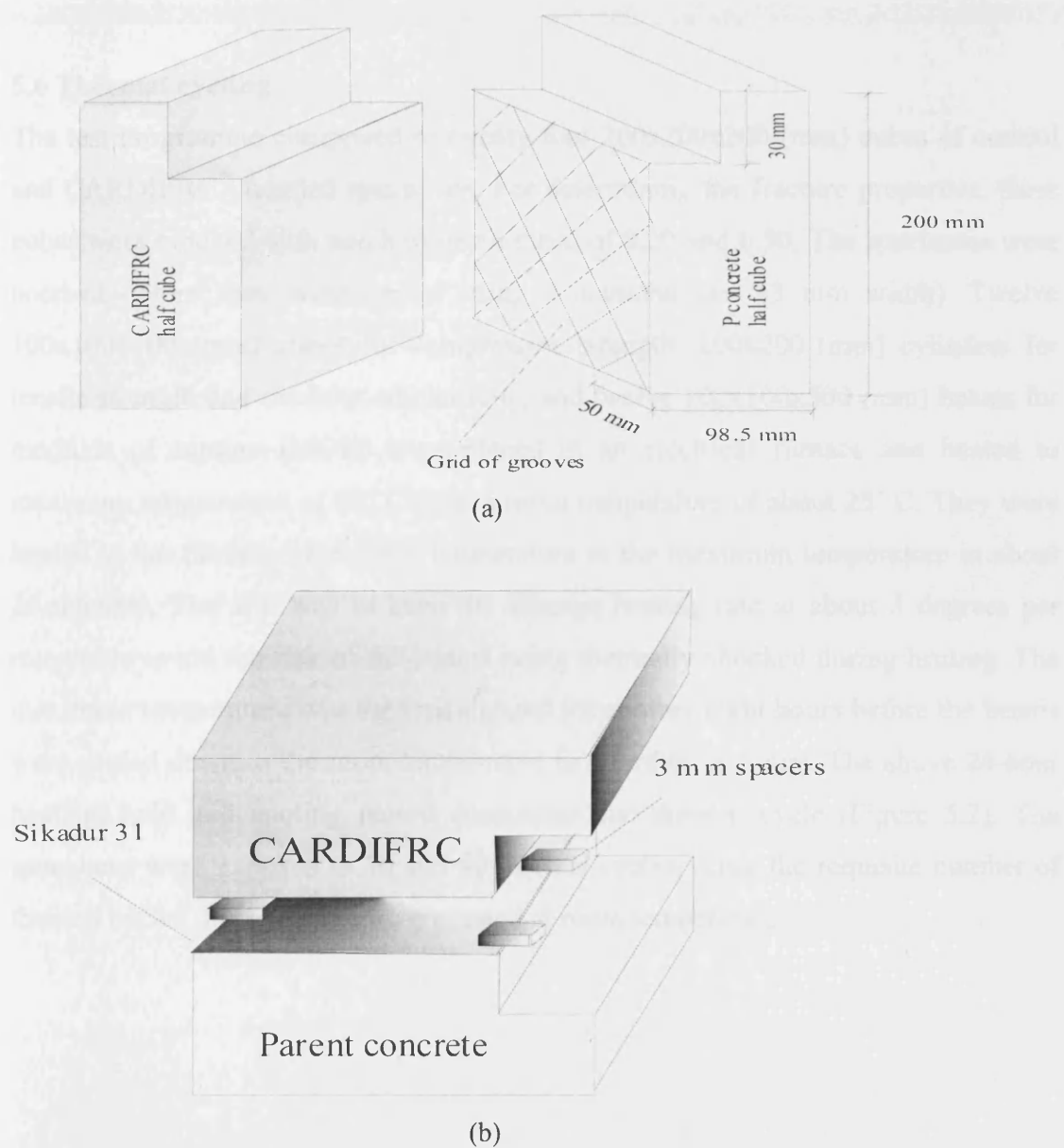


Figure 5.1 Configurations of specimen shapes and bonding techniques: (a) roughened and grooved surface of concrete half cube and (b) adhesive bonding procedure.

The CARDIFRC[®] was bonded to the prepared surfaces of concrete with a thixotropic epoxy adhesive, Sikadur[®] 31. The two parts of the adhesive were thoroughly mixed and applied with a serrated trowel to a uniform thickness of 3 mm. The CARDIFRC[®] half cube was placed on the concrete surface with adhesive and evenly pressed. To ensure that the adhesive had a uniform thickness of 3 mm three small plastic spacers were used during bonding (Figure 5.1a). They were removed after the adhesive hardened, i.e. after approximately 3 hours. In order to create a starter notch the bonded specimen was notched along the interface with a diamond saw with a blade thickness of 3 mm.

5.6 Thermal cycling

The test programme comprised of twenty-four 200x200x200 (mm) cubes of control and CARDIFRC[®] bonded specimens. For determining the fracture properties, these cubes were notched with notch to depth ratios of 0.20 and 0.50. The specimens were notched before they were heated using a diamond saw (3 mm width). Twelve 100x100x100 (mm) cubes for compressive strength, 100x200 (mm) cylinders for tensile strength and modulus of elasticity, and twelve 100x100x500 (mm) beams for modulus of rupture (MOR) were placed in an electrical furnace and heated to maximum temperature of 90° C from a room temperature of about 25° C. They were heated in the furnace from room temperature to the maximum temperature in about 20 minutes. The aim was to keep the average heating rate at about 3 degrees per minute, to avoid the risk of the beams being thermally shocked during heating. The maximum temperature was then maintained for another eight hours before the beams were cooled down to the room temperature in a further 16 hours. The above 24-hour heating, hold and cooling period constitutes one thermal cycle (Figure 5.2). The specimens were exposed to 30 and 90 thermal cycles. After the requisite number of thermal cycles, the specimens were tested at room temperature.

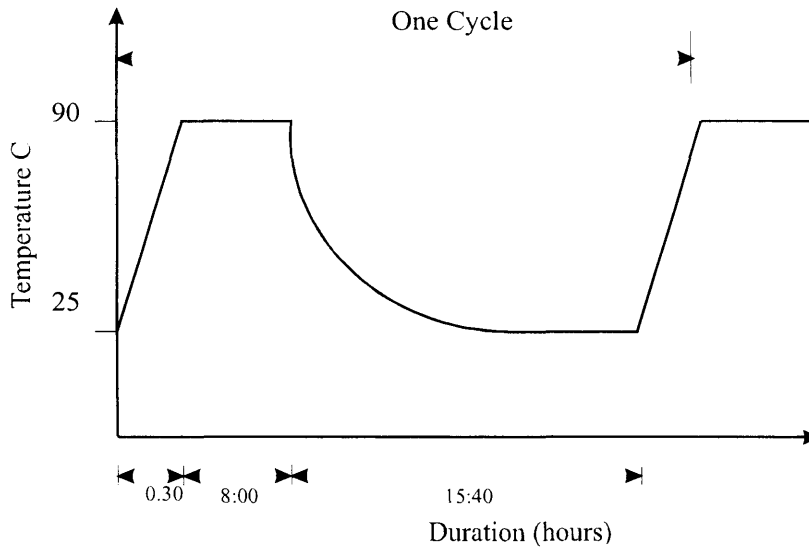


Figure 5.2 Schematic representation of thermal cycling

5.7 Mechanical tests

The mechanical properties of NSC and CARDIFRC[®], namely compressive, splitting strengths, MOR and modulus of elasticity were measured in accordance to the relevant British Standards.

5.7.1 Compressive strength f_c

The compressive strength of NSC and CARDIFRC[®] specimens was determined according to BS 1881-116 1983. Nine 100 x 100 x 100 mm cubes of each mix were tested. The tests were performed in a FARNELL Compression Testing Machine. The compressive strength results after 0, 30 and 90 thermal cycling are shown in Tables 5.2. The results reveal a relative increase in the compressive strength f_c at elevated temperature of 90° C, irrespective of the number of thermal cycles. For NSC the compressive strength of 41.60 MPa before heating increased to 46.40 MPa after 30 thermal cycles and then decreased slightly to 45.80 MPa after 90 cycles. Thus, an increase in compressive strength of 10.10 percent after 90 cycles has been observed.

The compressive strength of CARDIFRC[®] increased from 199.93 to 224.3 MPa after 30 thermal cycles with a further slight increase to 225.03 MPa after 90 thermal cycles, giving a total increase in the compressive strength of 12.5 percent.

The increase in compressive strength may be because elevated temperatures assist further hydration (Zhang et al., 2002). For the NSC, it also may be due to the fact that water, bound by capillary condensation, is partially expelled (Rostasy and Budelmann, 1976). The gain in strength may also be due to the age of concrete specimens, as the specimens tested at room temperature were about 35 days old while those tested after 30 and 90 thermal cycles were over 60 and 120 days, respectively. The thermal cycling regime may have contributed to the hydration of the remaining unhydrated cement, especially since the hydration process is accelerated by the rise in ambient temperatures (Neville, 1995).

Table 5.2 Cube crushing strength of NSC and CARDIFRC[®] after 0, 30 and 90 thermal cycling.

TC	Material	Specimen	Failure load (kN)	Compressive strength (MPa)	Ave. (MPa)	COV %
0	NSC	1	431	43.1	41.60	2.6
		2	407	40.7		
		3	410	41		
	CARDIFRC [®]	1	1993	199.30	199.93	0.30
		2	2008	200.80		
		3	1997	199.7		
30	NSC	1	480	48.0	46.33	3.80
		2	471	47.1		
		3	439	43.9		
	CARDIFRC [®]	1	2254	225.40	224.3	1.3
		2	2273	227.30		
		3	2203	220.3		
90	NSC	1	459.2	45.92	45.8	0.70
		2	453.6	45.36		
		3	461.6	46.16		
	CARDIFRC [®]	1	2194	219.4	225.03	1.8
		2	2276	227.6		
		3	2281	228.1		

The increase in strength associated with an increase in temperature can probably be attributed to the general stiffening of the cement gel particles due to the partial removal of adsorbed moisture. The moisture in specimens of concrete escapes soon after the temperature has reached 100° C (Castillo and Durrani, 1990). Earlier, Lankard et al. (1971) have shown that higher strength is obtained if moisture is allowed to escape.

The effect of age on concrete strength was also investigated (Table 5.5). As can be seen in the Table the compressive strength increases by 8.9 percent after 120 days. Basically, this is owing to further hydration with age.

5.7.2 Splitting strength f_t

The splitting strength f_t of the materials was measured according to BS 1881-117 1983. Nine cylinders of NSC and nine cylinders of CARDIFRC® 100 mm in diameter and 200 mm in length were tested. The tests were also performed in a FARNELL Compression Testing Machine. The cylinders were placed with their axes horizontal between the platens of the machine with hard board strips inserted between the cylinder and the machine platens to ensure even loading over the full length of the specimens. The specimens fail by splitting along the vertical diameter. The cylinder splitting strength f_t (MPa) was calculated as follows:

$$f_t = \frac{2F}{\pi DL} \quad (5.1)$$

where F is the maximum failure load in N, L is the length of the specimen in mm and D is the diameter of the specimen in mm.

The splitting strength results for NSC and CARDIFRC® after 0, 30 and 90 thermal cycling are shown in Table 5.3. The results show that the splitting strength for NSC increases from 3.80 MPa to 4.10 MPa after 30 thermal cycles and then decreases to reach a value of 3.85 after 90 thermal cycles. It is quite clear that the elevated temperatures assist the further hydration which leads to a gain in strength at early age. However, the reduction in strength at 90 thermal cycles could be due to the weakening of the surface forces (Van der Waals forces) between the gel particles, or due to the stresses generated at the interface between the aggregate and hardened cement paste. These stresses induce damage through microcracks. The results also show that the splitting strength of CARDIFRC® follows a monotonically increasing trend. The splitting strength of CARDIFRC® increases from 27 MPa to 30.71 MPa after 30 thermal cycles and further increases to reach a value of 31 MPa, giving a total increase of 14.8 percent after 90 thermal cycles. The splitting strength of

CARDIFRC® seems to be unaffected by thermal cycling, this could be attributed to the presence of fibres. The presence of fibres in concrete plays a role in reducing concrete damage by hot and cold cycles in the temperature range from 25 to 150 C (Rebat, 1999).

Table 5.3 Splitting strength results of NSC and CARDIFRC® after 0, 30 and 90 thermal cycling

TC	Materials	Specimens	Failure load (kN)	Splitting strength (MPa)	Ave. (MPa)	COV %
0	NSC	1	131	4.17	3.80	7.3
		2	116	3.69		
		3	110.5	3.52		
	CARDIFRC®	1	878	28.00	27.00	2.7
		2	840	26.78		
		3	823	26.25		
30	NSC	1	125	3.98	4.10	1.9
		2	129	4.11		
		3	131	4.17		
	CARDIFRC®	1	901	28.73	30.71	5.4
		2	1028	32.78		
		3	960	30.61		
90	NSC	1	125	3.98	3.85	2.5
		2	120	3.82		
		3	118	3.75		
	CARDIFRC®	1	1033	32.94	31.02	6.2
		2	890	28.38		
		3	995	31.73		

The effect of age on the indirect tensile strength of NSC is also presented in Table 5.5. The results show that f_t increases with age. The increase in f_t after 120 days is about 5.4 percent.

5.7.3 Modulus of rupture MOR

The Modulus of rupture MOR was determined according to BS 1881-118 1983, in four-bending tests. Nine beams of NSC and nine beams of CARDIFRC® having the dimensions 100x100x500 mm were tested and the maximum breaking loads were noted. The tests were performed in an AVERY-DENISON Type 7152, Servo-Hydraulic Testing Machine, with a load capacity of 600 kN. The MOR (MPa) was calculated as follows:

$$MOR = \frac{(F.l)}{(d_1.d_2^2)} \tag{5.2}$$

where F is the maximum failure load in (N), d_1 and d_2 are the lateral dimensions of the cross section in mm and l is the distance between supporting rollers in mm

Table 5.4 Flexural test results of NSC and CARDIFRC[®] after 0, 30 and 90 thermal cycling

TC	Materials	Specimens	Failure load (kN)	MOR (MPa)	Ave. MOR (MPa)	COV %
0	NSC	1	13.80	5.52	5.44	1.2
		2	13.65	5.46		
		3	13.40	5.36		
	CARDIFRC [®]	1	82.00	32.80	32.80	4
		2	78.51	31.20		
		3	86.06	34.40		
30	NSC	1	15.43	6.17	6.43	2.8
		2	16.45	6.58		
		3	16.31	6.52		
	CARDIFRC [®]	1	81.00	32.40	33.47	6.3
		2	79.12	31.60		
		3	91.00	36.40		
90	NSC	1	14.37	5.75	5.78	1.5
		2	14.78	5.90		
		3	14.20	5.69		
	CARDIFRC [®]	1	81.61	32.40	33.73	9.2
		2	77.23	30.80		
		3	95.06	38.00		

The MOR was directly calculated from the ultimate load, measured for specimens exposed to 0, 30 and 90 hot and cold cycles. As seen from Table 5.4, the MOR for NSC first increases from 5.44 for control specimens to 6.43 MPa after 30 thermal cycles (17.2 per cent increase), then decreases to 5.78 MPa after 90 thermal cycles. The observed decrease in flexural strength after 90 thermal cycles is probably due to the weakening in the bond forces between aggregate and cement matrix and/or the formulation of microcracks on the tension face. The values of MOR for CARDIFRC[®] changed very little after 30 or 90 thermal cycles

The results given in Tables 5.5 reveal that MOR for NSC increases with age, the increase after 120 days is 3.8 %. The results indicate that f_{cu} , f_t and MOR generally increase with age at room temperature owing to further hydration of unhydrated cement.

Table 5.5 f_{cs} , f_t and f_r of NSC after different environmental conditions and age.

Environmental conditions	Compressive strength (MPa)	Splitting strength (MPa)	MOR (MPa)
28 days at 20° C	41.60	3.80	5.44
120 days at 20° C	45.00	3.90	5.65
30 TC	46.33	4.10	6.43
90 TC	45.80	3.85	5.78

5.7.4 Modulus of Elasticity E

The modulus of elasticity of NSC and CARDIFRC[®] specimens was determined at room temperature after 0, 30 and 90 thermal cycles. The test was carried out according to BS 1881-121 1983. Table 5.6 shows that the modulus of elasticity for NSC increases from 32 GPa to 35.21 GPa after 30 thermal cycles and then drops to 28.25 after 90 thermal cycles. This finding is to some extent in agreement with that of Schneider (1988). The decrease in stiffness after 90 thermal cycles is most likely due to the internal micro-cracks caused by thermal cycling, especially at the interface between cement paste and coarse aggregates. The results showed that the modulus of elasticity for CARDIFRC[®] is not affected by thermal cycling.

Table 5.6 the effect of thermal cycling on the modulus of elasticity of NSC and CARDIFRC[®]

Thermal cycles	Materials	0	30	90
Modulus of elasticity (GPa)	NSC	32.00	35.21	28.25
	CARDIFRC [®]	48	49	49

It is interesting to note that, the total gain in strength, after 30 thermal cycles is influenced by the following factors: First, gain in strength with age of concrete as the specimens tested at (0) thermal cycles were about 30 days old, while those tested after 30 thermal cycles were over 65 days old. Second, the thermal cycling regime would have contributed to the hydration of the remaining unhydrated cement.

The results indicate that all strengths for NSC are reduced after 90 thermal cycles compared to the strength attained after 30 thermal cycles. The following factors may have contributed to this reduction; first, microcracking of the matrix (i.e. paste) due to thermal incompatibility between cement paste and aggregate might have occurred

during the thermal cycling process, and second, thermal cycling process may have affected the microstructure of the concrete by weakening the bond forces between the cement paste and aggregate, thereby creating debonding interfacial cracks.

5.8 Fracture tests

This section presents the fracture behaviour of control NSC specimens and of NSC specimens bonded to CARDIFRC® under thermal cycling, using the wedge splitting test (WST) method. The WST, put forward by Tschegg and Linsbauer (1986), and further refined by Bruhwiler and Wittmann (1990) and Tschegg (1990), is a very stable test and the specimen is compact requiring only a small amount of material. It is a novel procedure for measuring fracture properties of quasi-brittle materials, such as ceramics, rocks and concrete, for which one needs to perform a stable fracture test beyond the maximum load.

5.8.1 Test procedure

This procedure is characterised by simplicity of making and handling of specimens and by stable crack-growth conditions. Specimen shape, test configuration and load arrangement for control NSC specimens are shown in Figure 5.3 (see also Plates 5.1 and 5.2 for control and bonded specimens, respectively).

A cubic control or repaired specimen 200 x 200 x 200 mm has an initial rectangular groove for placement of two steel load transmission pieces fitted with roller bearings on either side. A steel wedge is placed between the roller bearings. A vertical force F_M on the wedge imparts a well-defined horizontal-force F_H to the bearings thus wedging open the starter crack. The test was carried out using a DARTIC closed loop machine (200 kN). The rate of loading was controlled by a crack mouth opening displacement (CMOD) gauge at a very low rate (0.0002 mm/s) so that the fracture occurred in a stable manner. During the propagation of the crack in the specimens, the deformation is measured by the crack mouth opening displacement (CMOD) along the line of application of the horizontal splitting force using an electronic CMOD gauge. The vertical load F_M on the wedge was measured by a load cell between the wedge and the testing machine. The horizontal splitting force F_H was calculated with the aid of wedge angle θ .

$$F_H = \frac{F_M(1 - \mu \tan \theta)}{2 \tan \theta(1 + \mu \cot \theta)} \approx \frac{F_M}{(1 + \mu \cot \theta)(2 \tan \theta)} \quad (5.3)$$

where F_M is the vertical force on the bearings and μ is the coefficient of friction between the wedge and roller bearing. The manufacturer of roller bearings quotes μ between 0.1 and 0.5%. For $\theta = 15^\circ$, (the half wedge angle for the WS used in this study) the contribution of $\mu \cot \theta$ in the previous expression is therefore between 0.40 and 1.9%. Therefore, in the WST, F_H may be approximately expressed by

$$F_H \approx \frac{F_M}{2 \tan \theta} \quad (5.4)$$

The area under the load-CMOD curve corresponds to the work done which is required to separate the specimens. Dividing this work by the fracture area or ligament area that was intact before the test began yields the measured specific energy G_f . This value characterises the crack propagation resistance of the tested material and can be simply calculated as follows

$$G_f = \frac{1}{(W^* - a)B} \int F_H d(CMOD) \quad (5.5)$$

where, B is the specimen thickness, $W^* = W - d_n$ (see Figure 5.3c).

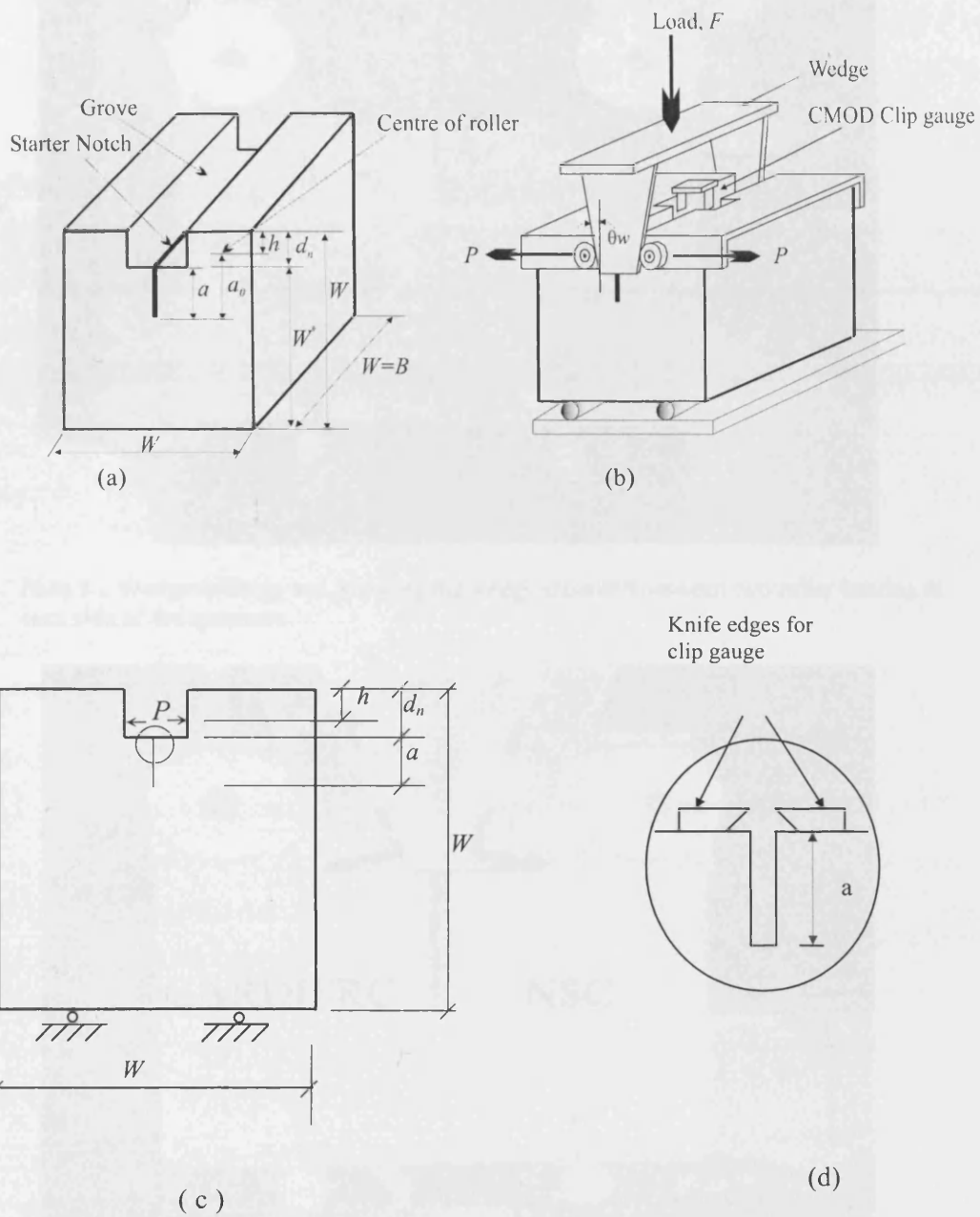


Figure 5.3 Configurations of WS test: (a) specimen shape, (b). loading arrangements, (c) the points of application of wedge force and (d) location of clip gauge for measuring CMOD.

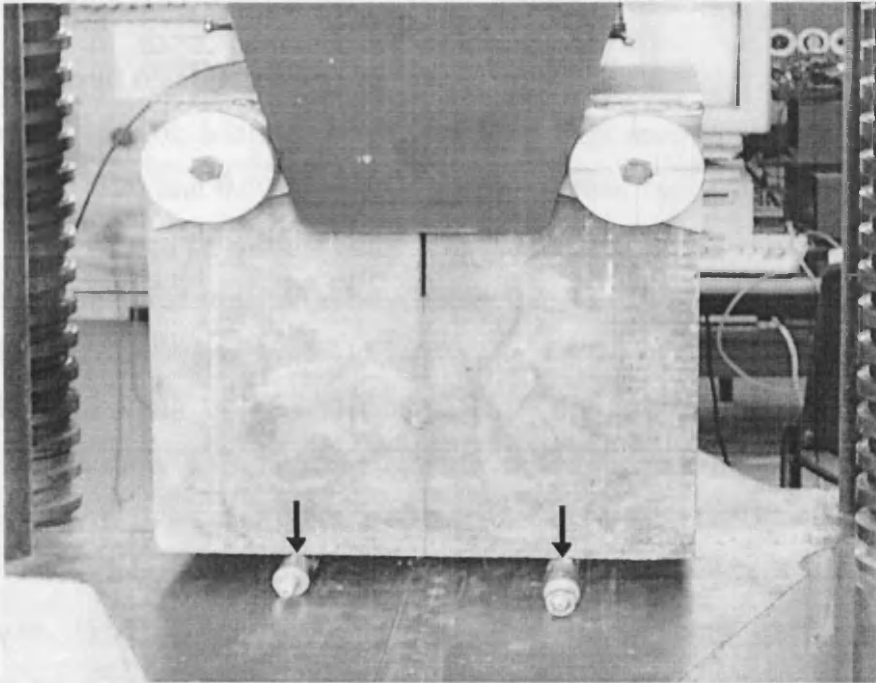


Plate 5.1 Wedge splitting test, showing the wedge mounted between two roller bearing at each side of the specimen.

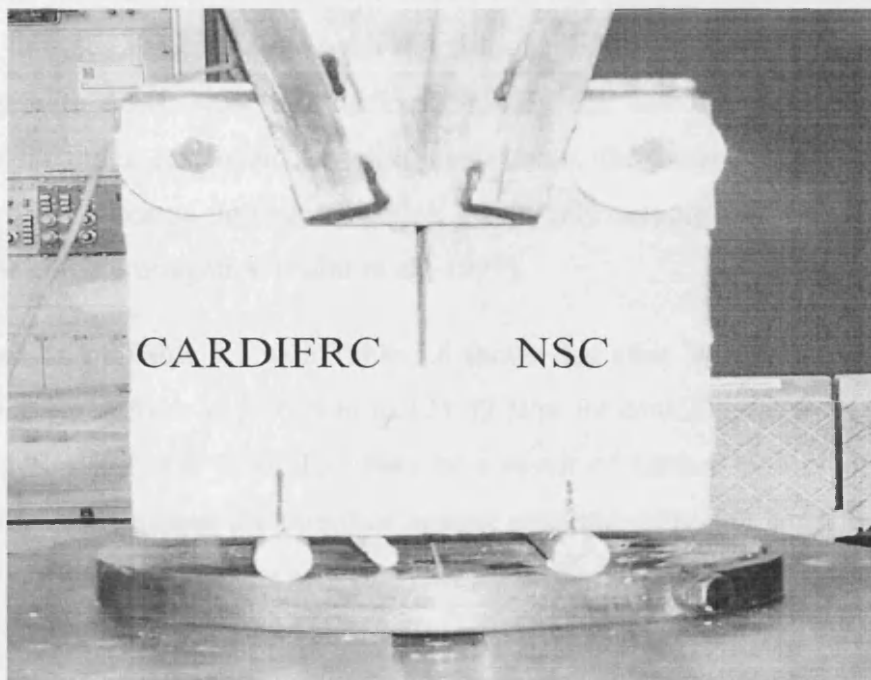


Plate 5.2 Wedge splitting test for bi-material system CARDIFRC[®]/NSC)

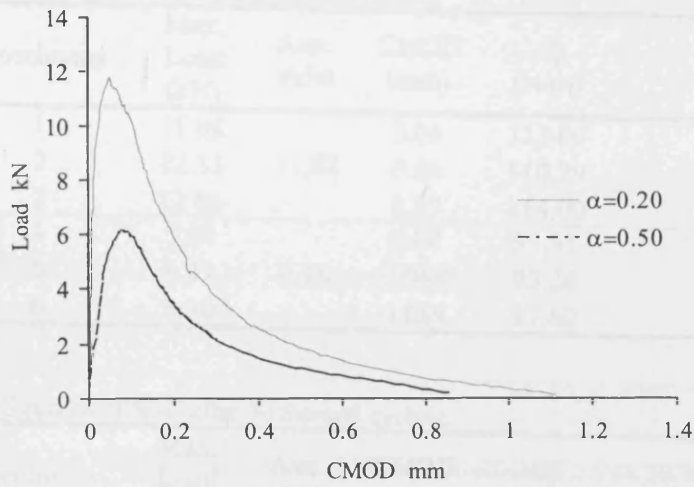
5.8.2 Control NSC specimens

The fracture behaviour of normal strength concrete under thermal cycling was evaluated using the WS test. Eighteen specimens with notch to depth ratios of 0.20 and 0.50 were tested at room temperature after different numbers of thermal cycles.

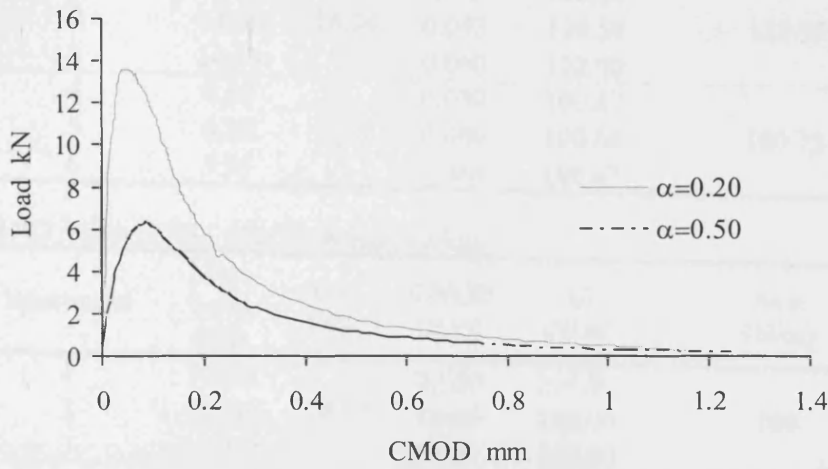
5.8.2.1 Measured fracture energy G_f

The measured specific fracture energy results for NSC specimens with the notch to depth ratios of 0.20 and 0.50 after 0, 30 and 90 thermal cycles are shown in Tables 5.7, 5.8 and 5.9, respectively. Figure 5.4a shows that the fracture energy $G_f(\alpha)$ decreases as the notch to depth ratio α increases. As can be seen in Table 5.7, the mean value of G_f decreases from 115.76 N/m for $\alpha = 0.20$ to 95.58 N/m for $\alpha = 0.50$. This is brought about by several factors. First, the propagating crack encounters resistance from more coarse aggregate particles for shorter initial notches. Second, the probability of flaws like voids, micro-cracks and bond cracks in the path of the growing crack increases with increasing ligament length (Karihaloo 1995 and Nallathambi, 1986). Similar trend for the variation of fracture energy with initial crack size has also been observed for test specimens after 30 and 90 thermal cycling (Figures 5.4b and 5.4c and Tables 5.8 and 5.9). It was observed that the crack path through the thickness of the NSC specimens was not straight. Moreover, it seems to be more tortuous for specimens with notch to depth ratio of 0.20. This variation in tortuosity with notch size may be explained by the fact that with a larger area available for crack extension, i.e. with small notch, the advancing crack front will encounter more coarse aggregates which are largely responsible for the tortuosity during the crack propagation (Sabir et al., 1997).

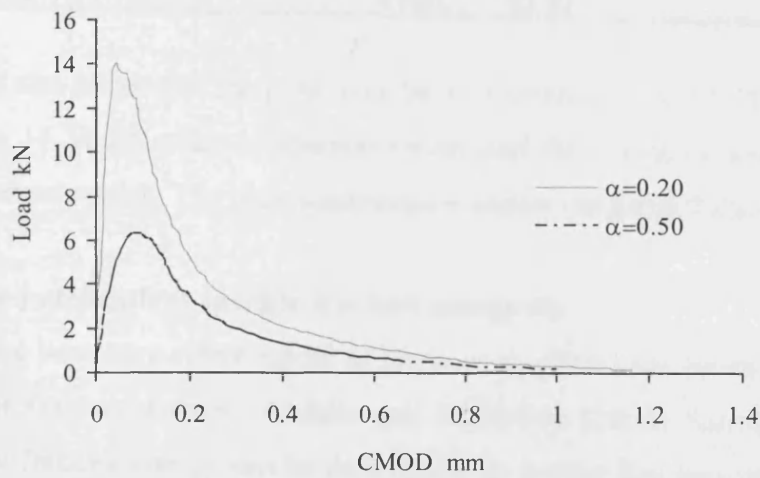
A comparison of Table 5.7 with Table 5.8 shows that after 30 thermal cycles the G_f slightly increases from 115.76 N/m to 121.52 N/m for $\alpha=0.20$, and from 95.58 N/m to 100.73 N/m for $\alpha = 0.50$. This may be a result of further hydration of cement paste, which strengthens the interface against cracking, although some microcracks are introduced at the interface as well. After 90 thermal cycles G_f reduces to 108 N/m and 88.63 N/m for $\alpha = 0.20$ and 0.50, respectively (Table 5.9). This could be attributed to the initiation of microcracks at the interfaces of cement paste and aggregate. These microcracks degrade the material resistance against cracking, and make the material more brittle.



(a)



(b)



(c)

Figure 5.4 The influence of notch size on the load-CMOD curves, after: (a) zero thermal cycles (b) 30 thermal cycles and (c) 90 thermal cycles.

Table 5.7 WS results of NSC after 0 thermal cycling

α	Specimens	Max. Load (kN)	Ave. (kN)	CMOD (mm)	G_f (N/m)	Ave. (N/m)
0.20	1	11.08		0.05	123.00	
	2	12.33	11.82	0.04	110.29	115.76
	3	12.06		0.07	114.00	
0.50	4	5.90		0.08	95.91	
	5	6.31	6.10	0.088	93.24	95.58
	6	6.10		0.089	97.60	

Table 5.8 WS results of NSC after 30 thermal cycling.

α	Specimens	Max. Load (kN)	Ave. (kN)	CMOD (mm)	G_f (N/m)	Ave. (N/m)
0.20	1	14.22		0.05	113.05	
	2	14.00	14.24	0.043	129.59	121.52
	3	14.50		0.060	122.00	
0.50	4	6.60		0.080	100.87	
	5	6.25	6.28	0.080	100.64	100.73
	6	5.95		0.088	100.67	

Table 5.9 WS results of NSC after 90 thermal cycling.

α	Specimens	Max. Load (kN)	Ave. (kN)	CMOD (mm)	G_f (N/m)	Ave. (N/m)
0.20	1	14.60		0.050	104.00	
	2	14.10	14.17	0.039	102.00	108
	3	13.80		0.050	118.00	
0.50	4	5.80		0.088	82.90	
	5	6.60	6.34	0.090	90.00	88.63
	6	6.70		0.060	93.00	

The results also show that the peak load for specimens with $\alpha = 0.20$ increases from 11.8 kN to 14.24 kN after 30 thermal cycles and then remains almost unchanged after 90 thermal cycles. The peak load remains almost unchanged for $\alpha = 0.50$.

5.8.2.2 Size-independent specific fracture energy G_F

Based on the boundary effect model of Duan et al. (2001) for determining the size-independent fracture energy, Abdalla and Karihaloo (2003) found that the size-independent fracture energy can be determined by testing just two specimens of the same size containing a shallow and deep starter notch (see § 3.6, page 51). It was for this reason that tests were conducted on WS specimens with $\alpha = 0.20$ and $\alpha = 0.50$

(Tables 5.7 to 5.9). The determination of the size-independent specific fracture energy G_F for concrete was based on the following equation

$$G_f(a/W) = \begin{cases} G_F \left[1 - \frac{1}{2} \cdot \frac{a_1/W}{1-a/W} \right] & 1-a/W > a_1/W \\ G_F \cdot \frac{1}{2} \cdot \frac{(1-a/W)}{a_1/W} & 1-a/W \leq a_1/W \end{cases} \quad (5.6)$$

Table 5.10 shows the results of the size-independent specific fracture energy G_F and transition ligament length after thermal cycling obtained from the $G_f(\alpha)$ values for $\alpha = 0.20$ and $\alpha = 0.50$. As it can be seen, the G_F first increases from 148 N/m to 158 N/m after 30 thermal cycles and then decreases to 141 N/m after 90 thermal cycles.

Table 5.10 size-independent fracture energy after 0, 30 and 90 thermal cycles.

Thermal cycles	G_F (N/m)	Transition ligament length a_l (mm)
0	148	36
30	158	43
90	141	37

The increase in the size-independent specific fracture energy may be attributed to the partial expulsion of capillary water. Gradual removal of capillary water further reduces the lubricating effect of the water and toughens the concrete (Zhang et al., 2000). Baker (1996) also showed that at low temperature less than 120° C, the slight thermal damage via microcracking that occurs before full drying out with moisture migration and steam escape, actually provides a toughening mechanism. Another factor that significantly contributes to the increase in G_F is the age of concrete specimens as pointed out by Petersson (1980). Temperature, which contributes to the hydration of the remaining unhydrated cement, densifies the cement matrix. The denser the microstructure of normal concrete, the higher its crack resistance will be (Karihaloo, 1995). For clarity, the measured and size –independent fracture energy for the NSC after different thermal cycles is plotted in Figure 5.5

The trend of fracture energy results obtained in this work seems to be in accord, to a certain extent, with the trend of the results obtained by Baker (1996) and Zhang et al. (2000). In contrast, there is a significant difference between the variation of G_f observed in this study and the results obtained by Bazant and Part (1988) and Abdel-Fattah and Hamoush (1997). This undoubtedly relates to testing conditions, thermal cycling, concrete strength and mixing conditions. Furthermore, the experimental results are difficult to compare due to differences in test specimens, temperature exposure and test procedure.

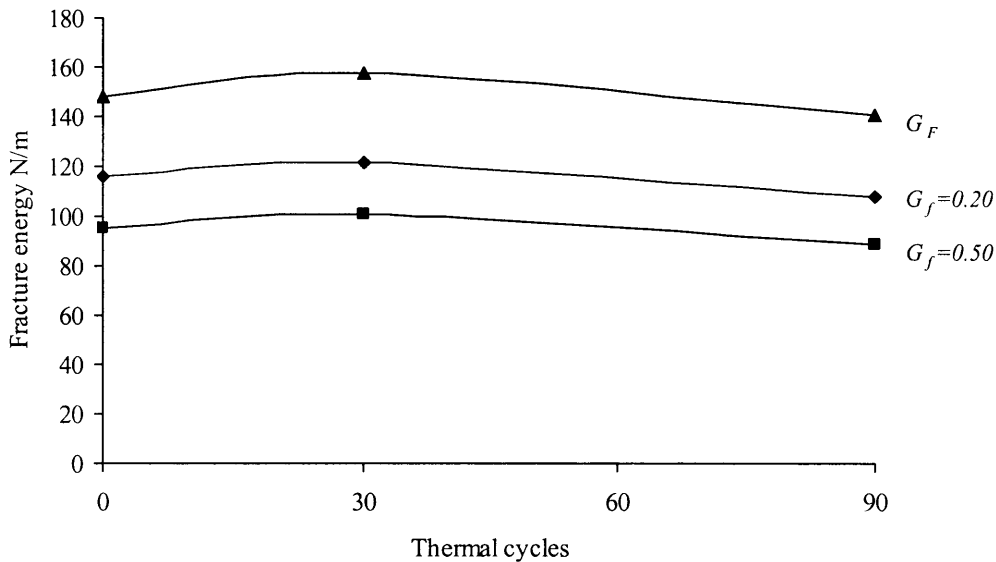


Figure 5.5 The effect of thermal cycling on measured and size-independent fracture energy of NSC.

5.8.2.3 Brittleness

Brittleness is defined as the tendency for a material or structure to fracture abruptly before significant irreversible deformation occurs. Conversely, toughness characterises the capacity of structure to resist fracture. Hillerborg et al. (1976) proposed the characteristic length l_{ch} as a brittleness parameter for concrete

$$l_{ch} = \frac{G_F E_c}{f_t^2} \quad (5.7)$$

where f_t is the tensile strength of the concrete and G_F is the size-independent specific fracture energy. Because l_{ch} includes a combination of energy, stiffness and strength

parameters, the larger the value of l_{ch} the less brittle or more ductile the concrete is. The results listed in Table 5.11 show that brittleness of normal concrete is almost unchanged after 30 thermal cycles but then decreases to reach a value of 268.73 mm after 90 thermal cycles. The observed decrease in l_{ch} after 90 thermal cycles is mainly due to thermally induced microcracks.

Table 5.11 Characteristic length l_{ch} of NSC after 0, 30 and 90 thermal cycles.

Thermal cycles	0	30	90
l_{ch} mm	327.97	330.94	268.73

5.8.3 CARDIFRC®/NSC bonded system

In order to evaluate the performance of CARDIFRC®/NSC bonded system, the WST procedure was again adopted. As mentioned in Chapter 3, very few researchers have used this method for the evaluation of the fracture properties of bonded dissimilar materials. Among these are Tschegg and Stanzel (1991) (old concrete-new concrete), Tschegg et al. (1995) (Aggregate-cement matrix), Tschegg (1997) (bituminous and layer bonds), Irhouma et al. (1998) (concrete-concrete) and Harmuth (1995) (concrete-polymer modified cement).

This section will present the test results of CARDIFRC® bonded to normal strength concrete specimens by using the WS test (Tschegg and Stanzel, 1991). It investigates the fracture behaviour of CARDIFRC®/concrete bonded system. As mentioned in the introductory section, emphasis will be placed on the main factors that affect the bond properties of interfaces, such as the roughness of mating surfaces and thermal cycling. The testing was performed in a similar manner those of NSC (see Figure 5.6a)

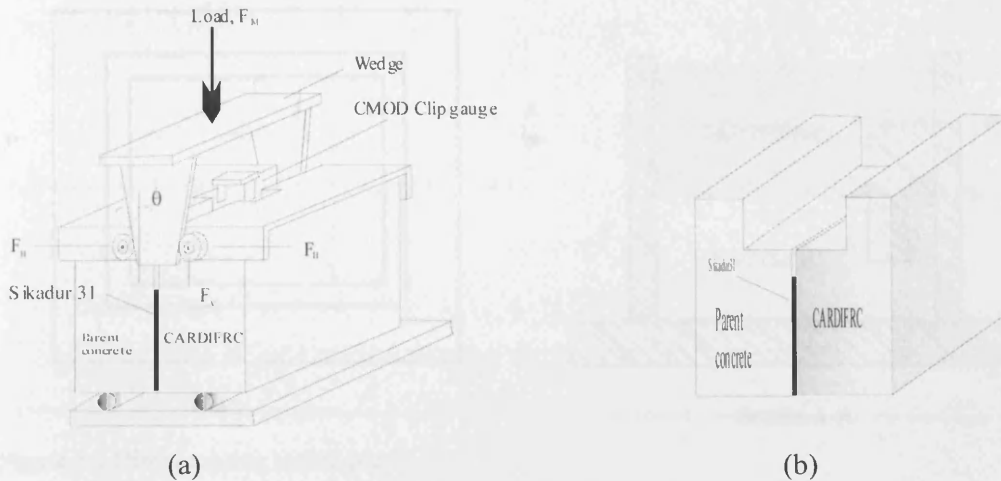


Figure 5.6 Configuration of bonded specimens: (a) Loading arrangements and (b) wedge splitting specimen of bonded system.

5.8.3.1 Direct wet casting

The initial trial casts of wet CARDIFRC[®] directly on to NSC showed no bond between the two materials (CARDIFRC[®]/NSC). Visual observation revealed that the specimens split apart when the applied load was still in the elastic stage. This was due to the casting configuration in which the specimens were horizontally cast and thus no mechanical interlocking had been achieved. Therefore, in order to create mechanical interlock between the two materials, the normal strength concrete half cube was laid horizontally and the CARDIFRC[®] was cast vertically on top of it (Figure 5.7). Moreover, pressure was applied whilst the repair material was still wet. After curing in a hot curing tank for 9 days at 90° C, the specimens were notched at the required notch to depth ratio and then tested using the WS test. Visual examination showed a remarkable improvement in bond characteristics. The results confirmed this visual observation. However, although the crack went through the interface, it kinked slightly into the normal strength concrete specimens. It was found by inspection that more than 30 percent of the failure occurred in the normal strength concrete and the remainder in the interface. Table 5.12 and Figure 5.8 show the direct casting results for two specimens of CARDIFRC[®]/NSC with a notch to depth ratio of 0.50. As seen in Table 5.12 the mean value of maximum load and fracture energy for bonded specimens is lower than those of the NSC control specimen.

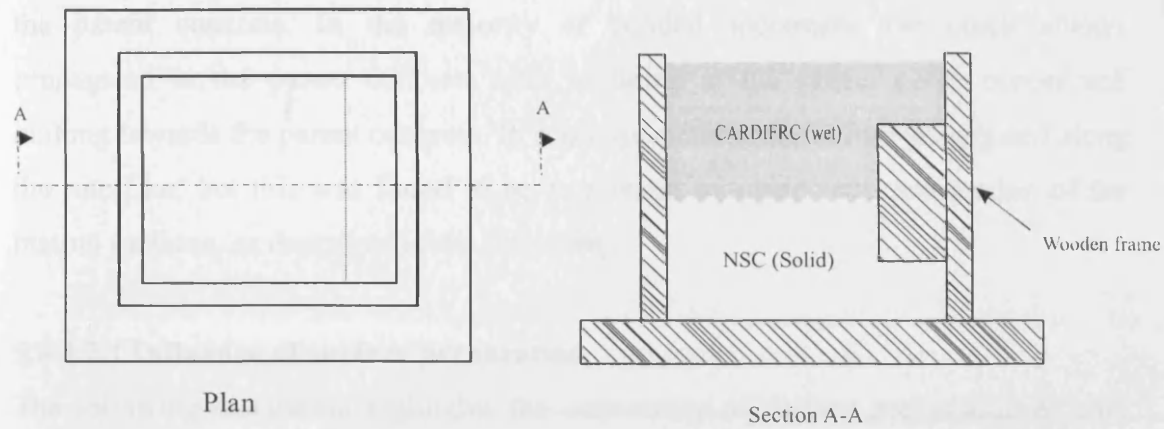


Figure 5.7 Direct casting technique

Table 5.12 NSC repaired with CARDIFRC[®] (direct casting) $\alpha = 0.50$

	Specimens	Max Load (kN)	Ave ML (kN)	CMOD (mm)	G_f (N/m)	Ave. G_f (N/m)	Failure location
Bonded	1	4.90	5.00	0.032	26.00	27.00	I/C
	2	5.10		0.02			I/C
Control	1	6.10	6.10		95.58	95.58	C

I/C, Crack starts at the interface and propagates slightly into concrete.

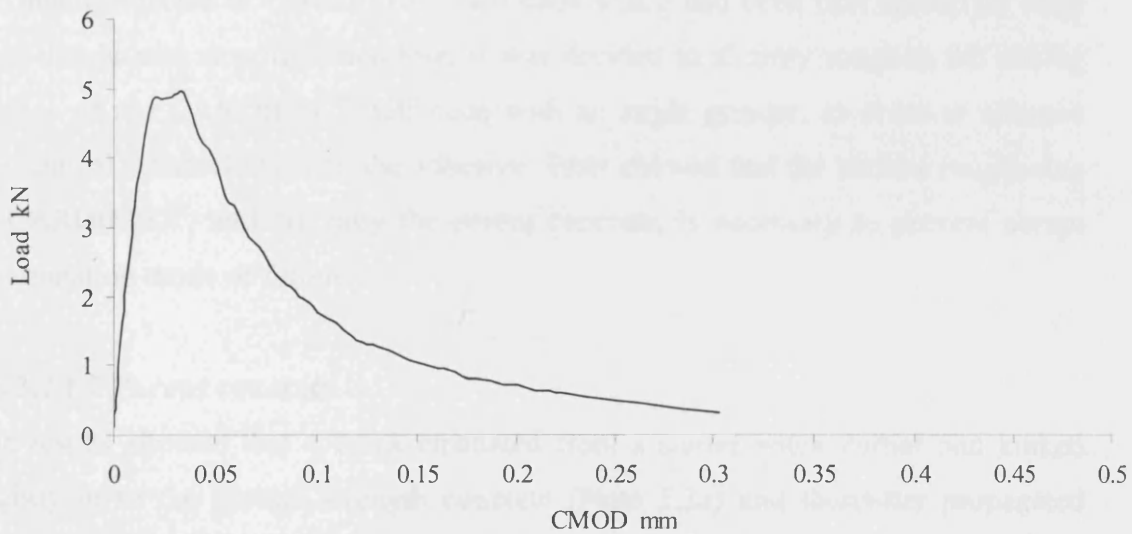


Figure 5.8 Load-CMOD curve for bonded NSC (direct casting)

5.8.3.2 Adhesive bonding

The WST results for normal strength concrete half cubes adhesively bonded to CARDIFRC[®] half cubes are presented below. Generally, after many bonding trials, visual observations showed no signs of interfacial fracture or delamination either at the interface between the CARDIFRC[®] and the adhesive or between the adhesive and

the parent concrete. In the majority of bonded specimens the crack always propagated in the parent concrete after initiating at the starter notch corner and kinking towards the parent concrete. In some specimens, the failure propagated along the interface, but this was found to be as a result of inadequate preparation of the mating surfaces, as described in the following.

5.8.3.2.1 Influence of surface preparation

The following discussion highlights the importance of surface preparation of both parent concrete and the repair material.

5.8.3.2.1.1 Repair material (CARDIFRC®)

In early tests, CARDIFRC® half cubes were adhesively bonded to the prepared surfaces of NSC concrete half cubes without preparing their mating surfaces. The results showed that failure took place in an abrupt manner, with a delamination that had occurred at the interface between CARDIFRC® half cube and the adhesive propagating spontaneously. This type of failure should have been expected because the mating surface of CARDIFRC® half cube which had been cast against an oiled steel mould was smooth. Therefore, it was decided to slightly roughen the mating surface of the CARDIFRC® half cube with an angle grinder, in order to enhance mechanical interlocking with the adhesive. Tests showed that the surface roughening of CARDIFRC®, and not only the parent concrete, is necessary to prevent abrupt delamination mode of failure.

5.8.3.2.1.2 Parent concrete

The results showed that a crack emanated from a starter notch corner and kinked slightly in to the normal strength concrete (Plate 5.3a) and thereafter propagated solely in the latter and almost parallel to the interface. However, as seen from the photograph of the fracture surface in Plate 5.4a the majority of coarse aggregates have been de-bonded from the matrix with very few being fractured. A comparison of these fracture surfaces with surfaces obtained after cutting the concrete half cube away from the mating surface revealed that the concentration of coarse aggregates in the fractured surfaces of the repaired concrete half cubes was less than that in the

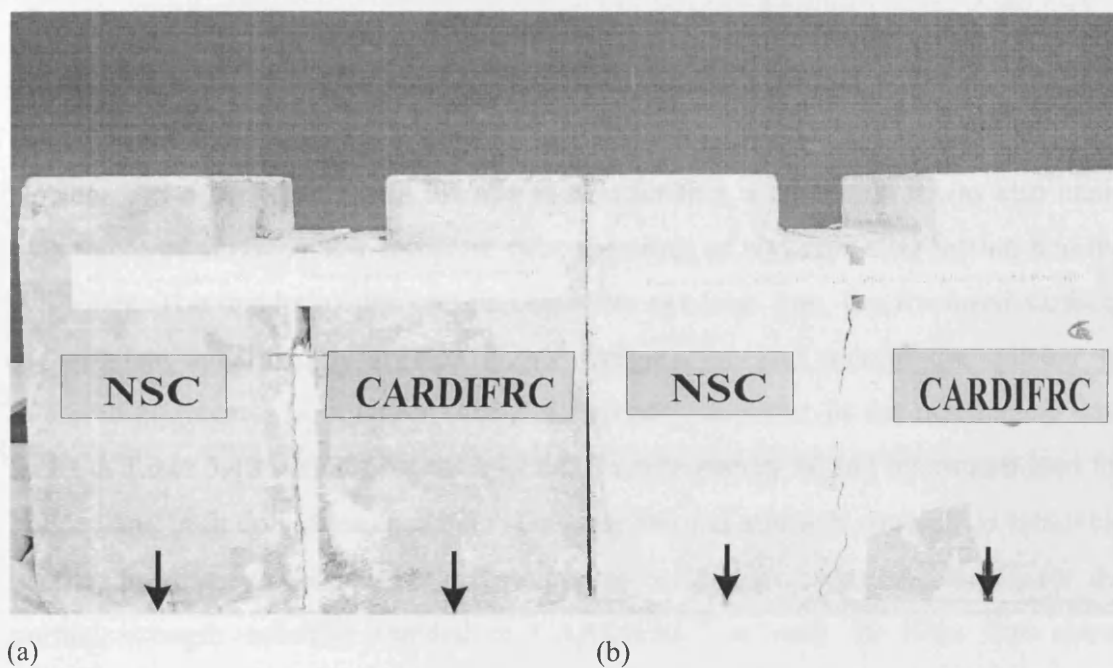


Plate 5.3 The effect of cement paste film on the failure mode of CARDIFRC[®]/NSC, (a) before, (b) after removal of film.

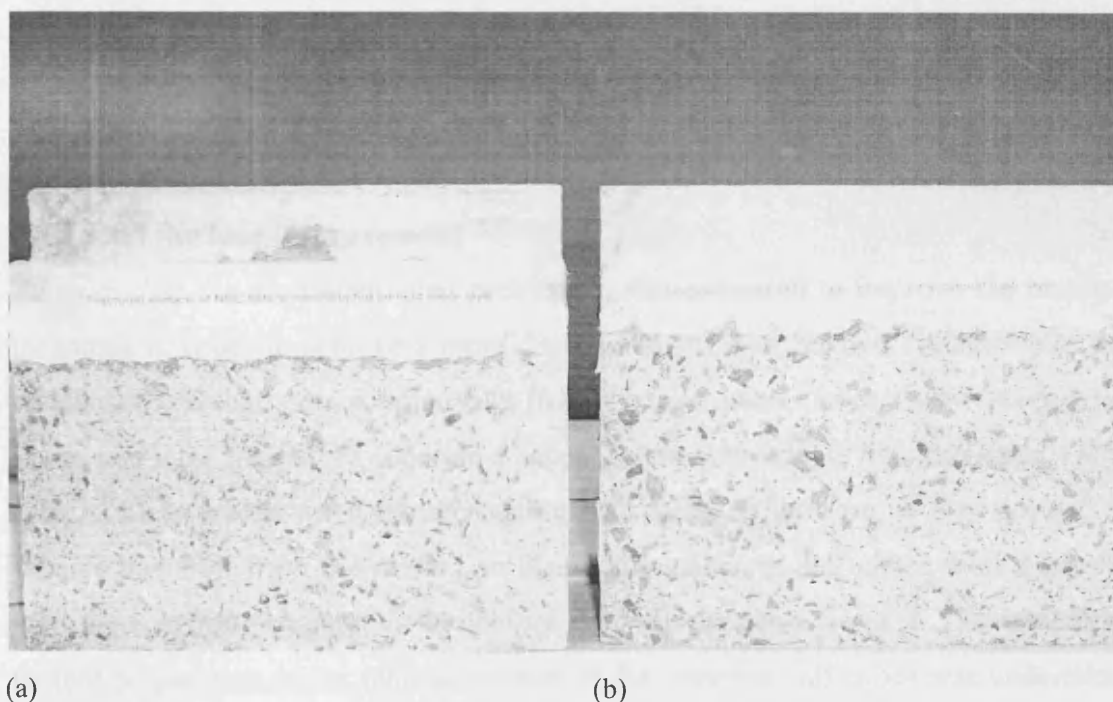


Plate 5.4 The effect of cement paste film on the fractured surface of CARDIFRC[®]/NSC: (a) before, (b) after removal of film.

bulk. This was initially thought to be a result of wall effect phenomenon in that the particles packed more loosely in the immediate vicinity of a mould wall than away from it.

However, in order to ascertain the true reason for this, a comparison was also made with fractured surfaces of a complete cube specimen of concrete after testing it in the WS mode. The results of this comparison were twofold; first, the fractured surfaces of complete specimens exhibited higher irregularity, and second the number of fractured aggregates was larger. These differences manifest in the mechanical data listed in Table 5.13 which give the specific fracture energy G_f and maximum load for bonded and bulk concretes. The data show that normal strength concrete is relatively ductile; the measured specific fracture energy is 98 N/m, whereas, the G_f for the normal strength concrete bonded to CARDIFRC[®] is only 39 N/m. The above differences in the fracture surfaces provide an explanation for this. Whereas the crack path went through the concrete matrix around the de-bonded aggregates of bonded normal strength concrete and did not propagate through the aggregate particles, in the solid NSC specimens it propagated not only around the aggregates but also through them. As the fracture energy of the aggregates is larger than that of the matrix of NSC, the control solid specimens exhibited higher ductility than did the bonded ones.

5.8.3.2.1.3 Surface improvement

To overcome the aforementioned problem, it was proposed to improve the bonding technique in order to achieve a more ductile and stronger bonded system. Since the results showed that a crack emanating from a starter notch corner always propagated in the region of the parent concrete adjacent to the interface, it was likely that a thin cement film formed there during casting and curing. Therefore, it was decided to remove this film from the mating surface of the concrete half cubes with a grinder until the aggregate became visible before applying the adhesive to it. This additional surface preparation of the mating surfaces of the concrete half cubes was undertaken before bonding them to CARDIFRC[®] half cubes. The CARDIFRC[®] half cube was slightly pressed on to the adhesive to remove any trapped air.

The results of this additional surface preparation were encouraging. The adhesive adhered very securely to the substrate (parent concrete) and the repair material (CARDIFRC[®]). As seen from Plate 5.3b the crack emanating from the starter notch corner kinked towards the concrete, with a kink angle of about 10° to 20° and propagated thereafter in concrete close to the interface. The fractured surface of the repaired NSC after the removal of the cement film exhibited higher irregularity (Plate 5.4b) approaching that of the unbonded solid concrete.

Figure 5.9 shows the influence of the additional surface treatment on the fracture behaviour of the repaired system. It presents a typical Load-CMOD curve for the NSC/CARDIFRC[®] system before and after the removal of the thin film of cement paste. The softening part of the untreated specimen is steeper than that of the treated one and consequently it needs less energy for full separation. Table 5.13 shows the corresponding maximum load and fracture energy. The maximum load that the repair system can sustain as well as the energy required to separate the specimens, have both increased substantially after the removal of cement film. The maximum load for the treated specimen is about 13.5 kN, but only 9.6 kN for untreated one and the specific fracture energy is 94 N/m and only 39 N/m for treated and untreated specimens respectively. These results show that the specific fracture energy depends only on interlocking of crack surfaces. Therefore, it is clear that the removal of thin film of cement paste from the mating surface of the parent concrete is essential for obtaining a tough and strong repair system.

Comparison has been made between the NSC/CARDIFRC[®] system and control specimens made of normal strength concrete. The load-CMOD curves are represented in Figure 5.10. The maximum load for repaired specimen is about 13.5 kN, whereas for control specimen is 11.4 kN. However, the specific fracture energy is almost the same, the G_f values are 94 N/m and 98 N/m for repaired and control specimens respectively.

From the preliminary tests it was concluded that, NSC can be repaired using both techniques, direct wet casting and adhesive bonding. However, the former requires great care to ensure that the repair material adheres very securely to concrete. This

requires thorough compaction of wet material which is often difficult to achieve. The adhesive bonding technique does not suffer from this drawback and therefore it was selected for repairing the HSC cubes in the rest of the experimental programme.

Table 5.13 WS results of CARDIFRC[®] adhesively bonded to NSC ($\alpha = 0.30$)

Type	Specimens	Max. Load (kN)	CMOD (mm)	Failure location	G_f (N/m)
Bonded	Before removing the cement paste film	10.00	0.025	CF	39.00
	After removing the cement paste film	13.50	0.45	NSC	94.00
Control	-	11.40	0.05	-	98.00

CF: cement film.

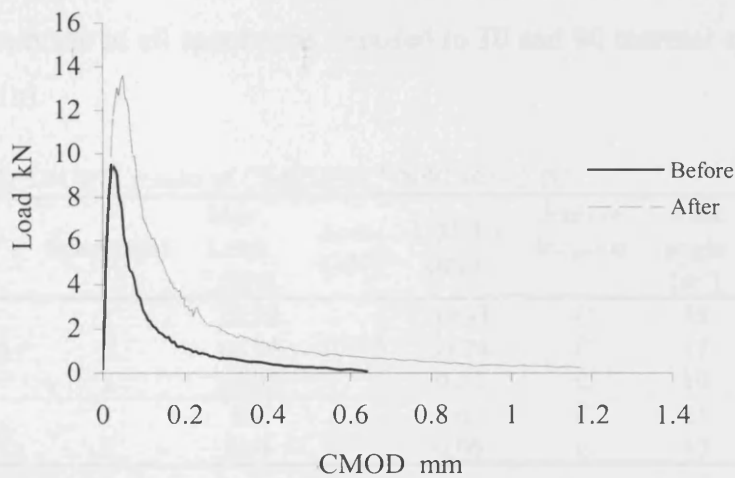


Figure 5.9 Load- CMOD curves for CARDIFRC[®] adhesively bonded to NSC with and without cement paste film.

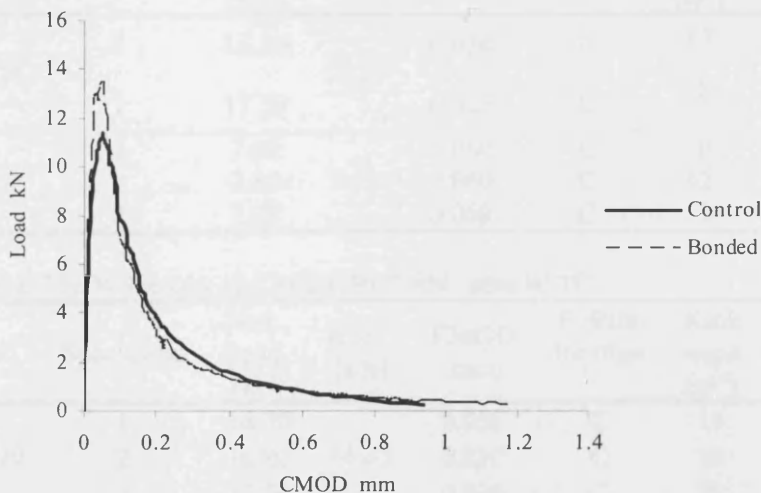


Figure 5.10 Load- CMOD curves for bonded and control NSC specimens, $\alpha = 0.30$

5.8.3.2.2 Effect of thermal cycling

Results of all bonded specimens exposed only to room temperature are presented in Table 5.14. Visual observations showed that in all bonded concrete specimens, a crack started at the corner of starter notch and kinked into the parent concrete at an angle of 15° to 20° for $\alpha = 0.20$, and 10° to 15° for $\alpha = 0.50$. Similar to those of WS control specimens, a variation of the measured fracture energy $G_f(\alpha)$ with the notch to depth ratios of 0.20 and 0.50 has also been observed (see Figure 5.11a). The specific fracture energy of bonded NSC specimens with notch to depth ratios of 0.20 and 0.50 is 107.43 N/m and 82.35 N/m, respectively. The results also show a decrease in peak load with increasing notch to depth ratio. As α increases from 0.20 to 0.50 the peak load decreases from 15.9 kN to 7.37 kN. This observation has also been made in all specimens exposed to 30 and 90 thermal cycling (Figures 5.11b and 5.11c).

Table 5.14 WS results of CARDIFRC®/NSC after 0 TC

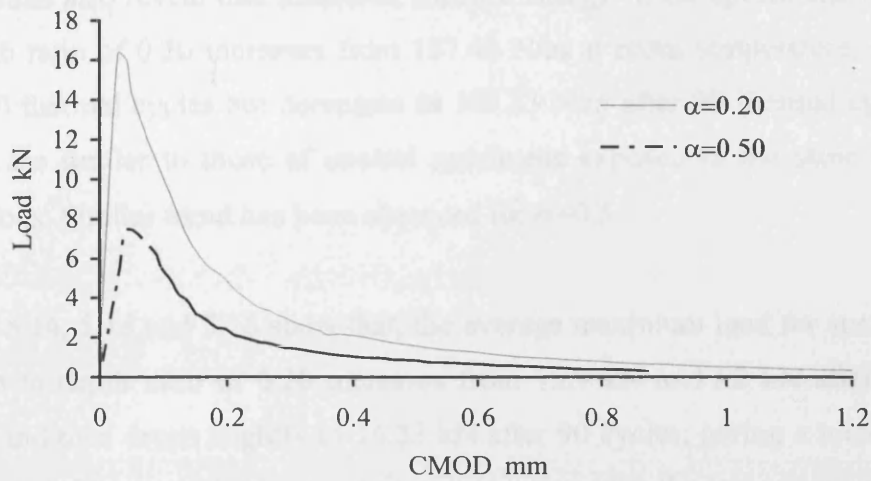
α	Specimens	Max. Load (kN)	Ave. (kN)	CMOD (mm)	Failure location	Kink angle (ω°)	G_f (N/m)	Ave. (N/m)
0.20	1	15.10	15.90	0.033	C	15	105.40	107.43
	2	16.79		0.028	C	17	116.39	
	3	16.92		0.03	C	19	100.51	
0.50	1	8.3	7.37	0.05	C	11	86.25	82.35
	2	6.44		0.05	C	15	78.54	

Table 5.15 WS results of CARDIFRC®/NSC after 30 TC

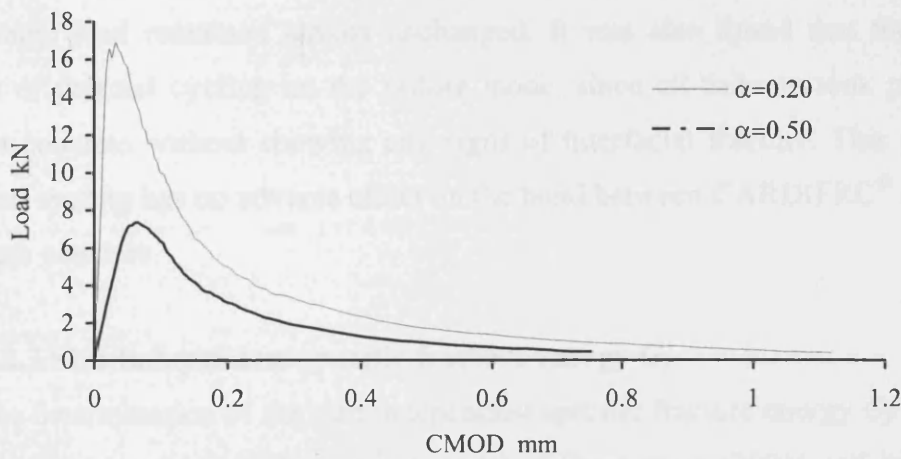
α	Specimens	Max. Load (kN)	Ave. (kN)	CMOD (mm)	Failure location	Kink angle (ω°)	G_f (N/m)	Ave. (N/m)
0.20	1	16.56	17.20	0.030	C	16	119.00	122.00
	2	17.60		0.025	C	18	125.00	
0.50	1	7.60	7.10	0.060	C	10	110.69	98.00
	2	7.50		0.060	C	12	95.50	
	3	7.20		0.060	C	13	90.50	

Table 5.16 WS results of CARDIFRC®/NSC after 90 TC

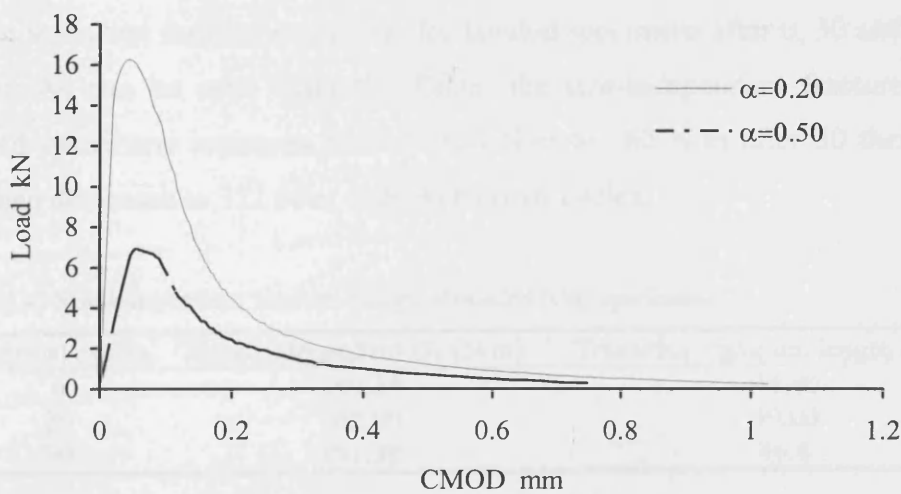
α	Specimens	Max. Load (kN)	Ave. (kN)	CMOD (mm)	Failure location	Kink angle (ω°)	G_f (N/m)	Ave. (N/m)
0.20	1	16.70	16.33	0.035	C	16	105.00	107.33
	2	16.80		0.030	C	18	108.00	
	3	15.50		0.026	C	20	109.00	
0.50	1	7.34	6.91	0.060	C	11	81.00	80.90
	2	6.90		0.055	C	12	78.00	
	3	6.50		0.05	C	9	83.7	



(a)



(b)



(c)

Figure 5.11: The influence of notch size on the load-CMOD curves of bonded NSC specimens, after: (a) zero thermal cycles, (b) 30 thermal cycles and (c) 90 thermal cycles.

The results also reveal that measured fracture energy G_f for specimens with a notch to depth ratio of 0.20 increases from 107.43 N/m at room temperature, to 122 N/m after 30 thermal cycles but decreases to 107.33 N/m after 90 thermal cycles. These results are similar to those of control specimens exposed to the same temperature conditions. Similar trend has been observed for $\alpha=0.5$.

Tables 5.14, 5.15 and 5.16 show that, the average maximum load for specimens with a notch to depth ratio of 0.20 increases from 15.9 kN to 17.2 kN after 30 thermal cycles and then drops slightly to 16.33 kN after 90 cycles, giving a total increase of 2.8 percent. These results, to a certain extent, agree with the test results of the control NSC specimens. However, for specimens with notch to depth ratio of 0.50 the maximum load remained almost unchanged. It was also found that there was no effect of thermal cycling on the failure mode, since all failures took place in the parent concrete without showing any signs of interfacial fracture. This proves that thermal cycling has no adverse effect on the bond between CARDIFRC[®] and normal strength concrete.

5.8.3.2.3 Size-independent specific fracture energy G_F

For the determination of the size-independent specific fracture energy G_F for bonded NSC specimens the boundary effect model of Duan et al. (2001) and its additional verification by Abdalla and Karihaloo (2003) was again used. Table 5.17 shows the size-independent fracture energy G_F for bonded specimens after 0, 30 and 90 thermal cycles. As can be seen from the Table, the size-independent fracture energy of bonded specimens increases from 149.24 N/m to 162 N/m after 30 thermal cycles and then decreases to 152 N/m after 90 thermal cycles.

Table 5.17 Size-independent fracture energy of bonded NSC specimens

Thermal cycles	Size-independent G_F (N/m)	Transition ligament length a_l (mm)
0	149.24	44.80
30	162.00	40.00
90	151.38	46.6

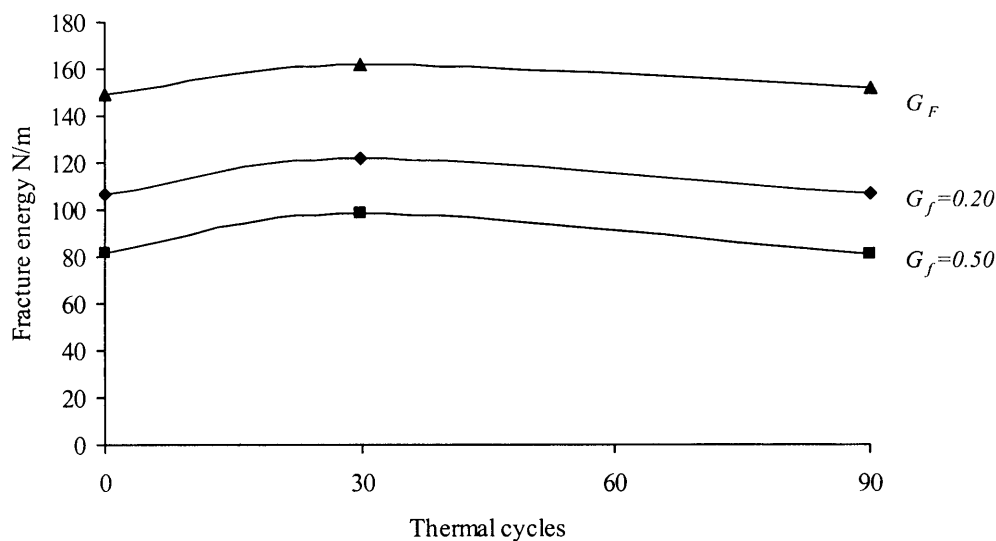


Figure 5.12 The effect of thermal cycling on measured and size-independent fracture energy of CARDIFRC[®]/NSC bonded system

The variation of the measured and size-independent fracture energy as it is clearly revealed in Figure 5.12 can be attributed to the change in material properties as a result of thermal cycling. The increase after 30 thermal cycles is probably due to the continued hydration of the cement paste, whereas the reduction after thermal cycles is due to the stress generated at the interface between the aggregate and the hardened cement paste which induce damage through microcracking.

5.9 Comparison of the results

5.9.1 Specimens exposed to 0 thermal cycles

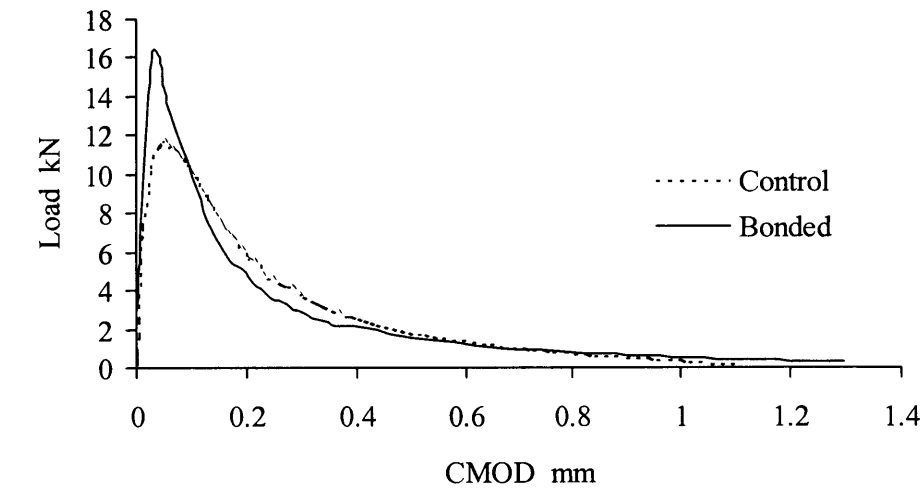
As expected, since the failure for both control and bonded specimens took place in the normal strength concrete, the fracture mode is classified as quasi-brittle. Figures 5.13a and 5.14a show the combination of load-CMOD curves for control and bonded normal strength concrete with notch to depth ratios of 0.20 and 0.50 after 0 thermal cycling, respectively. It can be seen that the stiffness and maximum failure load for bonded specimens increases compared to the control one. The mean value of maximum load for bonded NSC specimens with notch to depth ratio of 0.20 is 15.9 kN whereas, it is only 11.8 kN for the control NSC specimens. Similarly, the mean value of maximum load for bonded NSC specimens with notch to depth ratio of 0.50 is 7.37 kN, and 6.13 kN for the control NSC specimens. These results indicate that

the bonded specimens are somewhat stronger than that of control specimens (Table 5.18). As can be seen, the increase in the mean value of the maximum load of bonded NSC specimens with notch to depth ratio of 0.20 is 34.7 percent and 20.2 percent for notch to depth ratio of 0.50.

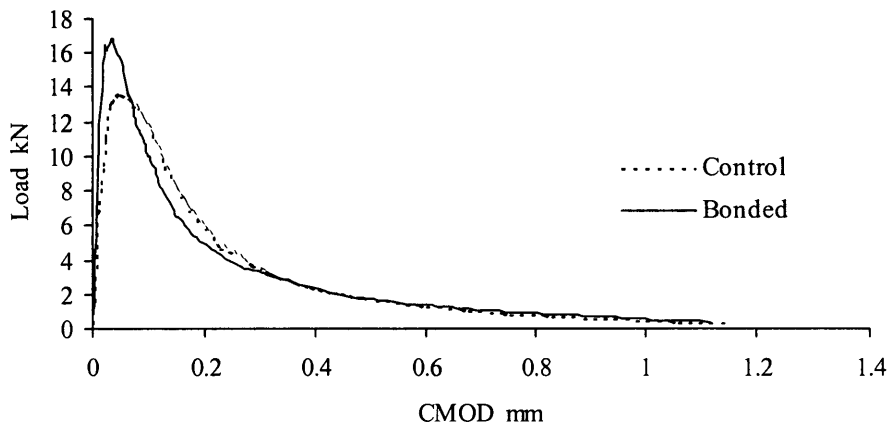
The Load-CMOD curves shown in Figures 5.13a and 5.14a reveal that bonding NSC with CARDIFRC® improves the peak load, reduces the pre-peak non-linearity, and the post-peak behaviour is steeper. The latter indicates that there is a slight decrease in G_f value for bonded specimens compared to that of control NSC. The reduction in fracture energy for bonded NSC could also be attributed to the fact that the crack path in such a bonded system is less tortuous than that in the control NSC specimens. This reduction is quite noticeable in specimens with a notch to depth ratio of 0.50 (Figure 5.14a).

5.9.2 Specimens exposed to 30 thermal cycles

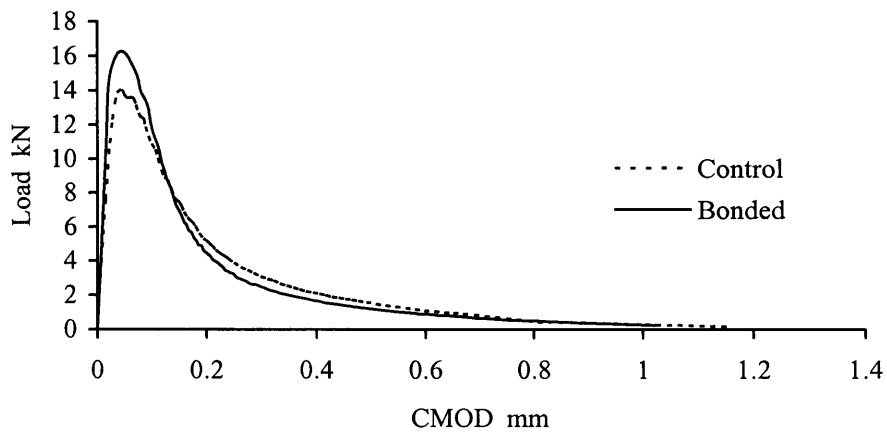
Figure 5.13b shows the typical Load-CMOD curves for control and bonded NSC specimens with a notch to depth ratio of 0.20 after 30 thermal cycles. As can be seen, the stiffness and maximum load of bonded specimens are higher than those of control specimens. The maximum load increases from 14.24 kN for the control normal strength concrete specimens to 17.2 kN for CARDIFRC® bonded specimens, giving an increase in maximum load of 20.78 percent. The Load-CMOD curves for control and bonded NSC specimens with a notch to depth ratio of 0.50 are shown in Figure 5.14b. As it can be seen, the behaviour of these specimens is similar to those with a notch to depth ratio of 0.20. The mean value of maximum load increases from 6.28 kN for the control specimens to 7.10 kN for the bonded specimens (Table 5.18). However, the post-peak response of bonded specimens seems to be steeper, which indicate that the bonded specimens are slightly more brittle than the control specimens.



(a)

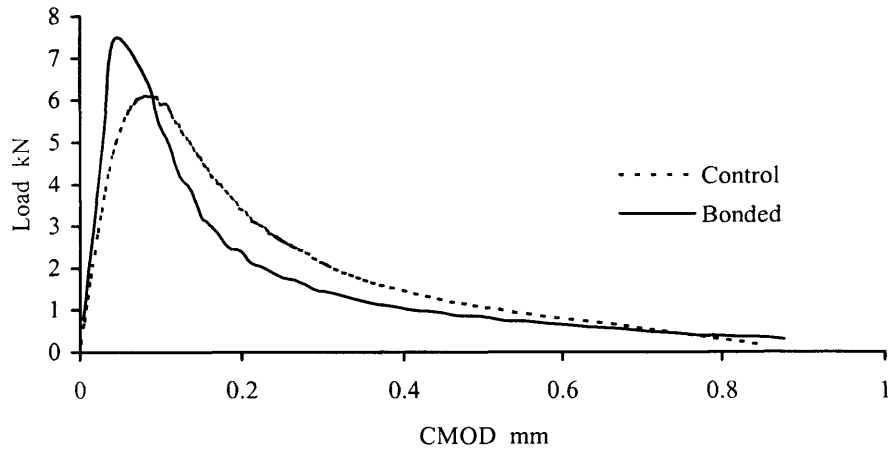


(b)

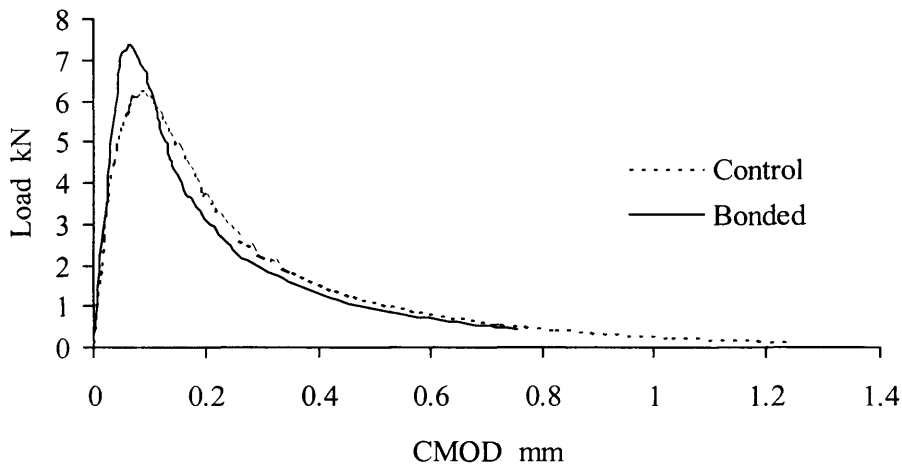


(c)

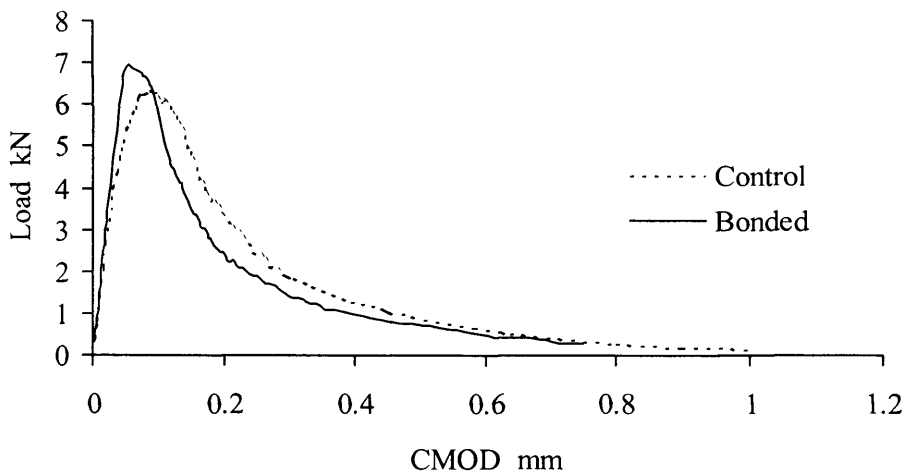
Figure 5.13: Load-CMOD curves for control and bonded NSC specimens with $\alpha=0.20$, after: (a) zero thermal cycles, (b) 30 thermal cycles and (c) 90 thermal cycles.



(a)



(b)



(c)

Figure 5.14 Load-CMOD curves for control and bonded NSC specimens with $\alpha=0.50$, after: (a) zero thermal cycles, (b) 30 thermal cycles and (c) 90 thermal cycles.

5.9.3 Specimens exposed to 90 thermal cycles

The typical load-CMOD curves for control and bonded NSC specimens with a notch to depth ratio of 0.20 after 90 thermal cycles are plotted in Figure 5.13c. As can be seen, the mean value of maximum loads increases from 14.17 kN for the control specimens to 16.33 kN for the bonded specimens. Therefore, a total increase in maximum load of the bonded specimens to that of the control ones is only 15.24 percent. Regarding specimens with a notch to depth ratio of 0.50, the increase in the mean value of maximum load of the bonded specimens over those of the control normal strength concrete specimens is 8.47 percent (Table 5.18).

Table 5.18 The effect of thermal cycling on failure load of repaired and control NSC specimens

Thermal cycles	Failure Load (kN)				Increase in Failure load (%)	
	Control α		Bonded α		0.20	0.50
	0.20	0.50	0.20	0.50		
0	11.80	6.13	15.90	7.37	34.74	20.23
30	14.24	6.28	17.20	7.10	20.78	13.05
90	14.17	6.37	16.33	6.91	15.24	8.47

Based on the LEFM analysis of bimaterial systems discussed in Chapter 3, the following analytical expressions will provide a simple explanation for the observed increase in the maximum failure load of bonded specimens over that of control specimens.

The Dundurs' elastic mismatch parameter is $\alpha = \frac{E_1 - E_2}{E_1 + E_2}$ (5.8)

Physically, α measures the magnitude of mismatch of the elastic moduli of the bimaterials. E_1 and E_2 for CARDIFRC® and NSC are 50 GPa and 33 GPa respectively. Thus, the parameter α is 0.20. The second Dundurs' parameter β is ≈ 0 . Substituting β in equation (3.38) gives

$$G_{com} = \frac{1}{E_*} k_*^2 \quad (5.9)$$

where

$$\frac{1}{E_*} = \frac{1}{2} \left(\frac{1}{E_1} + \frac{1}{E_2} \right) \quad (5.10)$$

Since $E_* = E_{Com}$ and E_1 and E_2 are equal to E_{NSC} and $E_{CARDIFRC}$

$$G_{com} = \frac{1}{2} \left(\frac{1}{E_{NSC}} + \frac{1}{E_{CARDIFRC}} \right) k_*^2 \quad (5.11)$$

Thus

$$k_* = \sqrt{\frac{2G_{com}}{\frac{1}{E_{NSC}} + \frac{1}{E_{CARDIFRC}}}} = \sqrt{\frac{2G_{com} E_{NSC} E_{CARDIFRC}}{(E_{CARDIFRC} + E_{NSC})}} \quad (5.12)$$

Since G_F of NSC is roughly equal to G_{com} and k_I of NSC is equal to $\sqrt{E_{NSC} G_F}$, at the same level of applied k_I , the ratio

$$\sqrt{\frac{2E_{CARDIFRC}}{E_{CARDIFRC} + E_{NSC}}} > \sqrt{\frac{100}{84}} = 1.09 \quad (5.13)$$

As a result, it follows from (5.12) that

$$k_* > k_I$$

This means that the maximum load level corresponding to the initiation of crack growth must be larger in the bonded system (P_{*max}) than the solid NSC (P_{max})

5.10 Conclusion

The principal findings and conclusions from the tests are:

- The mechanical and fracture properties of normal strength concrete are substantially improved after 30 thermal cycles, but not so after 90 thermal cycles. The increase in these properties after 30 thermal cycles is probably due to the continued hydration of unhydrated cement. However, the reduction after 90 thermal cycles could be due to the initiation of microcracks between the cement paste and aggregate.
- The mechanical properties of CARDIFRC[®] are improved even after 90 thermal cycles. This could be attributed to the continued hydration of unhydrated cement. This increase is most likely due to the presence of microsilica that activates the secondary reaction. The presence of fibres seems to counteract any possible deterioration due to microcracking.
- Normal strength concrete can be successfully repaired with CARDIFRC[®] using the technique of adhesive bonding
- To prevent delamination or interfacial fracture, both CARDIFRC[®] and the parent concrete mating surfaces have to be roughened. i.e., when the surfaces of both concrete and CARDIFRC[®] are deliberately roughened, a better rough surface of the substrate is created and this leads to higher interface toughness which delays interface crack propagation forcing the crack to kink into the weaker material and to eventually propagate through the concrete.
- To further improve the bond between the adhesive and parent concrete, the thin film of cement paste on the smooth cast surfaces of parent concrete must be removed if they form the mating surface;
- The load carrying capacity of bonded concrete appear to be higher than that of control specimens;

- Cracks in all bonded specimens started from a corner of the initial notch and propagated in the concrete under increased load;
- The measured fracture energy of control and bonded specimens decreases with increasing notch to depth ratios;
- No visual deterioration or bond degradation was observed after thermal cycling of the bonded specimens attesting to the good thermal compatibility between the concrete and CARDIFRC[®];
- The failure mode of bonded system remained almost unchanged even after thermal cycling;
- The size-independent specific fracture energy for control and bonded specimens follows a similar trend with the number of thermal cycles; it increases slightly after 30 cycles and then drops slightly after 90 cycles. However, even after 90 thermal cycles, G_F of bonded specimens is slightly larger than the room temperature value (Table 5.17).

Chapter 6

*Performance of HSC bonded to
CARDIFRC[®] after thermal cycling*

6.1 Introduction

High strength concrete (HSC) has become popular in modern construction over the last two decades. It offers significant economic and architectural advantages over NSC. Considerable research on the effect of high temperature on the properties of NSC has been done. However, there is little information on the effect of high temperature on the mechanical and fracture properties of HSC (Castillo et al., 1990; Zhang et al., 2000).

In Chapter 5, the behaviour of control and CARDIFRC® bonded to NSC specimens under thermal cycling was experimentally investigated. This chapter presents only the results of control and CARDIFRC® bonded to HSC obtained after 0, 30 and 90 thermal cycles. The thermal cycling and bonding techniques were identical to those mentioned in Chapter 5. The mechanical properties of HSC were determined according to the relevant British Standards and the fracture properties from the Load-CMOD curves, using WS test. The fracture behaviour of bonded CARDIFRC®/HSC after thermal cycling was evaluated through visual observations, load-CMOD curves, measured and size-independent fracture energy.

6.2 Control specimens

To determine the mechanical properties of HSC under thermal cycling, a total of nine 100 x 100 x 100 (mm) cubes for compressive strength, 100 x 200 (mm) cylinders for splitting strength and modulus of elasticity, and nine 100 x 100 x 500 (mm) beams for modulus of rupture were tested. For the determination of fracture properties, eighteen 200 x 200 x 200 (mm) cubes notched with a diamond saw to notch to depth ratios (a_0/W) of 0.20 and 0.50 and tested using WS test as in § 5.7. The specimens were tested at room temperature after 0, 30 and 90 thermal cycles.

6.2.1 Mix proportion of HSC

HSC mix was chosen based on previous work carried out by other researchers at the same laboratory (Taylor, 1997; Abousaif, 1997)

Table 6.1 Mix proportions for HSC

Mix proportions					
Cement	Sand	Aggregate	Micro-silica	Superplasticizer (%)	W/b ratio
1	1.32	2.21	0.11	1.8	0.22

The materials used were as follows:

- Cement: Blue circle OPC (BS12: 1996 complied).
- Fine aggregate: Local sea dredged sand.
- Coarse aggregate: Local crushed limestone with $d_a = 10$ mm.
- Micro silica (SF): Elkem microsilica undensified 983.
- Superplasticizer (SP) Adoflow extra (consisted of sodium salts of sulphonated naphthalene formaldehyde condensate and lignosulphonic acid).

The dry constituents were first mixed, water was added gradually to the dry mix while the mixer was in operation, and superplasticizer was added to achieve the required workability. Approximately two or three minutes after the addition of all the ingredients a trowel was scrapped along the side and into the corners of the drum to release materials which had been gathered away from the mixing plades, and the mixing continued. Immediately, after the mixing process was completed, the fresh mix was transferred into the specified test specimen moulds.

6.2.2 Mechanical properties

The mechanical properties of HSC namely, compressive, tensile and flexural strengths and modulus of elasticity were determined after 0, 30 and 90 thermal cycles. All tests were carried out at room temperature. The results after different thermal cycling are explained in the following section.

6.2.2.1 Compressive strength f_c

Table 6.2 shows the compressive strength results after 0, 30 and 90 thermal cycles. The results showed that the compressive strength of HSC increases from 102.30 to 131.06 MPa after 30 thermal cycles and then remained almost unchanged at 131.60 MPa after 90 cycles, giving an increase in compressive strength after 90 cycles of 28.4 percent. As mentioned earlier in § 5.7.1 the increase in compressive strength

may be because elevated temperatures assist further hydration. The 28.4 percent increase in strength is most likely due to the presence of micro-silica that activates the secondary reaction and leads to an additional strength. The effect of age on concrete strength was also investigated on HSC specimens. As can be seen in Table 6.5, the compressive strength of HSC specimens increased by 5.6 per cent after 120 days.

Table 6.2 Cube crushing test of HSC after different thermal cycling.

TC	Specimen	Failure load (kN)	Compressive strength (MPa)	Ave. (MPa)	COV %
0	1	1040	104.00	102.30	1.2
	2	1020	102.00		
	3	1010	101.00		
30	1	1353	135.30	131.06	2.5
	2	1306	130.60		
	3	1273	127.30		
90	1	1270	127.00	131.60	2.5
	2	1340	134.00		
	3	1338	133.8		

6.2.2.2 Splitting strength f_t

Table 6.3 shows the splitting strength results after 0, 30 and 90 thermal cycles. The splitting strength of HSC specimens slightly increases after 30 thermal cycles and then decreases to reach a value of 7.59 MPa after 90 thermal cycles. The effect of age on the splitting strength is also presented in Table 6.5. The results showed that f_t increases with age. The increase after 120 days is about 1.8 per cent.

Table 6.3 Splitting test of HSC after different thermal cycling.

TC	Specimen	Failure load (kN)	Splitting strength (MPa)	Ave. (MPa)	COV %
0	1	241.00	7.67	7.72	1.7
	2	248.00	7.89		
	3	238.00	7.58		
30	1	236.00	7.52	7.93	3.7
	2	254.00	8.09		
	3	257.00	8.18		
90	1	241.80	7.70	7.59	1.2
	2	238.00	7.58		
	3	235.00	7.48		

6.2.2.3 Modulus of rupture (MOR)

Table 6.4 shows the modulus of rupture (MOR) results after 0, 30 and 90 thermal cycles. The MOR has the same trend as f_t . It first increases from 9.72 MPa to 10.61 MPa and then decreases to 9.96 MPa after 90 thermal cycles. Therefore, the increase in flexural strength after 90 thermal cycles is about 1.85 per cent compared with the room temperature value. The results given in Table 6.5 indicate that the MOR generally increases with age at room temperature owing to continued hydration of unhydrated cement.

Table 6.4 Flexural strength test of HSC after different thermal cycling.

TC	Specimen	Failure load (kN)	MOR (MPa)	Ave. (MPa)	COV %
0	1	23.92	9.57	9.72	2.3
	2	25.10	10.04		
	3	23.90	9.56		
30	1	26.37	10.55	10.61	2.2
	2	27.30	10.92		
	3	25.90	10.36		
90	1	24.32	9.73	9.96	4.7
	2	23.89	9.56		
	3	26.56	10.62		

Table 6.5 f_c , f_t and f_r after different environmental conditions and age

Environmental conditions	Compressive strength (MPa)	Splitting strength (MPa)	Flexural strength (MPa)
28 days at 20	102.30	7.72	9.72
120 days at 20	108.00	7.86	9.89
30 TC	131.06	7.93	10.61
90 TC	131.60	7.59	9.96

6.2.2.4 Modulus of elasticity

Modulus of elasticity was determined for HSC, according to BS 1881-121 1983. It was determined at room temperature after 0, 30 and 90 thermal cycles. Table 6.6 shows the E value after different thermal cycles. It is seen that the E value slightly increases from 47.4 GPa to 48.7 GPa after 30 thermal cycles and then drops to reach a value of 42 GPa.

Table 6.6 The effect of thermal cycles on the Modulus of elasticity of concrete

Thermal cycles	0	30	90
<i>E</i> value GPa	47.40	48.70	42.00

6.2.3 Fracture properties

Fracture properties of HSC were determined from load-CMOD curve. The latter was obtained from the WS test (see § 5.8.1). The load-CMOD curve describes fully the fracture behaviour of concrete. The area under the curve divided by the ligament area yields the measured fracture energy of concrete.

6.2.3.1 Measured fracture energy G_f

Figure 6.1 shows the load-CMOD curves for HSC and NSC specimens with a notch to depth ratio of 0.20. As can be seen, the failure of HSC is characteristically more brittle than that of the NSC. This can be attributed to the compact HSC matrix and interfaces, which reduce the toughening that can occur during crack propagation (Gettu, et al, 1990).

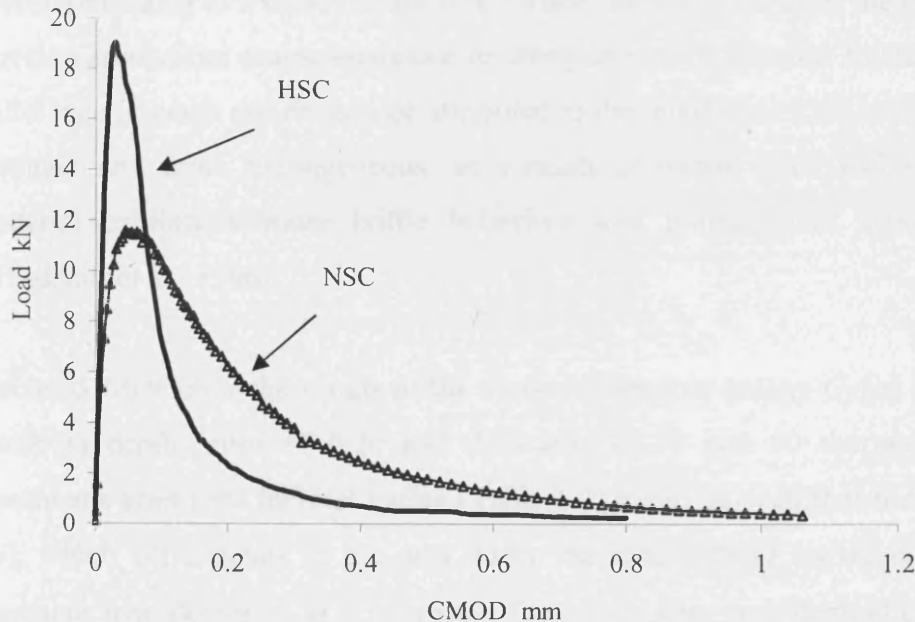


Figure 6.1 Load-CMOD curves for high and normal WS concrete specimens, with notch to depth ratio of 0.20.

In HSC, the total energy is contributed by two parts. The first part is utilized to overcome the surface forces of concrete (surface energy), while the second part is

utilised to overcome the cohesive forces due to aggregate bridging, aggregate interlocking, friction forces, and other mechanisms in fracture process zone. It has been reported in the literature review that the interface between cement paste with micro-silica and aggregate is very strong and the concrete behaves more like a composite material. As can be seen in Figure 6.1, the post peak response seems to be steeper for HSC than that of NSC. Due to the strong interface, the process zone in front of the initial crack tip localizes resulting in the decrease in the absorption of fracture energy in this zone.

As can be seen in Figure 6.1, the ascending part of the curve is more linear in HSC. After the peak value, the curve drops off gradually until about zero load is reached. The descending part of the curve becomes steeper for HSC. The tail of the descending branch is longer for NSC. This indicates that toughness of the concrete decreases with strength.

Visual investigations revealed that cracks in HSC travelled through the aggregate, therefore leading to a smoother fracture surface. In NSC, however, the cracks usually develop around the coarse aggregate resulting in a more tortuous fracture path. This difference in crack pattern can be attributed to the interfacial zone in HSC, which is stronger and more homogeneous, as a result of micro silica inclusion, and the material exhibits a more brittle behaviour and transgranular type of fracture (Tasdemir et al., 1996).

Tables 6.7-6.9 show the results of the measured fracture energy $G_f(\alpha)$ for HSC with notch to depth ratios of 0.20 and 0.50 after 0, 30 and 90 thermal cycles. For specimens after zero thermal cycles (Table 6.7) it can be seen that the measured $G_f(\alpha)$, which corresponds to the area under the load-CMOD curve, divided by the ligament area, decreases as α increases. The results after zero thermal cycles showed that $G_f(\alpha)$ decreases from 83.63 N/m for $\alpha = 0.20$ to 51.70 N/m for $\alpha = 0.50$. Furthermore, it can be seen that the peak load decreases as α increases. The average peak load decreases from 19.37 kN for $\alpha = 0.20$ to 8.08 kN for $\alpha = 0.50$. The variation in fracture energy and maximum loads with the initial notch size was briefly explained in Chapter 5. These results seem to be in accord with Abdalla and

Karihaloo (2003). Similar trend for the variation of fracture energy and peak loads with initial crack size have also been observed for test specimens after 30 and 90 thermal cycling (Tables 6.8 and 6.9).

As mentioned before, thermal cycling for WS HSC specimens was performed in a similar manner to that conducted on NSC specimens (see § 5.6). After the desired number of cycles, WS specimens were naturally cooled at room temperature 24 hours before testing.

As can be seen from Tables 6.7 - 6.9, the fracture energy slightly increases after 30 thermal cycles. The G_f increased from 83.63 N/m to 86.42 N/m for $\alpha = 0.20$ and from 51.70 N/m to 54.48 N/m for $\alpha = 0.50$. After 90 thermal cycles a decrease in G_f value has been observed for specimens with $\alpha = 0.20$, but not so for specimens with $\alpha = 0.50$. The G_f ($\alpha = 0.20$) value decreased from 86.42 N/m after 30 thermal cycles to 82.04 N/m after 90 thermal cycles.

Table 6.7 WS results of control HSC after 0 TC.

α	Specimen	Maximum Load (kN)	Ave. (kN)	CMOD (mm)	G_f (N/m)	Ave. G_f (N/m)
0.20	1	19.8	19.37	0.027	88.4	83.63
	2	18.3		0.04	78.6	
	3	20.02		0.027	83.89	
0.50	1	8.44	8.08	0.033	50.96	51.7
	2	8.1		0.028	51.45	
	3	7.71		0.04	52.69	

Table 6.8 WS results of control HSC after 30 TC.

α	Specimen	Maximum Load (kN)	Ave. (kN)	CMOD (mm)	G_f (N/m)	Ave. G_f (N/m)
0.20	1	21.3	20.03	0.028	89.2	86.42
	2	18.6		0.033	89	
	3	20.2		0.033	81.06	
0.50	1	10.75	10.17	0.027	51.9	54.49
	2	9.06		0.03	57.5	
	3	10.7		0.026	54.06	

Table 6.9 WS results of control HSC after 90 TC.

α	Specimen	Maximum Load (kN)	Ave. (kN)	CMOD (mm)	G_f (N/m)	Ave. G_f (N/m)
0.20	1	19.70	18.55	0.03	83.68	82.04
	2	17.56		0.031	88.38	
	3	18.4		0.035	74.05	
0.50	1	9.97	9.22	0.025	54.59	57.19
	2	8.70		0.035	58.50	
	3	9.00		0.38	58.48	

6.2.3.2 Size-independent fracture energy G_F

Based on the boundary effect model of Duan et al. (2001) for determining the size-independent specific fracture energy, Abdalla and Karihaloo (2003) found that the size-independent specific fracture energy can be determined by testing just two specimens of the same size which however contain a shallow and deep starter notch, respectively. The G_F was determined using equation (3.31).

Table 6.10 Size-independent specific fracture energy after different thermal cycles.

Thermal cycles	0	30	90
G_F (N/m)	136	140	123
a_l (mm)	62.20	61.22	53.9

Table 6.10 shows the variation of the true fracture energy and the transition ligament length a_l with thermal cycling. As can be seen, after 30 thermal cycles the G_F remains almost unchanged and then decreases to reach a value of 123 N/m. In fact, the variation of the fracture energy of HSC is due to the variation in its mechanical properties after thermal cycling. Therefore, it can be concluded that the 30 thermal cycles does not influence the ductility of HSC, whereas the concrete becomes more brittle after 90 thermal cycles. This could be attributed to the initiation of microcracks at the interfaces of cement paste and aggregate. For clarity, the measured and size independent fracture energy for the HSC after different thermal cycling is shown in Figure 6.2.

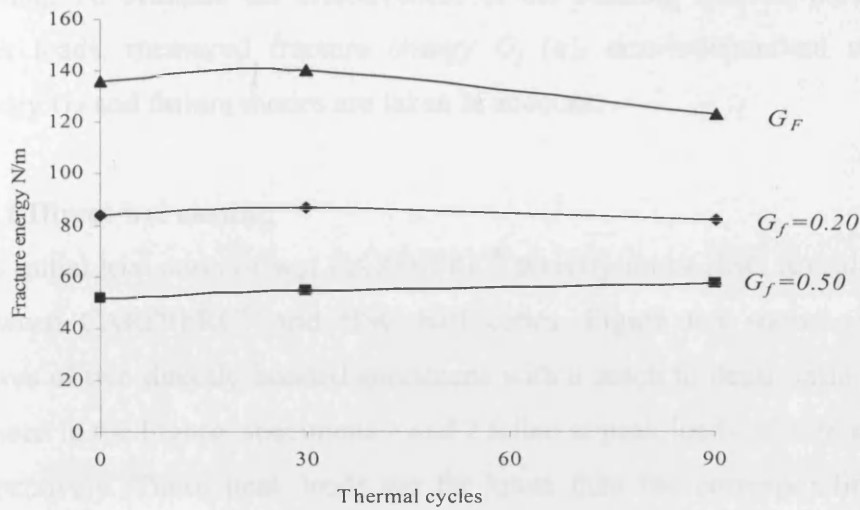


Figure 6.2 The effect of thermal cycling on measured and size-independent fracture energy of HSC.

6.2.3.3 Brittleness

The brittleness of concrete can be estimated by the characteristic length l_{ch} . The l_{ch} can be calculated using equation (3.2.1). The values of the characteristic length from different thermal cycles are shown in Table 6.11. As can be seen, the l_{ch} value is almost unchanged after 30 thermal cycles and then decreases after 90 thermal cycles. It can be concluded that after 90 thermal cycles the HSC becomes more brittle. By comparing these results with those of NSC specimens exposed to the same thermal cycling (see § 5.8.2.3), we can also conclude that both concretes showed the same behaviour after 90 thermal cycles.

Table 6.11 The effect of thermal cycles on l_{ch} for concrete

Thermal cycles	0	30	90
l_{ch} (mm)	108.16	108.42	89.67

6.3 CARDIFRC[®] bonded specimens

This section presents the WS test results of CARDIFRC[®] bonded to HSC half cubes using direct wet casting and adhesive bonding techniques. The casting of CARDIFRC[®] half cubes and the bonding were carried out in a similar way to that described in Chapter 5. As mentioned in the introductory section, emphasis will be placed on the main factors that affect the bond between HSC and CARDIFRC[®] half cubes, such as the roughness of the mating surface of the parent HSC and thermal

cycling. To evaluate the effectiveness of the bonding system, parameters such as peak loads, measured fracture energy G_f (α), size-independent specific fracture energy G_F and failure modes are taken in account.

6.3.1 Direct wet casting

The initial trial casts of wet CARDIFRC[®] directly on to HSC revealed a weak bond between CARDIFRC[®] and HSC half cubes. Figure 6.3 shows the load-CMOD curves of two directly bonded specimens with a notch to depth ratio of 0.30. As can be seen in the Figure, specimens 1 and 2 failed at peak loads of 3.98 kN and 5.76 kN, respectively. These peak loads are far lower than the corresponding HSC control specimens. Furthermore, visual observation showed that the failure location was situated almost at the interface between CARDIFRC[®] and concrete. As expected, this weak bond resulted from the casting configuration since specimens were horizontally cast.

As mentioned in § 5.8.3.1, to overcome the aforementioned problem, it was suggested to improve the bonding technique between the two materials. Therefore, it was decided to modify the casting configuration in such a way that the HSC half cube was laid horizontally in a wooden mould and CARDIFRC[®] was cast vertically on top of it (see Figure 5.8). Furthermore, pressure was applied while the repair material was still wet.

The results of this technique were encouraging. Figure 6.4 shows the load-CMOD curves of two bonded specimens with a notch to depth ratio of 0.30. As can be seen, the peak loads that the repair system can sustain have remarkably increased. As it can be seen in the Figure, the peak loads for specimens 1 and 2 are 13.65 kN and 13.87 kN, respectively. Visual observation showed that the crack started at the interface and kinked slightly into the concrete. The crack path, however, was observed to fluctuate between the interface and the parent concrete adjacent to the interface.

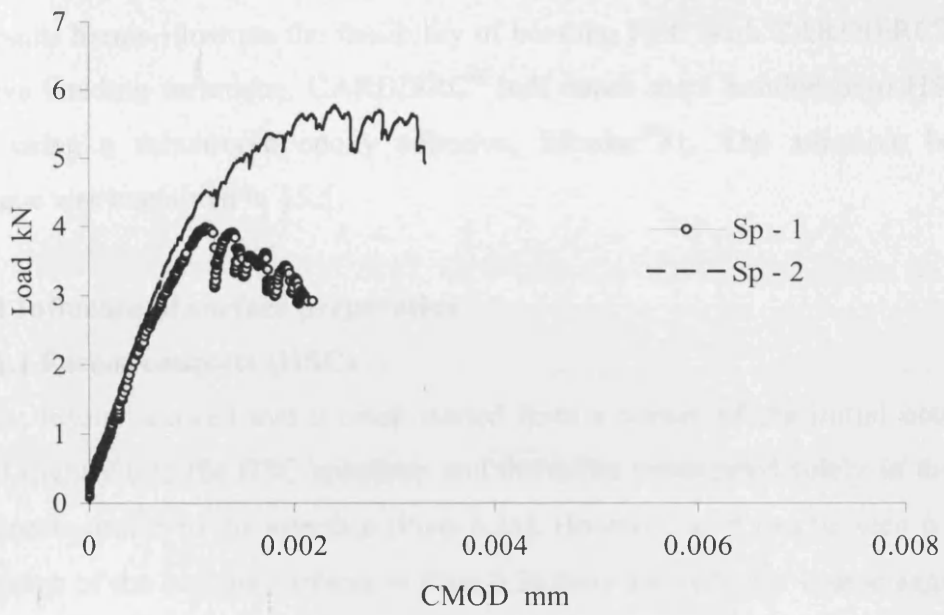


Figure 6.3 Load-CMOD curves of directly bonded CARDIFRC to HSC half cube with $\alpha=0.30$ (horizontal casting)

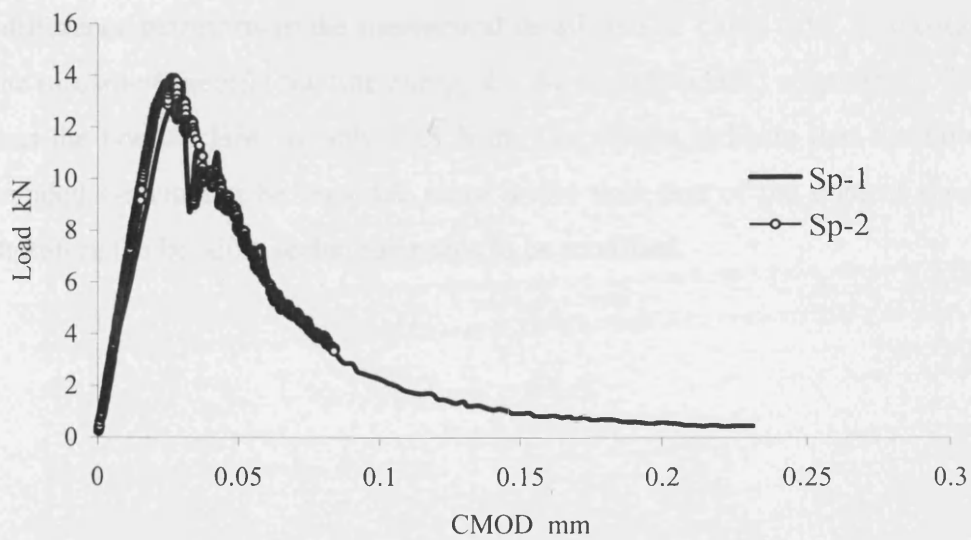


Figure 6.4 Load-CMOD curve of directly bonded HSC to CARDIFRC[®] half cube with $\alpha=0.30$ (vertical casting)

6.3.2 Adhesive bonding

The results herein illustrate the feasibility of bonding HSC with CARDIFRC® using adhesive bonding technique. CARDIFRC® half cubes were bonded onto HSC half cubes using a thixotropic epoxy adhesive, Sikadur®31. The adhesive bonding technique was explained in §5.5.

6.3.2.1 Influence of surface preparation

6.3.2.1.1 Parent concrete (HSC)

The test results showed that a crack started from a corner of the initial notch and kinked slightly into the HSC specimen and thereafter propagated solely in the latter and almost parallel to the interface (Plate 6.1a). However, as it can be seen from the photograph of the fracture surfaces in Plate 6.2a there are very few coarse aggregates on the surface. A comparison was made with fractured surfaces obtained after cutting the specimens away from the mating surface. This showed that the concentration of coarse aggregates in the fractured surfaces of the bonded concrete is less than that in the bulk.

A comparison was also made with fractured surfaces of complete WS HSC specimen. This revealed that the fracture surfaces of complete specimen exhibited higher irregularity and the number of fractured coarse aggregate was much larger. This difference manifests in the mechanical data listed in Table 6.12. The data show that the measured specific fracture energy for the complete HSC specimen is 72 N/m, whereas the bonded HSC is only 40.8 N/m. The results indicate that the failure of this bonded system can be regarded more brittle than that of the control specimen, and therefore the bonding technique needs to be modified.

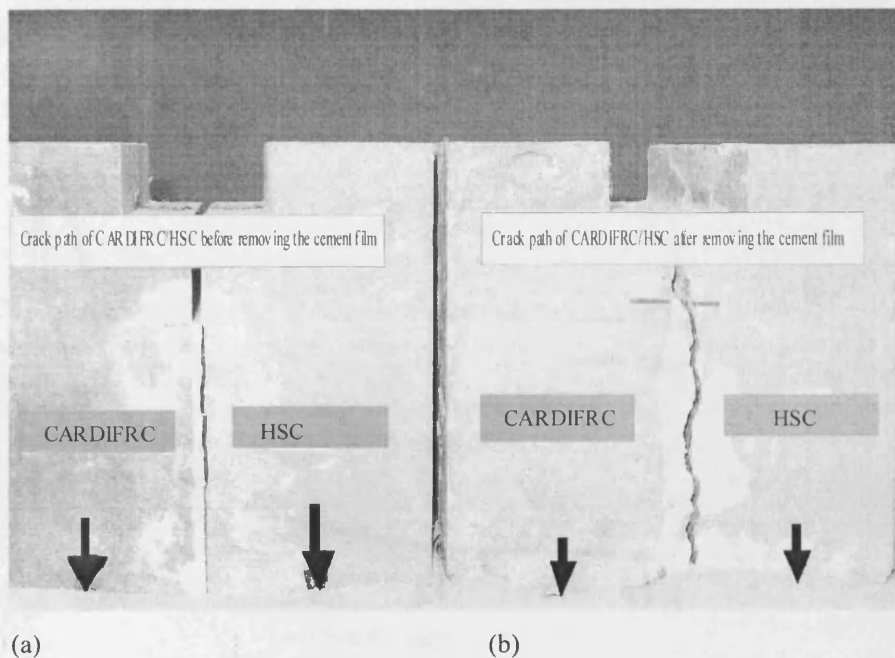


Plate 6.1 The effect of cement paste film on the failure mode of CARDIFRC[®]/HSC, (a) before, (b) after the removal of film.

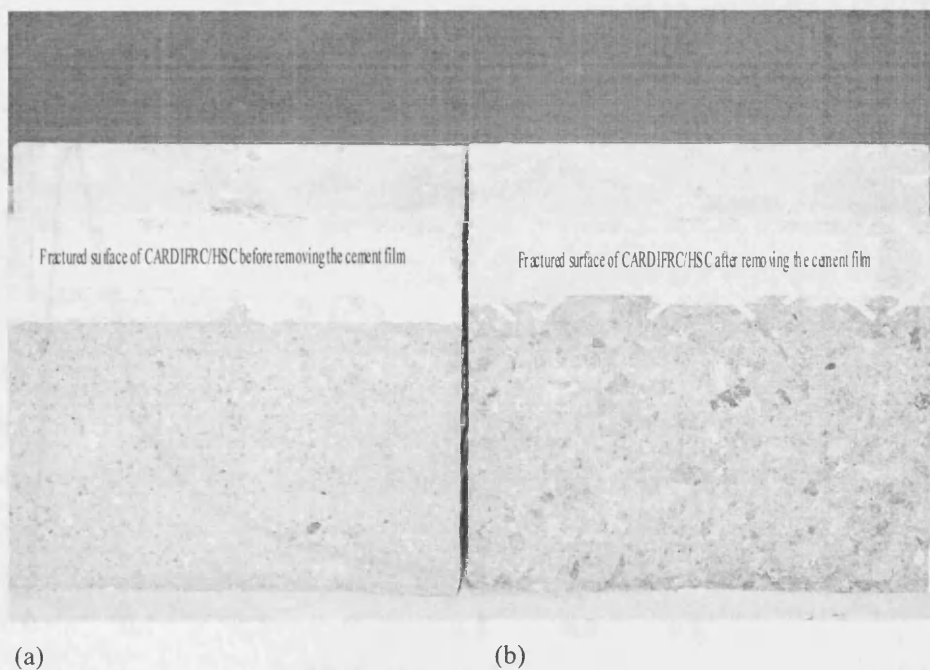


Plate 6.2 The effect of cement paste film on the fractured surface of CARDIFRC[®]/HSC, (a) before, (b) after the removal of film.

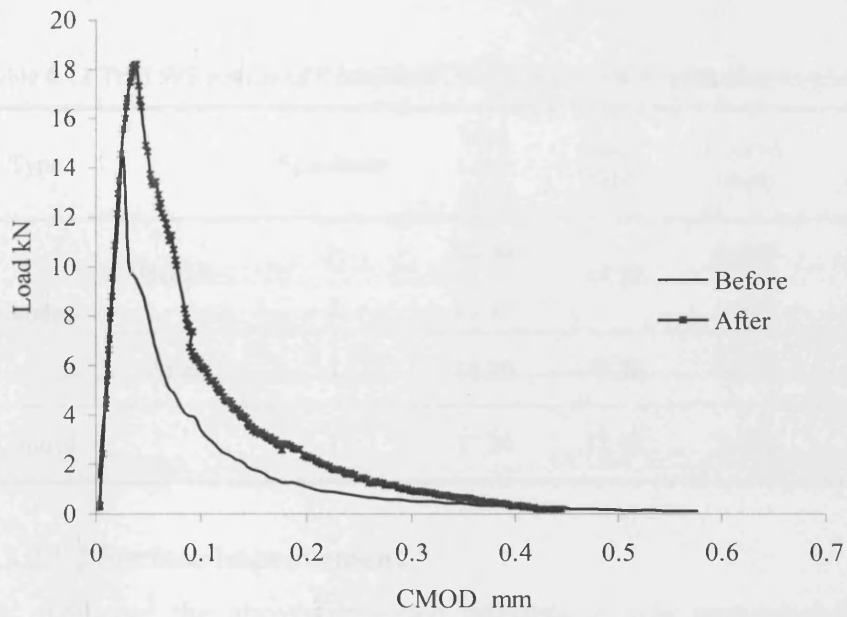


Figure 6.5 The effect of cement paste film of HSC on the bonded HSC/CARDIFRC[®] specimen with $\alpha = 0.30$.

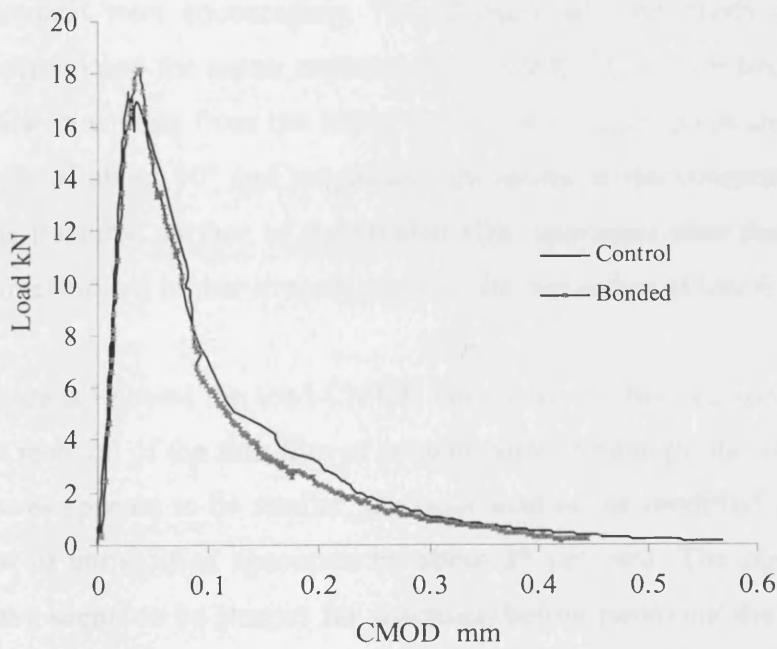


Figure 6.6 Load -CMOD curves for control and CARDIFRC[®] bonded to HSC specimens

Table 6.12 Trial WS results of CARDIFRC[®]/HSC with $\alpha=0.30$ (adhesive bonding)

Type		Specimen	Max Load (kN)	Ave. (kN)	CMOD (mm)	G_f (N/m)	Ave. G_f (N/m)
Bonded	Before	1	14.00	14.55	0.025	35.60	40.80
		2	15.10		0.027	46.00	
	After	1	18.20	18.20	0.037	68.30	68.30
Control		1	17.30	17.30	0.032	72.00	72.00

6.3.2.1.2 Surface improvement

To overcome the abovementioned problem, it was recommended to improve the bonding technique in a similar manner to that applied on CARDIFRC[®]/NSC bonded system (see § 5.8.3.2.1.3), which incorporated the removal of a cement paste film from the mating surface of the HSC half cubes. The results of this additional treatment were encouraging. The adhesive adhered firmly to the substrate (parent concrete) and the repair material (CARDIFRC[®]). As can be seen in Plate 6.1b, the crack emanating from the starter notch corner, kinked towards the HSC, with a kink angle of about 10° and propagated thereafter in the concrete close to the interface. The fractured surface of the bonded HSC specimen after the removal of the cement film exhibited higher irregularity than the one before (Plate 6.2b).

Figure 6.5 shows the load-CMOD curves for the bonded specimens before and after the removal of the thin film of cement paste. Although, the ascending part of the two curves appears to be similar, the peak load of the modified specimen is higher than that of unmodified specimen by about 28 per cent. The post peak response of the curve seems to be steeper for specimen before removing the film than the one after. Table 6.12 shows the corresponding maximum loads and fracture energy. The peak load and fracture energy required to separate the specimen, have both increased substantially after the removal of cement film.

The peak load for the treated specimen is about 18.20 kN, but only 14.55 kN for the non-treated one and the specific fracture energy is 68.33 N/m and only 40.80 N/m for treated and non-treated specimens, respectively.

Comparison has been made between the CARDIFRC®/HSC bonded system and control specimens made of HSC. The load-CMOD curves for bonded and control specimens are presented in Figure 6.6. The measured fracture energy for bonded specimens is 68.33 N/m and 72 N/m for control one (Table 6.12). The peak loads for bonded and control specimens are 18.2 kN and 17.30 kN, respectively.

From the preliminary tests it was concluded that, HSC can be repaired using both techniques, direct wet casting and adhesive bonding. However, the former requires great care to ensure that the repair material adheres very securely to concrete. This requires thorough compaction of wet material which is often difficult to achieve. The adhesive bonding technique does not suffer from this drawback and therefore it was selected for repairing the HSC cubes in the rest of the experimental programme.

Some HSC bonded specimens showed a different failure mode. Cracks propagated in the HSC half cube from one side and between CARDIFRC® half cube and the adhesive on the other side (Plate 6.3). This is believed to be due to the pre-existing crack which formed between CARDIFRC® half cube and the adhesive during the bonding process. During loading this crack penetrated partially into the plane of CARDIFRC® half cube. This happens only if the adhesive is squeezed onto the bonded surfaces of parent concrete thus forming a gap with the CARDIFRC® (Figure 6.7). This mode of failure can be avoided by exercising greater caution during adhesive bonding.

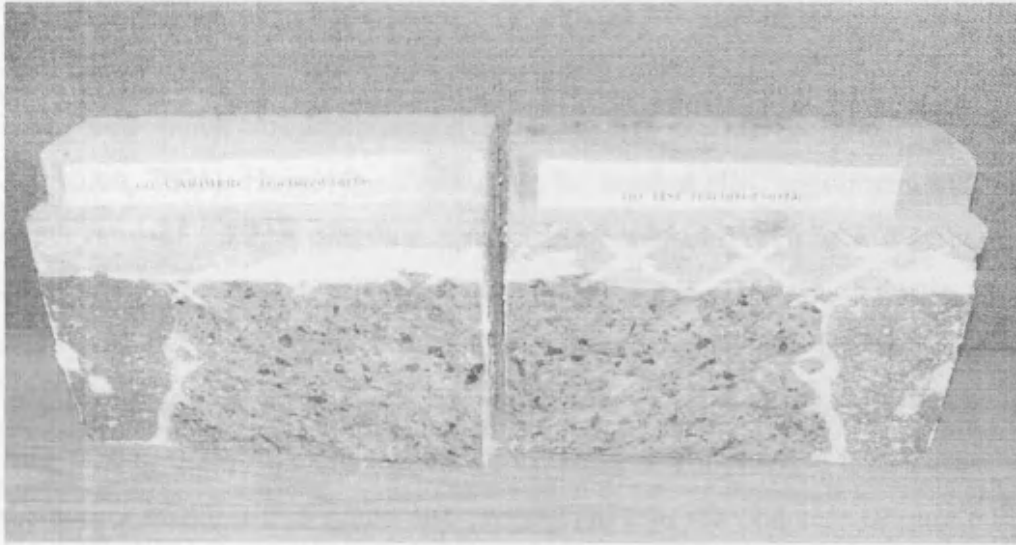


Plate 6.3 The effect of pre-existing crack on the fracture surfaces of bonded specimens.

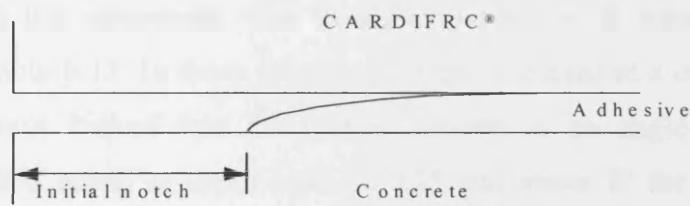


Figure 6.7 Schematic representation of pre-existing crack initiated between the adhesive and CARDIFRC[®]

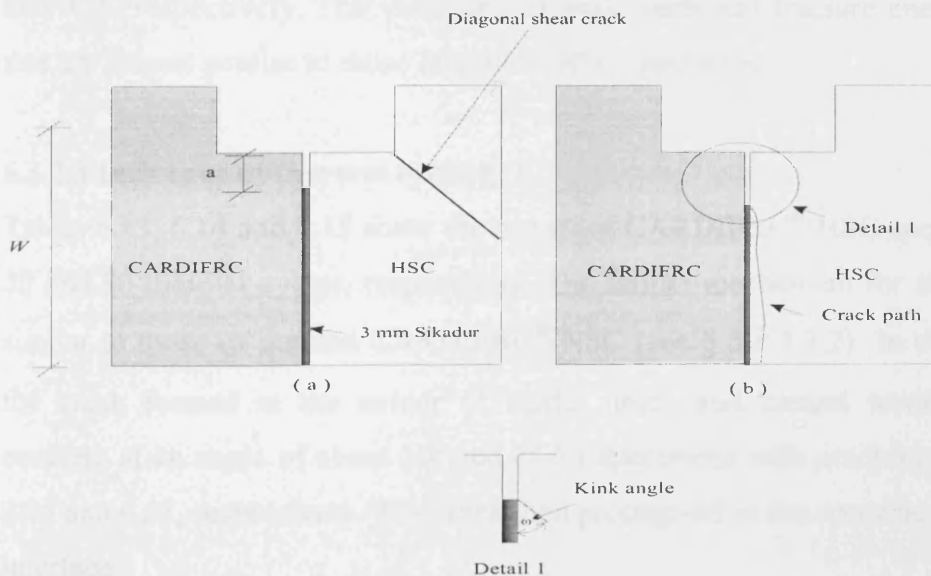


Figure 6.8 Schematic representation for tested CARDIFRC[®]/HSC: (a) $\alpha(0.20)$ with diagonal shear failure, (b) $\alpha(0.25)$ crack propagation through the HSC.

6.3.2.2 Influence of notch size

In order to determine the size-independent specific fracture energy G_F for bonded HSC, two notch to depth ratios of 0.20 and 0.50 were chosen (Abdalla and Karihaloo, 2003). However, after testing the bonded HSC specimens with a notch to depth ratio of 0.20, a diagonal shear failure was observed at a maximum load of 24.30 kN at the corner of the groove (Figure 6.8a). This was because the strength there had been exceeded before the starter notch could propagate, pointing to insufficient starter notch depth. Therefore, the notch to depth ratio α was increased from 0.20 to 0.25. As expected, after increasing α from 0.20 to 0.25 a crack started at the corner of the initial notch and propagated into the concrete (Figure 6.8b). Also, for the HSC specimens a deeper initial notch $\alpha=0.55$ has been used (instead of $\alpha=0.50$ as in control HSC).

Results of WS test specimens after zero thermal cycles at room temperature are presented in Table 6.13. In these specimens, a crack started at a corner of the starter notch and always kinked into the parent concrete at an angle of about 10° for specimens with a notch to depth ratio of 0.25 and about 8° for specimens with a notch to depth ratio of 0.55. The maximum failure load of bonded specimens with a notch to depth ratio of 0.25 is 22.09 kN, but only 8.89 kN for specimens with $\alpha = 0.55$. The fracture energy is 80.33 N/m and 52.33 N/m for specimens with α of 0.25 and 0.55, respectively. The variations of peak loads and fracture energy with notch size are almost similar to those of control HSC specimens.

6.3.2.3 Influence of thermal cycling

Tables 6.13, 6.14 and 6.15 show the results of CARDIFRC[®]/HSC specimens after 0, 30 and 90 thermal cycles, respectively. The failure mechanism for all specimens is similar to those of bonded CARDIFRC[®]/NSC (see § 5.8.3.2.2). In these specimens the crack formed at the corner of starter notch and kinked towards the parent concrete at an angle of about 10° and 8° for specimens with notch to depth ratios of 0.25 and 0.55, respectively. The crack then propagated in the concrete adjacent to the interface.

Table 6.13 WS results of CARDIFRC®/HSC after 0 TC.

α	Specimen	Maximum Load (kN)	Ave. (kN)	CMOD (mm)	Failure location	Kink angle (ω°)	G_f (N/m)	Ave. G_f (N/m)
0.25	1	17.65		0.029	C	12	84	
	2	21.5	20.45	0.03	C	10	81	80.33
	3	22.19		0.031	C	10	76	
0.55	1	9.7	8.89	0.026	C	10	50.89	
	2	9.85		0.05	C	8	55	52.23
	3	7.12		0.027	C	8	50.8	

Table 6.14 WS results of CARDIFRC®/HSC after 30 TC.

α	Specimen	Maximum Load (kN)	Ave. (kN)	CMOD (mm)	Failure location	Kink angle (ω°)	G_f (N/m)	Ave. G_f (N/m)
0.25	1	24.5		0.036	C	8	83.9	
	2	21.3	23.16	0.036	C	10	86.37	86.12
	3	23.7		0.035	C	12	88.1	
0.55	1	9.07	8.97	0.045	C	10	53.36	
	2	8.87		0.032	C	9	56.24	54.8

Table 6.15 WS results of CARDIFRC®/HSC after 90 TC.

α	Specimen	Maximum Load (kN)	Ave. (kN)	CMOD (mm)	Failure location	Kink angle (ω°)	G_f (N/m)	Ave. G_f (N/m)
0.25	1	20.32		0.035	C	12	66.00	
	2	23.5	21.98	0.042	C	12	76.85	73.22
	3	22.104		0.032	C	13	76.8	
0.55	1	8.89	9.27	0.027	C	9	56.2	
	2	9.66		0.026	C	11	54.57	55.38

As shown in the Tables, as the thermal cycles increase for specimens with a notch to depth ratio of 0.25 from 0 to 30 the average maximum load increases from 20.44 kN to 23.16 kN. With further increase in the thermal cycles to 90 the peak load decreases

to 21.97 kN. For specimens with a notch to depth ratio of 0.55 the average maximum load remained almost unchanged. As mentioned earlier, the increase in maximum load after 30 thermal cycles could be a result of increase in the tensile strength that may be related to the further hydration of the remaining anhydrous cement due to elevated temperatures.

The Tables also show the variation of the measured specific fracture energy $G_f(\alpha)$ with thermal cycling. As can be seen, the G_f for $\alpha = 0.25$ slightly increases from 80.33 N/m at room temperature to 86.12 N/m after 30 thermal cycles but drops to 73.21 N/m after 90 thermal cycles. For specimens with $\alpha = 0.55$ the G_f slightly increases from 52.23 N/m at room temperature to 54.8 N/m after 30 thermal cycles, and then remained almost unchanged after 90 thermal cycles.

6.3.2.3.1 Size-independent specific fracture energy G_F

The size-independent specific fracture energy G_F and the transition ligament length a_l for bonded HSC specimens was determined using equation (3.31). The results in Table 6.16 show that the G_F for bonded high strength concrete specimens increases from 122 N/m to 134 N/m after 30 thermal cycles and then decreases to 100 N/m after 90 thermal cycles.

Table 6.16 Size-independent specific fracture energy after different thermal cycles.

	0	30	90
G_F (N/m)	122	134	100.5
a_l (mm)	51.6	53.7	40.74

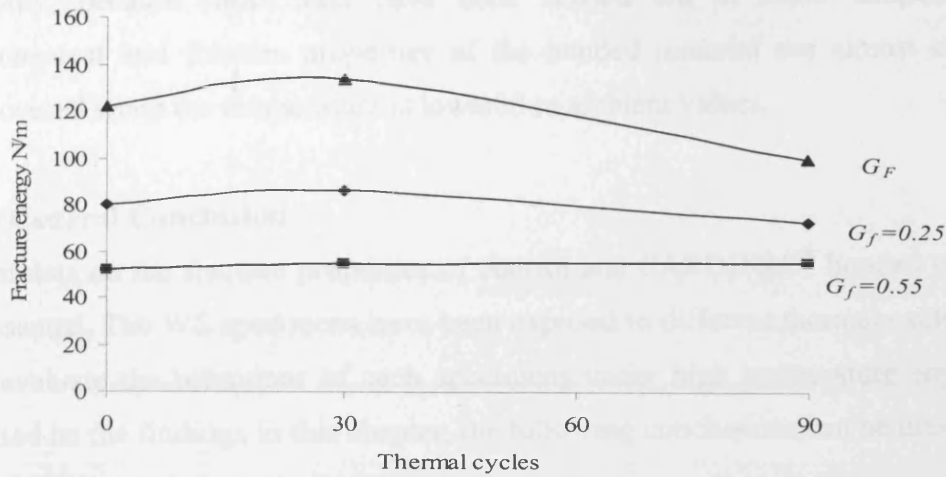


Figure 6.9 The effect of thermal cycling on measured and size-independent fracture energy of CARDIFRC[®]/HSC bonded system.

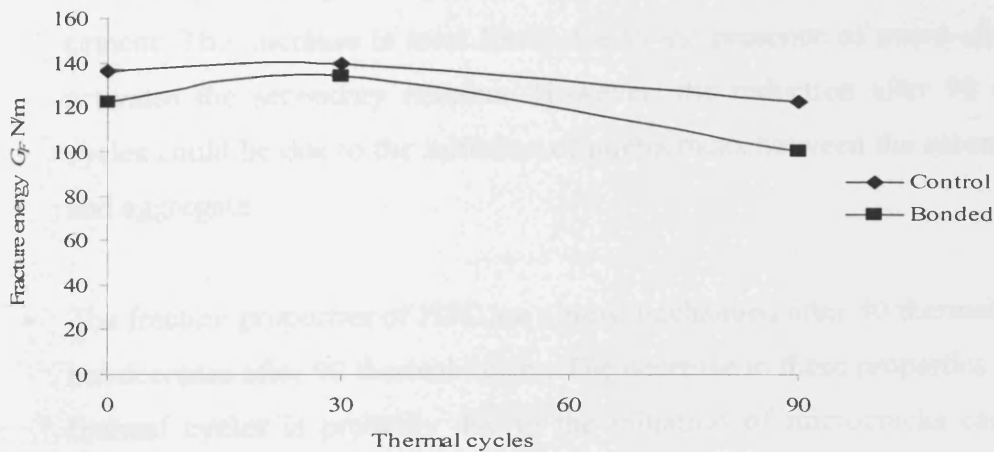


Figure 6.10 The effect of thermal cycling on size-independent fracture energy of control and CARDIFRC[®]/HSC bonded specimens..

A comparison has been made with control specimens exposed to the same thermal cycling as shown in Figure 6.10. As can be seen, the G_F for bonded specimens is less than that of control specimens after 0 and 30 thermal cycles. This indicates that the bonded system is slightly more brittle. Although there was no deterioration visible to the naked eye because of thermal cycling, the decrease in fracture energy after 90 thermal cycles could be associated with internal microcracking in HSC.

Finally, because most tests have been carried out at room temperature, the mechanical and fracture properties of the bonded material are almost completely recovered when the temperature is lowered to ambient values.

6.4 General Conclusion

Test data on the fracture properties of control and CARDIFRC[®] bonded to HSC are presented. The WS specimens have been exposed to different thermal cycles in order to evaluate the behaviour of such specimens under high temperature environment. Based on the findings in this chapter, the following conclusions can be drawn.

- The mechanical properties of HSC are enhanced after 30 thermal cycles, but not so after 90 thermal cycles. The increase in these properties after 30 thermal cycles is probably due to the continued hydration of unhydrated cement. This increase is most likely due to the presence of micro-silica that activates the secondary reaction. However, the reduction after 90 thermal cycles could be due to the initiation of microcracks between the cement paste and aggregate.
- The fracture properties of HSC are almost unchanged after 30 thermal cycles, but decrease after 90 thermal cycles. The decrease in these properties after 90 thermal cycles is probably due to the initiation of microcracks caused by thermal cycling.
- High strength concrete can be successfully repaired with CARDIFRC[®] using direct wet casting and adhesive bonding techniques.
- As has been also observed in Chapter 5 (CARDIFRC[®]/NCS), in order to prevent interfacial fracture, the mating surfaces of both concrete and CARDIFRC[®] must be roughened. A better rough surface of the substrate is created and that leads to higher interface toughness which excessively delay interface crack propagation forcing the crack to kink first before eventually propagating through the concrete.

- To further improve the bond between the adhesive and parent concrete, the thin film of cement paste on the smooth cast surfaces of parent concrete must be removed if they form on the mating surface.
- The measured fracture energy $G_f(\alpha)$ of bonded specimens decreases with increasing notch to depth ratios. The $G_f(\alpha)$ and the size-independent specific fracture energy G_F for control and bonded specimens varies with thermal cycling due to the observed change in the mechanical properties of concrete.
- No visual deterioration or bond degradation was observed after thermal cycling of the bonded specimens attesting to the good thermal compatibility between the concrete and CARDIFRC[®].

Chapter 7

*Retrofitting of reinforced concrete
beams with CARDIFRC[®] after thermal
cycling*

7.1 Introduction

The performance of current techniques for retrofitting concrete structures using externally bonded steel plates or fibre-reinforced plastics (FRP) has been extensively investigated (Ford 1999). Despite the fact that both techniques have gained widespread popularity, there is still concern about their durability and undesirable failure modes, which are due to the mismatch of their tensile strength, stiffness and coefficient of linear thermal expansion with that of concrete structure being retrofitted (Jones, et al., 1988; Hussain et al., 1995; Nanni, 1990; Sen et al., 1999; Sen et al., 2000; Toutanji and Gomez, 1997)

The development of CARDIFRC®, a material compatible with concrete overcomes some of the above mentioned problems associated with the current techniques based on externally bonded steel plates and FRP (fibre-reinforced polymer) (Karihaloo et al., 2002).

The results of Karihaloo et al. (2002) showed that retrofitting of flexural RC members using CARDIFRC® plates on the tension face improves the flexural load carrying capacity and also decreases the crack width and the deflection. Moreover, when the RC beams were retrofitted with three strips (one strip on the tension face and two strips on the sides), the damaged beams were strengthened not only in flexure, but also showed improved shear capacity.

This chapter investigates the feasibility of using CARDIFRC® as a retrofitting material in hot climatic conditions. It is the aim of this chapter to investigate the performance of reinforced concrete beams retrofitted with CARDIFRC® and subjected to thermal cycles between 25° C and 90° C. Each thermal cycle consists of a temperature rise period of 20 min in which the temperature is raised from 25° C to 90° C, a dwell period of 8 hours at 90° C and a cooling period of 16 hours in which the temperature is reduced from 90° C to 25° C (see §.5.6).

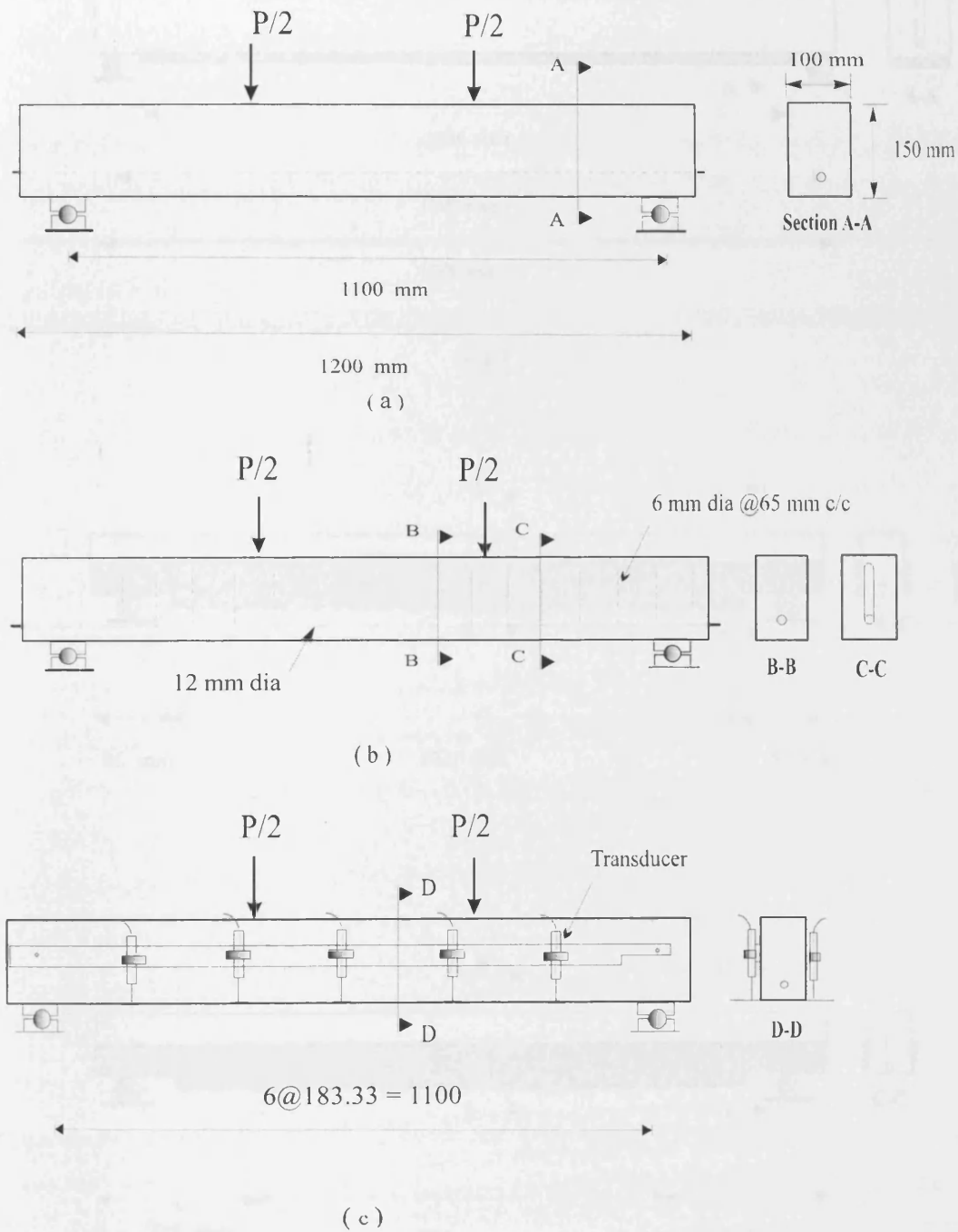
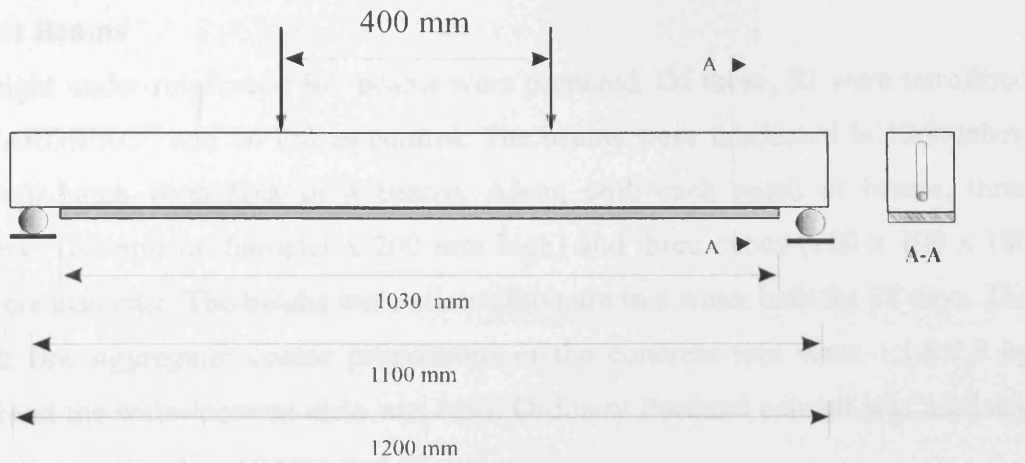
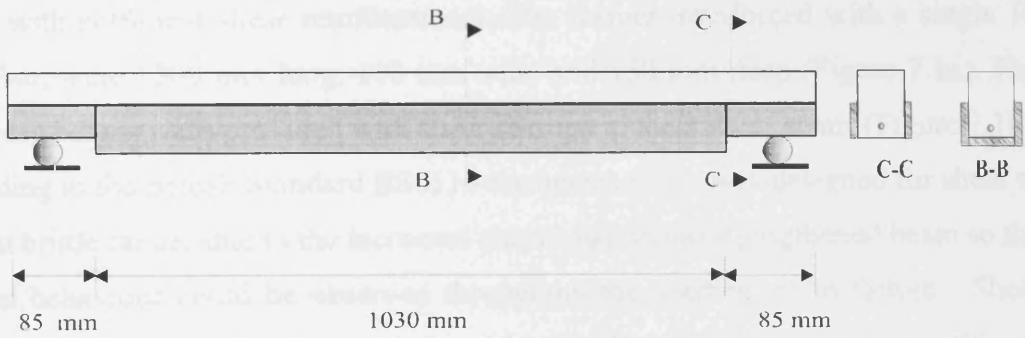


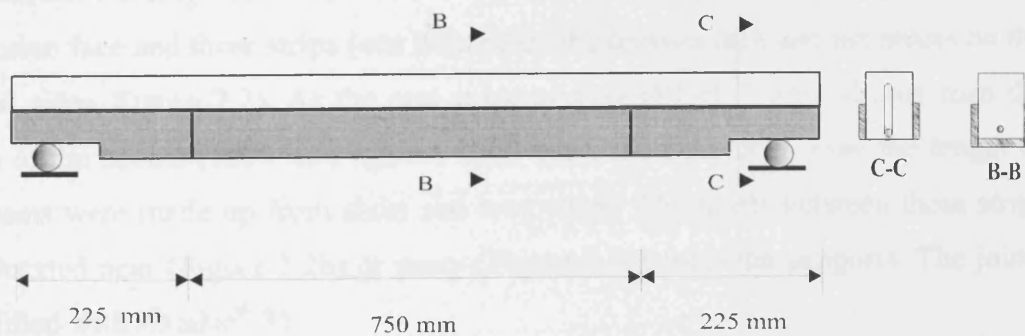
Figure 7.1 Beam details and arrangement of transducers: (a) beam dimensions, internal reinforcement, and load arrangement for beam without shear reinforcement, (b) beam with sufficient shear reinforcement and (c) arrangement of transducers.



(a)



(b)



(c)

Figure 7.2 Configurations of retrofitting: (a) beam retrofitted with one strip on the tension face, (b) beam retrofitted with one strip on the tension face, two long and four short strips on the sides and (c) beam retrofitted with one strip on the tension face, two long and four short strips on the sides.

7.2. Test Beams

Forty-eight under-reinforced RC beams were prepared. Of these, 32 were retrofitted with CARDIFRC[®] and 16 left as control. The beams were fabricated in 12 batches, with each batch consisting of 4 beams. Along with each batch of beams, three cylinders (100 mm in diameter x 200 mm high) and three cubes (100 x 100 x 100 mm) were also cast. The beams were allowed to cure in a water bath for 28 days. The cement: fine aggregate: coarse proportions in the concrete mix were 1:1.8:2.8 by weight and the water/cement ratio was 0.50. Ordinary Portland cement was used and the maximum size of aggregate was 10 mm.

Two types of reinforced concrete beam have been investigated in this study: beams without shear reinforcement, which were designed to fail in flexure or in shear, and beams with sufficient shear reinforcement. The former, reinforced with a single 12 mm rebar, were 1200 mm long, 100 mm wide and 150 mm deep (Figure 7.1a). The remaining beams were provided with shear stirrups in their shear spans (Figure 7.1b). According to the British Standard BS8110 the beams were over-designed for shear to prevent brittle failure due to the increased shear load on the strengthened beam so the flexural behaviour could be observed throughout the loading up to failure. Shear reinforcement consisted of 6 mm deformed bars placed at 65 mm spacing (Figure 7.1b).

Two different configurations of retrofitting were investigated; one strip bonded on the tension face and three strips (one bonded on the tension face and the others on the vertical sides, Figure 7.2). As the cast strips of CARDIFRC[®] were shorter than the length of the beams (1030 mm against 1200 mm), the side strips over the length of the beams were made up from short and long strips. The joints between these strips were located near (Figure 7.2b) or away (Figure 7.2c) from the supports. The joints were filled with sikadur[®] 31.

7.3. Test Procedure

All beams were simply supported on a clear span of 1100 mm and were tested under four-point loading. The loading points were 400 mm apart (Figure 7.1a). The beams were incrementally loaded to failure. Ten transducers (five on each side) were used

to record the deflection of the beams at various points along its span. The transducers were SOLARTON type ACR-25 and DCR-15 LVDTs. An aluminium frame (yoke) was designed with two bars and a total of ten slots, to accommodate the transducers. One bar was placed on each side of the beam at mid-height (Figure 7.1c).

Loading was controlled by the movement of the actuator (stroke control). The rate of loading was 0.01 mm/sec at the beginning of the tests, but it was increased to 0.05 mm/sec when the mid-span deflection exceeded about 3 mm.

7.4. CARDIFRC[®] strips

The retrofit material, CARDIFRC[®] was cast as flat strips in 1030 mm long and 100 mm wide steel moulds with a well oiled base and raised border of height 16 mm (Figure 7.3). The moulds were filled on a non-magnetic vibrating table at 50 Hz frequency and smoothed over with a float. To ensure a uniform thickness (within 1 mm) a glass panel was located on top of the raised border. The strips were left to cure in the moulds for 24 hours at 20° C before de-moulding. The retrofit strips were then hot-cured at 90° C for a further 7 days. In order to avoid large thermal gradients a gradual increase in temperature from ambient temperature to 90° C and vice versa was found necessary. The strips were left in the tank for a total period of 9 days. On the first day the temperature of the water was increased gradually from 20° C to 90° and on the ninth day it was decreased from 90° to 20° C.

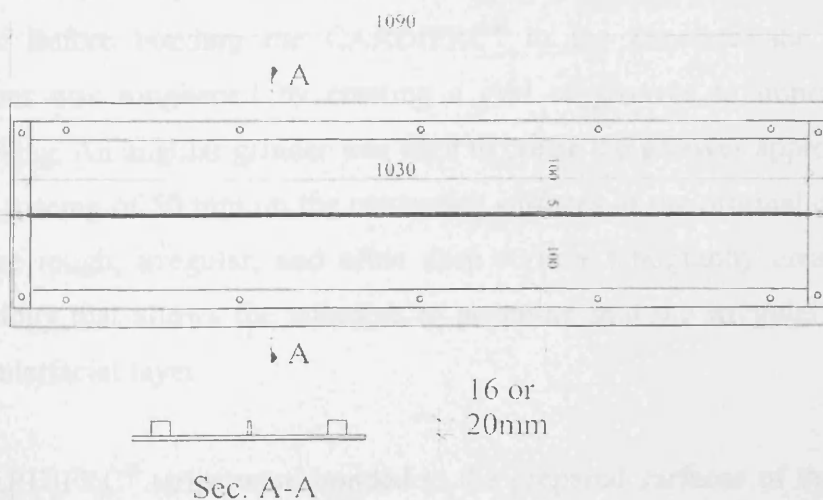


Figure 7.3 Steel moulds for casting two retrofit strips

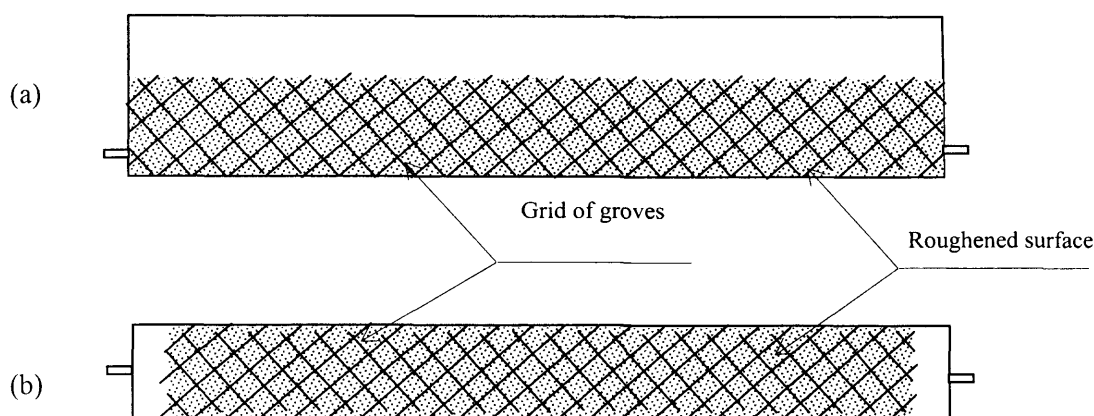


Figure 7.4 Roughened and grooved surface of damaged beams: (a) side face, (b) tension face.

7.5. Mechanical degradation (Pre-cracking)

Strengthening activities are often to be carried out on existing concrete structures that are normally cracked under the service load. To simulate a RC element more realistically, the test beams were pre-cracked at 75 percent of the ultimate strength of the control beams to induce flexural cracking.

7.6. Retrofitting Procedure

Having been loaded to 75 percent of the failure load at which flexural cracks became visible the beams were unloaded and retrofitted using CARDIFRC® strips and epoxy-based adhesive (Sikadur® 31). In order to improve the bond between the repair material and the original concrete, the contact surfaces of concrete were carefully cleaned. Before bonding the CARDIFRC® to the concrete, the surface of the specimens was roughened by creating a grid of grooves to improve mechanical interlocking. An angular grinder was used to create the grooves approximately 3 mm deep at spacing of 50 mm on the contacting surfaces of the original concrete (Figure 7.4). The rough, irregular, and often deep surface topography creates a structural morphology that allows the adhesive to penetrate into the irregularities, forming a strong interfacial layer

The CARDIFRC® strips were bonded to the prepared surfaces of the concrete with the thixotropic epoxy adhesive, Sikadur® 31. The two parts of the adhesive were

thoroughly mixed and applied with a serrated trowel to a uniform thickness of 3 mm. The repair material was placed on the adhesive and evenly pressed. For beams retrofitted with one plate on the tension face (Figure 7.2a) the adhesive was allowed to cure for 24 hours. For the retrofitted beam with more than one plate (Figure 7.2b-c), the beam was turned on its side to which the strip was bonded in the same way, as described above. After another 24 hours, this procedure was repeated on the other side of the damaged beam. It should be mentioned that in practice all three faces of the flexural member can be retrofitted at the same time and G-clamps used to aid the curing of the adhesive.

7.7 Thermal cycling

The test programme comprised of 12 control, 24 retrofitted reinforced concrete beams, six 100 mm cubes for compressive strength and six 100x200 mm cylinders for splitting strength. The specimens were placed in an electrical furnace and heated to the maximum temperature of 90° C from a room temperature of about 25° C. The furnace temperature was controlled automatically using a time-based controller. They were heated in the furnace from room temperature to the maximum temperature in about 20 minutes. The aim was to keep the average heating rate at about 3 degrees per minute, to avoid the risk of the beams being thermally shocked during heating. The maximum temperature was then maintained for another eight hours before the beams were cooled down to the room temperature in a further 16 hours. The above 24-hour heating, hold and cooling period constitutes one thermal cycle. The specimens were exposed to 30 or 90 thermal cycles. After the requisite number of thermal cycles, the beams were tested at room temperature in four-point bending. Due to the limited capacity of the furnace, it was not possible to accommodate all the beams at once. Therefore, the beams were placed in the furnace in sets of 12. The fact that the heat source was located at the bottom of the furnace allowed a temperature gradient to be produced. This gradient was measured using thermal couples.

7.8 Results

Compressive and splitting strengths of the concrete used for making the beams were determined according to BS 1881-116 1983 and BS 1881-117 1983, respectively.

Nine cubes 100 x 100 x 100 mm and nine cylinders having 100 mm diameter and 200 mm long were tested. The compressive and splitting strengths results after 0, 30 and 90 thermal cycling are shown in Tables 7.1. The results reveal a relative increase in the compressive and tensile strength at elevated temperature of 90° C, irrespective of the number of thermal cycles (see also § 5.6).

Table 7.1: Compression and splitting strength results for ordinary concrete

Thermal cycles	F_c (kN)	f_c (MPa)	Average (MPa)	F_t (kN)	f_t (MPa)	Average (MPa)
0	550	55.00	56.10	144	4.58	4.46
	574	57.40		141	4.49	
	560	56.00		136	4.33	
30	651	65.10	66.73	165	5.25	5.10
	676	67.60		164	5.22	
	675	67.50		155	4.49	
90	626	62.60	60.67	151	4.80	4.84
	605	60.50		157.8	5.02	
	589	58.90		148	4.71	

The results of 16 control and 32 retrofitted beams exposed to 0, 30 and 90 thermal cycles are summarized in Tables 7.2, 7.3 and 7.4. The failure mode and ultimate strength of each beam are noted. These results will be discussed next in more detail.

7.8.1 Control beams

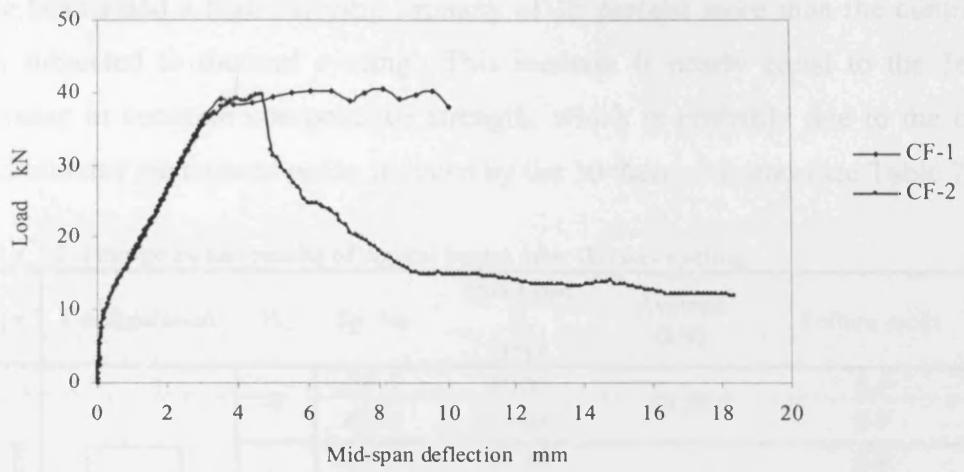
7.8.1.1 Beams without shear reinforcement

The measured load versus deflection curves for control beams with only flexural reinforcement without thermal cycling are shown in Fig 7.5a. The measured test results for beam CF-1 show a reduction in stiffness after the concrete cracked at a load of 11 kN. When the load exceeded 16 kN some hairline flexural cracks appeared on the tension face and the sides of the beam followed by a diagonal shear crack. As the load was increased, these cracks became visible and propagated towards the compressive zone. When the load carrying capacity reached 39 kN and the mid-span deflection exceeded 3.5 mm a slight drop in load was observed. This coincides with the onset of yielding of the steel. Thereafter, due to the strain hardening of steel, the load carrying capacity again increased. As the load was further increased, the shear crack which appeared 150 mm from the support propagated diagonally towards the nearest load point and became the dominant crack. This crack started to open while the other flexural cracks progressively closed. A branch of this crack propagated

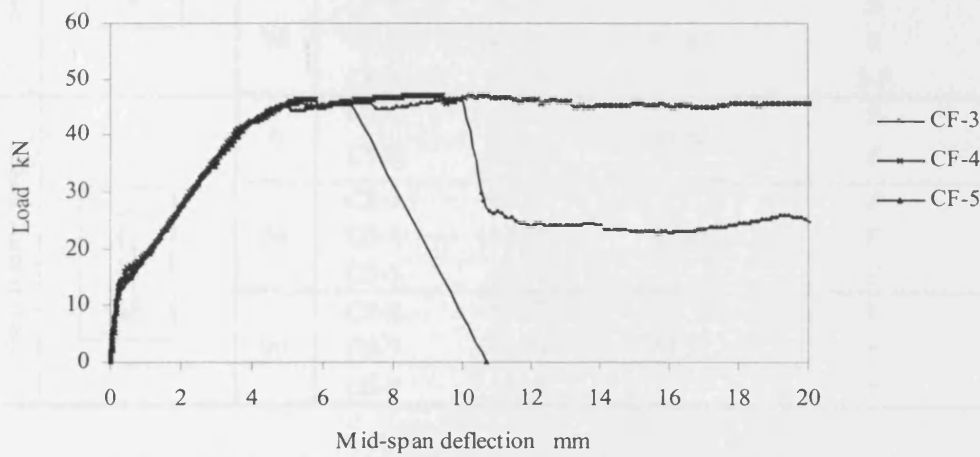
diagonally towards the support and caused a shear failure. In fact, due to the nature of this crack, this failure can be classified as a combination of shear and flexural modes.

Beam CF-2 followed the same trend as beam CF-1 in the initial stages of loading. For this beam flexural cracking started nearly at the same load as that of beam CF-1. At this point, no visible cracks appeared on the surface of the beam. At load of 15 kN some flexural hairline cracks appeared on the tension face and the sides. As the load was increased more cracks became visible on the sides and propagated towards the compression zone with a spacing of about 100-150 mm. As in beam CF-1, a diagonal shear crack started from a location nearly 150 mm from the right support and propagated towards the nearest loading point. This crack started to open while the other flexural cracks progressively closed until the beam failed in a combination of shear and flexural modes.

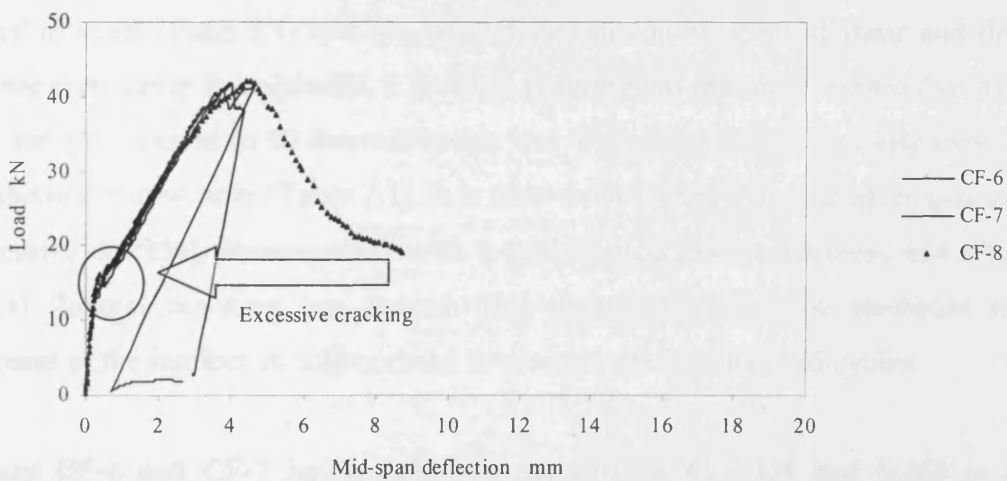
Of the three control beams exposed to 30 thermal cycles, two beams failed in a combination of shear and flexural modes and one in pure flexure. Figure 7.5b shows the load mid-span deflection responses of these beams. The responses shown in the Figure indicate that the stiffness of all three beams begins to reduce at a load of about 15 kN due to the formation of flexural cracks on the tension face. As the load was increased, these cracks propagated on the sides of the beams. This behaviour with nearly a constant stiffness was observed in all three beams. At a load of 45 kN and a mid-span deflection of 4.9 mm this trend changed for beam CF-3 with a local drop in the load displacement response. This is due to the fact that the yielding of steel started at this instance. Because of the strain hardening behaviour of steel, the load carrying capacity was still increasing. When the load carrying capacity reached 46.4 kN and mid-span deflection of 9.4 mm, a sudden drop in the curve was observed. This is due to the expected shear failure. Beam CF-5 also failed in a combination of shear and flexural modes at maximum load carrying capacity of 45.9 kN and mid-span deflection of 6 mm, whereas beam CF-4 failed in a flexural ductile manner with a maximum load carrying capacity of 47.20 kN. As a result of exposure to the 30 thermal cycling, there is a definite trend of an increase in the beam capacity.



(a)



(b)

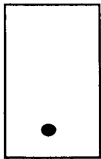
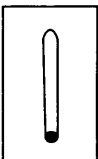


(c)

Figure 7.5: Load-Deflection responses of control beams without shear reinforcement, after: (a) 0 thermal cycles, (b) 30 thermal cycles, and (c) 90 thermal cycles.

The beams had a load carrying capacity of 15 percent more than the control beams not subjected to thermal cycling.. This increase is nearly equal to the 16 percent increase in concrete compressive strength, which is probably due to the continued hydration of the cement paste, induced by the 30 thermal cycles (see Table 7.1).

Table 7.2: Four-point test results of control beams after thermal cycling.

Type	Configuration	TC	Sp. No	Max Load P (kN)	Average (kN)	Failure mode
Beams without shear reinforcement		0	CF-1	40.20	39.92	S-F
			CF-2	39.64		S-F
		30	CF-3	47.39	46.85	S-F
			CF-4	47.24		F
			CF-5	45.92		S-F
		90	CF-6	41.4	41.62	S
			CF-7	41.35		S
			CF-8	42.10		S-F
Beams with sufficient shear reinforcement		0	CS-1	45.10	45.64	F
			CS-2	46.18		F
		30	CS-3	47.78	47.65	F
			CS-4	48.80		F
			CS-5	46.59		F
		90	CS-6	47.77	47.37	F
			CS-7	47.79		F
			CS-8	47.55		F

The typical load-deflection curves of beams exposed to 90 thermal cycles are presented in Figure 7.5c. The test results show that of the three beams, two beams failed in shear (Plate 7.1) and one beam failed in combination of shear and flexure. Before comparing these results, it is worth pointing out that the compressive strength of concrete exposed to 90 thermal cycles was lower than that of concrete exposed to 30 thermal cycles only (Table 7.1). It is clear from Figure 7.5c that all beams exhibit excessive cracking accompanied with a further reduction in stiffness just after the initial flexural cracking has started. This phenomenon can be attributed to the increase in the number of microcracks in concrete after 90 thermal cycles.

Beams CF-6 and CF-7 had an ultimate capacity of 41.4 kN and failed in shear whereas beam CF-8 had an ultimate capacity of 42 kN and failed in a combination of shear and flexure. By comparing these results with those obtained from the test

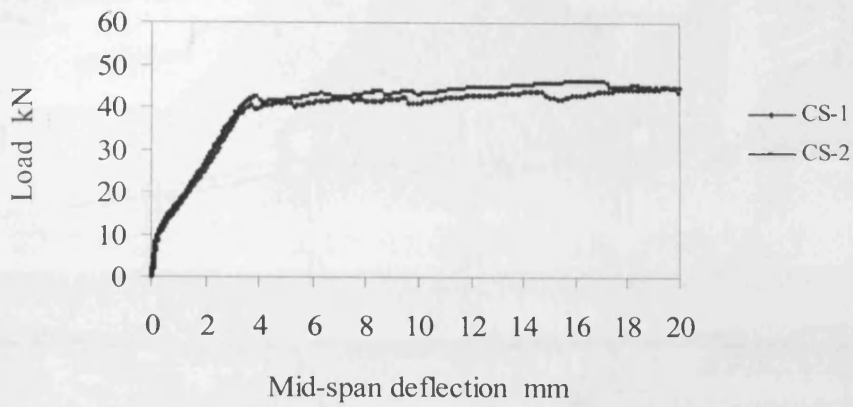
beams exposed to 30 thermal cycles, it can be seen that there is a 9 percent reduction in ultimate capacity.

This is probably due to the weakening of the surface forces (Van der Waals forces) between the gel particles, or due to the stresses generated at the interface between the aggregate and hardened cement paste. These stresses induce damage through microcracks. Investigations have shown that microcracks exist at the interface between coarse aggregate and cement paste even prior to the application of the load on concrete. In the case of concrete subjected to thermal cycles, the density of microcracks further increases.

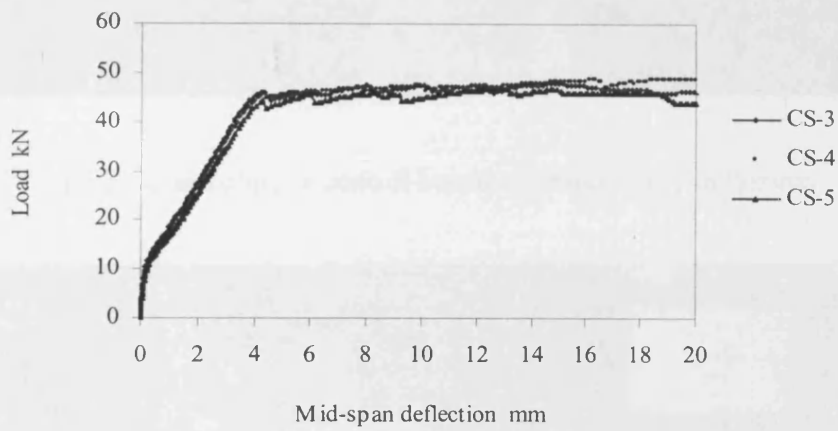
7.8.1.2. Beams with sufficient shear reinforcement

Figure 7.6a shows the load deflection response of two control beams with full shear reinforcement after zero thermal cycles. The test results show that both beams CS-1 and CS-2 exhibit the same behaviour. At about 11 kN and when the mid-span deflection has exceeded 0.40 mm, the stiffness of the beams was substantially reduced. At this instance no cracks were visible to the naked eye. Thereafter flexural hairline cracks became visible on the tension face and propagated vertically along the sides. These cracks opened up gradually and formed a well-distributed pattern within the loading span. As the load increased further, these cracks propagated towards the compressive zone. At about 41 kN, and a mid-span deflection of 4 mm, a slight drop in load carrying capacity was observed. Due to the strain hardening of the steel, the load carrying capacity increased slightly. Thereafter the beams failed with crushing of concrete between the two applied load points (Plate 7.2). The maximum load carrying capacity of beams CS-1 and CS-2 was 45.1 kN and 46.18 kN, respectively.

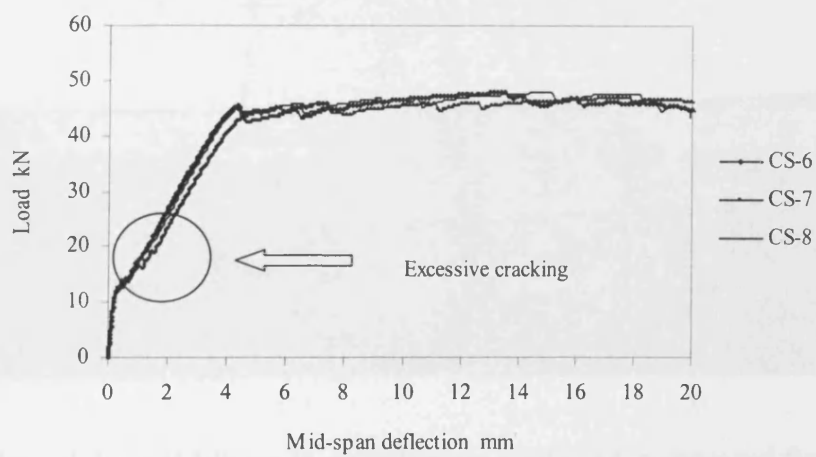
Figure 7.6b shows the typical behaviour of three beams exposed to 30 thermal cycles. All three beams exhibited a reduction in stiffness just after the flexural cracking started at a load of 12 kN. Thereafter, beams CS-3 and CS-4 carried more load with nearly a constant stiffness until the steel yielded at load of 45 kN. The load carrying capacity of the beams increased slightly until the compression failure of concrete. The behaviour of beam CS-5 is quite similar but with a slightly lower



(a)



(b)



(c)

Figure 7.6: Load-Deflection responses of control beams with shear reinforcement, after: (a) 0 thermal cycles, (b) 30 thermal cycles, and (c) 90 thermal cycles.

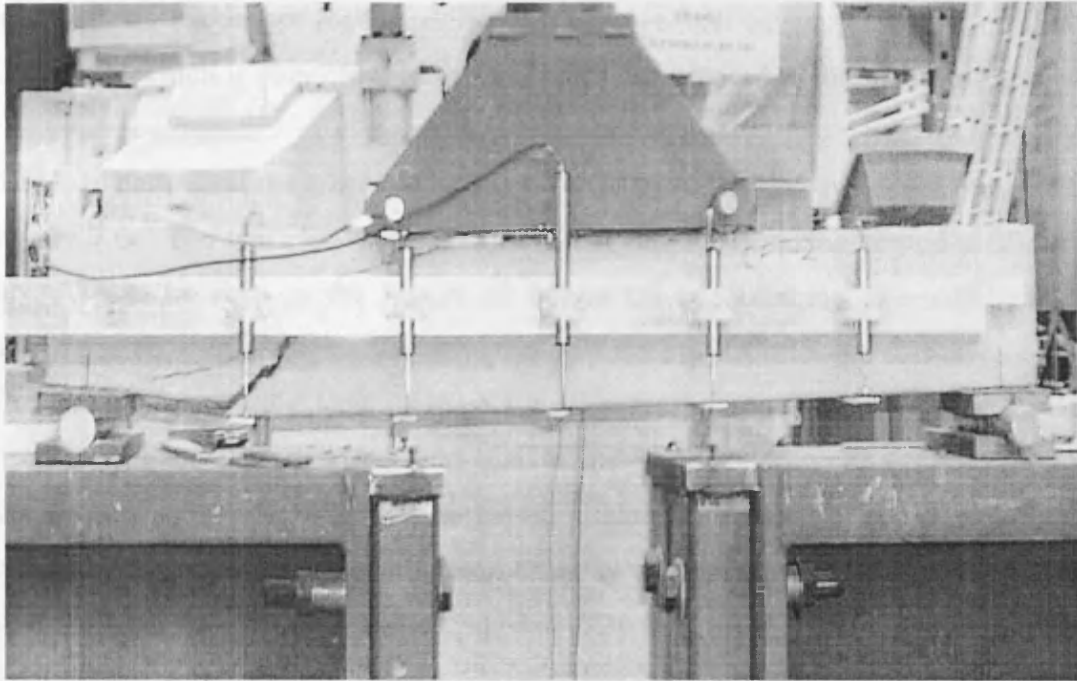


Plate 7.1: Typical shear failure in control beams reinforced only in flexure.

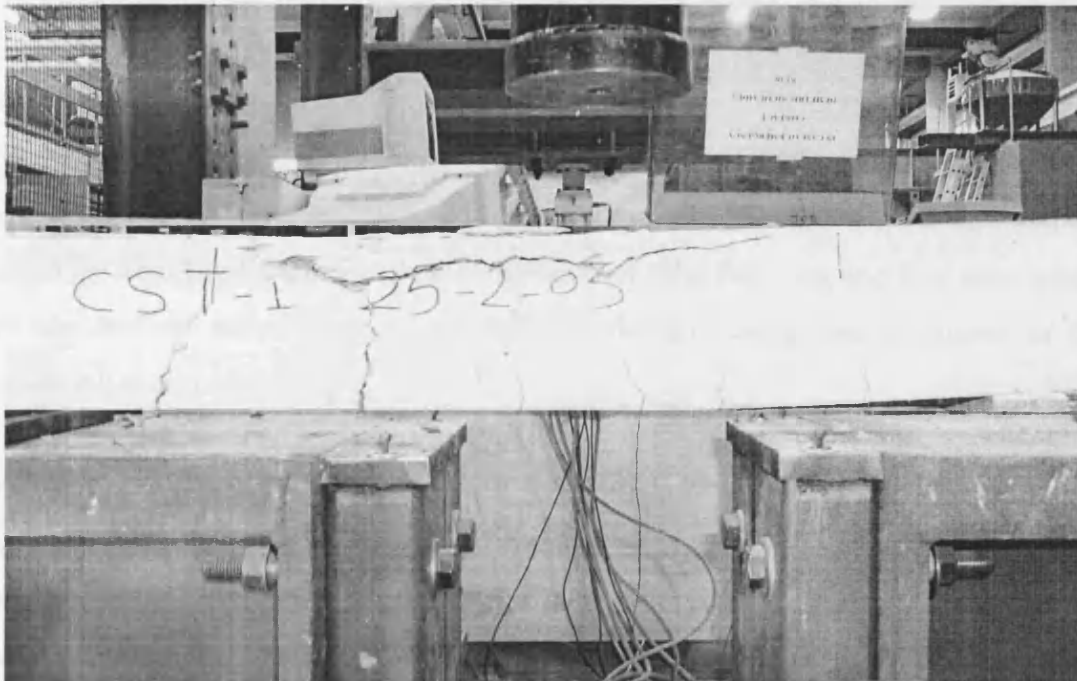


Plate 7.2: Typical flexural failures in control beams reinforced in shear and flexure.

stiffness and maximum load capacity. The average load carrying capacity of this set is 47.7 kN which is very close to that of beams not exposed to thermal cycling.

The load deflection responses of beams exposed to 90 thermal cycles are presented in Figure 7.6c. The test results reveal that initial flexural cracking started at about 12 kN. As can be seen in the Figure all beams are experiencing excessive cracking accompanied with a substantial reduction in stiffness just after the formation of first flexural crack. As the load increased, further cracks appeared on the sides of the beams until a slight drop in load due to the steel yielding. Thereafter, the load carrying capacity of the beams increased slightly until the compression failure of concrete. The average maximum load capacity of these beams is 47.37 kN which is slightly lower than those of beams exposed to 30 thermal cycles.

It appears that thermal cycling has very little effect on the load carrying capacity of control beams reinforced in flexure and shear. The shear reinforcement seems to counteract the reduction expected after 90 thermal cycles due to the reduction in compressive strength (Table 7.1).

7.8.2 Retrofitted beams

The results of 32 retrofitted beams (16 beams retrofitted on the tension face and the remainder retrofitted with one plate on the tension face, two long and four short plates on the vertical sides) exposed to different thermal cycles are discussed in the following sections.

7.8.2.1 Pre-cracking

As mentioned earlier, of the 48 beams, 32 were pre-cracked to approximately 75% of the failure load of control beams (32kN) to induce flexural cracking. These cracks were well distributed and appeared in the middle third of the beams when the load exceeded 15kN. Figure 7.7 shows the typical load-deflection response of the beams during pre-loading and unloading. It can be seen that pre-loading causes a permanent mid-span deflection of about 0.57mm in the beams.

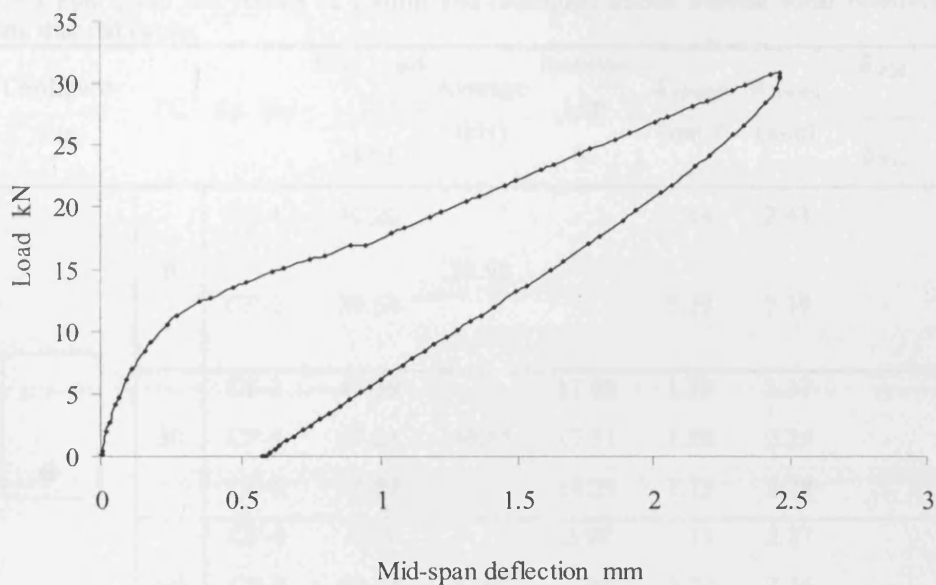


Figure 7.7 Load-Deflection response of beams during pre-loading and unloading.

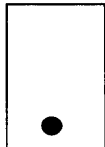
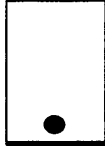

7.8.2.2 Beams without shear reinforcement

For the evaluation of the performance of retrofitted beams reinforced only in flexure after thermal cycling, parameters such as maximum load, failure mode and deflection of the beam were considered. The results are presented in Table 7.3.

7.8.2.2.1 Beams retrofitted with one strip on the tension face

Load-deflection responses for typical beams retrofitted with one strip on the tension face after 0 thermal cycles are shown in Figure 7.8a. The responses shown in the Figure indicate that beam RF-1 failed in flexure with a failure load of 47.39 kN. As the applied load to this beam reached 26 kN, the pre-existing hairline induced by pre-loading cracks became visible. As the load increased further, these cracks propagated towards the compressive zone. When the load reached about 40 kN, one of these cracks started penetrating the tension strip. At this stage the bridging action of the tension plate was clearly visible. This crack started opening and became the dominant crack while the other cracks progressively closed. While the beam was carrying more load with a reduced stiffness, some unusual cracks with different directions started branching from the dominant crack. At about 47.46 kN this beam failed in flexure without any shear distress.

Table 7.3 Four-point test results of control and retrofitted beams without shear reinforcement after different thermal cycles

Configurations	TC	Sp. No	Max Load		Average	Increase in P %	$\delta_{(P=20)}$ (mm)	$\delta_{(P=30)}$ (mm)	δ_{P20}	δ_{P30}	Failure mode	
			P (kN)	P (kN)					δ_{P20}	δ_{P30}		
Control 	0	CF-1	40.20				1.34	2.43	-	-	S-F	
		CF-2	39.64		39.92		1.29	2.39	-	-	S-F	
	30	CF-3	47.39			17.88	1.25	2.37	-	-	S-F	
		CF-4	47.24	46.85		17.51	1.20	2.29	-	-	F	
		CF-5	45.92			14.23	1.13	2.28	-	-	S-F	
	90	CF-6	41.4			2.99	1.13	2.27	-	-	S	
		CF-7	41.35	41.62		2.86	1.25	2.34	-	-	S	
		CF-8	42.10			4.73	1.04	2.24	-	-	S-F	
Retrofitted 	0	RF-1	47.39		49.49	17.89	0.34	0.61	0.26	0.25	F	
		RF-2	51.6			28.36	0.39	0.77	0.30	0.32	S	
	30	RF-3	65.67			40.17	0.33	0.54	0.28	0.23	S	
		RF-4	58.27	62.88		28.92	0.34	0.73	0.28	0.32	F	
		RF-5	64.7			38.10	0.34	0.70	0.28	0.30	D	
	90	RF-6	55.00			32.16	0.28	0.59	0.24	0.26	F	
		RF-7	59.30	56.37		42.49	0.32	0.63	0.27	0.27	F	
		RF-8	54.80			31.68	0.33	0.57	0.28	0.25	S	
	Retrofitted 	0	RF-9	76.00		75.10	89.05	0.12	0.22	0.09	0.09	F
			RF-10	74.20			84.57	0.18	0.33	0.14	0.14	S
		30	RF-11	93.14			98.80	0.12	0.19	0.10	0.08	F
			RF-12	87.40	88.92		86.55	0.22	0.37	0.18	0.16	F
			RF-13	86.23			84.06	0.2	0.31	0.17	0.13	F
		90	RF-14	88.87			113.54	0.25	0.39	0.21	0.17	D
			RF-15	87.78	86.94		110.93	0.14	0.21	0.12	0.10	F
			RF-16	84.32			102.61	0.24	0.38	0.20	0.16	F

TC: Thermal cycles, S: Shear Failure, F: Flexural failure, S-F: Shear and flexural failure, D: Debonding

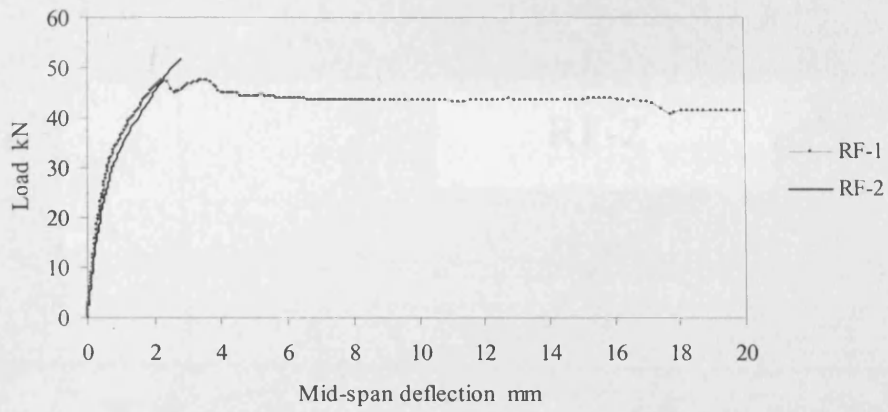
As can be seen in the Figure 7.8a, the behaviour of Beam RF-2 is quite similar to that of beam RF-1 at the initial loading stages. As the load was increased, the hairline cracks resulting from pre-loading started to appear on the sides of the beam. As the load increased further, these cracks became visible. During these stages, the retrofitted beam was under a constant stiffness until the load reached 29 kN at which

the stiffness slightly reduced. At about 42 kN one of the pre-existed cracks situated nearly at the mid-span started to penetrate into the tension strip. At 49 kN a shear crack emanated from the left support, progressed diagonally towards the left loading point causing a shear failure at 51.6 kN. This shear failure happened in a brittle manner (Plate 7.3).

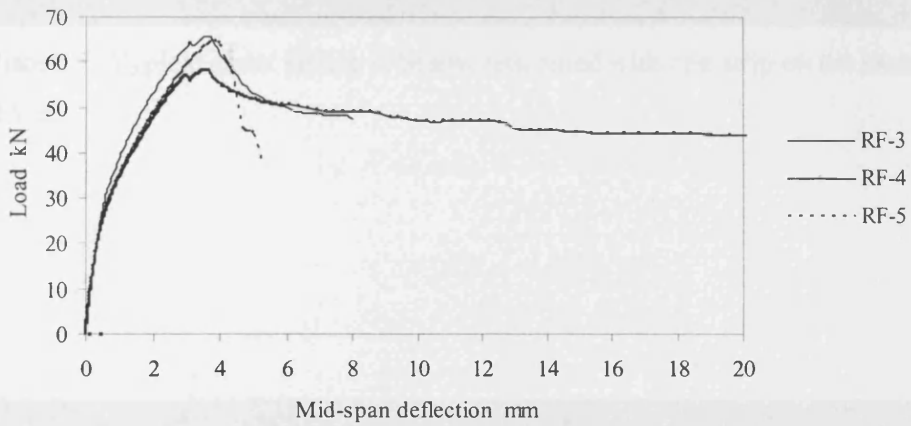
Both beams RF-1 and RF-2 exhibit greater load carrying capacity and stiffness than do the control beams.

As mentioned earlier, three pre-cracked beams were retrofitted on the tension face and exposed to 30 thermal cycles. Of these, beam RF-3 failed in combination of shear and flexure and beam RF-4 in flexure and the third beam RF-5 failed due to interfacial debonding (Plate 7.4). Figure 7.8b shows the load-deflection response of these beams.

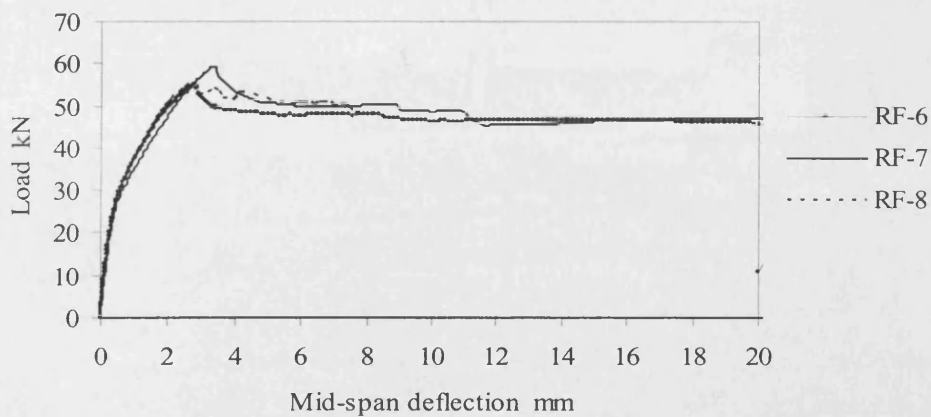
When the load was first applied to beam RF-3, the hairline cracks induced by pre-cracking started to become visible. As the beam carried more loads these cracks became more visible and propagated towards the compression fibre of the beams (between the two loading points). At about 50 kN and mid-span deflection of 1.9 mm one crack started penetrating the tension strip. In fact, this crack is not situated exactly in the mid-span of the beam as the same cracks observed in the previous beams. While the beam carries more load with a reduced stiffness a local drop in load was observed at about 64 kN and mid-span deflection of 3.3 mm. This drop in load was mainly influenced by a shear crack which had originated 150 mm from the support. As can be seen in the Figure, this drop was partially recovered. At 65.67 kN and mid-span deflection of 3.69 mm the load-deflection curve started to descend gently. Thereafter, the shear crack started opening up and propagated diagonally towards the nearest loading point. This crack also penetrated downwards into the retrofit strip. A branch of this crack propagated diagonally towards the support. This beam failed in a combination of shear and flexure with a failure load of 65.67 kN.



(a)



(b)



(c)

Figure 7.8: Load-Deflection responses of beams without shear reinforcement retrofitted with one strip on the tension face, after: (a) 0 thermal cycles, (b) 30 thermal cycles, and (c) 90 thermal cycles.

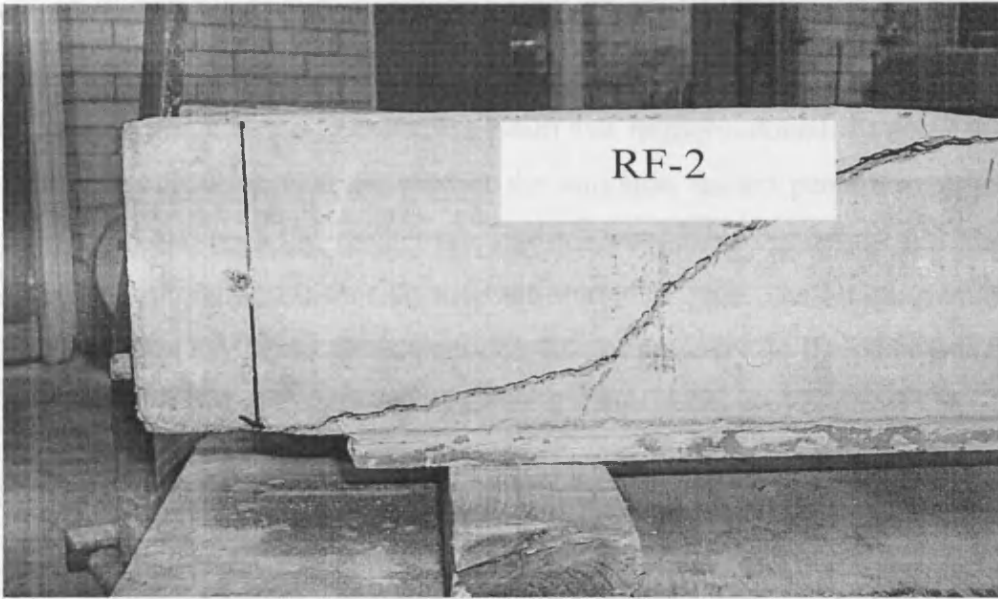


Plate 7.3: Typical shear failure in beams retrofitted with one strip on the tension face.

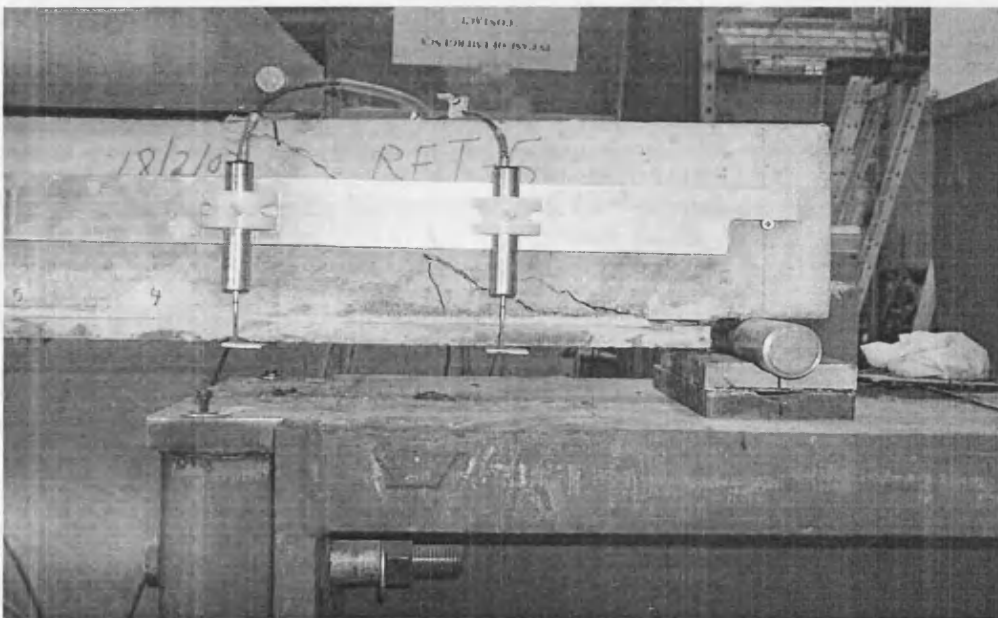


Plate 7.4: Debonding at the end of the strip.

Figure 7.8b shows the load versus mid-span deflection response of beam RF-4. The response of this beam was very close to that of beam RF-3 until the load reached about 32 kN at which the stiffness of the beam was further reduced. At about 40 kN one of the pre-existing cracks situated at the mid-span started penetrating into the tension strip. At about 48 kN another crack which was situated under the left loading point also penetrated into the tension strip and started to open. The bridging action of steel fibres to transfer tensile force from one face of the crack to the other was quite clear. This beam failed in pure ductile flexure at a maximum load of 58.27 kN.

Beam RF-5 exhibited the same behaviour in the early stages of loading as beam RF-4. However, after about 45 kN, a diagonal shear crack emanated 160 mm from the right support and propagated diagonally towards the right load point. A branch of this crack penetrated into the tension strip. As the load further increased, another crack branched from the main diagonal shear crack and propagated diagonally close to the interface. This beam failed at 64.7 kN due to interfacial failure at the strip-adhesive interface situated at the end of the retrofit strip. Visual investigation revealed that this debonding (see Plate 7.4) occurred due to poor bonding with a failure load of at 64.7 kN.

Figure 7.8c shows the load-deflection responses of three retrofitted beams exposed to 90 thermal cycles. As can be seen in the Figure, beam RF-6 failed in pure flexure with the opening of a pre-existing crack after it had penetrated into the retrofit strip. No sign of shear cracking or drop in the load was observed in this beam. When the load reached the maximum 55 kN and the mid-span deflection was 2.8 mm, the load-displacement curve descended gently and the beam exhibited a plastic behaviour with the yielding of steel.

The behaviour of beam RF-7 was very similar to that of RF-6. The beam failed in pure flexure with a maximum failure load of 59.30. Contrary to the very ductile failure of beams RF-6 and RF-7, beam RF-8 failed in shear at a failure load of 54.80 kN.

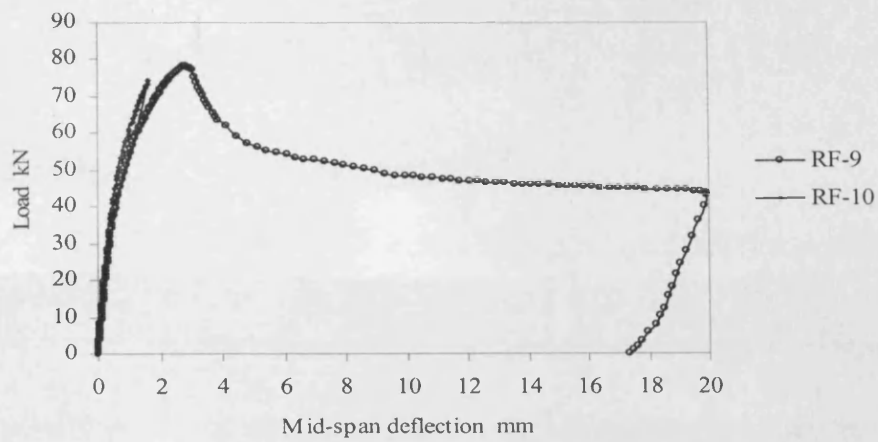
7.8.2.2.2 Beams retrofitted with three long and four short strips

As mentioned before, this configuration of retrofitting consisted of one long strip bonded on the tension face, two continuous and four short strips on the sides. The use of long and short strips to cover the sides of the beams was necessitated by the limited length of the strips (1030 mm) which was shorter than the length of the beams. Eight beams were tested after different thermal cycling. Of these, two beams were tested after exposure to non-thermal cycling, three after 30 thermal cycles and the remaining three after 90 thermal cycles.

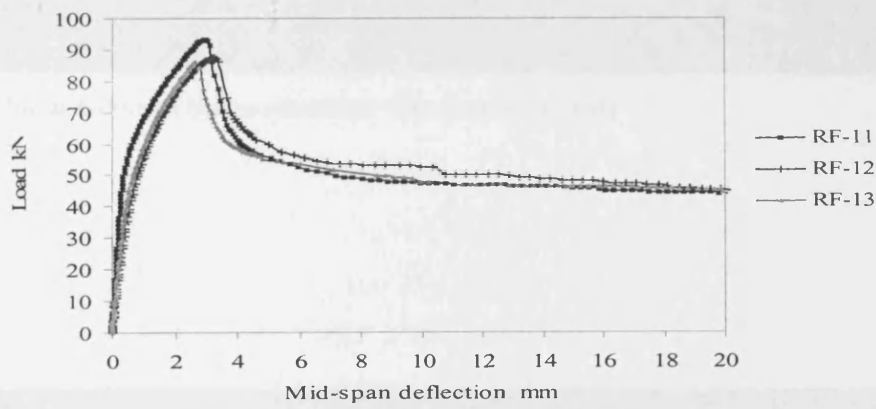
Load deflection responses of beams retrofitted on the tension face and the sides after 0 thermal cycles are shown in Figure 7.9a. A preliminary test on a beam RF-10 retrofitted with three continuous long strips (one on the tension face and two on the sides, the side strips did not extend the full length of the beam) resulted in a sudden shear failure. The reason for this was that the flexural strength at the mid-span of the beam exceeded the shear strength of the beam near the supports (see Plate 7.5). Due to the over strengthening of the mid-span, the weakest point of the beam shifted to the supports, where the shear stresses are considerable and there is no external strip to improve the shear capacity of the section. Therefore, a shear crack formed in this region, which led to very brittle failure.

Although the failure surface passed through the two side retrofit strips, no delamination of the strips occurred confirming the very good bond between the retrofit strip and concrete beam

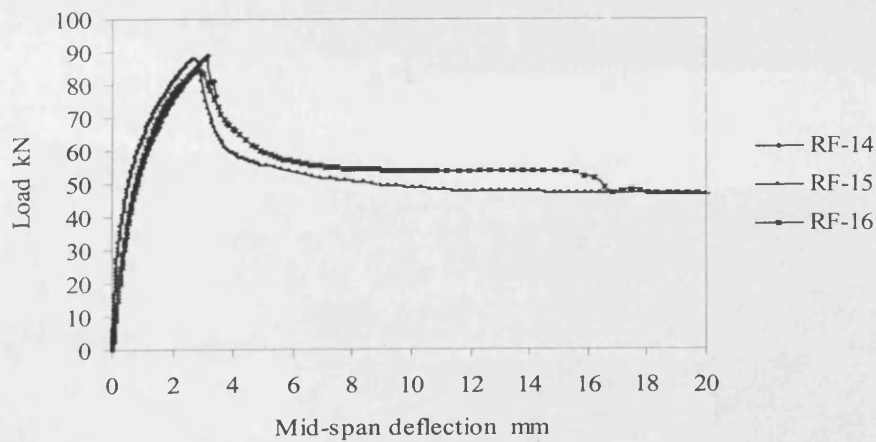
To prevent such shear failure, a system of repair with three continuous strips and four short strips was adopted. As can be seen in Figure 7.9a, the behaviour of the other beam RF-9 was as expected; in the first stage of loading the beam exhibited a linear elastic behaviour. Then, the load-deflection response deviated gradually from the initial straight line. The first crack appeared in the middle third of the tension strip (Plate 7.6), propagated through the side strips and opened up gradually until the load reached the maximum and the load-deflection curve started to descend gently. As can be seen from Table 7.3 the average failure load increased from 40 kN to 75.1 kN for beams kept at room temperature.



(a)



(b)



(c)

Figure 7.9 Load-Deflection responses of beams retrofitted with three long and four short strips strip, after: (a) 0 thermal cycles, (b) 30 thermal cycles, and (c) 90 thermal cycles.

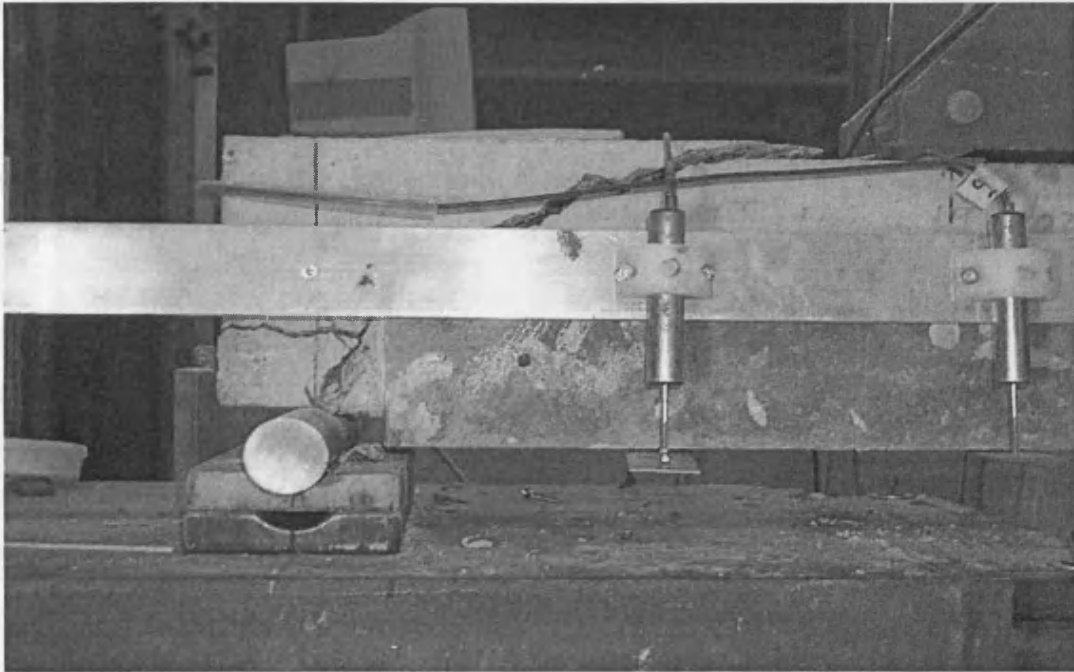


Plate 7.5: Shear failure of beams retrofitted with three plates only

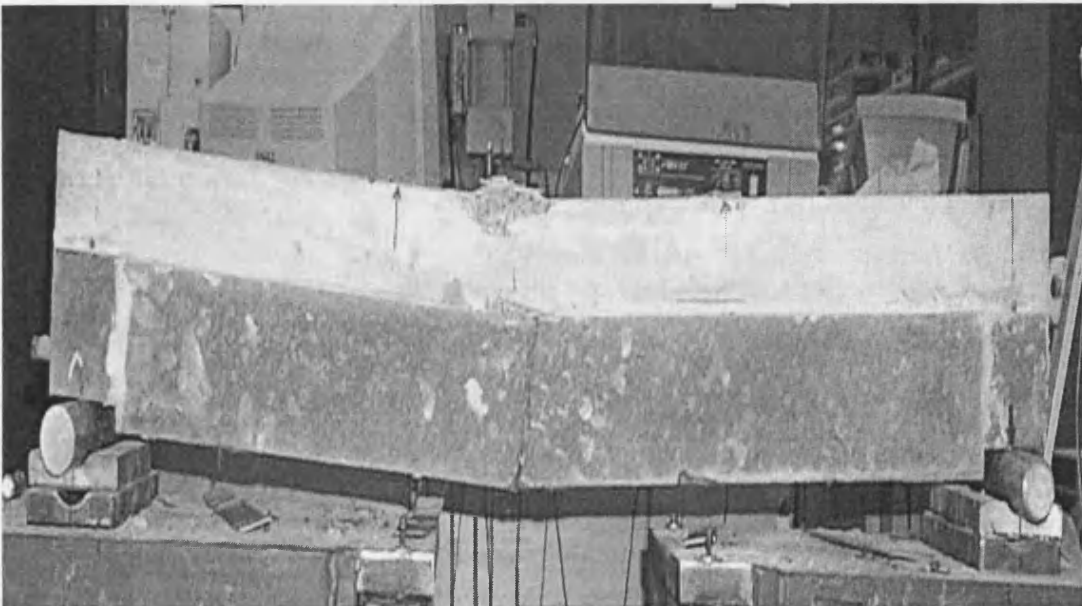


Plate 7.6: Typical flexural failure of beams retrofitted with three long and four short strips

Figure 7.9b shows the load-deflection responses of three retrofitted beams exposed to 30 thermal cycles. As can be seen in the Figure, all beams exhibited a linear elastic-plastic behaviour up to 50 kN, followed by a deviation in the load-deflection curve due to the opening of the pre-existing cracks. In fact, these cracks could not be seen because the side strip blocked the view of concrete beam sides.

As expected, the first crack appeared in the middle third of the tension strip. Then it propagated vertically in the side strips and opened up gradually until the load reached the maximum, thereafter, the load-displacement curve started to descend gently. Finally, the beam failed in pure flexure. As can be seen from Table 7.3 the average failure load increased from 46.85 kN to 88.92 kN for beams exposed to 30 thermal cycles. It can also be concluded that the load carrying capacity of retrofitted beams exposed to 30 thermal cycles increased by 18.40 percent over the room temperature value.

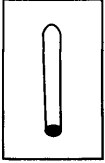
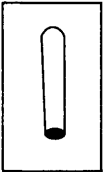
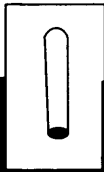
Figure 7.6c shows the load-deflection responses of three retrofitted beams exposed to 90 thermal cycles. As shown in the Figure, the response of these beams is very similar to those exposed to 30 thermal cycles in the early stages of loading. Of the three retrofitted beams, two beams RF-15 and RF-16 failed in pure flexure with a maximum failure load of 87.78 kN and 84.32 kN respectively. The beam RF-14 however failed at a maximum load of 88.87 due to weak bonding of the side short strip at the support.

As can be seen from Table 7.3 after 90 thermal cycles the average failure load increases from 41.62 kN for the corresponding control beams to 86.94 kN, giving a total increase of 108.9 per cent. Furthermore, After 90 thermal cycles the average load carrying capacity increased by 15.76 percent compared to those of unheated beams.

7.8.2.3 Beams with sufficient shear reinforcement

For the evaluation of the performance of retrofitted beams reinforced in shear and flexure after thermal cycling, parameters such as maximum load, failure mode and deflection of the beam were considered. The results are presented in Table 7.4.

Table 7.4 Four-point test results of control and retrofitted beams with sufficient shear reinforcement after different thermal cycles

Configurations	TC	Sp. No	Max Load		Increase in P %	$\delta_{(P=20)}$ (mm)	$\delta_{(P=30)}$ (mm)	δ_{P20} ----- δ_{P20}	δ_{P30} ----- δ_{P30}	Failure mode	
			P (kN)	Ave. (kN)							
Control 	0	CS-1	45.10		-	1.38	2.40	-	-	F	
		CS-2	46.18	45.64	-	1.34	2.32	-	-	F	
	30	CS-3	47.78		4.69	1.18	2.30	-	-	F	
		CS-4	48.80	47.65	6.46	1.24	2.29	-	-	F	
		CS-5	46.59		2.08	1.41	2.47	-	-	F	
	90	CS-6	47.77		4.67	1.30	2.31	-	-	F	
		CS-7	47.79	47.37	2.52	1.67	2.72	-	-	F	
		CS-8	47.55		4.18	1.39	2.45	-	-	F	
Retrofitted  	0	RS-1	49.80	51.50	9.11	0.32	0.74	0.24	0.31	F	
		RS-2	53.20		16.57	0.35	0.64	0.26	0.27	F	
	30	RS-3	57.57		20.81	0.33	0.65	0.26	0.28	F	
		RS-4	55.24	57.73	15.92	0.32	0.59	0.25	0.25	F	
		RS-5	60.40		22.28	0.34	0.63	0.27	0.25	F	
	90	RS-6	53.38		12.69	0.43	0.66	0.30	0.26	F	
		RS-7	48.82	52.06	3.06	0.51	0.83	0.35	0.33	F	
		RS-8	53.97		13.93	0.35	0.73	0.23	0.29	F	
	0	RS-9	74.00	76.00	62.14	0.16	0.28	0.12	0.12	F	
		RS-10	78.19		71.32	0.24	0.39	0.18	0.17	F	
		30	RS-11	92.68		94.49	0.14	0.29	0.11	0.12	F
			RS-12	89.30	90.18	88.52	0.22	0.38	0.17	0.16	F
			RS-13	88.55		85.82	0.25	0.42	0.20	0.18	F
		90	RS-14	79.48		67.68	0.23	0.44	0.16	0.18	F
			RS-15	87.60	85.22	84.93	0.26	0.41	0.18	0.60	F
			RS-16	88.60		85.93	0.20	0.32	0.12	0.13	S

7.8.2.3.1 Beams retrofitted with one strip on the tension face

This configuration of retrofitting is shown in Figure 7.2a. Eight beams were tested after different thermal cycling. Of these, two beams were tested after exposure to no thermal cycling, three after 30 thermal cycles and the remaining three after 90 thermal cycles.

Figure 7.10a shows the load-deflection responses of two beams retrofitted with one strip on the tension face and exposed to non-thermal cycles. As shown in the Figure, both beams exhibited the same behaviour in the early stages of loading. At about 40 kN a tiny shear crack emanated from the left support of beam RS-1 and propagated towards the nearest loading point. This crack caused a local drop in load. The beam however, recovered its load carrying capacity immediately but at a slightly reduced stiffness.

The flexural failures observed for these two beams were generally characterized by a single flexural crack occurring in the middle third of the beam extending upwards to the concrete top fibre between the load points and downwards through the retrofit material (Plate 7.7). Both beams failed at loads higher than the average failure load of control beams. As can be seen from Table 7.4 the average failure load increased from 45.64 kN to 51.50 kN.

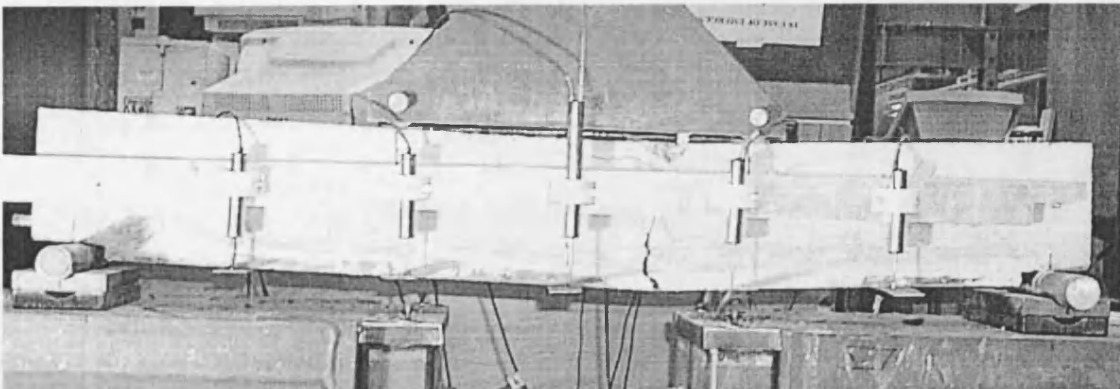
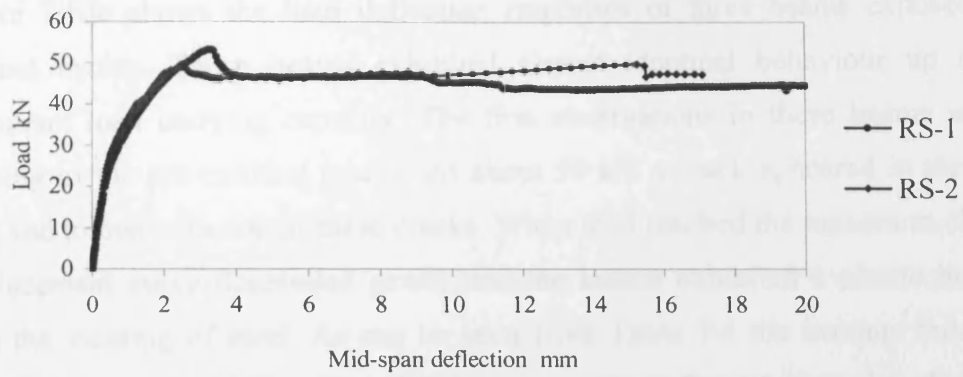
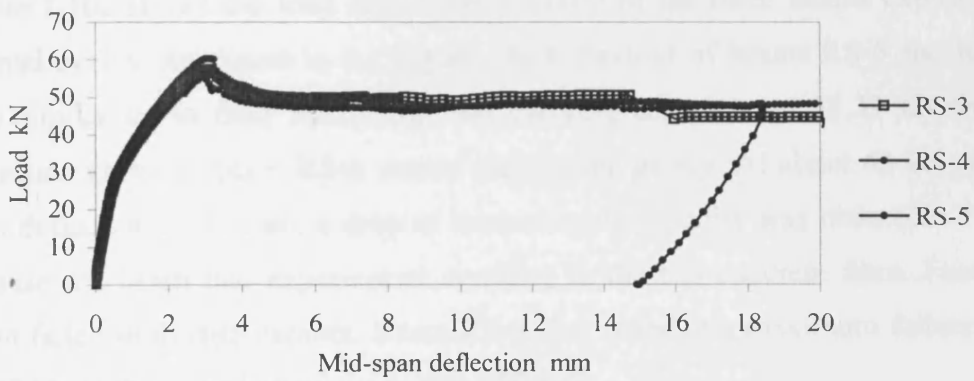


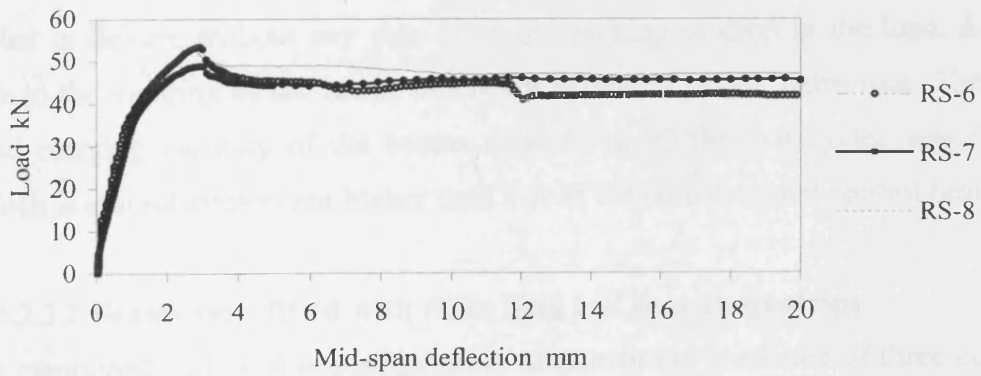
Plate 7.7 Typical flexural failure of beams reinforced in shear and flexure and retrofitted with one strip on the tension face.



(a)



(b)



(c)

Figure 7.10: Load-Deflection responses of beams retrofitted with one strip on the tension face, after: (a) 0 thermal cycles, (b) 30 thermal cycles and (c) 90 thermal cycles.

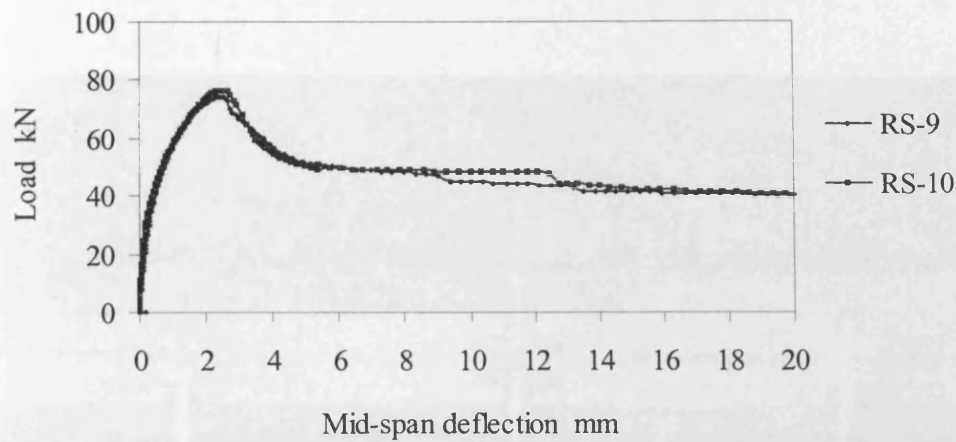
Figure 7.10b shows the load deflection responses of three beams exposed to 30 thermal cycles. These beams exhibited almost identical behaviour up to their maximum load carrying capacity. The first observations in these beams were the opening of the pre-existing cracks. At about 50 kN a crack appeared in the retrofit strip and joined with one of these cracks. When load reached the maximum, the load-displacement curve descended gently and the beams exhibited a plastic behaviour with the yielding of steel. As can be seen from Table 7.4 the average failure load increased from 47.65 kN to 57.37 kN for beams exposed to 30 thermal cycles

Figure 7.10c shows the load deflection response of the three beams exposed to 90 thermal cycles. As shown in the Figure, the behaviour of beams RS-6 and RS-8 are very similar up to their maximum load carrying capacity. At 53.39 kN the load-deflection curve of beam RS-6 started descending gently. At about 43 kN and mid-span deflection of 11 mm, a drop in load-carrying capacity was observed. This was because the beam had experienced cracking in the top concrete fibre. Finally, the beam failed in ductile manner. Beam RS-8 also failed at a maximum failure load of 53.97 kN in the same behaviour as that of RS-6.

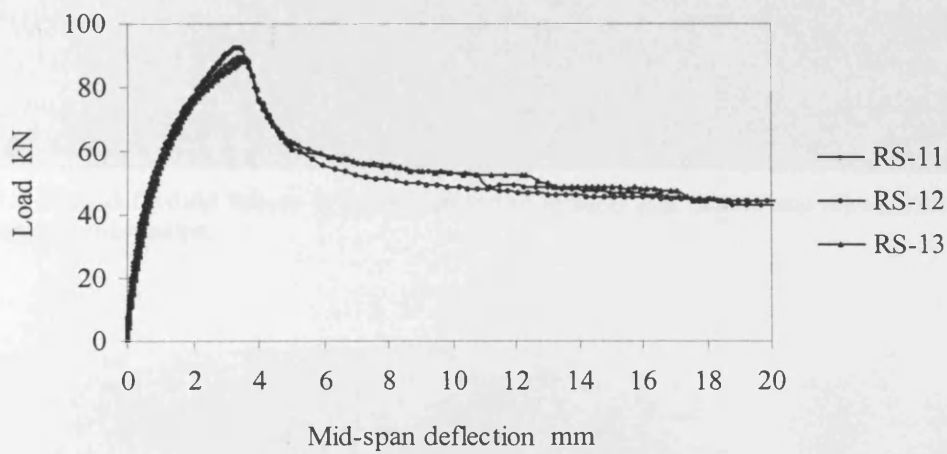
Beam RS-7 carried lower load than the other two beams. At 48.82 kN, this beam also failed in flexure without any sign of shear cracking or drop in the load. After that, due to the yielding of the rebar, this beam exhibited plastic behaviour. The average load carrying capacity of the beams exposed to 90 thermal cycles was 52.06 kN which is around 20 per cent higher than that of the corresponded control beams.

7.8.2.3.2 Beams retrofitted with three long and four short strips

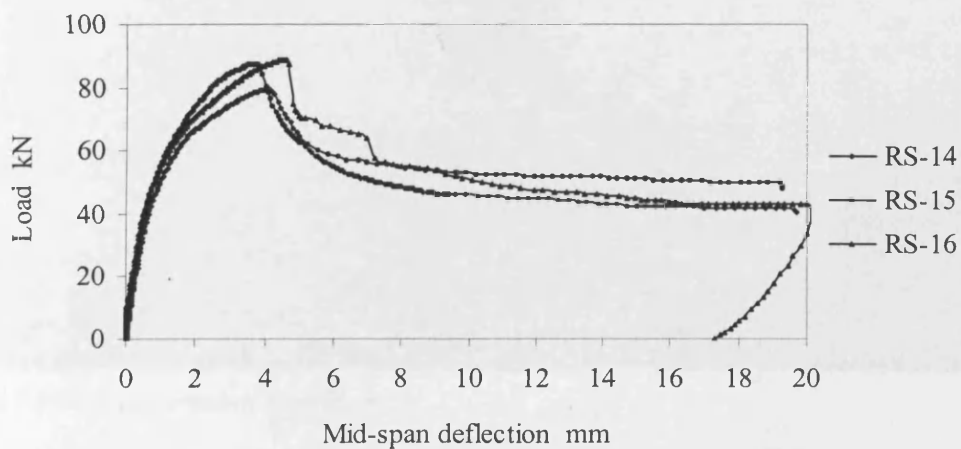
As mentioned earlier, this configuration of retrofitting consisted of three continuous and four short strips. One strip bonded on the tension face, two continuous and four short strips bonded to the vertical sides, fully covering the supports and the tension strip sides. Eight beams were tested after different thermal cycling. Of these, two beams were tested after exposure to no thermal cycling, three after 30 thermal cycles and the remaining three after 90 thermal cycles.



(a)



(b)



(c)

Figure 7.11: Load-Deflection responses of beams retrofitted with one strip on the tension face and two strips on the sides, after: (a) 0 thermal cycles, (b) 30 thermal cycles, and (c) 90 thermal cycles.

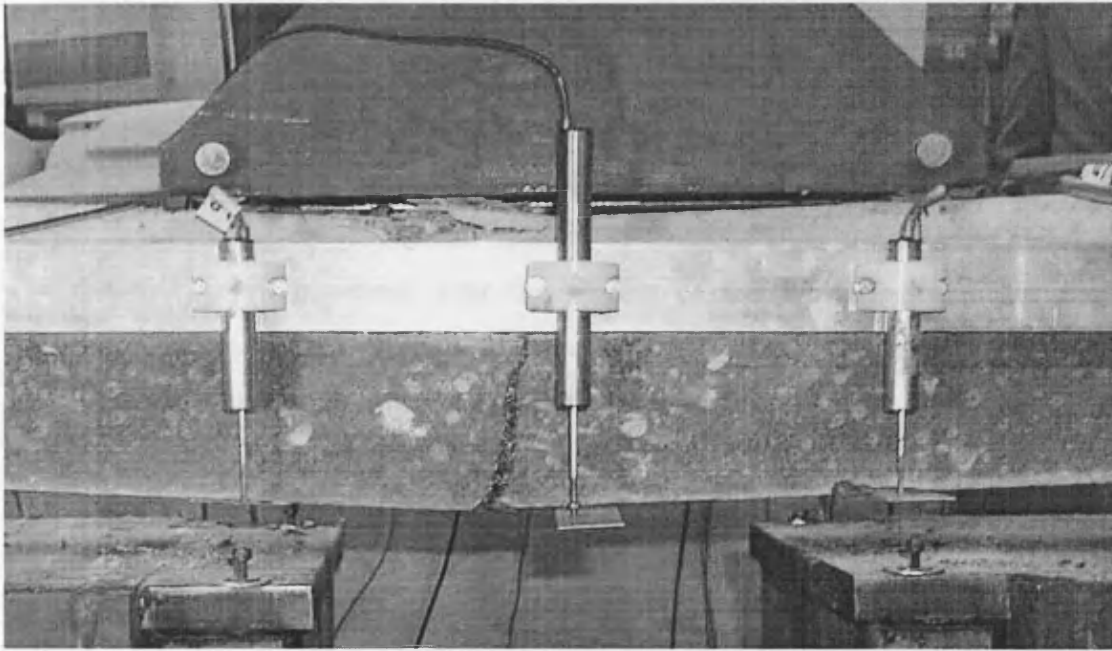


Plate 7.8 Typical flexural failure of beams reinforced in shear and flexure and retrofitted with three long and four short strips.



Plate 7.9 Bridging action of steel fibres.

Figure 7.11a shows the load-deflection response of the two retrofitted beams exposed to non-thermal cycling RS-9 and RS-10. It is clear that the test results are very consistent and the responses of the beams are quite close to each other, especially before the attainment of the maximum load.

As can be seen, both beams exhibited a linear elastic behaviour up to 40 kN, then the curves deviated slightly due to the opening of the pre-existing cracks. At about 60 kN, the first crack appeared near the middle of the tension strip. This crack propagated vertically in the side strip (Plates 7.8 and 7.9) and opened up gradually until the load reached the maximum and the load displacement curve started to descend gently. The average load carrying capacity of the beams with this configuration of retrofitting was around 65 percent higher than that of control beams (Table 7.4).

Figure 7.11b shows the load-deflection response of the three retrofitted beams exposed to 30-thermal cycling RS-11, RS-12 and RS-13. As can be seen, the behaviour of these beams is similar to each other. Due to the strengthening of the sides of the beams as well as the strip bonded on the tension face, there was no sign of shear cracking at the end of the retrofit strips or any local drop in the load-deflection response. The failure of the beams is quite ductile and can be classified as a typical flexural failure.

The average load carrying capacity of these beams increased by only 18 per cent over those exposed to no thermal cycling. This expected behaviour is likely to be due to the increase in compressive strength, which is due to the continued hydration of the cement paste, induced by the 30 thermal cycles. Moreover, the average load carrying capacity of the corresponding control beams increased from 47.65 kN to 90.18 kN, giving a total increase of 91 percent.

Of the three beams retrofitted with three continuous and four short strips after 90 thermal cycles RS-14, RS-15 and RS-16 only beam RS-16 failed in shear at a maximum load of 88.60 kN (Figure 7.11c). This failure occurred through the joint connecting the long and short side strips. Due to the bridging action of the tension

strip, the crack was arrested in the CARDIFRC[®] tension strip. This type of failure can be classified as a ductile shear failure. Beams RS-14 and RS-15 failed in pure flexure at a maximum failure load of 79.48 kN and 87.60 kN respectively.

The behaviour of these beams is quite similar to those tested after 30 thermal cycles. The first crack appeared in the middle third of the tension strip. As the load was increased, this crack propagated vertically in the side strips and the mouth of the initial crack in the tension strip opened gradually. As the load was further increased, the propagation of the cracks on both sides of the beam towards the compression top fibre became visible. After the peak load, the load-deflection curves descended gently. The test was left running until the mid-span deflection reached 20 mm when the test was stopped deliberately. It can be concluded that, the average load carrying capacity decreased from 90.18 kN after 30 thermal cycles to 85.22 kN after 90 thermal cycles. This decrease in load could be associated with the reduction in compressive strength caused by thermal cycling. The average load carrying capacity of the corresponding control beams increased from 47.37 kN to 85.22 kN, giving a total increase of 80.85 percent.

As mentioned above retrofitting RC beam with CARDIFRC[®] increases the load carrying capacity of the beams. Moreover, the residual load carrying capacity of retrofitted beam even after reaching the mid-span deflection of 20 mm is still higher than that of the corresponding control beams (See Figures 7.6 and 7.11).

7.9 Discussion

As expected, the control beams that were reinforced only in flexure exhibited both modes of failure i.e. flexural and shear. Of the eight beams one beam failed in flexure, four beams failed in shear, and three in a combination of shear and flexure. As a result of exposure to the 30 thermal cycles, there is a definite trend of an increase in the beam's capacity. These beams had a higher load carrying capacity than the control beams, which were not exposed to thermal cycling (see Table 7.2). The increase in load carrying capacity is more than 15 percent. This increase is nearly equal to the 16 percent increase in the concrete compressive strength, which is probably due to the continued hydration of the cement paste, induced by the 30

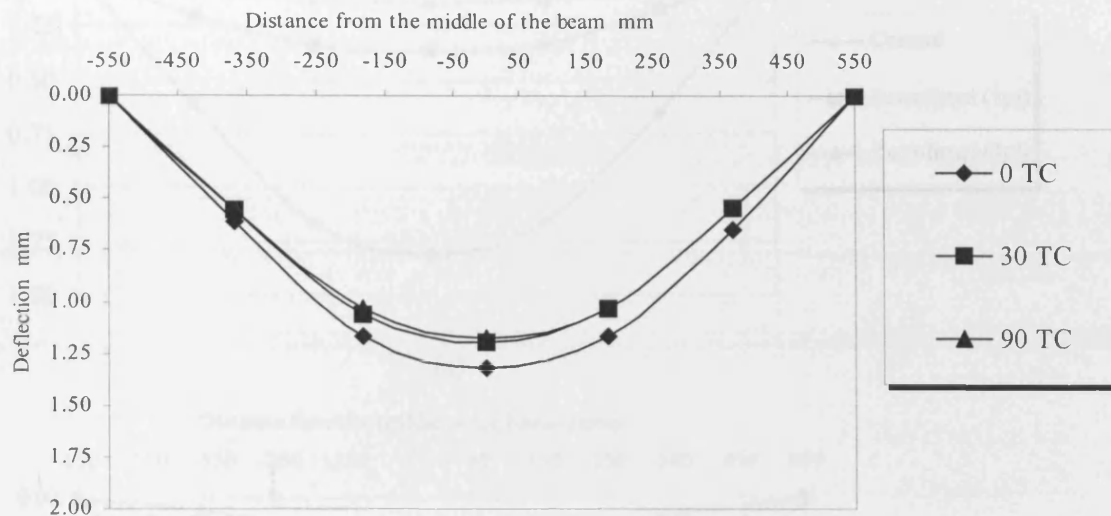
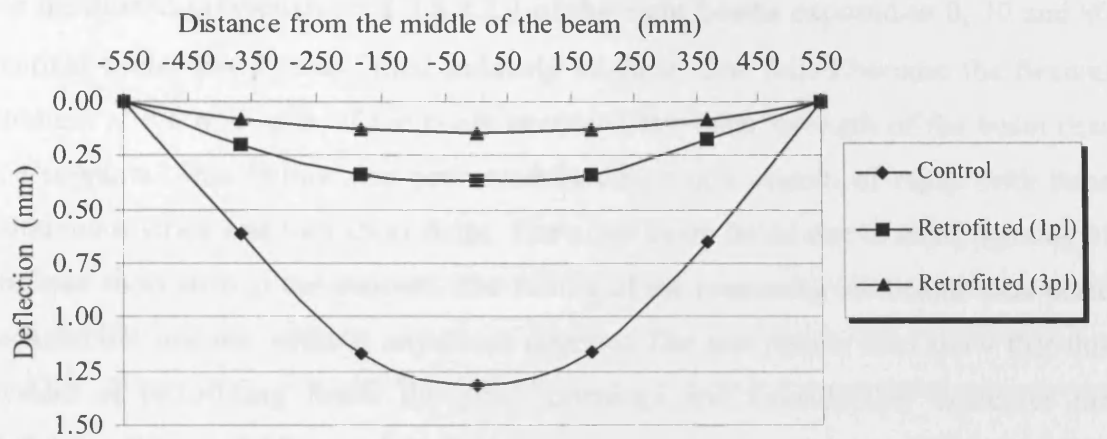


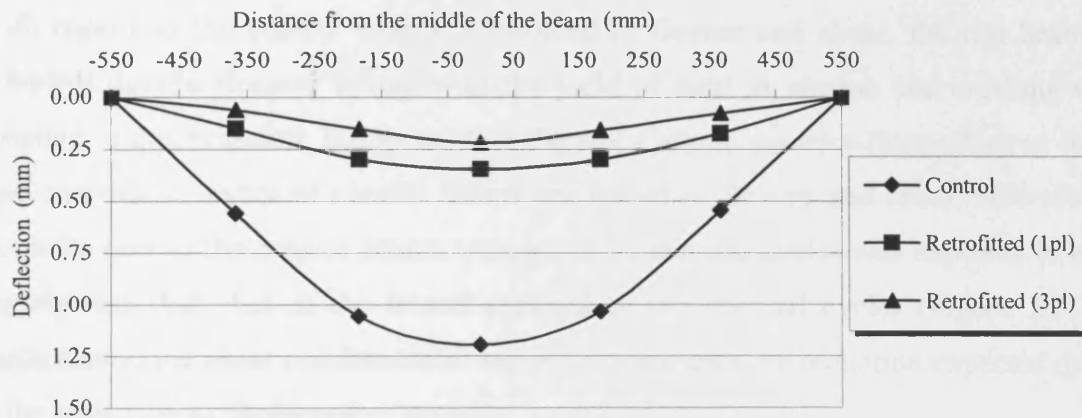
Figure 7.12 Typical deflection of control beams without shear reinforcement after 0, 30 and 90 thermal cycles.

thermal cycles (see Table 7.1). As far as the stiffness is concerned, the deflection of the control beams exposed to 30 thermal cycles was expected to be slightly less than that of the beams exposed to no thermal cycles. Figure 7.12 compares the typical deflection of the beams exposed to, 0, 30 and 90 thermal cycles.

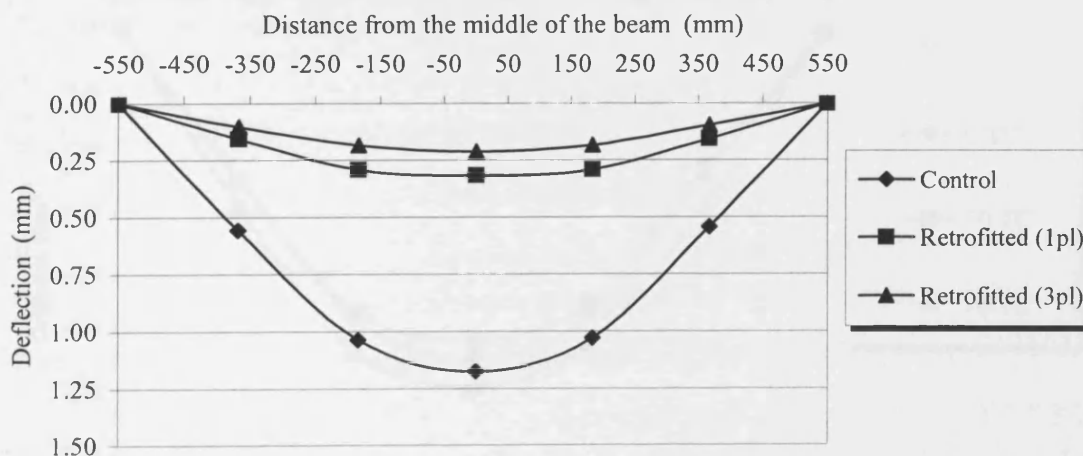
Retrofitted beams with only one plate on the tension face and exposed to 0, 30 and 90 thermal cycles exhibited the same mode of failures as those of control beams i.e. shear, shear/flexure and flexure. However, as we have seen in § 7.8.2.2.1, the failure load increases and the crack opening and deflection decrease. The typical deflected shapes of the retrofitted beams are compared with that of the control beams at 20 kN in Figure 7.13. As far as the load carrying capacity of retrofitted beams is concerned, this system of retrofitting can increase it by 24, 34 and 35 percent over that of control beams after 0, 30 and 90 thermal cycles, respectively (Table 7.3).



(a)



(b)



(c)

Figure 7.13: Typical deflection of beams without shear reinforcement retrofitted with one plate on the tension face and three continuous and four short plates compared with that of control beams at 20 kN, after: (a) 0 thermal cycles, (b) 30 thermal cycles, and (c) 90 thermal cycles.

As mentioned previously in § 7.8.2.2.2 of the eight beams exposed to 0, 30 and 90 thermal cycles two beams failed suddenly in shear. One failed because the flexural strength at the mid-span of the beam exceeded the shear strength of the beam near the supports. This failure was prevented by adapting a system of repair with three continuous strips and four short strips. The other beam failed due to weak bonding of the side short strip at the support. The failure of the remaining six beams took place in a ductile manner without any shear distress. The test results also show that this system of retrofitting limits the crack openings and considerably decreases the deflection (Figure 7.13).

With regard to the control beams, reinforced in flexure and shear, the test beams exhibited ductile flexural failure with the yield of steel in tension and crushing of concrete in compression. It appears that thermal cycling has very little effect on the load carrying capacity of control beams reinforced in flexure and shear. However, the deflection of the control beams exposed to 30 thermal cycles was expected to be slightly less than that of the beams exposed to non-thermal cycles (Figure 7.14). Furthermore, the shear reinforcement seems to counteract the reduction expected due to the reduction in compressive strength.

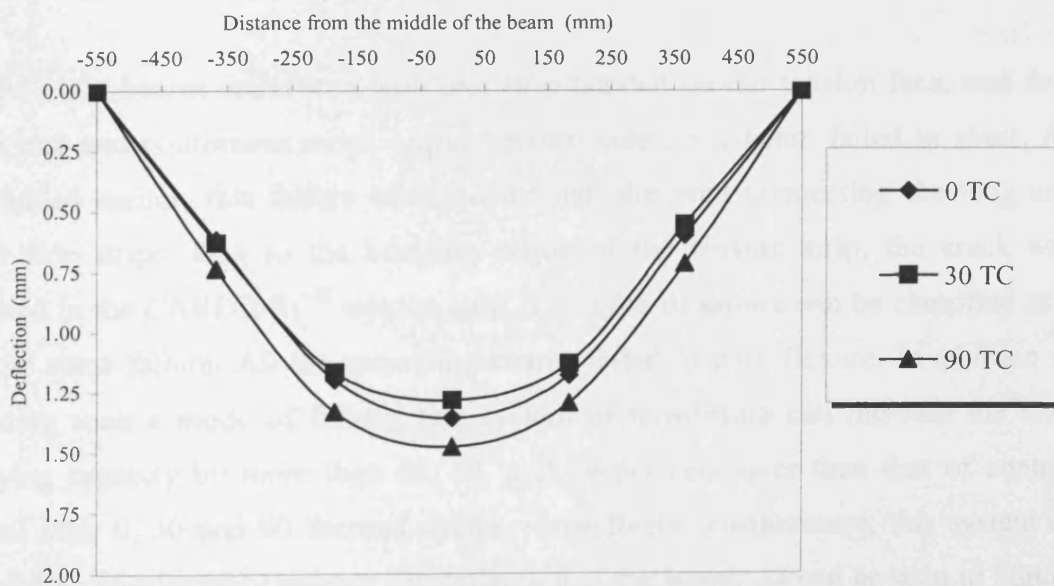
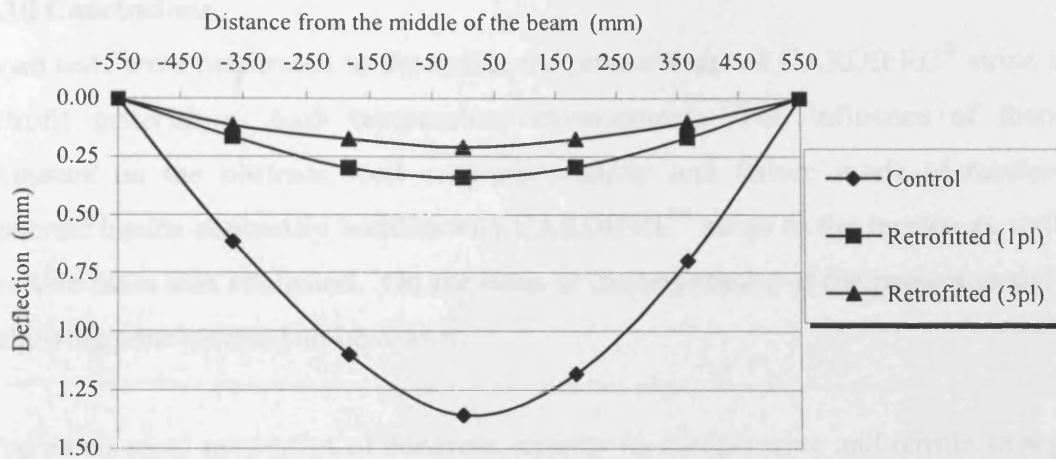


Figure 7.14 Typical deflections of control beams with sufficient shear reinforcement after 0, 30 and 90 thermal cycles.

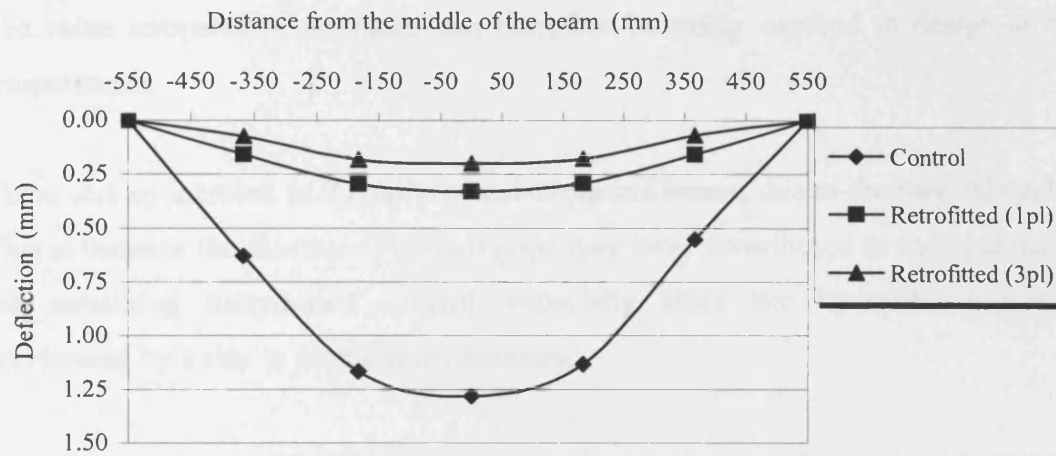
All beams retrofitted with one plate on the tension face and exposed to thermal cycling failed in pure flexure. As mentioned earlier, the flexural failures observed were generally characterized by a single flexural crack occurring in the middle third of the beam extending upwards to the concrete top fibre between the load points and downwards through the retrofit material. These beams failed at an average load higher than that of control beams. Retrofitting RC beams with one plate on the tension face not only improves the load carrying capacity but it can also decrease the crack opening and stiffness (Figure 7.13). As can be seen in the Figure, the mid-span deflection of the retrofitted beams at 20 kN load is about 24, 25 and 29 per cent lower than that of the control beams after 0, 30 and 90 thermal cycles.

It can also be seen that both the deflection behaviour and failure modes were similar for all exposure conditions. As can be seen in Table 7.4 the average failure load increased from 45.64 kN to 51.50 kN for beams kept at room temperature, from 47.65 kN to 57.37 kN for beams exposed to 30 thermal cycles and from 47.37 kN to 52.06 kN for beams exposed to 90 thermal cycles. The average failure load of the non-heat-cycled beams of 51.5 kN increased to 57.73 kN after 30 thermal cycles and then decreased to 52.06 kN after 90 cycles. Thus a slight increase in failure load of 1 percent after 90 cycles has been observed.

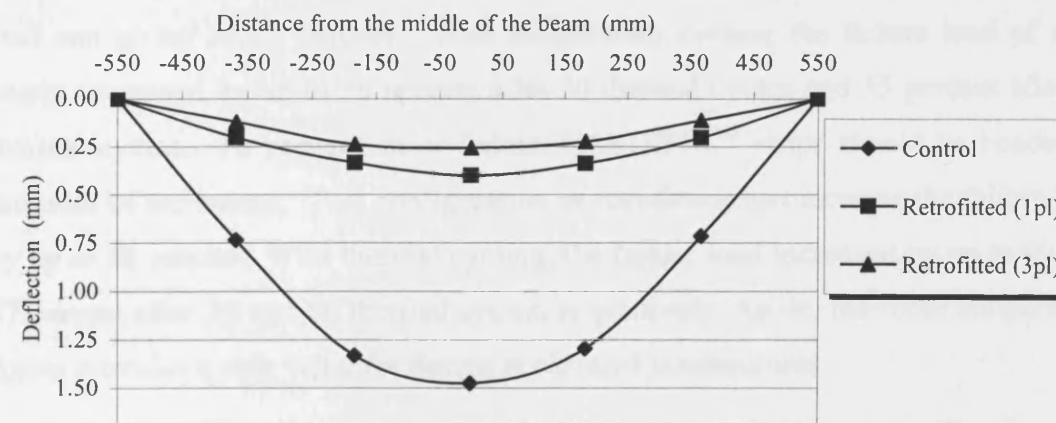
Of the eight beams retrofitted with one strip bonded on the tension face, and four short and two continuous strips on the vertical sides, one beam failed in shear. As mentioned earlier, this failure occurred through the joint connecting the long and short side strips. Due to the bridging action of the tension strip, the crack was arrested in the CARDIFRC® tension strip. This type of failure can be classified as a ductile shear failure. All the remaining beams failed in pure flexure. In addition to ensuring such a mode of failure, this system of retrofitting can increase the load carrying capacity by more than 66, 89, and 79 per cent over than that of control beams after 0, 30 and 90 thermal cycles, respectively. Furthermore, this system of retrofitting considerably reduces the deflection of the beam. As can be seen in Figure 7.15 the mid-span deflection of the retrofitted beams at a load level of 20 kN is about 14.7, 15.9 and 15.8 per cent of that of the control beams after 0, 30 and 90 thermal cycles.



(a)



(b)



(c)

Figure 7.15: Typical deflection of beams with sufficient shear reinforcement retrofitted with one plate on the tension face and three continuous and four short plates compared with that of control beams at 20 kN, after: (a) 0 thermal cycles, (b) 30 thermal cycles and (c) 90 thermal cycles.

7.10 Conclusions

Load tests were performed to determine the potential use of CARDIFRC® strips as a retrofit material in high temperature environments. The influence of thermal exposure on the ultimate load carrying capacity and failure mode of reinforced concrete beams externally bonded with CARDIFRC® strips to the tension as well as the side faces was evaluated. On the basis of the test results of the present study, the following conclusions can be drawn.

The mechanical properties of concrete, namely its compressive and tensile strengths are substantially improved after 30 thermal cycles, but not so after 90 thermal cycles. The room temperature strengths can therefore be safely assured in design at high temperatures.

There was an increase in the failure load of control beams due to the thermal cycling. This is because the thermal cycling regime may have contributed to the hydration of the remaining unhydrated cement, especially since the hydration process is accelerated by a rise in ambient temperature.

Retrofitting with CARDIFRC® strips bonded to the tension face only improves the load carrying capacity and the serviceability of the beam. The increase in failure load can go up to 23 percent. With temperature cycling the failure load of such beams increased by up to 36 percent after 30 thermal cycles and 35 percent after 90 thermal cycles. To prevent shear failure, CARDIFRC® strips should be bonded to the sides of the beams. This configuration of retrofitting can increase the failure load by up to 86 percent. With thermal cycling, the failure load increased by up to 90 and 87 percent after 30 and 90 thermal cycles, respectively. Again, the room temperature figure provides a safe value for design at elevated temperatures.

No visual deterioration or bond degradation was observed after thermal cycling of the retrofitted beams (the bond between the repair material and the concrete substrate remained intact) attesting to the good thermal compatibility between the concrete and CARDIFRC®. Therefore, this type of retrofit material can be successfully used in hot climates.

In order to avoid any possible shear failure for beams retrofitted with one strip on the tension face, two continuous and for short strips on the sides (e.g. RS-16), it is suggested that a continuous strip cover entire side length of the beam eliminating the joints in the areas of the maximum shear forces.

Chapter 8

*Analysis of the reinforced concrete
beams retrofitted with CARDIFRC[®]*

8.1 Introduction

In the preceding Chapter, the behaviour of CARDIFRC® retrofitted RC beams was experimentally investigated. The results showed clearly the viability and effectiveness of this new retrofitting technique. A parametric study is also essential to correlate the experimental results, and thus to quantify the general structural behaviour. This chapter introduces two analytical models for the prediction of moment resistance and the load-deflection behaviour of the retrofitted beams. These models were originally developed by Alaei and Karihaloo (2003a and 2003b) and have been further refined in this work. The first model is based on the classical strength theory, but takes into account fully the tensile contributions (i.e. pre-peak and post-peak) from concrete and CARDIFRC®. The second analytical model is based on the fracture mechanics concepts. This model mimics the initiation and growth of the flexural crack that eventually leads to the failure of the retrofitted beam. The results of these models will be compared with that of the current test data and conclusions will be presented.

8.2 Constitutive relations

8.2.1 Concrete

The response of a structure under load depends to a large extent on the stress-strain relation of the constituent materials and the magnitude of stress. Since concrete is used mostly in compression, the stress-strain relation in compression is of primary interest. The concrete stress-strain relation exhibits a nearly linear elastic response up to about 30 % of the compressive strength. This is followed by gradual softening up to the concrete compressive strength, when the material stiffness momentarily drops to zero. Beyond the compressive strength, the concrete exhibits strain softening until failure takes place by crushing (Figure 8.1).

In the present study, the distribution of concrete stresses in compression zone was found from the following stress-strain curve for concrete (CEB-FIP code 1990)

$$\sigma_c = \frac{\frac{E_c}{E_{cl}} \cdot \varepsilon_c}{1 + \left(\frac{E_c}{E_{cl}} - 2 \right)} \cdot f_{cm} \quad \text{for } \varepsilon_c < \varepsilon_{cu} \quad (8.1)$$

where

f_{cm} is the mean value of compressive strength of cylindrical specimens (150 mm diameter and 300 mm height)

E_c is the tangent modulus,

ϵ_{cl} is -0.0022,

E_{cl} is the secant modulus from the origin to the peak compressive stress.

ϵ_{cu} : ultimate strain

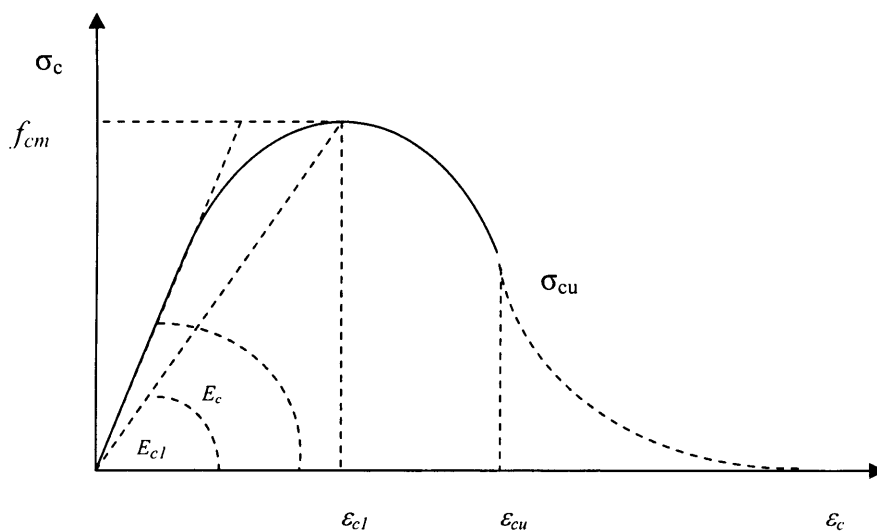


Figure 8.1 Stress-strain diagram for concrete in compression

The cylindrical compressive strength f_{cm} can be determined from the cubic compressive strength f_{cu} using Table 2.1.1 (CEB-FIP). The tangent modulus E_c and the ultimate strain of concrete ϵ_{cu} can also be calculated from the compressive strength of concrete using Table 2.1.7 (CEB-FIP). Table 8.1 shows the values of these parameters used in the model.

Table 8.1 Assumed parameters for modelling the compressive strength behaviour of concrete

TC	f_{cm} N/mm^2	E_c kN/mm^2	E_{cl} kN/mm^2	ϵ_{cl} -	ϵ_{cu} -
0	47.00	36.10	21.36	0.0022	0.0033
30	54.81	37.98	24.91	0.0022	0.0034
90	50.36	36.93	22.88	0.0022	0.0032

Although the tensile strength of concrete is usually ignored in the design of reinforced concrete flexural members, the concrete in between the cracks does contribute to the beam stiffness, and hence influences the moment curvature-relationship. The behaviour of concrete in tension is divided into two stages; un-cracked and cracked sections. For un-cracked section, the concrete exhibits a linear elastic stress-strain behaviour until 90 percent of the ultimate tensile stress f_{ctm} , the slope of the curve then changes to account for pre-peak micro-cracking (Figure 8.2a).

$$\sigma_1 = E_c \varepsilon_{ct} \quad \varepsilon_{ct} \leq \varepsilon_1 \quad (8.2)$$

$$\sigma_2 = f_{ctm} - \frac{0.1 f_{ctm}}{0.00015 - (0.9 f_{ctm} / E_c)} \cdot (0.00015 - \varepsilon_{ct}) \quad \varepsilon_1 < \varepsilon_{ct} < \varepsilon_m \quad (8.3)$$

where

ε_{ct} : tensile strain at which the tensile stress has to be calculated

ε_1 : tensile strain according to Figure 8.2.

ε_m : tensile strain at maximum tensile stress

f_{ctm} : direct tensile strength which is estimated to be 90 percent of splitting tensile strength.

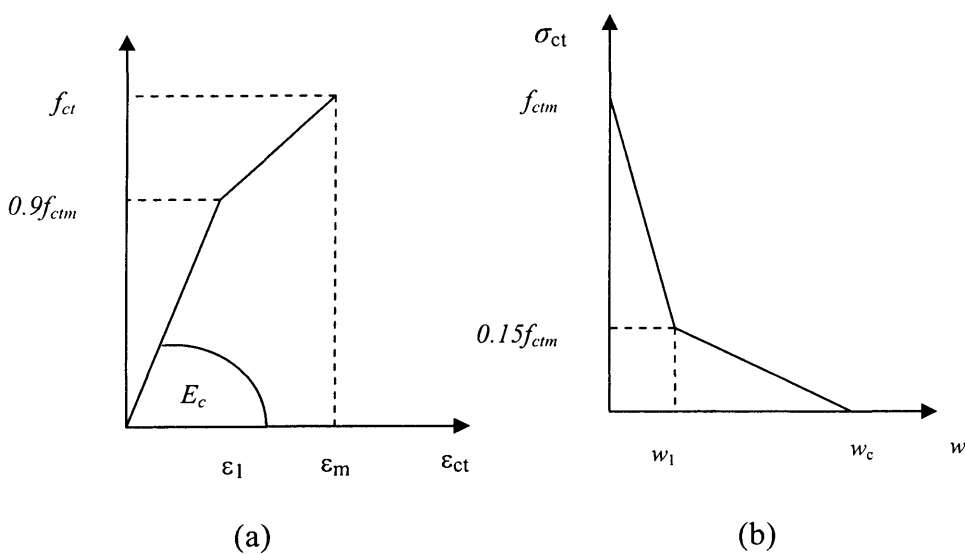


Figure 8.2 Stress-strain and stress-crack opening diagrams for concrete in tension: (a) pre-cracking region and (b) post-cracking region.

Cracked section starts beyond the maximum tensile strength. For this section a bilinear softening relation is recommended. The concrete between the cracks still carries a certain amount of stress and this is the so-called tension softening behaviour. Figure 8.2b shows the tension softening behaviour of concrete. The descending curve changes when the tensile stress in concrete reaches 15 percent of the tensile strength of the section. The initial steep part of this curve is primarily a result extensive post-peak micro-cracking, while the more gradual tail part is primarily a result of aggregate interlocking (Karihaloo, 1995)

$$\sigma_1 = f_{ctm} \left(1 - 0.85 \frac{w}{w_1} \right) \quad w \leq w_1 \quad (8.4)$$

$$\sigma_2 = \frac{0.15 f_{ctm}}{w_c - w_1} (w_c - w) \quad w_1 < w < w_c \quad (8.5)$$

and

$$w_1 = \frac{G_F - 0.075 w_c f_{ctm}}{0.5 f_{ctm}} \quad (8.6)$$

where

w : crack opening at which the stress has to be calculated

w_1 : crack opening according to Figure 8.2b

w_c : crack opening at the termination of tension softening

α_F : coefficient depends on the maximum aggregate size d_{max} from Table 2.1.3 of CEB-FIP

G_F : specific fracture energy, calculated using the maximum aggregate size and the compressive strength of concrete from Tables 2.1.8 and 2.1.4 of CEB-FIP 1990.

Table 8.2 Assumed parameters for modelling the tensile strength behaviour of concrete

TC	f_{ctm} MPa	G_f N/m	w_1 mm	w_c mm
0	4.01	76	0.0195	0.125
30	4.59	84	0.0180	0.125
90	4.36	81	0.0186	0.125

8.2.2 Steel reinforcement

To determine the mechanical properties of steel, namely yield stress and modulus of elasticity, three lengths of reinforced steel bar (50 mm each) were tested in the laboratory. Table 8.3 shows the characteristics of stress-strain diagram of these specimens. Using the average values of test results, i.e. the yield stress and modulus of elasticity- a perfect elasto-plastic diagram was assumed for steel reinforcing bar, as shown in Figure 8.3.

Table 8.3 Tensile test results of steel reinforcing bar

Diameter mm	Area mm ²	0.2% Proof		Ultimate		Elongation		Elastic Modulus GPa
		Load kN	Stress MPa	Load kN	Stress MPa	mm	%	
12	113.1	58.5	517.2	65.4	578.2	15.3	30.6	200
12	113.1	54.2	479.2	67.3	595.0	15.8	31.6	198.8
12	113.1	53.8	475.7	67.8	599.5	14.7	29.4	201.5
Average Values		55.5	490.7	66.8	590.9	15.3	30.5	200.1

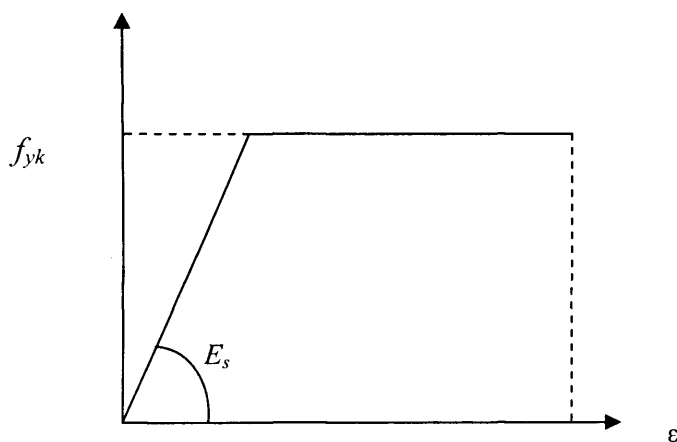


Figure 8.3 stress-strain diagram for steel

8.2.3 CARDIFRC®

As mentioned in § 4.6.3.6.5, numerical expressions have been fitted to the test data to describe the behaviour of CARDIFRC® in uniaxial tension. The constitutive behaviour of CARDIFRC® thus can be classified into two sections (i.e. un-cracked and cracked). For un-cracked section, the stress-strain curve was divided into two stages: linear elastic (stage I) and strain hardening (stage II). As can be seen in

Figure 8.4, the stress-strain curve is linear up to the tensile strength of the matrix, this stress can be determined by the following linear equation

$$\sigma_1 = 0.046\varepsilon \quad 0 < \varepsilon < 200 \text{ microstrain} \quad (8.7)$$

The stress for strain hardening region (stage II) can be determined by the following equation:

$$\sigma_2 = -4.34 \times 10^{-10} \varepsilon^4 + 8.32 \times 10^{-7} \varepsilon^3 - 6.03 \times 10^{-4} \varepsilon^2 - 0.199 \varepsilon - 12.62$$

$$200 < \varepsilon < 600 \text{ microstrain} \quad (8.8)$$

Finally, the stress for (cracked section) tension softening region (Stage III), can be determined by the following equation:

$$\sigma = 3.07 * 10^{-3} w^7 - 0.08 w^6 + 0.82 w^5 - 4.42 w^4 + 12.79 w^3 - 18.11 w^2$$

$$+ 5.73 w + 12.89 \quad 0 < w < 6.5 \text{ mm} \quad (8.9)$$

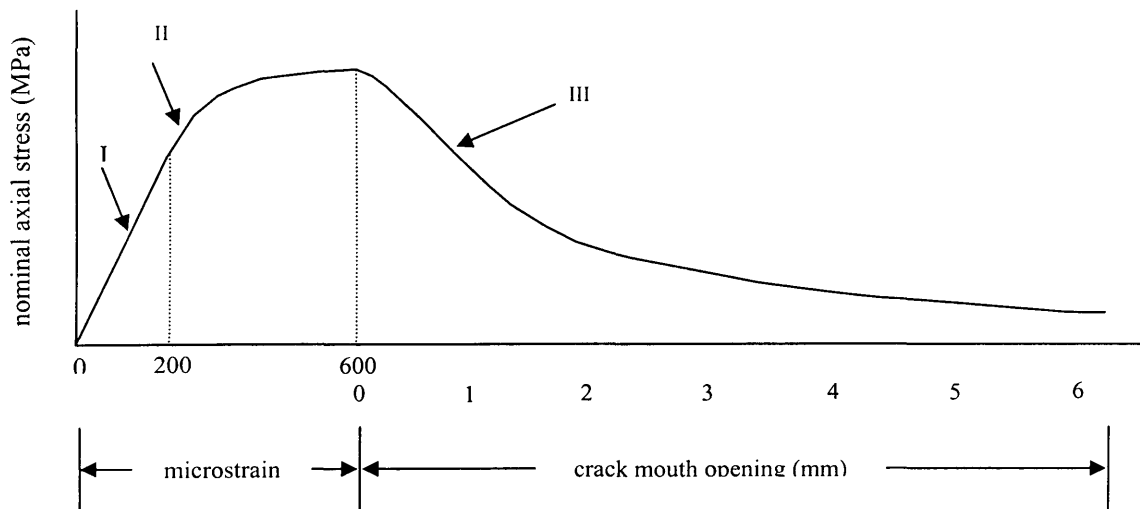


Figure 8.4 Complete pre- and post peak tensile curve for CARDIFRC® (After Benson, 2004)

8.3 First analytical model (Classical theory)

The analytical model for CARDIFRC® retrofitted rectangular beams subjected to bending was used based on the material properties discussed above. Unlike most other analytical methods which only deal with the elements at ultimate failure, this

model was intended to predict the element's behaviour during the whole loading process.

8.3.1 Model assumptions

In this model the moment resistance of a section retrofitted with CARDIFRC[®] can be calculated based on the distribution of stresses caused by bending. To determine the strain distribution along the height of the section the following assumptions are made:

- Plane sections remain plane after bending. In other words, the strain distribution across the section depth is linear (Bernoulli hypothesis);
- The presence of adhesive layer between the concrete and CARDIFRC[®] strip is ignored. Instead, perfect bonding between the retrofit strips and the original beam, as a result of the adhesive bonding, was assumed. This assumption was considered to be reasonable as no failure in the actual adhesive bonding layer, or on the concrete-adhesive and/or adhesive-CARDIFRC[®] interfaces had been observed in the current loaded beam tests (see § 7.8);
- The stress distribution in concrete and CARDIFRC[®] strips cannot be assessed directly from the value of strain after cracking, as the constitutive relations are expressed in terms of stress-crack opening rather stress-strain.

Using the following assumptions, the evaluation of crack opening from the strain distribution becomes possible:

- The crack opening at the tension strip (w) is the product of the strain at this level (ε_f), and effective length of retrofit strip (L_{eff}).
- The dominant flexural crack tip is located at the level of the neutral axis. The crack faces open in a linear manner (see Figures 8.5 and 8.6).

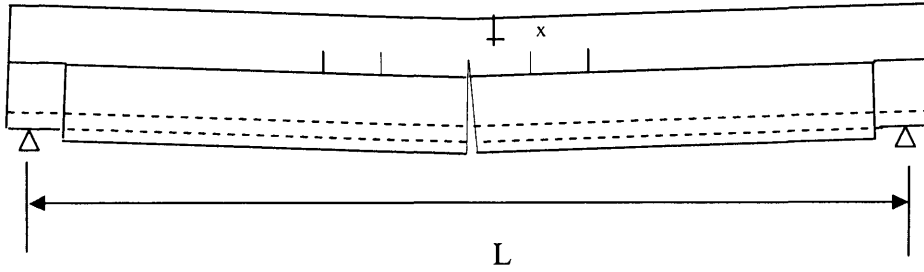


Figure 8.5 Beam strengthened with one strip on the tension face, two continuous and four short strips on the sides

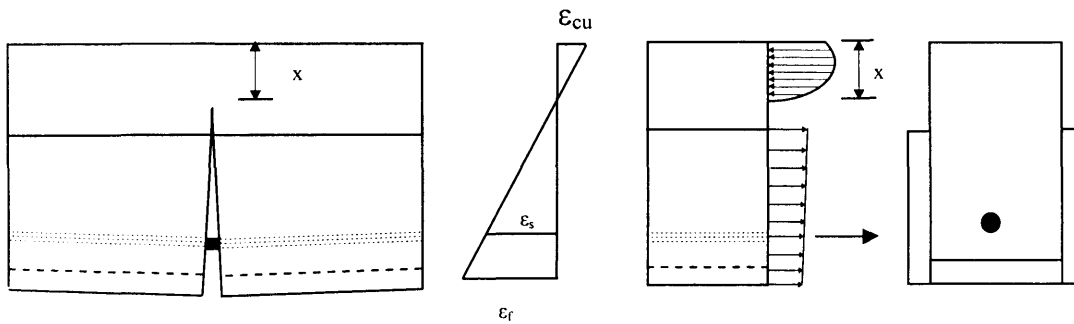


Figure 8.6 Modelling of the flexural crack in the middle of the beam strengthened with one strip on the tension face, two continuous and four short strips on the sides (After Alaei, 2002)

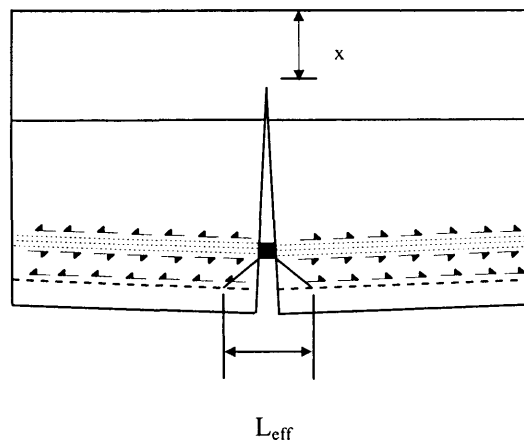


Figure 8.7 Effective length of strip for calculation of crack opening

In fact, the strain over the effective length of retrofit strip (L_{eff}) is released in the form of a local crack. To determine L_{eff} , the length of strain-free part of the retrofit strip should be calculated. If the tensile stress carried by the cracked strips is ignored in comparison with the tensile stress transferred by the reinforcement, the shear stress at the interface is dependent on the shear stress applied by the reinforcement (Figure 8.7). Assuming the shear stress at the level of reinforcement is distributed at 45°, a length of retrofit strip (L_{eff}) is stress-free and consequently strain-free. The deformation of this length of strip is localised in the crack opening. Therefore, to calculate the crack opening of the tension retrofit strip, the strain at this level (ε_f) can be multiplied by this effective length (L_{eff}) i.e. twice the distance between the reinforcement and the tension strip. In the case of the beams retrofitted by three strips, as the crack opening changes linearly along the height of the beam, the crack opening of the side strips can be easily calculated using the crack opening in the tension strip (w) and the depth of neutral axis (x). In fact, as the crack opening is constrained by the side strip, the strain is smaller and the effective length must be larger. It can be seen that by using this method the stress distribution in the repair material can also be worked out from the strain distribution. Due to the fact that the crack opening displacements (i.e. crack widths) of the test beams were too small for accurate measurement, the crack openings calculated from the above method could not be compared directly with measured values. However, the consequences of the above assumptions to the calculation of the moment resistance and the load deflection response of the beams will become clear when the model is compared with the test results.

8.3.2 Calculation procedure

For the evaluation of the moment resistance of the control and CARDIFRC® retrofitted beams, a computer program was used (see Appendix C). First, a strain in the top concrete fibre and a neutral axis depth are assumed. Then, the linear strain distribution along the height of the beam is defined in terms of these assumed values. The compression and tension zones were divided into a finite number of narrow sections. Since the beam depth of 150 mm in the current test configuration is relatively small, it was decided to use 20 strips in the model, namely 10 each in the compression and tension zones, respectively. The stresses can now be found from

their corresponding relations. The forces are then determined as the product of the section area and the corresponding stress. A similar calculation is made for the retrofit strips, and the reinforced steel.

Having calculated all the forces the location of the neutral axis is obtained from the equilibrium of internal forces. This is solved iteratively until the equilibrium of forces across the depth of the cross section is satisfied (i.e. the sum of the compressive forces equals the sum of tensile forces). The internal moment of resistance is then obtained by summing the compressive and tensile forces times their moment arms about a single point. The curvature value of a given load can now be determined from the concrete compressive strain and the neutral axis depth using the following equation

$$\omega'' = \frac{\varepsilon_c}{x} \quad (8.10)$$

The above process is repeated for different assumed strains in the concrete top fibre. The maximum moment resistance of the section occurs when either the moment reduces for an increase in the top fibre strain, or the top fibre concrete strain exceeds the ultimate strain of concrete in compression.

8.3.3 Moment-curvature relationship

The analytical model described above was applied to simulate the control and retrofitted beams. The curvature was determined from the compressive strain for a given load. Figure 8.8 contains the moment-curvature diagrams for the control and CARDIFRC® retrofitted beams (beams retrofitted with one strip on the tension face and beams retrofitted with one strip on the tension face, two continuous and four short strips on the sides). It can be seen that the moment-curvature diagram for the control beam consists of three stages. The first stage represents the cracking of concrete in tension, the second stage represents yielding of steel reinforcement, and the third stage represents the limit of strain at the concrete top fibre. The diagrams representing the retrofitted beams also show three distinct stages. In the first stage, the strain at the concrete top fibre increases which results in an increase in stress in

both the steel and CARDIFRC®. As can be clearly seen in the Figure, for both types of retrofitted beams, a deviation in the curve occurs at about 3.5 kNm and 5.5 kNm for beams retrofitted only on the tension face and the sides, respectively (stage II). This deviation occurs due to the cracking of CARDIFRC® strips. In fact, this cracking causes a decrease in stresses carried by these strips. However, since the resultant force in steel is higher than that in the retrofit strip the moment resistance curve continues to rise until the strain in the steel exceeds its yield value. This point represents the maximum resistance moment, after which the curve begins to descend (stage III). As can be observed the descending part of the curve occurs in a gradual manner. The gradual decrease in the moment resistance in this stage is due to the following: firstly, cracks are fragmented at the peak load which indicates that at this load a through crack has not formed, and secondly, the transition from fragmented crack to a through crack takes place progressively through the formation of branches.

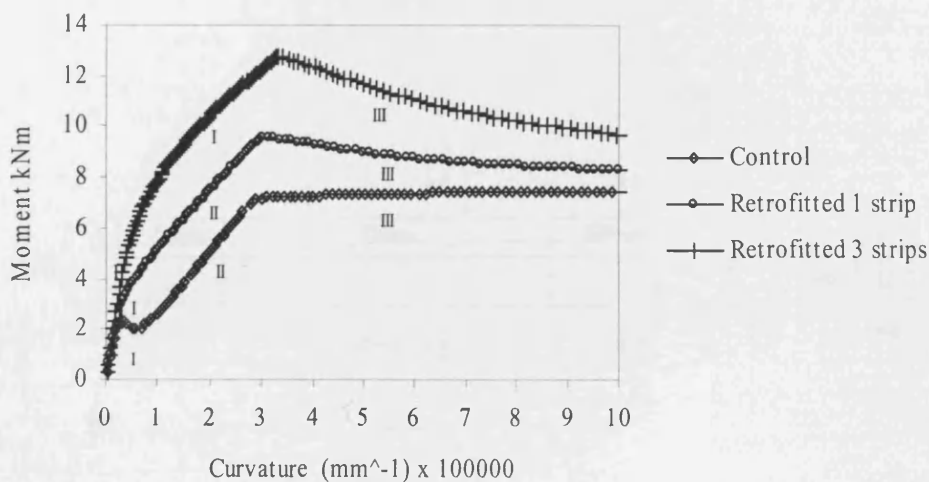


Figure 8.8 Relation between moment resistance of sections and curvature.

Due to the fact that all the beams tested are statically determinate, their bending moment diagrams at any stage of loading are uniquely defined. This information can be combined with the moment curvature diagram of sections to produce the curvature diagram at different load levels by dividing the beam span into a number of intervals (Figure 8.9). The moment area method is then used to compute the slope and deflection of any point of the beam.

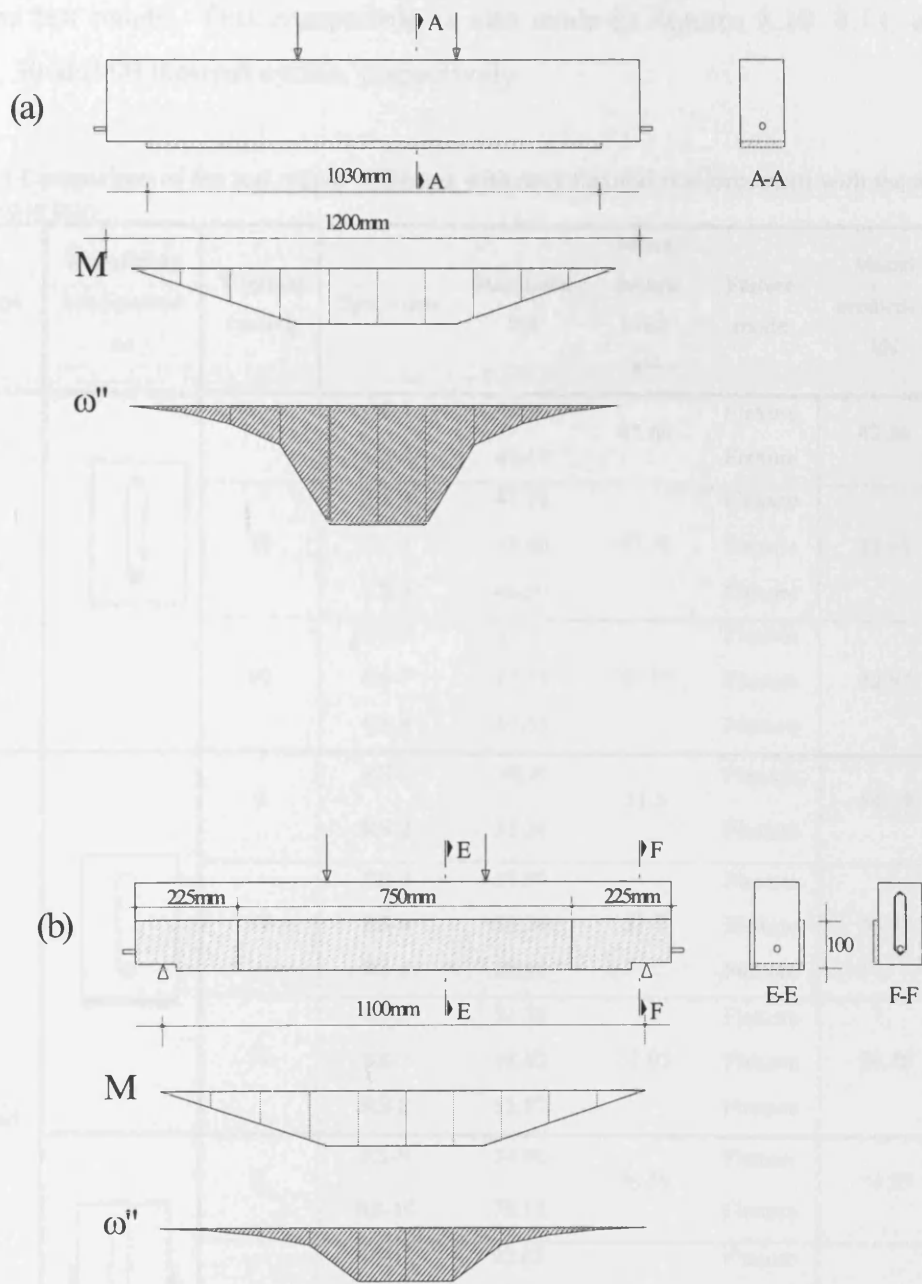
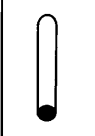
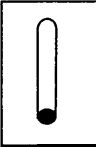



Figure 8.9: Moment and curvature diagrams of the beams retrofitted with:
 (a) one strip under four-point bending,
 (b) three continuous and four short strips on the sides

8.3.4 Model results

Table 8.4 compares the maximum failure load of the beams predicted by the model with the test results. This comparison is also made in Figures 8.10, 8.11, and 8.12 after 0, 30 and 90 thermal cycles, respectively

Table 8.4 Comparison of the test results of beams with only flexural reinforcement with the analytical model prediction.

Beam type	Retrofitting configurations	Thermal cycling	Specimen	Max Load kN	Mean failure Load kN	Failure mode	Model prediction kN
Control		0	CS-1	45.10	45.64	Flexure	42.86
			CS-2	46.18		Flexure	
		30	CS-3	47.78	47.72	Flexure	43.43
			CS-4	48.80		Flexure	
	90	CS-5	CS-6	47.77	47.70	Flexure	42.97
			CS-7	47.79		Flexure	
		CS-8	CS-8	47.55	Flexure		
Retrofitted		0	RS-1	49.8	51.5	Flexure	54.29
			RS-2	53.20		Flexure	
		30	RS-3	57.57	57.7	Flexure	55.14
			RS-4	55.24		Flexure	
			RS-5	60.40		Flexure	
		90	RS-6	53.38	52.05	Flexure	54.86
			RS-7	48.82		Flexure	
			RS-8	53.97		Flexure	
		0	RS-9	74.00	76.09	Flexure	74.57
			RS-10	78.19		Flexure	
		30	RS-11	92.68	90.17	Flexure	76.00
			RS-12	89.30		Flexure	
			RS-13	88.55		Flexure	
		90	RS-14	79.48	85.22	Flexure	75.90
			RS-15	87.60		Flexure	
			RS-16	688.60		Shear	

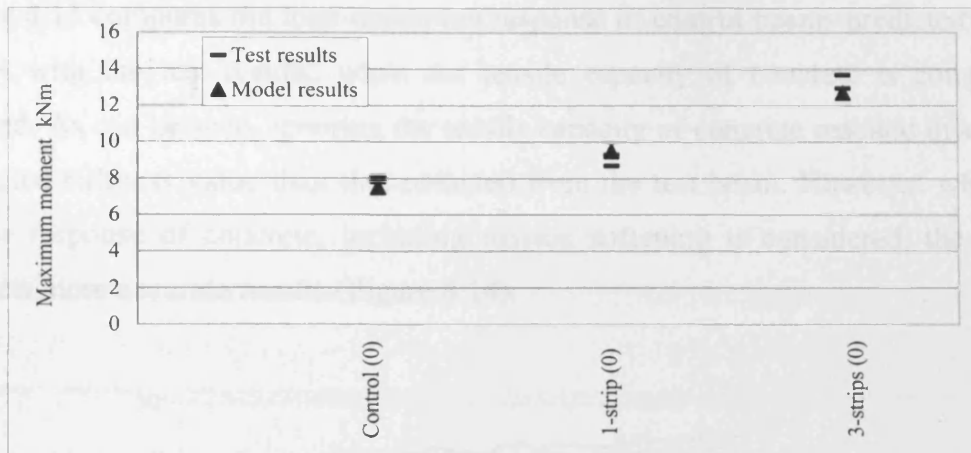


Figure 8.10 comparison of the moment resistance of beams tested after 0 thermal cycles with that predicted by the model

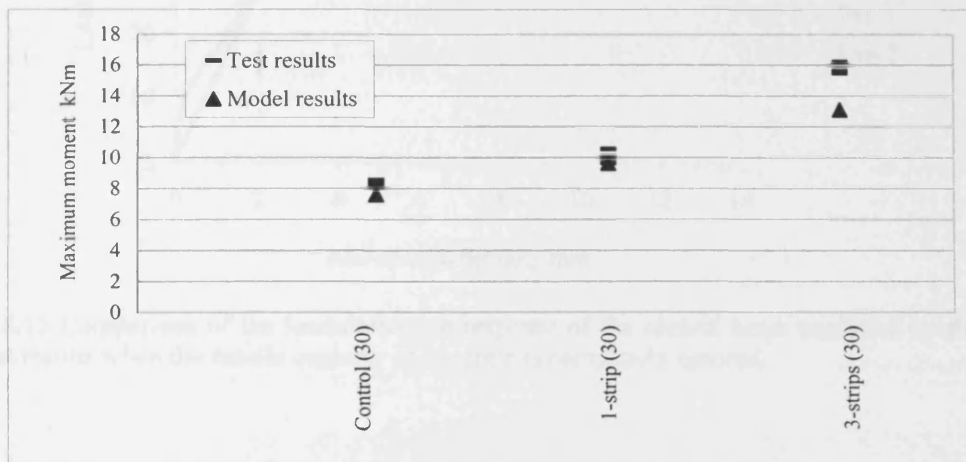


Figure 8.11 comparison of the moment resistance of beams tested after 30 thermal cycles with that predicted by the model.

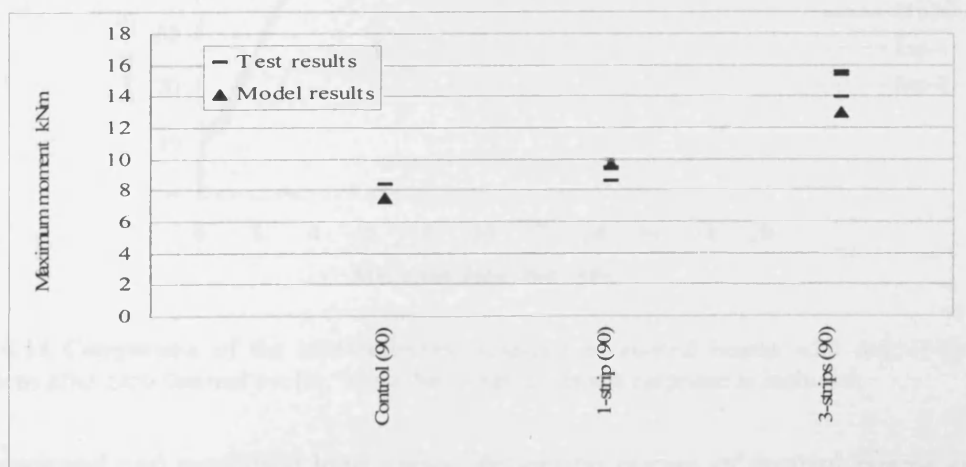


Figure 8.12 comparison of the moment resistance of beams tested after 90 thermal cycles with that predicted by the model.

Figure 8.13 compares the load-deflection response of control beams predicted by the model with the test results, when the tensile capacity of concrete is completely ignored. As can be seen, ignoring the tensile capacity of concrete resulted in a lower predicted stiffness value than that obtained from the test beam. However, when the tensile response of concrete, including tension softening is considered, the model predicts more accurate results (Figure 8.14).

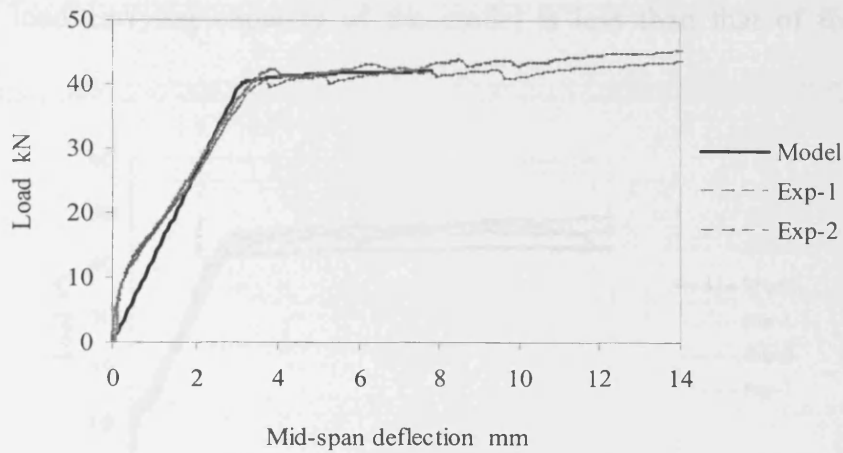


Figure 8.13 Comparison of the load-deflection response of the control beam predicted by the model with test results when the tensile capacity of concrete is completely ignored.

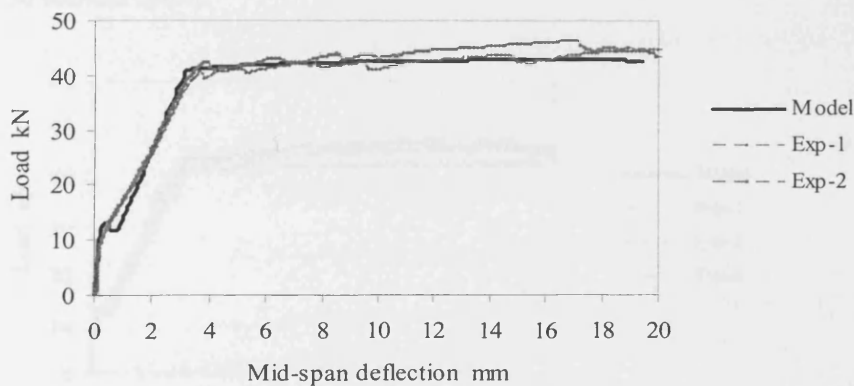


Figure 8.14 Comparison of the load-deflection response of control beams with that of the model predictions after zero thermal cycles, when the complete tensile response is included.

The measured and predicted load versus deflection curves of control beams exposed to non-thermal cycles are shown in Figure 8.14. It can be seen that the predicted and measured response correlate well in the initial stage of loading (i.e. before the cracking of concrete in tension). The difference between them begins to become

apparent in the initial cracked region at which the model predicts a larger deflection than the measured value. This difference is attributed to the fact that the model assumes that cracked section conditions are applicable for all sections in the region of the maximum moment. As the load exceeds the cracking point, both the measured and predicted curves exhibit a considerable reduction in stiffness and they tend to show the same trend. Finally, a ductile failure with the yielding of steel is observed in both the measured and predicted results. As can be seen in Table 8.4, the predicted maximum load carrying capacity of the model is less than that of the measured results.

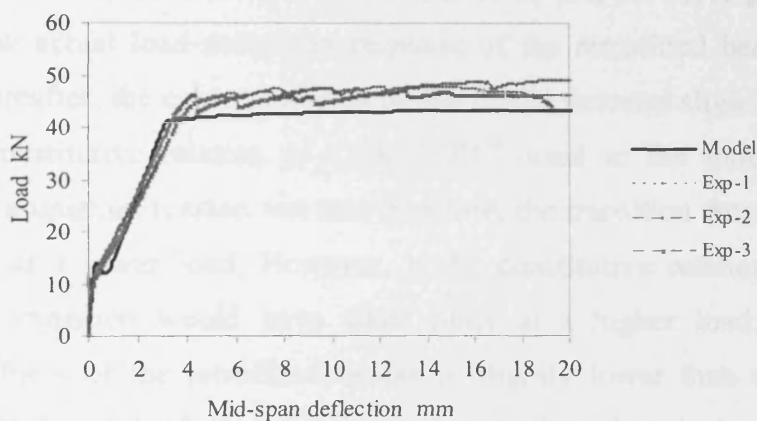


Figure 8.15 Comparison of the load-deflection response of control beams with that of the model predictions after 30 thermal cycles.

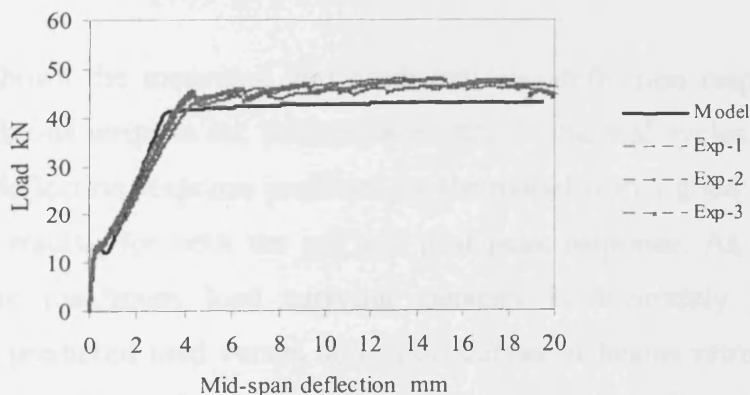


Figure 8.16 Comparison of the load-deflection response of control beams with that of the model predictions after 90 thermal cycles.

The measured and predicted load versus deflection curves of control beams after 30 thermal cycles are shown in Figure 8.15. Both the predicted and measured responses are quite close to the beams exposed to non-thermal cycles. The increase in the

deflection for the predicted curve just after cracking is again observed. As the load is increased, the model prediction approaches the test results, and finally a ductile failure occurs due to the yielding of steel is in both the model and the test results.

Figure 8.16 shows the measured and predicted load-deflection response of control beams after 90 thermal cycles. As shown in the Figure, the behaviour of this set of results is quite similar to those after 30 thermal cycles.

Figure 8.17 compares the measured and predicted load-deflection curves of the beams retrofitted with one strip bonded on the tension face and exposed to no thermal cycles. It may be seen that up to a load of 25 kN, the curve predicted by the model and the actual load-deflection response of the retrofitted beams are almost identical. Thereafter, the curve predicted by the model deviates slightly. This may be due to the constitutive relation of CARDIFRC[®] used in the model, which was derived from a uniaxial tension test and therefore, the transition from linear to non-linear occurs at a lower load. However, if the constitutive relation is derived in bending this transition would have taken place at a higher load. Although the predicted stiffness of the retrofitted beams is slightly lower than that of the test results, the maximum load carrying capacity is well predicted. As can be seen in Table 8.4 the maximum load carrying capacity is 54.29 kN and 51.5 kN for the predicted and measured results, respectively.

Figure 8.18 shows the measured and predicted load-deflection response of beams retrofitted with one strip on the tension face after 30 thermal cycles. It can be seen that the load-deflection response predicted by the model is in a good agreement with the measured results, for both the pre and post peak response. As can be seen in Table 8.4, the maximum load carrying capacity is accurately predicted. The measured and predicted load versus deflection curves of beams retrofitted with one plate on the tension face, after 90 thermal cycles, are shown in Figure 8.19. It may be seen from the Figure that the measured and predicted responses agree closely.

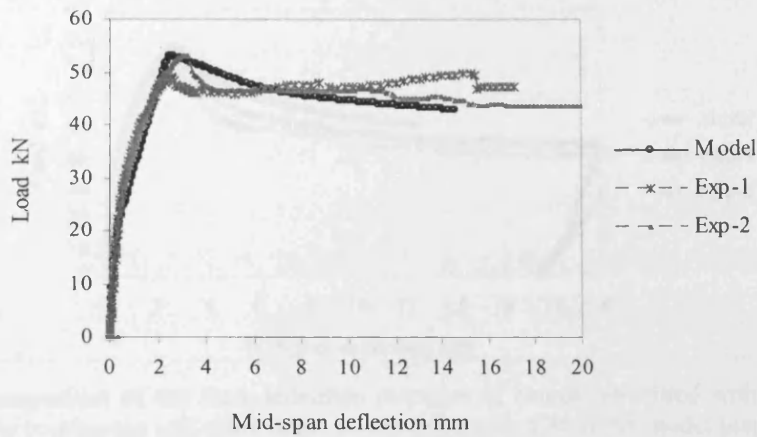


Figure 8.17: Comparison of the load-deflection response of beams retrofitted with one plate on the tension face with that of the model predictions after zero thermal cycles.

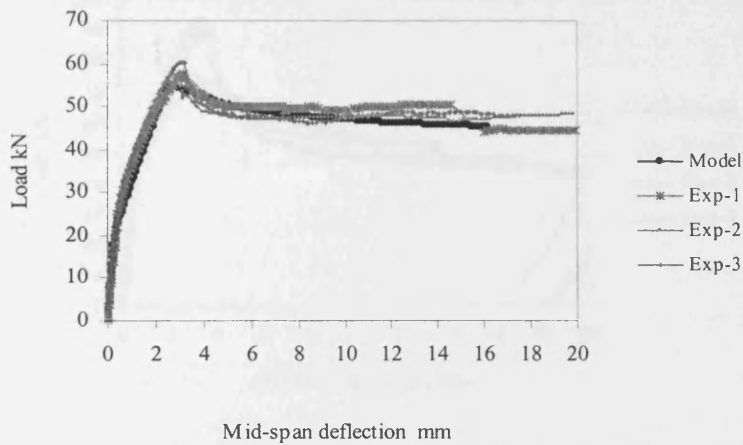


Figure 8.18: Comparison of the load-deflection response of beams retrofitted with one plate on the tension face with that of the model predictions after 30 thermal cycles.

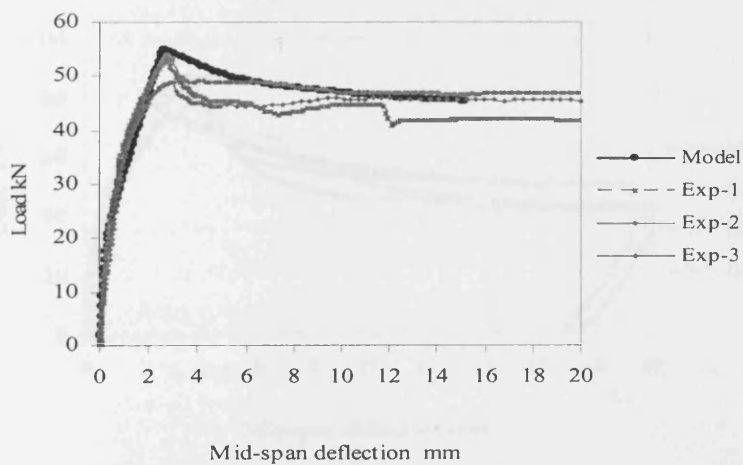


Figure 8.19: Comparison of the load-deflection response of beams retrofitted with one plate on the tension face with that of the model predictions after 90 thermal cycles.

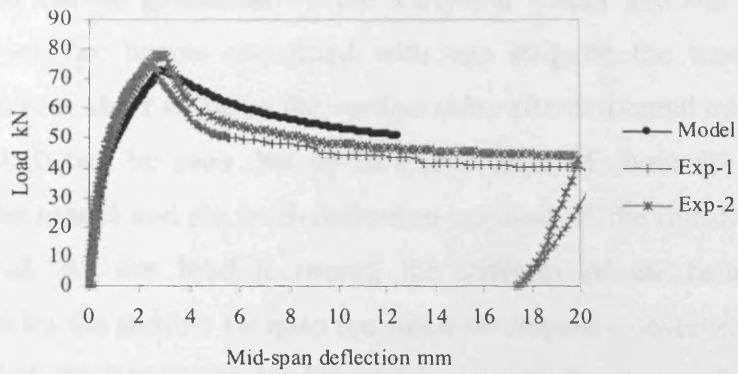


Figure 8.20: Comparison of the load-deflection response of beams retrofitted with one plate on the tension face, two continuous and short strips on the sides with that of the model predictions after zero thermal cycles.

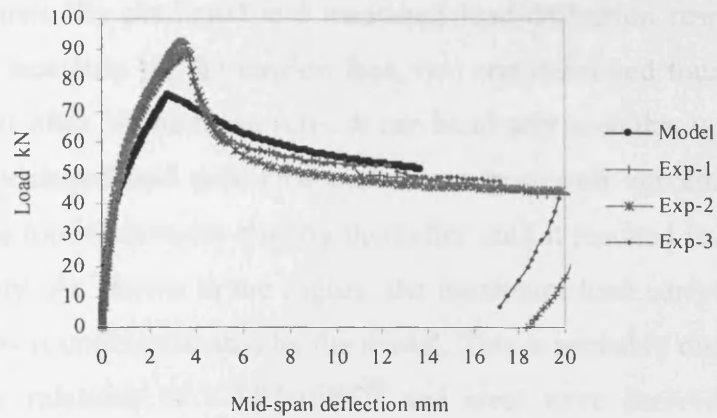


Figure 8.21: Comparison of the load-deflection response of beams retrofitted with one plate on the tension face, two continuous and short strips on the sides with that of the model predictions after 30 thermal cycles.

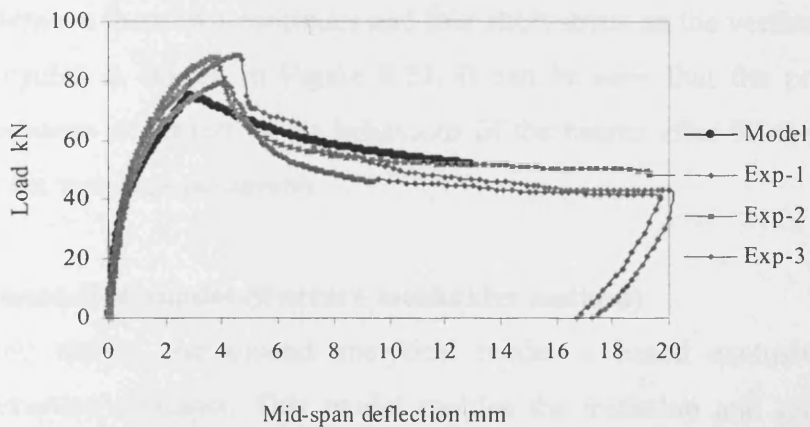


Figure 8.22: Comparison of the load-deflection response of beams retrofitted with one plate on the tension face, two continuous and short strips on the sides with that of the model predictions after 90 thermal cycles.

Load-deflection curves generated by the analytical model and the corresponding measured curves, for beams retrofitted with one strip on the tension face, two continuous and four short strips on the vertical sides after 0 thermal cycles are shown in Figure 8.20. It can be seen that up to a load level of about 45 kN, the curve predicted by the model and the load–deflection response of the retrofitted beams are almost identical. As the load increases, the stiffness of the beams is slightly underestimated by the model. Despite the small discrepancy observed in the Figure the prediction of the maximum load carrying capacity by the model is in a good agreement with the experimental result.

Figure 8.21 shows the predicted and measured load-deflection response of beams retrofitted with one strip on the tension face, two continues and four short strips on the vertical sides after 30 thermal cycles. It can be clearly seen that up to a load of 40 kN both the measured and predicted curves are in a well agreement. The curve predicted by the model deviates slightly thereafter until it reached its maximum load carrying capacity. As shown in the Figure, the maximum load carrying capacity for this set of beams is underestimated by the model. This is probably due to the fact that the constitutive relations of CARDIFRC® and steel were derived only at room temperature.

The load deflection response of measured and predicted of beams retrofitted with one strip on the tension face, two continues and four short strips on the vertical sides after 90 thermal cycles is shown in Figure 8.22. It can be seen that the predicted and measured response is similar to the behaviour of the beams after 30 thermal cycles described in the previous paragraph

8.4 Second analytical model (fracture mechanics method)

As mentioned earlier, the second analytical model is based exclusively on the fracture mechanics concepts. This model mimics the initiation and growth of the flexural crack that eventually leads to the failure of the retrofitted beam. To model the response of a structure based on fracture mechanics, it is necessary to have a good knowledge of the details of the formation and growth of cracks in the structure.

8.4.1 Sequence of crack growth

As discussed in Chapter 7, all the beams were pre-damaged prior to retrofitting. During the process of pre-loading, a few flexural cracks appeared in the beams and opened up. These cracks closed and became invisible to the naked eye, when the load was removed from the beams (Figure. 8.23a).

After the beams were retrofitted, they were loaded again to failure. As the applied load was increased, the existing hairline cracks, resulting from pre-loading, became visible again (Figure. 8.23b). One of these cracks in the pre-damaged beam opened and with a further increase in load this crack opened further and propagated into the tension strip (Figure 8.23c). Even after thermal cycling none of the test beams showed any indication of this crack branching into the interface. The pre-existing crack and the new crack that formed in the tension strip, continued to open until the maximum load was reached (Figure. 8.23d). At this stage the crack could be seen across the entire width of the tension strip.

However, no attempt was made to measure the crack mouth opening displacement at the maximum load because it was too small for accurate measurement. The approximate load levels corresponding to the above sequence of crack growth are shown schematically in Figure. 8.23e.

For beams retrofitted with a tension strip and side strips, the load increased further until the crack in the tension strip extended along the side strips. However, the crack was still within the side strips when the maximum load was reached (Figure 8.24b). It extended beyond the side strips and into the concrete beam after the attainment of the maximum load. The approximate load levels are shown schematically in Figure. 8.24c.

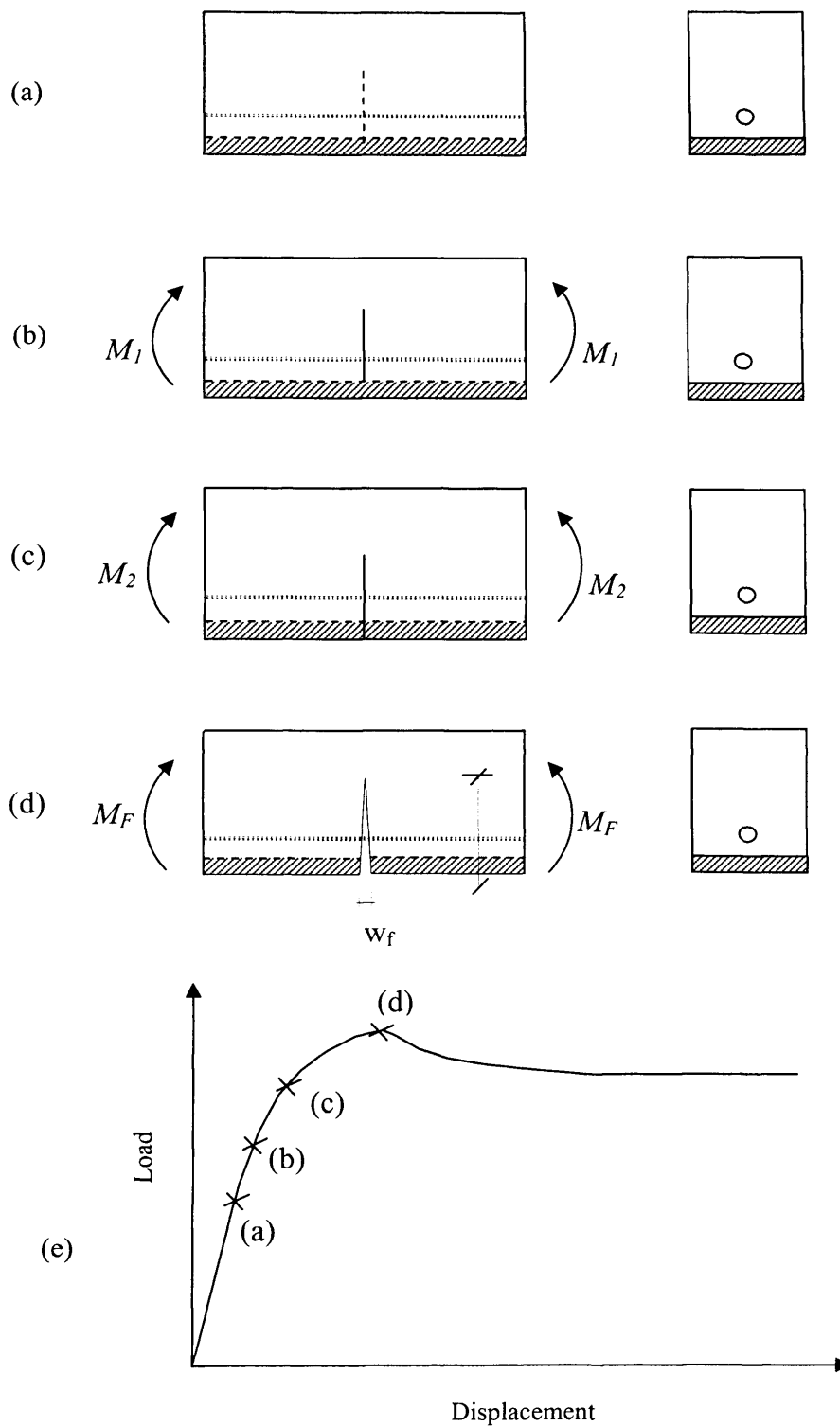


Figure 8.23 Sequence of crack growth in the middle part of the beams retrofitted with one strip: (a) existing crack in the pre-damaged beam, (b) reopening of the existing crack in the pre-damaged beam, (c) propagation and penetration of the dominant crack into the tension strip, (d) opening of the dominant crack, and (e) load levels corresponding to the observed crack growth sequence (After Alaei and Karihaloo, 2003b)

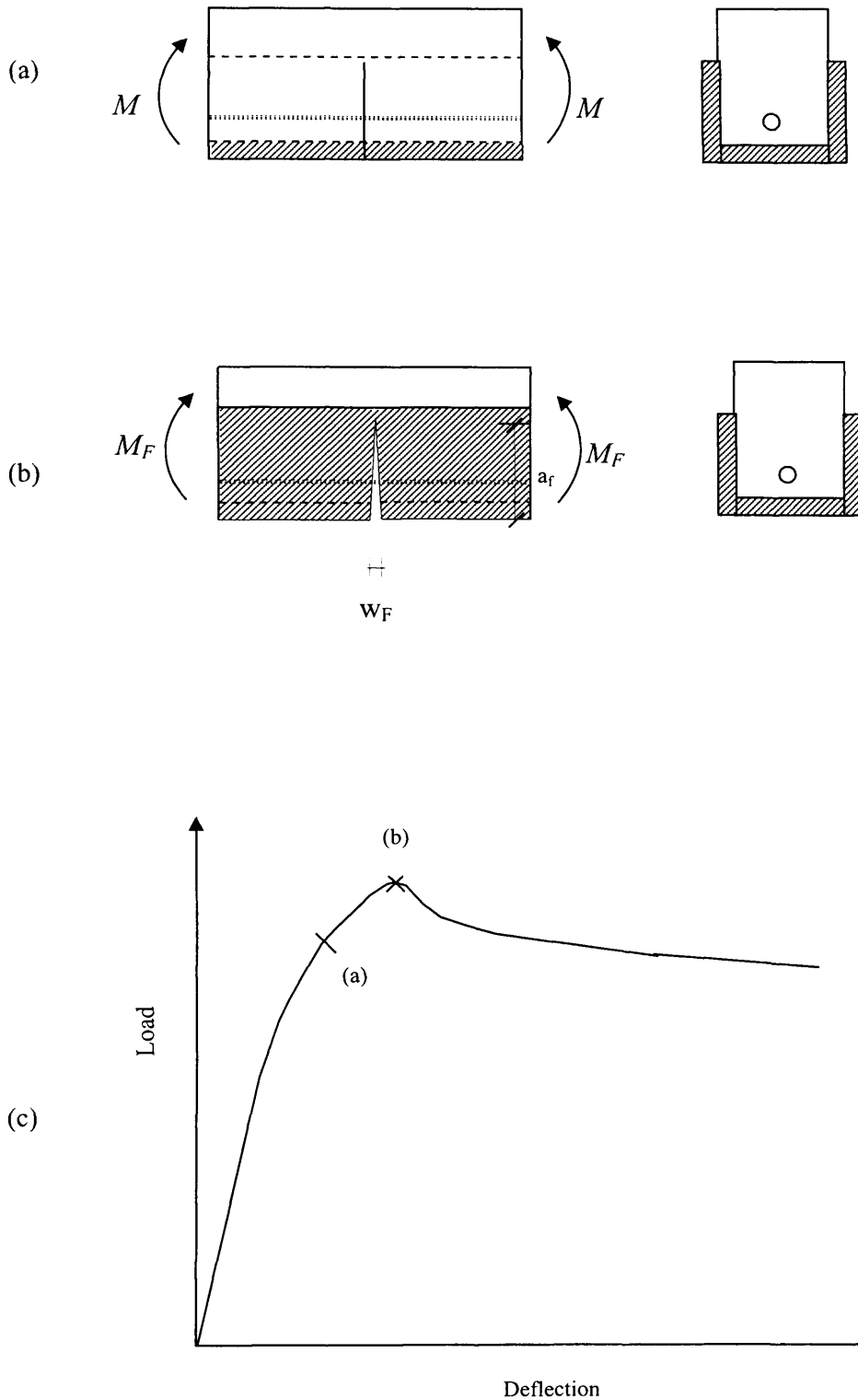


Figure 8.24 Cracking in middle part of beams retrofitted with three strips: (a) when pre-existing crack penetrated into tension strip. For clarity side strip is not shown. Note that stages (a) and (b) of Figure 8.23 are obscured by side strips; (b) at maximum load, and (c) load levels corresponding to stages (a) and (b). (After Alaei and Karihaloo, 2003b)

8.4.2 Modelling of dominant flexural crack

We shall follow the procedure first proposed by Alaei and Karihaloo (2003b) and consider the free body diagram of a part of the retrofitted beam containing the dominant flexural crack and study the effect of different loads on it (Figure 8.25). It can be seen that in addition to the moment due to the applied load, there are three loads which appear in the free body diagram. The first load is due to the bridging force across the crack faces from the reinforcing steel, the second is from the post-peak tension softening response of concrete, and the third is from the bridging stresses in the retrofit strips. It is evident that only the external moment tends to open the crack and the remaining loads tend to close it.

To simplify the computations, it is assumed that the crack profile is always linear. Therefore, a crack can be specified by its depth a and the opening w at its mouth. To compute the moment resistance of the retrofitted beams M_F , the condition of the dominant crack at the maximum load is important. In fact, M_F cannot be found, unless the crack depth (a_F) and the crack mouth opening at the maximum load (w_F) are calculated. This will become clear from the analytical expressions below.

The bridging force from steel F_s is the most significant closing force on the crack faces. There is no definite relationship between the geometrical properties of the crack (w and a) and the bridging force in steel. However, there are some empirical relations, which will be discussed later.

Concrete, even after the attainment of its tensile strength, is capable of carrying residual tensile stresses thanks to its tension softening behaviour (Figure 8.25a). The amount of the stress transmitted along the crack faces depends upon the crack opening; it decreases with an increase in the crack opening. As can be seen in Figure 8.25, the residual tensile stress in concrete σ_c , acts as a closure pressure on the dominant crack faces. This stress varies from f_{ctm} (the tensile strength of concrete) at the crack tip, to nothing where the crack opening equals to the critical crack opening of concrete w_c . If the crack mouth opening w and the crack depth a are given

(Figure. 8.25), the distribution of this bridging stress can be easily worked out from the tension softening diagram of concrete (Figure 8.2).

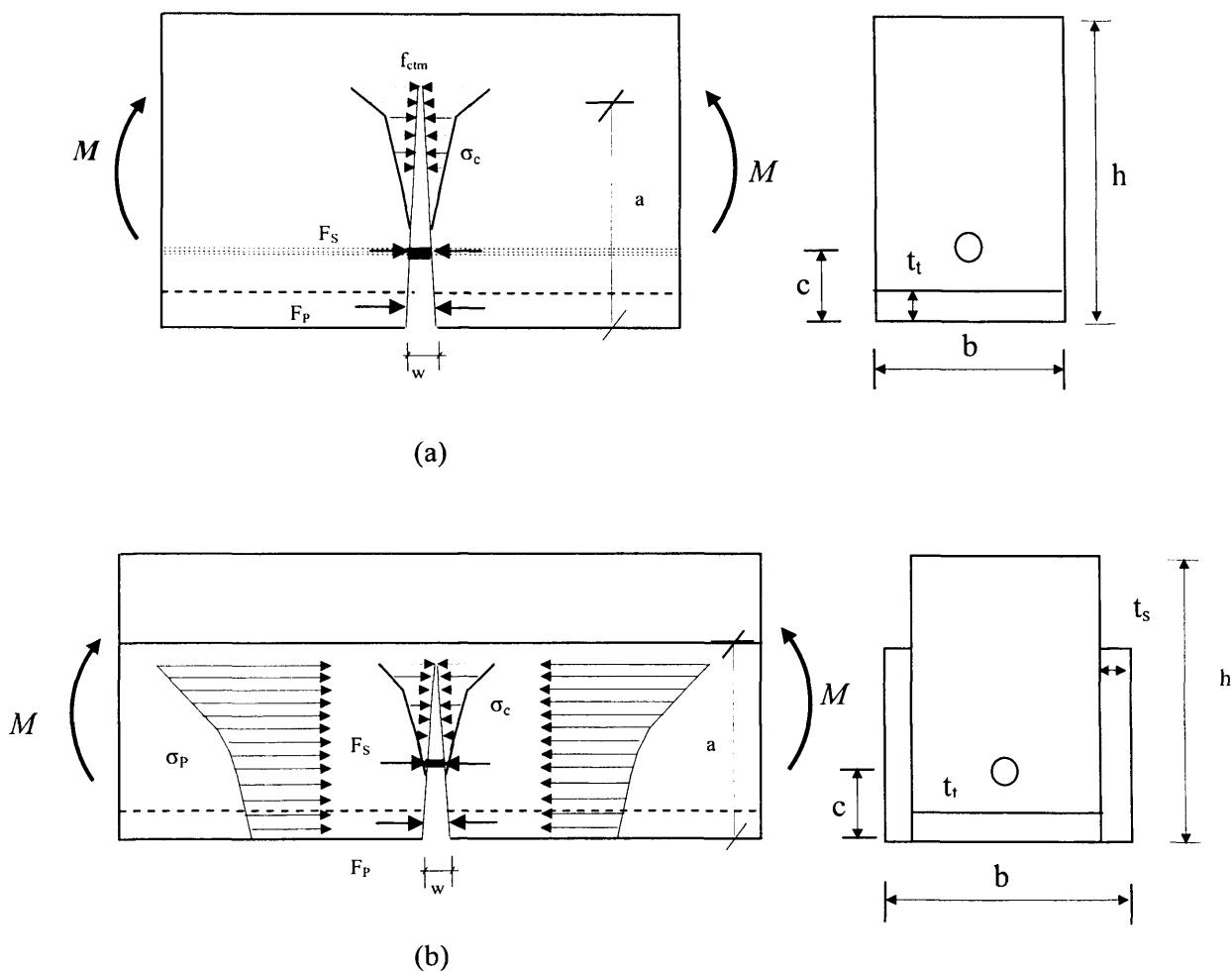


Figure 8.25 Free body diagram of dominant flexural crack in retrofitted beams. Beams retrofitted with (a) one tension strip, and (b) one tension strip and two side strips. (After Alaei and Karihaloo, 2003b)

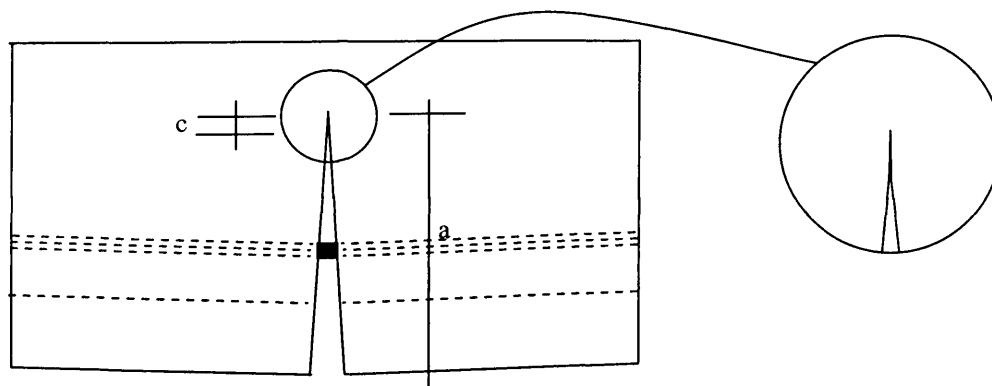


Figure 8.26 Smooth closure of crack faces. (After Alaei and Karihaloo, 2003b)

The effect of the retrofit strips on the dominant crack is very similar to that of the concrete. CARDIFRC[®] with its tension softening behaviour produces a closure pressure on the crack faces, which again is a function of the crack opening (Figure. 8.4).

Next we relate the applied moment M to the crack depth a and crack mouth opening w .

8.4.3 The condition of smooth closure of crack faces

As mentioned in the previous section, when the retrofitted beam is under bending, the resistance to crack opening consists of three different components. The first component is due to the bridging force across the crack faces from the reinforcing steel, the second is from the post-peak tension softening response of concrete, and the third is from the bridging stresses in the retrofit strips. The closure pressure exerted counteracts the opening action of the applied moment M . As the stress at the crack tip is finite, the net stress intensity factor at the crack tip must vanish (Barenblatt 1959). In fact, this requires that the crack faces close smoothly near the tip (see Figure 3.5). This would seem to contradict the assumption of linear crack profile. However, Alaei and Karihaloo (2003b) have shown that the inclusion of non-zero K_I at the crack tip, implied by non-smooth closure of crack tip faces introduces an error of less than 1 percent. We shall therefore assume $K_I = 0$ at the crack tip. The net K_I at the crack tip is obtained by superimposing the stress intensity factors produced at the crack tip by the applied moment (K_{IM}), and the closure forces exerted by steel (K_{IS}), concrete (K_{Iconc}), tension retrofit strips ($K_{I(t-strip)}$), and side retrofit strips ($K_{I(s-strip)}$) (if they are used). The condition of finite stress at the crack tip, i.e. $K_I = 0$ is therefore

$$K_{IM} - K_{IS} - K_{Iconc} - K_{I(t-strip)} - K_{I(s-strip)} = 0 \quad (8.11)$$

The various stress intensity factors appearing in the above equation will be calculated in the following sub-sections

8.4.3.1. Stress Intensity factor due to the applied moment K_{IM}

As mentioned in § 3.8.1 (Equation 3.49) the stress intensity factor produced at the crack tip by the moment M is (Guinea et al., 1998)

$$K_{IM}(\xi) = \frac{M}{h^{3/2}b} Y_M(\xi) \quad (8.12)$$

where ξ is the ratio of the depth of the crack to the height of the beam a/h , b is the width of the beam and $Y_M(\xi)$ is

$$Y_M(\xi) = \frac{6\xi^{1/2}(1.99 + 0.83\xi - 0.31\xi^2 + 0.14\xi^3)}{(1-\xi)^{3/2}(1+3\xi)} \quad (8.13)$$

Substitution (8.13) into (8.12) gives

$$K_{IM} = \frac{M}{h^{3/2}b} \left[\frac{6\xi^{1/2}(1.99 + 0.83\xi - 0.31\xi^2 + 0.14\xi^3)}{(1-\xi)^{3/2}(1+3\xi)} \right] \quad (8.14)$$

8.4.3.2. Stress Intensity factor due to the steel force

Similarly, from equation (3.50) the stress intensity factor produced at the crack tip by the concentrated steel force F_S is (Tada et al., 1985)

$$K_{IS}(\xi) = \frac{F_S}{h^{1/2}b} Y_S(\xi, \beta) \quad (8.15)$$

where $\beta=c/h$, c is the distance from the centre of the reinforcing bar to the bottom of the beam and the function $Y_S(\xi, \beta)$ is given by

$$Y_S(\xi, \beta) = \left\{ \frac{3.52(1-\beta/\xi)}{(1-\xi)^{3/2}} - \frac{4.35-5.28\beta/\xi}{(1-\xi)^{1/2}} + \left[\frac{1.30-0.30(\beta/\xi)^{3/2}}{(1-(\beta/\xi)^2)^{1/2}} + 0.83-1.76\beta/\xi \right] [1-(1-\beta/\xi)\xi] \right\} \frac{2}{\sqrt{\pi\xi}} \quad (8.16)$$

8.4.3.3 Stress intensity factor due to the residual tensile stress of concrete K_{Iconc}

To calculate the stress intensity factor at the crack tip produced by the residual tensile stress of concrete, this stress is discretized into infinitely many concentrated forces. Each force is applied over small crack segments of length dy at a distance $y(=y^*h)$ from the bottom of the crack (see Figure 8.27). The magnitude of each force is

$$dF_c = \sigma_c (w_y) b dy \equiv \sigma_c (w_y) b h dy^* \quad (8.17)$$

where

$$w_y = w(1-y/a) = w(1-y^*/\xi) \quad (8.18)$$

In the above equations, w_y is the crack opening at the level of the point load dF_c .

Now, using equation (8.15) the stress intensity factor produced by this point load can be calculated

$$dK_{Iconc} = \frac{\sigma_c (w_y) b h}{h^{1/2} b} Y_S(\xi, y^*) dy^* \quad (8.19)$$

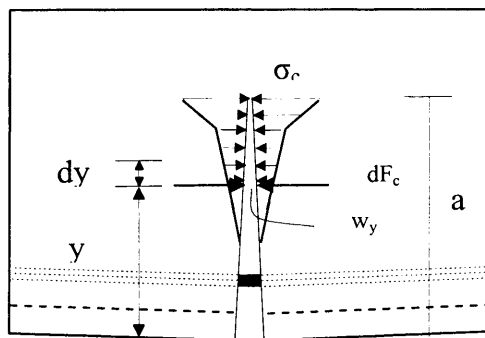


Figure 8.27 Towards the discretisation of the bridging stresses in concrete (After Alaei and Karihaloo, 2003b)

The relation in equation (8.19) is integrated over the length of the crack in concrete (i.e. excluding the retrofit strip)

$$K_{Iconc}(\xi) = \int_{t_r/h}^{\xi} \sigma_C(w_y) h^{1/2} Y_S(\xi, y^*) dy^* \quad (8.20)$$

where t_r is the thickness of the retrofit strip and $Y_S(\xi, y^*)$ is

$$Y_S(\xi, y^*) = \left\{ \frac{3.52(1-y^*/\xi) - 4.35 - 5.28y^*/\xi}{(1-\xi)^{3/2} (1-\xi)^{1/2}} + \left[\frac{1.30 - 0.30(y^*/\xi)^{3/2}}{(1-(y^*/\xi)^2)^{1/2}} + 0.83 - 1.76y^*/\xi \right] \left[1 - (1-y^*/\xi)\xi \right] \right\} \frac{2}{\sqrt{\pi\xi}} \quad (8.21)$$

8.4.3.4. Stress intensity factor due to the closure force of tension strip $K_{I(t-strip)}$

To determine $K_{I(t-strip)}$ the magnitude of the closure force F_P exerted by the tension retrofit strip is calculated using the corresponding crack opening w_P at the level of F_P

$$F_P = \sigma_P(w_P) b t_r \quad (8.22)$$

where w_P can be calculated from the following equation:

$$w_P = w(1-t_r/2a) \equiv w\{1-t_r/(2h\xi)\} \quad (8.23)$$

Substitution of (8.22) into (8.15) gives the stress intensity factor produced at the crack tip by the closure force exerted by the tension strip

$$K_{I(t-strip)}(\xi) = \frac{\sigma_P(w_P) t_r}{h^{1/2}} Y_S\left(\xi, \frac{t_r}{2h}\right) \quad (8.24)$$

where the geometry function $Y_S\left(\xi, \frac{t_r}{2h}\right)$ is

$$Y_S\left(\xi, \frac{t_r}{2h}\right) = \left\{ \frac{3.52(1-t_r/2h\xi) - 4.35 - 5.28t_r/2h\xi}{(1-\xi)^{3/2} (1-\xi)^{1/2}} + \left[\frac{1.30 - 0.30(t_r/2h\xi)^{3/2}}{(1-(t_r/2h\xi)^2)^{1/2}} + 0.83 - 1.76t_r/2h\xi \right] \left[1 - (1-t_r/2h\xi)\xi \right] \right\} \frac{2}{\sqrt{\pi\xi}} \quad (8.25)$$

8.4.3.5 Stress intensity factor due to the closure force of side strip $K_{I(s-strip)}$

The stress intensity factor produced at the crack tip by the closing force of the side strips can be calculated in the same manner as K_{Iconc} . Dividing each of the side strips into infinitesimal elements of height $dy(=hdy^*)$, the closure force on each element of the two side strips is

$$dF_{SP} = 2\sigma_P (w_y) t_S dy \equiv 2 \sigma_P (w_y) t_S h dy^* \quad (8.26)$$

where t_S is the thickness of the side strip, w_y is the crack opening at the level of the closure force dF_{SP}

$$w_y = w(1-y/a) = w(1-y^*/\xi) \quad (8.27)$$

Substitution of (8.26) into (8.15) gives the stress intensity factor produced by this point load at the crack tip

$$dK_{I(s-strip)} = \frac{2\sigma_P (w_y) t_S h^{1/2}}{b} Y_S (\xi, y^*) dy^* \quad (8.28)$$

To calculate $K_{I(s-strip)}$, this relation is integrated as follows:

$$K_{I(s-strip)} (\xi) = \int_0^{\alpha} \frac{2\sigma_P (w_y) t_S h^{1/2}}{b} Y_S (\xi, y^*) dy^* \quad (8.29)$$

where α is $\min \{\xi, h_s/h\}$ (i.e. the smaller of α or h_s), h_s is the height of the side strips. The choice of the upper integration is dictated to the fact that, when the crack depth exceeds the height of the side strip, the side strips do not exert any closure pressure over the part of the crack that is beyond the side strips. The geometry function $Y_S(\xi, y^*)$ is

$$Y_S(\xi, y^*) = \left\{ \begin{array}{l} \frac{3.52(1-y^*/\xi)}{(1-\xi)^{3/2}} - \frac{4.35-5.28y^*/\xi}{(1-\xi)^{1/2}} \\ + \left[\frac{1.30-0.30(y^*/\xi)^{3/2}}{(1-(y^*/\xi)^2)^{1/2}} + 0.83-1.76y^*/\xi \right] [1-(1-y^*/\xi)\xi] \end{array} \right\} \frac{2}{\sqrt{\pi\xi}} \quad (8.30)$$

Finally, substitution (8.14), (8.15), (8.20), (8.24), and (8.29) into (8.11) gives

$$\begin{aligned} & \frac{M}{h^{3/2}b} Y_M(\xi) - \frac{F_S}{h^{1/2}b} Y_S(\xi, \beta) - \int_{t_i/h}^{\xi} \sigma_c(w_y) h^{1/2} Y_S(\xi, y^*) dy^* - \frac{\sigma_P(w_P)}{h^{1/2}} Y_S(\xi, \frac{t_i}{2h}) - \\ & \int_0^{\alpha} \frac{2\sigma_P(w_y) t_s h^{1/2}}{b} Y_S(\xi, y^*) dy^* = 0 \end{aligned} \quad (8.31)$$

8.4.4 Crack opening compatibility equation

In addition to the condition of smooth closure of crack faces at its tip, we must consider the compatibility of crack opening displacement of a retrofitted beam (Leung, 1998). The crack opening displacement can again be written as the vectorial sum of the contribution from the applied bending moment and the closure forces exerted by steel, concrete and retrofit strips. The compatibility condition of the crack opening need be satisfied only at the level of the steel reinforcement, because of the assumed known (i.e. linear) variation along the length of the crack:

$$(w_S)_M - (w_S)_S - (w_S)_{conc} - (w_S)_{t-strip} - (w_S)_{s-strip} = w_S \quad (8.32)$$

where $(w_S)_i$ are the crack opening displacement at the level of the steel bar produced by the applied bending moment and the closure forces exerted by steel, concrete, tension strip, and side strips, respectively. Note that the crack opening w_S at the level of the reinforcement is not known, but is to be determined. Each term in the left hand side of (8.32) can be expressed in terms of the corresponding compliance coefficients. For instance, the crack opening at the level of the steel bar produced by the applied moment is

$$(w_S)_M = \lambda_{SM} M \quad (8.33)$$

where λ_{SM} (compliance coefficient) is the crack opening at the level of steel when a unit bending moment is applied to the crack. The compliance coefficients can be computed from energy principles and Clapeyron's theorem (see § 3.8.1). The following sections present the relations for the computation of the required compliance coefficients.

8.4.4.1 Compliance coefficient due to a unit moment λ_{SM}

The derivation of the compliance coefficient due to a unit moment has been presented in § 3.8.1. In this section equation (3.53) can be rewritten as (Bosco and Carpinteri, 1992)

$$\lambda_{SM} = \frac{2}{hbE} \int_{\beta}^{\xi} Y_M(x) \cdot Y_S(x, \beta) dx \quad (8.34)$$

where E is the Young modulus of concrete, and $Y_S(x, \beta)$ is the geometry function given by (8.16). The crack opening due to the applied moment is obtained by substituting equation (8.34) into (8.33).

$$(w_S)_M = \frac{2M}{hbE} \int_{\beta}^{\xi} Y_M(x) \cdot Y_S(x, \beta) dx \quad (8.35)$$

8.4.4.2 Compliance coefficient due to a unit steel force λ_{SS}

Similarly, the compliance coefficient due to a unit steel force is given by (Bosco and Carpinteri, 1992)

$$\lambda_{SS} = \frac{2}{bE} \int_{\beta}^{\xi} Y_S^2(x, \beta) dx \quad (8.36)$$

The crack opening $(w_S)_S$ is then obtained as

$$(w_S)_S = \lambda_{SS} F_S \quad (8.37)$$

8.4.4.3 Compliance coefficient due to a unit tensile force in concrete λ_{SConc}

To work out the crack opening at the level of the steel bar produced by tension softening of concrete $(w_s)_{conc}$, the continuous closure stresses exerted by concrete is again discretized into infinitely many concentrated loads dF_c , each acting on an infinitesimal crack length dy (see Figure 8.27). The crack opening $(w_s)_{dF_c}$ produced by one of these concentrated loads is calculated by using the compliance method. The corresponding compliance coefficient λ_{S-dF_c} can again be computed from energy principles (Bosco and Carpinteri, 1992) considering the point load dF_c acting simultaneously with the steel force F_s

$$\lambda_{S-dF_c} = \frac{2}{E} \int_{\beta^*}^{\alpha} Y_S(x, \beta) Y_S(x, y^*) dy^* \quad (8.38)$$

where β^* is $\max \{y^*, \beta\}$ (i.e. the larger of y and c). Multiplying this compliance factor by dF_c from equation (8.17) gives

$$(w_s)_{dF_c} = \frac{2\sigma_c(w_y)hdy^*}{E} \int_{\beta^*}^{\xi} Y_S(x, \beta) Y_S(x, y^*) dy^* \quad (8.39)$$

To calculate the crack opening at the level of reinforcement due to the tension softening of concrete, equation (8.39) is integrated over the length of the crack in concrete

$$(w_s)_{conc} = \int_{l_1/h}^{\xi} \left\{ \frac{2\sigma_c(w_y)h}{E} \int_{\beta^*}^{\xi} Y_S(x, \beta) Y_S(x, y^*) dx \right\} dy^* \quad (8.40)$$

8.4.4.4 Compliance coefficient due to a unit force in retrofit tension strip $\lambda_{S(t-strip)}$

Using the same procedure as above, the compliance coefficient due to a unit force in the tension retrofit strip $\lambda_{S-(t-strip)}$ can be written as

$$\lambda_{S-(t-strip)} = \frac{2}{Eb} \int_{\beta}^{\xi} Y_S(x, \beta) Y_S\left(x, \frac{t_t}{2h}\right) dx \quad (8.41)$$

Multiplying this compliance factor by F_p from equation (8.22) gives

$$(w_S)_{t-strip} = \frac{2\sigma_p(w_p)t_t}{E} \int_{\beta}^{\xi} Y_S(x, \beta) Y_S\left(x, \frac{t_t}{2h}\right) dx \quad (8.42)$$

8.4.4.5 Compliance coefficient due to a unit force in retrofit side strips $\lambda_{S-(s-strip)}$

To calculate $(w_S)_{S-strip}$, exactly the same procedure as that adopted for concrete is followed. equation (8.38) in this case becomes

$$\lambda_{S-dF_{sp}} = \frac{2}{Eb} \int_{\beta}^{\xi} Y_S(x, \beta) Y_S(x, y^*) dx \quad (8.43)$$

Multiplying this compliance coefficient by the magnitude of the point load dF_{sp} from equation (8.26) gives the crack opening produced by this point load

$$(w_S)_{dF_{sp}} = \frac{4\sigma_p(w_y)t_s h}{Eb} dy^* \int_{\beta}^{\xi} Y_S(x, \beta) Y_S(x, y^*) dx \quad (8.44)$$

Again, to compute the crack opening at the level of steel due to the forces exerted by the side strips, equation (8.44) is integrated over the length of the cracked side strips

$$(w_S)_{S-strip} = \frac{4t_s h}{Eb} \int_0^{\alpha} \left\{ \sigma_p(w_y) \int_{\beta}^{\xi} Y_S(x, \beta) Y_S(x, y^*) dx \right\} dy^* \quad (8.45)$$

All the crack openings mentioned in the right hand side of equation (8.32) have now been expressed in terms of the corresponding forces and the geometry of the crack and the beam, and of the Young modulus of concrete

$$\begin{aligned}
 & \frac{2M}{hbE} \int_{\beta}^{\xi} Y_M(x) \cdot Y_S(x, \beta) dx - \frac{2F_S}{bE} \int_{\beta}^{\xi} Y_S^2(x, \beta) dx \\
 & - \frac{2h}{E} \int_{t_i/h}^{\xi} \left\{ \sigma_c(w_y) \int_{\beta}^{\xi} Y_S(x, \beta) Y_S(x, y^*) dx \right\} dy^* - \frac{2\sigma_P(w_P) t_i}{E} \int_{\beta}^{\xi} Y_S(w, \beta) Y_S\left(x, \frac{t_i}{2h}\right) dx - \\
 & \quad \frac{4t_S h}{Eb} \int_{\beta}^{\alpha} \left\{ \sigma_P(w_y) \int_{\beta}^{\xi} Y_S(x, \beta) y_S(x, y^*) dx \right\} dy^* = w_S \quad (8.46)
 \end{aligned}$$

It should be mentioned that the constitutive relation of CARDIFRC[®] (post-peak response) and the material properties of concrete and steel described earlier in this chapter will be used. The bridging closure forces exerted by concrete and CARDIFRC[®] strips can be easily worked out from the corresponding relations. However, the relationship between the geometrical properties of a crack and the bridging force exerted by steel crossing this is quite complicated and this will be discussed in the next section.

8.4.5 Bridging force exerted by steel F_S

The bridging force from steel F_S is a very significant closing force on the crack faces. There is no definite relationship between the geometrical properties of the crack (w and a) and the bridging force in steel. However, some semi-theoretical and empirical formulas have been proposed and will be presented in the following.

8.4.5.1 Carpinteri's approximation

Bosco and Carpinteri (1992) assumed that the displacement discontinuity in a cracked cross section at the level of reinforcement is zero up to the moment of yielding or slippage of the reinforcement. They considered a rigid perfectly plastic behaviour of the reinforcement and obtained the moment at plastic flow or slippage. In fact, they assumed that the reinforcement steel yields as soon as the crack at this level starts to open. It is obvious that this simplifying assumption will overestimate the moment resistance of the beam. According to this assumption, the bridging force exerted by steel is simply

$$F_S = A_S f_y \quad (8.47)$$

where f_y is the yield stress of the reinforcing bar and A_s the area of steel. The steel force is therefore uncoupled from the crack opening displacement at the level of steel.

8.4.5.2 Kaar's formula

In another study, Kaar and Mattock (1963) expressed the tensile stress in steel as a function of the crack width w_s at the level of deformed bar reinforcement

$$f_s = \frac{F_s}{A_s} = \frac{11876.5 w_s}{A^{1/4}} \quad (8.48)$$

where A is the area of concrete surrounding each bar ($A = A_e/n$, where n is the number of bars) (see Figure 28)

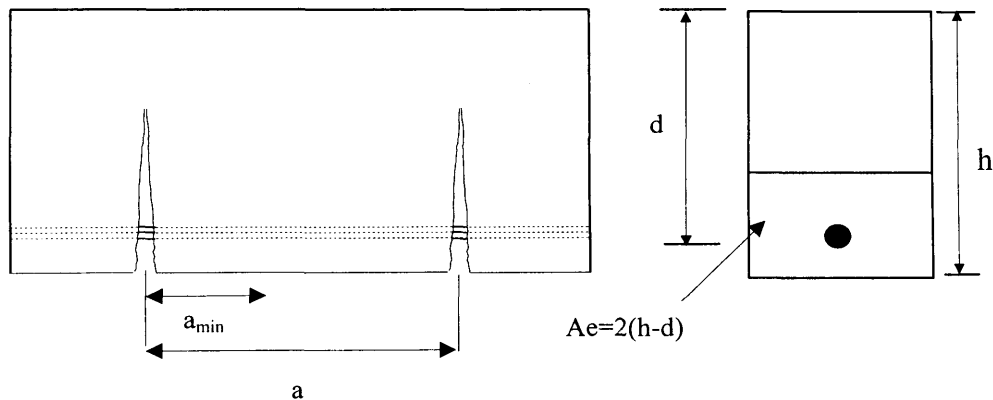


Figure 8.28 Cracking of a reinforced concrete member under flexure (After Park and Paulay 1975)

Alaee and Karihaloo (2003b) used the aforementioned Carpinteri's approximation and Kaar's formula and concluded that none of these has been found to be consistent with their test results. They found that the model results based on Carpinteri's approximation were higher than the test results and those based on the Kaar's formula were significantly lower. Moreover, their analyses showed that the crack opening at the maximum load was not zero as Carpinteri assumes or as large as Kaar proposes.

8.4.5.3 Modified Kaar's formula

Lange-Kornbak and Karihaloo (1999) conducted an experimental programme and compared the test results with approximate nonlinear fracture mechanical prediction of the ultimate capacity of three-point bend, singly-reinforced concrete beams. They found that Kaar's formula (8.48) overestimates the crack opening by the factor of 3.5 to 4. Alaei and Karihaloo (2003b) further improved Kaar's formula by calibrating the results against the test data with the least variation. This calibration suggested the following relationship between the tensile stress in steel and the crack width at the level of deformed bar

$$f_s = \frac{F_s}{A_s} = \frac{4.8 \times 11876.5 w_s}{A^{1/4}} \quad (8.49)$$

Due to the similarity between the test beams in Alaei and Karihaloo (2003b) and those in the present study equation (8.49) will be used in the analysis as the bridging force of steel.

8.4.6 Evaluation of moment resistance of the beams

As mentioned in the previous sections, from the fracture mechanics point of view, two equations should be simultaneously satisfied for a flexural crack; the equation of smooth closure of the crack faces (8.31) and the equation of the crack opening compatibility (8.46). The unknown parameters in these equations are the crack depth a , the crack mouth opening w and the applied moment M .

The moment resistance of the beams was computed in four stages:

- First, the equation of smooth closure of the crack faces (8.31) was solved for all the possible crack depths and crack mouth openings, and the corresponding moment M was calculated.
- Next, the equation of the crack opening compatibility (8.46) was solved for the same ranges of values of a and w .



- The results of the previous two steps were compared and the intersection of the two sets identified. This set satisfies both the smooth closure condition (8.31) and the crack opening compatibility equation (8.46).
- Among the set of values identified in the previous step, the maximum moment was selected. In fact, this moment M_F is the moment resistance of the beam, and the corresponding crack length a_F and crack mouth opening w_F describe the condition of the dominant flexural crack at the maximum moment.

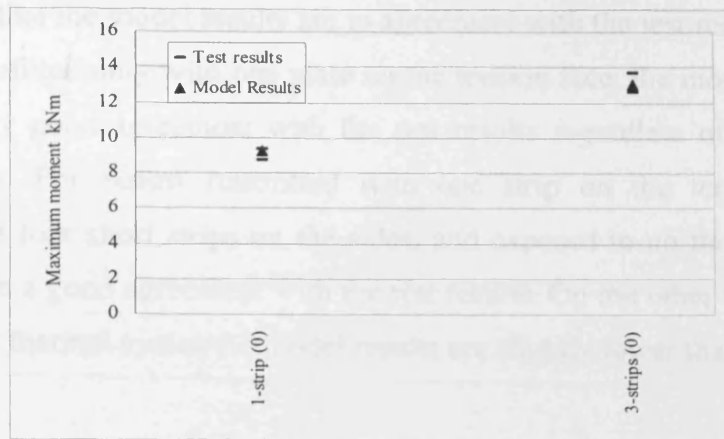
A flowchart of the above procedure is given in Appendix C.

8.4.7 Model results

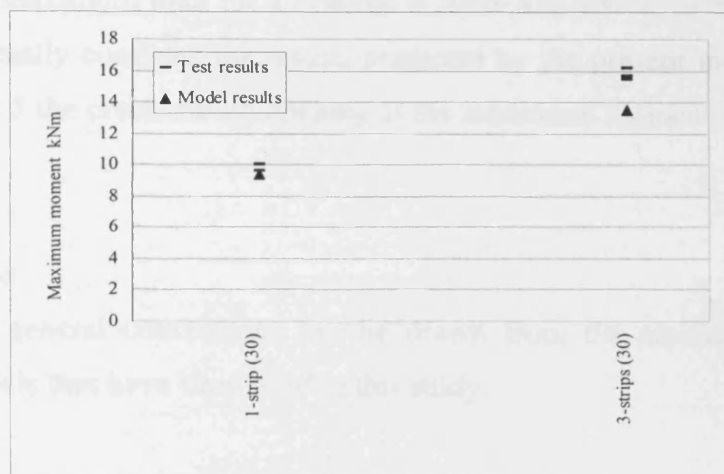
The method described in § 8.4.6 was applied to the critical section of all test beams (i.e. the section in which the dominant flexural crack forms). Their moment resistance M_F , crack mouth opening w_F and crack depth a_F at the maximum load were calculated. Table 8.5 gives the model results for the retrofitted beams (beams retrofitted with one strip on the tension face and beams retrofitted with one strip on the tension face, two continuous and four short strips on the sides) after, 0, 30 and 90 thermal cycles. Figure 8.29 compares the moment resistance of the beams predicted by the model with the test results.

Table 8.5 Crack opening w_F , crack depth a_F and the moment resistance M_F of the beams at the maximum load predicted by the model after 0, 30 and 90 thermal cycles.

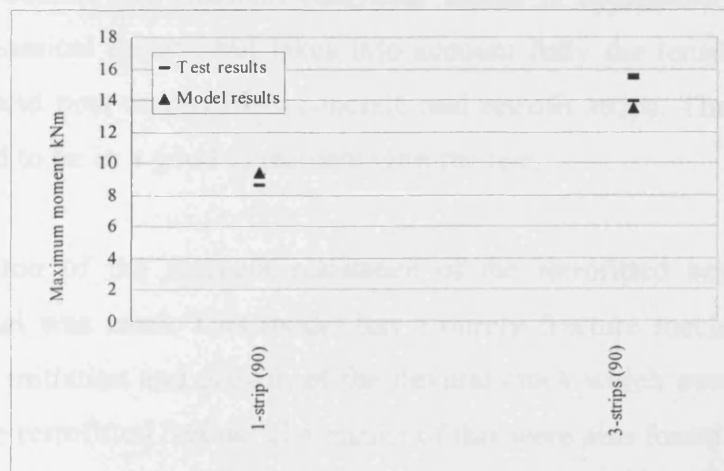
Configuration of retrofitting at critical section	Results	Thermal cycles		
		0	30	90
	w_F (mm)	0.12	0.11	0.11
	a_F (mm)	112	110	111
	M_F (kNm)	9.25	9.41	9.41
	w_F (mm)	0.13	0.12	0.14
	a_F (mm)	84	82	82
	M_F (kNm)	13.01	13.52	13.48



(a)



(b)



(c)

Figure 8.29 Comparison of the moment resistance of retrofitted beams with the prediction of the model after: (a) 0 thermal cycles, (b) 30 thermal cycles and (c) 90 thermal cycles.

It can be seen that the model results are in agreement with the test results. Moreover, for beams retrofitted only with one plate on the tension face, the model results seem to be in a very good agreement with the test results regardless of the number of thermal cycles. For beams retrofitted with one strip on the tension face, two continuous and four short strips on the sides, and exposed to no thermal cycles the model is also in a good agreement with the test results. On the other hand, for beams after 30 and 90 thermal cycles the model results are slightly lower than the test.

It has been observed in the experimental program (Chapter 7) that the crack mouth opening at the maximum load for all beams is finite and visible to naked eyes. This observation actually confirms the results predicted by the present model. As can be seen in Table 8.5 the crack mouth opening at the maximum moment resistance is not zero.

8.5 Conclusions

The following general conclusions can be drawn from the classical and fracture mechanics models that have been used in this study.

To predict the moment resistance and the load-deflection behaviour of the control and retrofitted beams, the classical analytical model is applicable. This model is based on the classical theory, but takes into account fully the tensile contributions (i.e. pre-crack and post-crack) from concrete and retrofit strips. The results of this model are found to be in a good agreement with the test.

For the prediction of the moment resistance of the retrofitted beams, a fracture mechanics model was used. This model has a purely fracture mechanics approach and follows the initiation and growth of the flexural crack which eventually leads to the failure of the retrofitted beams. The results of this were also found to be in a good agreement with the test results.

Chapter 9

Conclusions and recommendation for future work

9.1 Conclusions

Detailed conclusions of each aspect of the investigation have been drawn and reported at the end of each Chapter. This Chapter therefore provides a brief and succinct summary of these major conclusions.

- The mechanical properties of NSC and HSC are improved after 30 thermal cycles, but not so after 90 thermal cycles. The increase in the properties after 30 thermal cycles is probably due to the continued hydration of unhydrated cement. However, the slight reduction after 90 thermal cycles is believed to be due to the initiation of microcracks between the cement paste and aggregate (Chapters 5 and 6).
- The mechanical properties of CARDIFRC[®] are improved even after 90 thermal cycles. This could be attributed to some degree to the continued hydration of unhydrated cement. The major increase is most likely due to the presence of micro-silica that activates the secondary reaction. The presence of fibres seems to counteract any possible deterioration due to microcracking (Chapter 5).
- The fracture properties, namely the size-dependent fracture energy $G_f(\alpha)$, size-independent fracture energy G_F , and the brittleness of NSC and HSC are slightly increased after 30 thermal cycles, but not so after 90 thermal cycles. The increase in these properties after 30 thermal cycles is probably due to the partial expulsion of capillary water. However, the slight reduction after 90 thermal cycles could be due to the initiation of microcracks at the interface of cement paste and aggregate. These microcracks degrade the material resistance against cracking, and make the material more brittle (Chapters 5 and 6).
- The wedge splitting test has been found to be an efficient technique to evaluate the bond performance of NSC and HSC repaired with CARDIFRC[®]. By using this technique, CARDIFRC[®] has been found to be a successful

material for repairing NSC and HSC. The repair can be achieved by adhesive bonding and direct casting (Chapters 5 and 6).

- To prevent delamination or interfacial fracture, both CARDIFRC[®] and the parent concrete mating surfaces should be roughened. Moreover, to further improve the bond between the adhesive and parent concrete, a thin film of cement paste on the smooth cast surface of the parent concrete must be mechanically removed. Removing such film will therefore expose the aggregate, thus creating a rough surface. The rough substrate surface leads to higher interface toughness which delays interface crack propagation, forcing the crack to kink into the weaker material and to eventually propagate through the concrete (Chapters 5 and 6).
- It has been found (Chapters 5 and 6) that the measured fracture energy and the maximum load carrying capacity of bonded specimens change as the notch to depth ratio changes. As the notch to depth ratio increases the fracture energy and maximum load decrease.
- The size-independent fracture energy G_F of CARDIFRC[®] bonded specimens after thermal cycling follows the same trend as that of control specimens; it increases slightly after 30 cycles and then drops slightly after 90 cycles (Chapters 5 and 6).
- No visual deterioration or bond degradation was observed after thermal cycling of the CARDIFRC[®] bonded specimens attesting to the good thermal compatibility between the CARDIFRC[®] and concrete (Chapters 5 and 6).
- Thermal cycling can increase the maximum load carrying capacity of reinforced concrete beams. This is because the thermal cycling regime activates the hydration of the remaining unhydrated cement (Chapter 7).
- Retrofitting RC beams with CARDIFRC[®] strips bonded to the tension face only improves the load carrying capacity and the serviceability of the beam

(i.e. reduce crack opening). The increase in failure load can be up to 23 percent. With temperature cycling the failure load of such beams can increase by up to 36 percent after 30 thermal cycles and 35 percent after 90 thermal cycles (Chapter 7).

- To achieve a very high load carrying capacity and stiffness and also to prevent shear failure, CARDIFRC[®] strips should also be bonded to the sides of the beams. This configuration of retrofitting can increase the failure load by up to 86 percent. With thermal cycling, the failure load can be increased to 90 and 87 percent after 30 and 90 thermal cycles, respectively. Therefore, the room temperature figure provides a safe value for design at elevated temperature (Chapter 7).
- The adhesive bonding technique can be applied even in hot environment, since the findings of this work showed that no bond degradation was observed after thermal cycling of the retrofitted beams. This is due to the good thermal compatibility between the CARDIFRC[®] and concrete. In fact, retrofitting concrete beams using CARDIFRC[®] strips does not suffer from the drawbacks of the existing techniques (Chapter 8).
- Two analytical models for the prediction of the moment resistance of the retrofitted beams can be used. The first model is based on the classical strength theory, but takes into account fully the tensile contributions (i.e. pre-peak and post-peak) from concrete and CARDIFRC[®]. The second analytical model is based on the fracture mechanics concepts. This model mimics the initiation and growth of the flexural crack that eventually leads to the failure of the retrofitted beam. The results of these models are found to be in a good agreement with the test results (Chapter 8).

9.2 Recommendations for future work

- Since the thermal cycling program conducted in this thesis did not control humidity, it is therefore recommended that future research utilises an environmental chamber that allows both temperature and humidity control.

Using this chamber, it will be possible to simulate precisely the hot wet environment, and consequently the test results will be applicable in tropical regions.

- To develop an extensive evaluation of the effect of thermal cycling on concrete it is recommended that experiments containing a greater number of cycling intervals, in addition to a larger number of cycles, are performed.
- In order to verify the experimental work (control and CARDIFRC[®] bonded to NSC and HSC) (Chapters 6 and 7), a parametric analytical study is essential to correlate the experimental results.
- To further improve the model results (Chapter 8), it is recommended to evaluate the constitutive relation of CARDIFRC[®] after thermal cycling.
- In order to avoid any possible shear failure for beams retrofitted with one strip on the tension face, two continuous and four short strips on the sides, it is suggested that a continuous strip should cover the entire side length of the beam, thus eliminating joints particularly in the areas of maximum shear force.

List of References

List of References

Abdalla, H.M. and Karihaloo B.L. (2003). Determination of size-independent specific fracture energy of concrete from three-point bend and wedge splitting tests, *Magazine of Concrete Research*, **55**(2), pp. 133-141.

Abdel-Fattah, H. and Hamoush, S. (1997). Variation of the fracture toughness of concrete with temperature. *Construction and Building Materials*, **11**(2), pp 105-108.

Abousaif, H. F. (1997). Damage and fracture behaviour of concrete, PhD Thesis, Division of Civil Engineering, School of Engineering, Cardiff University, Wales.

ACI (2001). *Guide for the Design and Construction of Externally Bonded FRP Systems for Strengthening Concrete Structures*, Committee 440 Draft Document, *American Concrete Institute*, Farmington Hills, MI, USA.

ACI Committee 446.1R. (1991). Fracture mechanics of concrete: Concepts, Models and Determination of Material Properties, *American Concrete Institute*, Detroit, USA.

Adhikary, B. B., Mutsuyoshi, H. and Sano, M. (2000). Shear strengthening of reinforced concrete beams using steel plates bonded on beam web: experiments and analysis, *Construction and Building Materials*, **14**(5), pp. 237-244.

Alaee, F. (2002) Retrofitting of concrete structures using high performance fibre reinforced composite (HPFRCC), PhD. Thesis, Cardiff University. U.K.

Alaee, F. J., Benson, S. and Karihaloo, B. L. (2001). Strengthening of RC beams with High Performance Cementitious Composites, *Proceedings International Conference on Civil Engineering*, Technical Committee ICCE (eds), Interline Publishing, Bangalore, India, pp.1-13.

List of References

Alaee, F.J. and Karihaloo B. L. (2003a) Retrofitting of reinforced concrete beams with CARDIFRC[®], *Journal of Composites for Construction*, 7(3), pp. 174-186.

Alaee, F.J. and Karihaloo B. L. (2003b). A fracture model for flexural failure of beams retrofitted with CARDIFRC[®]. *ASCE Journal of Engineering Mechanics*, 129(9), pp.1028-1038.

Al-Sulaimani, G. J., Sharif, A., Basunbul, I. A., Balush, M. H. and Ghaleb, B. N. (1994) Shear repair for reinforced concrete by fibreglass plate bonding, *ACI Structural Journal*, 91(3), pp. 458-464.

Ansari, F. (1989). Mechanics of microcrack formation in concrete, *ACI Material Journal*, 86(5), pp. 459-464.

Anthony E. and Newman K. (1965). The structure of concrete and its behaviour under load, *Proceeding of an International Conference*, London.

Apicella, F. and Imbrogno, M. (1999). Fire performance of CFRP-composites used for repairing and strengthening concrete, *Proceedings of the Fifth ASCE Materials Engineering Congress*, L.C.Bank, (ed), ASCE, Cincinnati, Ohio, pp. 260-266.

Bache, H. H. (1981). Densified cement ultra-fine particle-based materials, CBL Report No, 40, Aalborg Portland, Denmark, pp.35.

Bache, H. H. (1987). Compact reinforced composite, Basic principles, Aalborg Portland, Cement-og Betonlaboratoriet, CBL Report No. 41.

Bache, H. H. (1989). Fracture mechanics in integrated design of new, ultra-strong materials and structures. In: Elfgren L, (editor). *Fracture mechanics of concrete structures, from theory to application*. London, New York: Chapman & Hall, pp. 382-398.

Bairagi, N. K, and Dubal, N. S. (1996). Effect of thermal cycles on the compressive strength, modulus of rupture and dynamic modulus of concrete, *The Indian concrete journal*, pp 423-426.

Baker, G. (1996). The effect of exposure to elevated temperatures on the fracture energy of plain concrete, *RIELM Materials and Structures*, **29**, pp.383-388.

Bakis, C., Bank, L., Brown, V., Cosenza, E., Davalos, J., Lesko, J., Machida, A., Rizkalla, S. and Triantafillou, T. (2002) Fibre reinforced polymer composites for construction-state-of the-art review, *Journal of Composites for Construction*, **6**(2), pp. 73-87.

Balaguru P.N. and Kendzulak J. (1986). Flexural behaviour of slurry infiltrated fibre concrete (SIFCON) made by using condensed silica fume, In *Fly Ash, Silica Fume, Slag and natural Pozzolans in Concrete*, SP-91, *ACI*, Detroit, pp. 1215-1229.

Balaguru, P. N. and Shah. (1992). *Fibre-Reinforced Cement Composites*, McGraw-Hill, New York.

Ballinger, C., Maeda, T. and Hoshijima, T. (1993). Strengthening of Reinforced Concrete Chimneys, Columns and Beams with Carbon Fibre Reinforced Plastics, *Fibre-Reinforced-Plastic (FRP) Reinforcement for Concrete Structures: Properties and Applications*, A. Nanni, (ed), Elsevier Science Publishers B.V, pp. 59-86.

Bank, L.C. (1993). Properties of FRP Reinforcements for Concrete, *Fibre-Reinforced-Plastic (FRP) Reinforcements for Concrete Structures: Properties and Applications*, Elsevier Science Publishers B.V, pp. 59-86.

Barenblatt, G.I. (1959). On equilibrium cracks forming during brittle fracture (in Russian), *Prikladnaya Matematika I Mekhanika (P M M)*, **23**, pp.434-444.

List of References

Barnes, R. A., Baglin, P. S., Mays, G. C. and Subedi, N. K. (2001). External steel plate systems for the shear strengthening of reinforced concrete beams, *Engineering Structures*, **23**(9), pp. 1162-1176.

Bazant, Z.P. and Oh B.H. (1983). Crack band theory for fracture of concrete, *Materials and Structures*, **16**, pp.155-157.

Bazant, Z. P and Part, P. C. (1988). Effect of temperature and humidity on fracture energy of concrete, *ACI Material Journal*, **85**, pp. 262-271.

Benson, S. D. P. (1999). Retrofitting damaged reinforced concrete flexural members with HPFRCC, MEng Thesis, Cardiff University, U.K.

Benson, S. D. P. (2003). CARDIFRC- Development and constitutive behaviour, PhD. Thesis, Cardiff University. U.K.

Bentur, A. and Mindess, S. (1986). The effect of concrete strength on crack patterns, *Cement and Concrete Research*, **16**, pp. 59-66.

Bertero, V. V. and Polivka, M. (1972). Influence of thermal exposures on mechanical characteristics of concrete, *International Seminar on Concrete for Nuclear Reactors*, American Concrete Institute, Detroit, *ACI Special Publication* **1**(34), pp. 505-531

Berwanger, C. and Sarkar, X. (1973). Effect of temperature and age on thermal expansion and modulus of elasticity of concrete, Behaviour of concrete under temperature extremes, SP-39, *American Concrete Institute*, Farmington Hills, pp. 1-22

Bilby, B.A., Cottrell, A. H. and Swinden K.H. (1963). The spread of plastic yield from a notch, *Proceedings of Royal Society*, London, A272, pp.304-314.

Billington S. L. (2004). Damage-tolerant cement-based materials for performance-based earthquake design: research needs, *Proceedings of Fracture Mechanics of*

List of References

Concrete Structures FRAMCOS 5, **1**, Li V, Leung, C, William, K and Billington, S (eds). pp. 53-60.

Birchall, J. D., Howard, A. J. and Kendall, K (1981). Flexural strength and porosity of cements, *Nature*, **289**, pp. 388-390.

Blontrock, H., Taerwe, L. and Matthys, S. (1999). Properties of fibre reinforced plastics at elevated temperatures with regard to fire resistance of reinforced concrete members, *Fourth International Symposium on Fibre Reinforced Polymer Reinforcement for Reinforced Concrete Structures*, C.W. Dolan, S.H. Rizkalla, A. Nanni, (eds), *American Concrete Institute*, Farmington Hills, Michigan, pp. 43-54.

Bosco, C. and Carpinteri, A. (1992). Fracture mechanics evaluation of minimum reinforcement in concrete structures, in *Application of Fracture Mechanics to Reinforced Concrete. Proc Int Workshop*, Turin, Italy 1990), Carpinteri, A (ed), Elsevier, London, pp.347-377.

Bosco, C., Carpinteri, A. and Debernardi, P. G. (1990a). Fracture of reinforced concrete: scale effect and snab-pack instability, Presented at the International Conference on Fracture and Damage of Concrete and Rock. 4-6 July 1988, Vienna, Austria, *Engineering Fracture Mechanics*, **35**(4-5), pp.665-677.

Bosco, C., Carpinteri, A. and Debernardi, P. G. (1990b). Minimum reinforcement in high strength concrete, *ASCE Journal of Structural Engineering*, **116**, pp. 427-437.

Broek, D. (1978). *Elementary Fracture Mechanics*, Sijthoff and Noordhoff, The Netherlands.

Broek, D. (1989). *The practical Use of Fracture Mechanics*, Kluwer Academic Publishers, The Netherlands.

List of References

Brown W.F. and Srawley J.E. (1966). Plane strain crack toughness testing of high strength metallic materials, Special Technical Publication STP410 *American Society for Testing and Material (ASTM)*, Philadelphia, p.163.

Bruhwieler, E. and Wittmann, F. H. (1990). The wedge splitting test, a new method of performing stable fracture mechanics tests, *Engineering Fracture Mechanics*, **35**, pp.117-126.

Buyukozturk O, Hearing B. (1998). Failure behaviour of pre-cracked concrete beams retrofitted with FRP. *Journal of Composites for Construction*, **2**(3) pp.138–44.

Castillo, C. and Durrani, A. J. (1990). Effect of transient high temperature on high-strength concrete, *ACI Materials Journal*, **87**(1), pp.47-53.

CEB-FIP Model Code, (1993) Lausanne, Switzerland,.

Chaallal, O., Nollet, M. J. and Perraton, D. (1998a) Shear strengthening of RC beams by externally bonded side CFRP strips, *ASCE Journal of Composites for Construction*, **2**(2), pp. 111-113.

Chaallal, O., Nollet, M. J. and Perraton, D. (1998b) Strengthening of reinforced concrete beams with externally bonded fibre-reinforced-plastic plates: design guidelines for shear and flexure, *Canadian Journal of Civil Engineering*, **25** (4), pp. 692-704.

Chajes, M. J., Januszka, T. F., Mertz, D. R., Thomson T. A. and. Finch, W. W (1995a). Shear strengthening of reinforced concrete beams using externally applied composite fabric, *ACI Structural Journal*, **92**(3), pp. 295-303

Chajes, M. J., Thomson, T. A. and Farschman, C. A. (1995b). Durability of concrete beams externally reinforced with composite fabrics, *Construction and Building Materials*, **9**(3), pp. 141-148.

List of References

Collins, P. and Roper, H. (1990). Laboratory investigation of shear repair of reinforced concrete beams loaded in flexure, *ACI Material Journal*, pp. 149-159.

Cusson, D. and Malivaganam, N. (1996). Durability of repair materials, *Concrete International*, **18**(3), pp. 34-38.

De Larrard, F and Sedran, T. (1994). Optimisation of ultra-high-performance concrete by the use of a packing model, *Cement and Concrete Research*, **24**(6), pp 997-1009.

Domone, P L and Soutsos, M N. (1995). Properties of high strength concrete mixes containing pfa and ggbs, *Magazine of Concrete Research*, **47**(173), pp 355-367.

Duan, K., Hu, X. Z. and Wittmann, F. H. (2001). Boundary effect on concrete fracture induced by non-constant fracture energy distribution. In R. De Borst, J. Mazars, G. Pijaudier-Cabot and J. G. M. Van Mier (editors), *Fracture Mechanics of Concrete Structures (Proc. FRAMCOS-4)*, 49-55. A. A. Balkema Publishers, The Netherlands.

Dugat, J., Roux N and Bernier G. (1996). Mechanical properties of reactive powder concretes (RPC), *Materials and Structures*, **29**, pp. 133-240.

Dugdale, D.S. (1960). Yielding of steel sheets containing slits, *Journal of the Mechanics and Physics of Solids*, **8**, pp.100-104.

Dunstan, I. (1987). Fibre reinforced cement and concrete: research into practice, *FRC-86 Symposium*, Keynote lecture (RILEM), pp 147-150.

Elices, M., Guinea, G. F. and Planas, J. (1992). Measurement of the fracture energy using three point-bend tests: part 3-influence of cutting the P- δ tail. *Material and Structures*, **25**, pp.327-334.

List of References

Emmons, P. H. (1994). *Concrete Repair and Maintenance Illustrated*. Concrete Publishers and Consultants, Kingston.

England, A.H. (1965). A crack between dissimilar media, *Journal of Applied Mechanics*, **32**, pp.400-402.

Evans, A. G. and Hutchinson, J. W. (1989). Effects of non-planarity on the mixed mode fracture resistance of bi-material interfaces, *Acta Metall*, **37**, pp. 909-916.

Ewalds, H. L. and Wanhill, R. J. H. (1985). *Fracture Mechanics*, Edward Arnold, UK and Delftse Uitgevers Maatschappij, The Netherlands (co-publishers).

Fanella, D. A and Naaman, A. E. (1985). Stress-strain properties of fibre reinforced mortar in compression, *Journal of The American Concrete Institute*, **82** (4), pp 475-483.

Ford, M. C. (1999). Structural faults & repair- 99: 8th International Conference London, Edinburgh, Engineering Techniques, Press

Gettu, R., Bazant, Z. P. and Karr, M. E. (1990). Fracture properties and brittleness of high strength concrete, *ACI Material Journal*, **87**, pp. 608-618.

Gopalaratnam, V. S and Shah, S. P. (1986). Properties of steel fibre reinforced concrete subjected to impact loading, *Journal of the American Concrete Institute*, **83**(1), pp 117-126.

Gray, R. J. (1984). Analysis of the effect of embedded fibre length on fibre debonding and pull-out from an elastic matrix, *Journal of Materials Science*,**19**(3), pp.861-70. UK.

Griffith, A. A. (1920). The phenomena of rapture and flow in solids, *Philosophical Transactions of Royal Society, London*, A221, pp. 163-198.

List of References

Guinea, G.V., Pastor, J. Y Planas J. and Elices M. (1998). Stress intensity factor compliance and CMOD for a general three-point bending beam, *International Journal of Fracture*, **89**, pp. 103-116

Guinea, G.V., Planas J. and Elices M. (1992). Measurement of the fracture energy using three-point bend tests: part 1-Influence of experimental procedures, *Materials and Structures*, **25**, pp.212-218.

Hammil, N. (1999). Retrofitting damaged reinforced concrete flexural members with high performance fibre reinforced concrete, MEng Thesis, University of Wales, Cardiff.

Hancox, N. L. and Mayer, R. M. (1994). *Design Data for Reinforced Plastics*, Chapman and Hall, London.

Harmuth, H. (1995) Investigation of the adherence and the fracture behaviour of polymer cement concrete, *Cement and Concrete Research*, **25**(3), pp.497-502.

He, J. H., Pilakoutas, K. and Waldron, P. (1997). Strengthening of reinforced concrete beams with CFRP plates, *Proceedings of the 3rd International Symposium on Non-Metallic (FRP) Reinforced Concrete Structures*, I, pp. 343-350.

Hewlett, P. C. and Morgan, J. G. D. (1982). Static and cyclic response of reinforced concrete beams repaired by rein-injection, *Magazine of Concrete Research*, **34**(118), pp. 5-17

Hillerborg A., Modéer M. and Petersson P.E. (1976). Analysis of crack formation and crack growth in concrete by means of fracture mechanics and finite elements, *Cement and Concrete Research*, **6**, pp.773-782.

Horii, H., Hasegawa, A. Nishino, F. (1989) Process zone model an influencing factors in fracture of concrete, In *Fracture of Concrete and Rocks*, Shah, SP, Swartz, SE, (eds), New York: Springer-Verlag, pp. 205-219.

List of References

Howie, I. (1995). A Study on the Use of Composite Wraps for the Rehabilitation of Deteriorated Concrete Columns. MSc Thesis, Dept. of Civil Engineering, University of Delaware, New York.

Hoy, C.W. and Bartos P.J.M. (1999). Interaction and packing of fibers: Effects on the mixing process, In *High Performance Fiber Reinforced Cement Composites (HPFRCC3)*, Reinhardt H.W. and Naaman A.E. (eds), RILEM Publishers, pp. 181-191.

Hu, X. Z. (1990). Fracture process zone and strain softening in cementitious materials. ETH Building Materials Report No.1, ETH, Switzerland. (AEDIFICATIO Publishers, Freiburg, 1995).

Hu, X. Z. and Wittmann, F. H. (1992). Fracture energy and fracture process zone, *Material and structures*, **25**, pp.319-326.

Hu, X.Z. and Wittmann F.H. (2000). Size effect on toughness induced by crack close to free surface. *Engineering Fracture Mechanics*, **65**, pp.209-211.

Hussain, M., Sharif, A., Basenbul, I. A., Baluch, M.H. and Al-Sulaimani, G.I. (1995). Flexural behaviour of pre-cracked reinforced concrete beams strengthened externally by steel plates, *ACI Structural Journal*, **92**(1), 14-22.

Hutchinson, A. R. and Rahimi, H. (1993). Behaviour of reinforced concrete beams with externally bonded fibre reinforced plastics, *Proceedings of the 5th International Conference on Structural Faults and Repair*, Edinburgh, pp. 221-228.

Hutchinson, J.W., Mear, M.E., and Rice, J. R. (1987). Crack paralleling an interface between dissimilar materials, *Journal of Applied Mechanics*, **54**, pp.828-832.

Inglis C.E. (1913). Stress in a plate due to the presence of cracks and sharp corners, *Transactions of the Institution of Naval Architects*, pp.219-241.

List of References

Irhouma, A. M., Ayari, M. L. and Robinson, L. C. (1998). Effect of low temperature on fracture energy of concrete joints and repair materials, *In Fracture Mechanics of Concrete Structures Volume III*, Mihashi, H., Rokugo, K. (eds) AEDIFICATIO Publishers, Freiburg, Germany, pp. 1593-1604.

Irwin, G.R. (1957). Analysis of stresses and strains near the end of a crack traversing a plate, *ASME Journal of Applied Mechanics*, **24**, pp. 361-364.

Jansze, W., den Uji, J. and Walraven, J. (1996). Anchorage of externally bonded steel plates, *Proceedings of Concrete in the Service of Mankind Congress, Concrete Repair, Rehabilitation and Protection*, Dhir RK, Jones M. R. (eds), University of Dundee, E and FN Spon, pp. 591-598.

Jennings, H. M. (1991). Advanced cement-based matrices for composites, in High Performance Fibre Reinforced Cement composites, *Proceedings of the International RILEM/ACI Workshop*, Reinhardt H.W. and Naaman A.E. (eds), Mains, Germany, , pp. 3-17.

Johnston, C. D. and Skarendahl, A. (1992). Comparative flexural performance evaluation of steel fibre-reinforced concretes according to ASTM C1018 shows importance of fibre parameters, *Materials and structures*, **25**, pp. 191-200

Jones, R. and Swamy, R. N. (1995). Plate bonding-what can it do to your beam? *Construction Repair*, pp.43-47.

Jones, R., Swamy, R. N. and Charif, A. (1988). Plate separation and anchorage of reinforced concrete beams strengthened by epoxy-bonded steel plates, *Structural Engineer* (London), **66**(5), pp. 85-94.

Jones, R., Swamy, R. N., Bloxham, J. and Bouderbalah, A. (1980). Composite behaviour of concrete beams with epoxy bonded external reinforcement, *International Journal of Cement Composites and Lightweight Concrete*, **2**(2), pp. 91-107.

List of References

Kaar, P. H. and Mattock, A. H. (1963). High strength bar as concrete reinforcement, Part 4. Control of Cracking. *Journal of the PCA Research and Development Laboratories*, **7**(1), pp 15-38.

Kamada, T. and Li, V. (2000). The effect of surface preparation on the fracture behaviour of ECC/concrete repair system, *Cement and Concrete Composites*, **22**, pp. 423-431.

Karbhari, V. M. (2002) Response of fibre reinforced polymer confined concrete exposed to freeze and freeze-Thaw regimes, *Journal of Composites for Construction*, **6**(1), pp. 35-40.

Karbhari, V. M. (1998). Materials and Design Considerations in FRP Rehabilitation of Concrete Structures, In *Fracture Mechanics of Concrete Structures Volume III*, Mihashi, H., Rokugo, K. (eds), AEDIFICATIO Publishers, pp. 1805-1816.

Karbhari, V. M. (2001). Materials considerations in FRP rehabilitation of concrete structures, *Journal of Materials in Civil Engineering*, **13**(2), pp. 90-97.

Karbhari, V. M., Rivera, J. and Dutta, P. K. (2000). Effect of short-term freeze-thaw cycling on composite confined concrete, *Journal of Composites for Construction*, **4**(4), pp. 191–197.

Karihaloo B.L. (1995). *Fracture Mechanics and Structural Concrete*, Addison Wesley Longman, London.

Karihaloo B.L., Abdalla H.M and Imjai, T. (2003). A simple method for determining the true specific fracture energy of concrete, *Magazine of Concrete Research*, **55**(5), pp.471-481.

Karihaloo, B L, Benson, S D P, Didiuk, P M, Fraser, S A, Hamill, N and Jenkins, T A. (2000). Retrofitting damaged RC beams with high-performance fibre-reinforced

concrete, *Proceedings of the Tenth Annual BCA, British Cement Association*, Birmingham University, pp. 153-164.

Karihaloo, B L. and Lange-Kornbak, D (2001). Optimisation techniques for the design of high performance fibre-reinforced concrete, *Structural and Multidisciplinary Optimisation*, **21**, pp.32-39.

Karihaloo, B. L. and De Vriese, K M B. (1999). Short-fibre reinforced reactive powder concrete, *Proceedings of Concrete Communication Conference, British Cement Association*, pp. 67-77.

Karihaloo, B. L. and Wang, J. (1997). Micromechanical modelling of strain hardening and tension softening in cementitious composites, *Computational Mechanics*, **19**, pp.453-462.

Karihaloo, B. L. and Wang, J. (2000). Mechanics of fibre-reinforced cementitious composites, *Computers and Structures*, **76**, pp 19-34.

Karihaloo, B. L., Alaei, F. J. and Benson S D P. (2001). A new technique for retrofitting damaged concrete structures, *Concrete Communication Conference*, pp 293-304.

Karihaloo, B. L., Alaei, F. J. and Benson S D P. (2002). A new technique for retrofitting damaged concrete structures, *Proceedings of the Institution of Civil Engineers, Building & Structures*, **152**(4), pp. 309-318.

Karihaloo, B. L., Benson S D P. and Alaei, F. J. (2003). Retrofitting of RC beams with CARDIFRC[®], *Proceedings of the 10th International Conference on Structural faults & repair*, Forde, M. C. (ed), London, CD-ROM.

Karihaloo, B. L., Wang, J. and Grzybowski, M. (1996). Doubly periodic arrays of bridged cracks and short fibre-reinforced cementitious composites, *Journal of the Mechanics and Physics of Solids*, **44**(10), pp. 1565-1586.

List of References

Karihaloo, B.L. and Jefferson, A.D. (2001). Looking into concrete, *Magazine of Concrete Research*, **53**(2), pp. 135-147.

Knott, J.F. (1973). *Fundamentals of Fracture Mechanics*, Butterworths, London.

Krstulovic-Opara, N., LaFave, J.M., Dogan, E. and Uang, C. M. (2000). Seismic retrofit with discontinuous slurry infiltrated mat concrete (SIMCON) jackets, in *High-Performance Fibre Reinforced Concrete in Infrastructural Repair and Retrofit*, (ACI SP-185, American Concrete Institute, Farmington Hills), pp. 141-185.

Kunieda, M., Kurihara, N., Uchida, Y. and Rokugo, K. (2000). Application of tension softening diagrams to evaluation of bond properties at concrete interfaces. *Engineering Fracture Mechanics*, **65**, pp. 299-315.

Lange-Kornbak, D and Karihaloo, B L. (1999). Fracture mechanical prediction of transitional failure and strength of singly reinforced beams. In *Minimum Reinforcement in Concrete Members*, ESIS Publication 24, Carpinteri, A. (ed), Elsevier, London, pp. 31-42.

Lange-Kornbak, D and Karihaloo, B L. (1998). Design of fibre-reinforced cementitious composites for minimum brittleness, *Journal of Advanced Cement-Based Materials*, **7**, pp 89-101.

Lange-Kornbak, D. and Karihaloo, B.L. (1997). Tension softening of fibre-reinforced cementitious composites, *Cement and Concrete Composites*, **19**, pp. 315-328.

Lange-Kornbak, D. (1997). The role of brittleness in the fracture of plain and reinforced concrete, PhD. Thesis, University of Sydney

Lankard, D R. (1985). Slurry infiltrated fibre concrete (SIFCON): properties and applications, *Materials Research Society*, **42**, pp 227-286.

List of References

Lankard, D R. and Newell, J. K. (1984). Preparation of highly reinforced steel fibre reinforced concrete composites, ACI Special Publication, SP-81, *American Concrete Institute*, Detroit, pp. 286-306

Lankard, D. R., Birkimer, D. L., Fondfriest, F. F. and Snyder, M. J. (1971). Effects of moisture content the structural properties of Portland cement concrete exposed to temperatures up to 500 F, *Temperature and Concrete*, SP-25, *American Concrete Institute*, Detroit, pp. 59-102.

Leung, C. K. Y. (1998). Delamination failure in concrete beams retrofitted with a bonded plate. In *Fracture Mechanics of Concrete Structures Volume III*, Mihashi, H., Rokugo, K. (eds), AEDIFICATIO Publishers, Freiburg, Germany, pp. 1783-1792.

Leung, C. K. Y. (2001). Delamination failure in concrete beams retrofitted with a bonded plate, *ASCE Journal of Materials in Civil Engineering*, **13**(2), pp. 106-113.

Lewis, j. A and Kriven, W M. (1993). Microstructure property relationships in Macro-Defect-Free Cement, *MRS Bulletin*, pp. 72-77.

Li, A., Diagana, C. and Delmas, Y. (2001). CFRP contribution to shear capacity of strengthened RC beams, *Engineering Structures*, **23**(10), pp. 1212-1220.

Li, V. C. and Kanda, T. (1998). Engineered cementitious composites for structural applications. *ASCE Journal of Material in Civil Engineering*, **10**(2), pp 66-69

Li, V. C. (1992). A simplified micromechanical model of compressive strength of fibre reinforced cementitious composites, *Cement and Concrete Composites*, **14**, pp. 131-141

List of References

Li, V. C. (1993). From micromechanics to structural engineering- the design of cementitious composites for civil engineering applications, *JSCE Journal of Structural Mechanics and Earthquake Engineering*, **10**(2), pp 37-48

Li, V. C. (1998) Repair and retrofit with engineered cementitious composites, in *Fracture Mechanics of Concrete Structures Volume 3*, Mihashi, H., Rokugo, K. (eds), AEDIFICATIO Publishers, pp. 1715-1726.

Li, V. C., Lim, Y. M. and Foremsky, D. J. (1995). Interfacial fracture toughness of concrete repair materials, *Proceedings of Fracture Mechanics of Concrete Structures II* Wittman FH (ed), AEDIFICATIO Publishers, pp. 1329-1344.

Li, V. C., Wang, Y. and Backer, S. (1991). A micromechanical model of tension softening and bridging toughening of short random fibre reinforced brittle matrix composites, *Journal of the Mechanics and physics of Solids*, **39**(5), pp. 607-625.

Lim, Y. M. and Li, V.C. (1997). Durable repair of aged infrastructures using trapping mechanism of engineering cementitious composites, *Journal of Cement and Concrete Composites*, **19**(4), pp. 373-385.

Lin, Z. and Li, V. (1997). Crack bridging in fibre reinforced cementitious composites with slip-hardening interfaces, *Journal of the Mechanics and Physics of Solids*, **45**(5), pp. 763-787.

Maalej, M. and Li, V. (1995). Introduction of strain-hardening engineered cementitious composites in design of reinforced concrete flexural members for improved durability, *ACI Structural Journal*, **92**(2), pp.167-176.

Macdonald, M. D. and Calder, A. J. J. (1982). Bonded steel plating strengthening concrete structures, *International Journal of Adhesion and Adhesives*, **2**(2), pp. 119-127.

List of References

Meier, U. and Kaiser, H. (1991). Strengthening of structures with CFRP laminates, *Advanced Composites Materials in Civil Engineering Structures*, ASCE, New York, pp. 224-232.

Meier, U., (1997) Post strengthening by continuous fibre laminates in Europe, non-metallic (FRP) reinforcement for concrete structures, *Japan Concrete Institute*, **1**, pp. 41-56.

Meier, U., Deuring, M., Meier, H. and Schwegler, G. (1992) Strengthening of structures with CFRP Laminates: Research and application in Switzerland, *Advanced Composite Materials in Bridges and Structures*, *Canadian Society for Civil Engineering*, pp. 243-251.

Milke, J.A., and Vizzini, A.J. (1993). The Effects of simulated fire exposure on glass-reinforced thermoplastic materials, *Journal of Fire Protection Engineering*, **5**(3), pp. 113-124.

Mobasher, B., Stang, H. and Shah, S. P. (1990) Microcracking in fibre reinforced concrete, *Cement and Concrete Research*, **20**, pp. 665-676.

Morin, V., Cohen Tenoudji, F., Feylessoufi, A. and Richard, P. (2001) Superplasticizer effects on setting and structuration mechanisms of ultrahigh-performance concrete, *Cement and concrete Research*, **31**, pp. 63-71

Munawar, H. (1992) Flexural and shear behaviour of damaged RC beams repaired by plate bonding, MSc Thesis, King Fahd University of Petroleum and Minerals, K.S.A.

Naaman, A E and Shah, S. P. (1976). Pull-out mechanism in steel fibre reinforced concrete, *ASCE Journal of the Structural Division*, **102**(ST8), pp. 1537-1548.

Naaman, A E. (1991). SIFCON: tailored properties for structural performance, in High Performance Fibre Reinforced Cement composites, *Proceedings of the*

List of References

International RILEM/ACI Workshop, Reinhardt, H. W., & Naaman, A.E. (eds), Mains, Germany, pp 18-38.

Naaman, A E., Reinhardt, H. W. and Fritz, C. (1990). Reinforced concrete beams using SIFCON as a matrix, Darmstadter Massivbau Report, Germany, 85 pages

Nallathambi, P. (1986). A study of fracture of plain concrete, PhD Thesis, University of Newcastle, N.S.W, Australia.

Nanni, A. (1990). Concrete repair with externally bonded FRP reinforcement: examples from Japan, *Concrete International*, **97**, pp. 22-26.

Narayanan, R and Kareem, A S. (1982). Factors influencing the workability of steel fibre reinforced concrete-part1, *Concrete*, **16**, pp 45-48.

Nelson, G.L. (1995). Fire and polymers: an overview, *fire and polymers II: Materials and Tests for Hazard Prevention*, G.L. Nelson, (ed), *American Chemical Society Symposium Series 599*, Washington, DC, pp. 1-26.

Neville, A M. (1995), *Properties of Concrete*, 4th Edn. Longman Group, UK and New York: John Wiley & Sons.

Neville, A. and Aitcin, P C. (1998). High performance concrete—An overview, *Materials and Structures*, **31**, pp 111-117.

Neville, A. M. (1997). Aggregate bond and modulus of elasticity of concrete, *ACI Material Journal*, **94**(1), pp. 71-74.

Newman, K. (1965). The structure and properties of concrete-an introductory review, in *The Structure of Concrete and its Behaviour under Load* (Brooks, A.E. & Newman, K. (eds)), *Cement and Concrete Association*, London, pp. xiii-xxxii.

List of References

Nielsen, L. F. (1992) Stiffness of fibre composite, Report TR-264, Technical University of Denmark.

Oehlers, D. J. and Moran, J. P. (1990). Premature failure of externally plated reinforced concrete beams, *ASCE Journal of Structural Engineering*, **116**(4), pp. 978-995.

Oehlers, D. J., Ali, M. and Luo, W. (1998) Upgrading continuous reinforced concrete beams by gluing steel plates to their tension faces, *Journal of Structural Engineering*, **124**(3), pp. 224-232.

Okamura, H., Watanabe, K. and Takano, T (1973). Applications of the compliance concepts in fracture mechanics. *ASTM STP 536*, pp 423-438.

Okamura, H., Watanabe, K. and Takano, T. (1975) Deformation and strength of cracked member under bending moment and axial force. *Engineering Fracture Mechanics*, **7**, pp 531-539.

Ortiz, M. (1988). Microcrack coalescence and macroscopic crack growth initiation in brittle solids, *International Journal of Solids and Structures*, **24**, pp. 231-250.

Park, P. and Paulay, T. (1975) *Reinforced Concrete Structure*, Wiley-Interscience, New York, p 769.

Parra-Montesinos, G. (2003). HPCFRCC in earthquake-resistance structures: current knowledge and future trends, *Proceedings of HPCFRCC-4*, Ann Arbor, Michigan, USA, pp.453-472

Petersson, P. E. (1980) Fracture energy of concrete: Practical performance and experimental results. *Cement and concrete Research*, **10**, pp. 91-101

Prokoski, G., (1995) Fracture toughness of concrete at high temperature, *Journal of Materials Science*, **30**, pp. 1609-1612.

List of References

Quantrill, R., Hollaway, L. C., Thorn, A. M. and Parke, G. A. R. (1996a). Experimental and Analytical investigation of FRP strengthened beam response- Part I, *Magazine of Concrete Research*, **48**(177), pp. 331-342.

Quantrill, R., Hollaway, L. C., Thorn, A. M. and Parke, G. A. R. (1996b). Predictions of the maximum plate end stresses of FRP strengthened beam- Part II, *Magazine of Concrete Research*, **48**(177), pp. 343-352.

Rahimi, H. and Hutchinson, A. R. (2001). Concrete beams strengthened with externally bonded FRP plates, *Journal of Composites for Construction*, **5**(1) pp. 44-56.

Ramakrishnan, V. (1995). Concrete fibre composites for the twenty-first century, Real World Concrete, Singh, G (editor), Elsevier Science Ltd, UK, pp 111-144.

Ramakrishnan, V., Gollapudi, S. and Zellers, R. (1987). Performance characteristics and fatigue of polypropylene fibre reinforced concrete, ACI SP-105, Fibre Reinforced Concrete- Properties and Applications, *American Cement Institute*, Detroit, pp. 159-177.

Ramakrishnan, V., Wu, George Y and Hosalli, G. (1989). Flexural behaviour and toughness of fibre reinforced concretes, Transport Research Record 1226, National Research Council, Washington DC, pp 69-77.

Raouf, M., El-Rimawi, J. A. and Hassanen, M. A. H. (2000). Theoretical and experimental study on externally plated RC beams, *Engineering Structures*, **22**, pp. 85-101.

Rebat, K. H. (1999). Behaviour of fibre reinforced concrete as subjected to thermal cycling, MSc Thesis, Civil Engineering Department, Irbid, Jordan.

List of References

Reinhardt, H W. (1991). Fibres and cement, a useful co-operation: Introductory note, High Performance Fibre Reinforced Cement Composites, *Proceedings of the International RILEM/ACI Workshop*, Reinhardt, H. W., & Naaman, A.E. (eds), Mains, Germany.

Reinhardt, H W. (1995). Relation between the microstructure and structural performance of concrete. in Concrete Technology: New Trends, Industrial Applications; *Proceedings of the International RILEM Workshop on Technology Transfer of the New Trends in Concrete* (Eds: Aguado A., Gettu, R. and Shah, A.P.), E&FN Spon, London, pp. 19-32.

Rice, J. R. and Sih, G.C. (1965). Plane problems of cracks in dissimilar media, *Journal of Applied Mechanics*, pp.418-423.

Rice, J.R. (1998). Elastic fracture mechanics concepts for interfacial cracks, *Journal of Applied Mechanics*, Transactions ASME, **55**, pp.98-103.

Richard, P. and Cheyrezy, M H. (1994). Reactive powder concretes with high ductility and 200-800Mpa compressive strength, *ACI Spring Convention*, San Francisco, USA.

Richard, P. and Cheyrezy, M H. (1995). Composition of reactive powder concretes, *Cement and Concrete Research*, **25**(7), pp.1501-1511.

RILEM Committee FMC 50. (1985) Determination of the fracture energy of mortar and concrete by means of the three-point bend tests on notched beams. *Materials and structures*, **18**, pp.285-290.

Roa, G.A. (2001). Influence of silica fume on long-term strength of mortars containing different aggregate fractions, *Cement and Concrete Research*, **31**, pp. 7-12.

List of References

Rossi, P. and Chanvillard, G. (1992). A new geometry of steel fibre for fibre reinforced concretes, in *High performance fibres reinforced cement composites, Proceedings of the International RILEM/ACI Workshop*. (Reinhardt, H.W. & Naaman, A.E.), E&FN Spon, London, pp. 129-139.

Rossi, P., Brühwiler, E., Chhuy, S., Jenq, Y. S and Shah, S. P. (1991). Fracture properties of concrete as determined by means of wedge splitting tests and tapered double cantilever beam tests, In S. P. Shah and A. Carpinteri (editors), *Fracture Mechanics Test Methods for Concrete*, pp.87-128. Chapman & Hall, London.

Rostasy, F. S. and Budelmann, H. (1986). Strength and deformation of concrete with variable content of moisture at elevated temperature up to 90° C, *Cement and Concrete Research*, **16**, pp. 353-362.

Saad M., Abo-El-Enein S. A., Hanna, G. B. and Kotkata, M. F. (1996). Effect of temperature on physical and chemical properties of concrete containing silica fume, *Cement and Concrete Research*, **26**(5), pp. 669-675.

Saadatmanesh, H. and Ehsani, M. R. (1991). RC beams strengthened with GFRP. I: Experimental study, *Journal of Structural Engineering, ASCE*, **117**(11), pp. 3417-3433.

Sabir, B B. (1995). High strength condensed silica fume concrete, *Magazine of Concrete Research*, **47**(172), pp 219-226.

Sabir, B.B., Wild, S. and Asili, M. (1997). On the tortuosity of the fracture surface in concrete, *Cement and concrete Research*, **27**(5), 785, 795.

Said, S and Mandel, J A. (1989). Micromechanical studies of crack growth in steel fibre reinforced mortar, *ACI Material Journal*, **86**(3), pp. 225-235.

Sato, Y., Ueda, Y. and Tanaka, T. (1996). Shear reinforcing effect of carbon fibre sheet attached to side of reinforced concrete beams, *Proc. Int. Conf. Advanced*

List of References

Composite Materials in Bridges and Structures, El-Badry, M. M (eds), *Canadian Society for Civil Engineers*, Montreal, Canada, pp. 621-628.

Schneider, U. (1988). Concrete at high temperatures-a general review, *Fire Safety Journal*, **13**, pp. 55-68

Schneider, U., (1976) Behaviour of concrete under thermal steady state and non-steady state conditions, *Fire and Materials*, **1**, pp.103-115.

Sen R, Mullins G, Shahawy M., and Spain J. (2000). Durability of CFRP/epoxy/Concrete bond, *Composites in the Transportation Industry, Proceedings of the ACUN-2 International Composite Conference*, University of South Wales. Australia

Sen, R., Shahawy, M, Mullins, G and Spain, J. (1999). Durability of carbon fiber reinforced polymer CFRP/Epoxy/concrete bond in marine environment', *ACI Structural Journal*, **96** pp. 906-914

Shah S.P., Swartz S.E. and Ouyang C. (1995). *Fracture Mechanics of Concrete: Applications of Fracture Mechanics to Concrete, Rock and other Quasi-brittle Materials*, John Wiley and Sons, USA.

Shah, S P, Peled, A. Aldea, C M and Akkaya, Y. (1999). Scope of high performance fibre reinforced cement composites, *In Third International Workshop on high Performance Fibre Reinforced Cement composites (HPFRCC3)*, Reinhardt, H. W., & Naaman, A.E. (eds), Mains, Germany, pp 113-129.

Shah, S P. and Young, J. F. (1990). Current research at the NSF Science and Technology Centre for Advanced Cement-Based Materials, *American Ceramic Society Bulletin*, pp. 1319-1331.

Shannag, M j and Hansen, W. (2000). Tensile properties of fibre-reinforced very high strength DSP mortar, *Magazine of Concrete Research*, **52**(2), pp 101-108.

List of References

- Sharif, A., Al-Sulaimani, G. J., Basunbul, I. A., Baluch, M. H. and Husain, M. (1995) Strengthening of shear-damaged RC beams by external bonding of steel plates, *Magazine of Concrete Research*, **47**(173), pp. 329-334.
- Shih, C.F. and Asaro, R. (1988). Elastic-plastic analysis of cracks on bimaterial interfaces; part 1: small scale yielding, *Journal of Applied Mechanics*, **55**, pp.299-316.
- Soroka, I. and Jaigermann, C. (1984) Deterioration and durability of concrete in hot climate. *Proceeding of RILEM Seminar on the Durability of Concrete Structures under Normal Outdoors Exposure*, Hanover, FRG, 52-60.
- Soudki, K. A. and Green, M. F. (1997). Freeze-thaw response of CFRP wrapped concrete, *ACI Concrete International*, **19**(8), pp. 64-67.
- Struble, L., Skalny, J. and Mindess, S. (1980). A review of the cement-aggregate bond, *ACI Material Journal*, **3**, pp. 277-286.
- Sullivan, A P. (1999). The effect of hydrothermal curing at 90°C and the use of 12 mm steel fibres on reactive powder concrete, MSc. Thesis, Cardiff University.
- Swamy, R. N., Jones, R. and Bloxham, J. W. (1987). Structural behaviour of reinforced concrete beams strengthened by epoxy-bonded steel plates, *The Structural Engineer*, **65**(2), pp 59-68.
- Tada, H., Paris, P. and Irwin, G. (1985) *The Stress Analysis of Cracks Handbook*. Del Research Corporation, St. Louis, Missouri, Part 2, pp 16-17.
- Taljsten, B. and Teknik, S. (2001). Strengthening concrete beams for shear with CFRP sheets, *Proceedings of the 9th International Conference on Structural faults & repair*, Forde, M. C. (ed), London, CD-ROM.

List of References

Tann D. B. (2001). Retrofitting of mechanically degraded concrete structures, using fibre reinforced polymer composites, PhD Thesis, University of Glamorgan.

Tasdemir, C. and Tasdemir, M.A. (1995). Microstructural effects on the brittleness of high strength concretes. In Wittmann, F.H (editor), *Fracture Mechanics of Concrete Structures*, (Proc FRAMCOS-2), AEDIFICATIO, Freiburg, pp. 125-134

Tasdemir. C., Tasdemir, M. A., Lydon, F. D. and Barr, B. I. G. (1996). Effects silica fume and aggregate size on the brittleness of concrete, *Cement and Concrete Research*, **26**(1), 63-68.

Taylor, M. R., Lydon, F.D. and Barr, B.I. (1996). Mix proportions of high strength concrete, *Construction and Building Materials*, **10**(6), 445-450.

Teng, J.G., Chen, J.F., Smith, S.T. and Lam, L. (2002). *FRP Strengthened RC Structures*, John Wiley & Sons Ltd., Chichester, UK.

Tjiptobroto, P and Hansen, W. (1993). Tensile strain hardening and multiple cracking in high-performance cement-based composites containing discontinuous fibres, *ACI Materials Journal*, **90**(1), pp 16-25

Toutanji, H. A. and Gomez, W. (1997). Durability characteristics of concrete externally bonded with FRP composite sheets, *Cement and Concrete Composites*, **19**, pp.351-358.

Triantafillou, T. C. and Plevris, N. (1992). Strengthening of RC beams with epoxy-bonded fibre composite materials, *Materials and Structures*, **25**(148), pp. 201-211.

Tschegg, E. K. (1991). New equipment for fracture tests on concrete, *Materials Testing*, pp. 338-342.

Tschegg, E. K. (1997). An efficient fracture test method for bituminous and layer bonds. Mechanical tests for Bituminous Materials, *Proceedings of the Fifth*

List of References

International RILEM Symposium, Di Benedetto, H and Francken, L. (eds), pp.405-411.

Tschegg, E. K. (1990). Patent specification No. A 408/90, Austrian Patent Office.

Tschegg, E. K. and Linsbauer, H. N. (1986). Test method for the determination of fracture mechanics properties. Patent specification No. A-233/86 390 328, Austrian Patent Office.

Tschegg, E. K. and Stanzel, S. E (1991) Adhesive power measurements of bonds between old and new concrete, *Journal of Material Science*, **26**, pp.5189-5194.

Tschegg, E. K., Rotter, H. M., Roelfstra, P. E., Bourgund, U. and Jussel, P. (1995). Fracture mechanical behaviour of Aggregate-cement matrix interfaces, *Journal of Materials in Civil Engineering*, pp. 199-203

Van Mier, J. G. M. (1997). *Fracture Processes of Concrete*, CRC Press.

Wang, J and Karihaloo, B.L. (2000). Material instability in the tensile response of short-fibre-reinforced quasi-brittle composites, *Archives of Mechanics*, **52**, pp. 839-855.

Williams, B. K., Bisby, L. A., Green, M. F. and Kodur, V. K.R. (2003). An investigation of the fibre behaviour of FRP strengthened reinforced concrete beams, *Proceedings of the 10th International Conference on Structural Faults and Repair*, London, CD ROM.

Williams, M. L. (1959) The stress around a fault or crack in dissimilar media, *Bulletin of the Seismological Society of America*, **49**, pp. 199-204.

Winistoerfer, A., Meier, U. and Lees, J. M. (2001) CARBOSTRAP – Advanced Composite Tendons, *Proceedings of the ACUN-3 international conference*

List of References

Technology Convergence in composites applications, Bandyopadhyay, S., Gowripalan, N. and Drayton, N. (eds), University of New South Wales, pp 24-30.

Wu Z., Matsuzaki, T. and Tanabe, K. (1997). Interface crack propagation in FRP strengthened concrete structures, In: *Non-Metallic (FRP) Reinforcement for Concrete Structures, Vol I*, Japan Concrete Institute, pp. 319-326.

Yogendran, V., Langan, B.W., Haque, M.N. and Ward, M.A. (1987). Silica fume in high strength concrete, *ACI materials Journal*, pp. 124-129.

Zanni, H., Cheyrezy, M., Maret, V., Philipot, S. and Nieto, P. (1996). Investigation of hydration and pozzolanic reaction in reactive powder concrete (RPC) using ^{29}Si NMR, *Cement and Concrete Research*, **26**(1), pp. 93-100.

Zhang, Z., Bicanic, N., Pearce, C and Phillips, D. (2002). Relationship between brittleness and moisture loss of concrete exposed to high temperatures, *Cement and Concrete Research*, **32**, pp. 363-371.

Zhang, Z., Bicanic, N., Pearce, C. and Balabanic. (2000). Residual fracture properties of normal and high strength concrete subjected to elevated temperatures, *Magazine of Concrete Research*, **52**(2), pp. 123-136

Zhen, M. and Chung, D. D. L. (2000). Effects of temperature and stress on the interface between concrete and its fibre-matrix composite retrofit, studies by electrical resistance measurement, *Cement and Concrete Research*, **30**, pp.799-802.

Ziraba, Y. N., Baluch, M. B., Basenbul, I. A., Sharif, A. M., Azad, A. K. and Al-Sulaimani, G. J. (1994). Guideline towards the design of reinforced concrete beams with external plates, *ACI Structural Journal*, **91**(6), pp. 639-646.

Appendix A

Product information sheets

Uniclass	L5171	E271	EPIC
C/SFB		Yq2	

Blue Circle Portland Cements (CEM I 42,5 52,5)

A range of Blue Circle Portland cements are available for civil engineering, building applications, readymix concrete and for concrete products.



Blue Circle™

BULK RANGE

**BLUE CIRCLE
PORTLAND CEMENTS**

Winter 2002

Blue Circle Portland cements are quality assured cements carrying both CE Marking and the British Standards Institution Kitemark with independent third party certification.

Applications

Portland PC CEM I 42,5

Cement for civil engineering and building applications.

Portland PC-RM CEM I 42,5 52,5

Cement with enhanced properties for Ready Mix Concrete.

Portland PC-CP CEM I 52,5

Cement with higher early strength for concrete producers and precast manufacturers.

To achieve optimum performance from Portland cements in concrete, mortar or grout, it is essential that they are correctly specified and used. Attention should be given to an adequate cement content, a water/cement ratio as low as possible consistent with satisfactory placing and thorough compaction and to adequate curing. Reference should be made to the following documents:

BS 5328 *Specifying concrete*.

BS 5628: Part 3 *Use of Masonry*.

Blue Circle Sulfacrete should be used where increased resistance to sulfates is required.

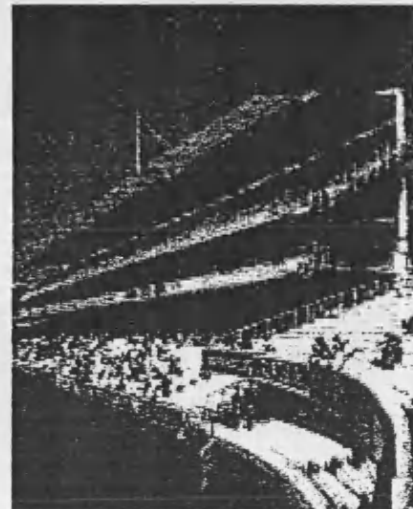
Blue Circle Lightning high alumina cement should be used to give heat-resisting and refractory properties.

Properties

- Grey colour.
- Consistent strength meeting all the conformity criteria in BS EN 197-1.



Photograph courtesy of the Concrete Society



Photograph courtesy of the Concrete Society

BLUE CIRCLE PORTLAND CEMENTS

- Compatible with admixtures such as air-entraining agents and workability aids, with cement replacement materials such as fly ash and ground granulated blastfurnace slag and with pigments. Trial mixes are recommended to determine the optimum mix proportions.

Availability

Blue Circle Portland cements are available throughout the United Kingdom in bulk tankers.

Technical Support

Further information or specification advice on Blue Circle Portland Cements and the full range of Blue Circle cements can be obtained from the contacts listed below.

Health and Safety

Contact between cement powder and body fluids (eg sweat and eye fluids) may cause irritation, dermatitis or burns. Cement is classified as an irritant under

the Chemicals (Hazard Information and Packaging) Regulations. For further information refer to the Blue Circle Health and Safety Information Sheet.

**BLUE CIRCLE
PORTLAND CEMENTS**

Typical properties		
Surface area	(m ² /kg)	290 to 420
Setting time – initial	(mins)	80 to 200
EN196-1 Mortar		
– compressive strength		
2 day	(N/mm ²)	25 to 35
7 day	(N/mm ²)	40 to 50
28 day	(N/mm ²)	54 to 64
Apparent particle density	(kg/m ³)	3080 to 3180
Bulk density	(kg/m ³)	
	Aerated	1000 to 1300
	Settled	1300 to 1450
Colour	Y value	27.5 to 37.5
Sulfate	SO ₃ (%)	2.5 to 3.5
Chloride	Cl (%)	Less than 0.06
Alkali	Eq Na ₂ O (%)	0.4 to 0.75
Tricalcium Silicate	C ₃ S (%)	45.0 to 60.0
Dicalcium Silicate	C ₂ S (%)	15.0 to 25.0
Tricalcium Aluminate	C ₃ A (%)	7.0 to 12.0
Tetracalcium Aluminoferrite	C ₄ AF (%)	6.0 to 10.0

Portland cements are predominantly compounds of calcium silicate and calcium aluminate with a small proportion of gypsum. They are produced by burning or sintering, at a temperature in excess of 1400°C, a finely ground mixture of raw materials which contain predominantly calcium carbonate, aluminium oxide, silica and iron oxide. The cooled clinker formed is ground under controlled conditions with the addition of typically 5% gypsum.

For further information:

Technical helpline 0870 609 0011
 E-mail info@lafargecement.co.uk
 Customer services 0870 600 0203
 E-mail customerservice@lafargecement.co.uk
 Facsimile 01635 280250
 Website www.lafargecement.co.uk
 Lafarge Cement United Kingdom, Manor Court,
 Chilton, Oxon OX11 0RN



United Kingdom

A leading company...

and a leading brand



ADOFLOW EXTRA

Super Plasticiser for Concrete and Mortar

Description

A liquid plasticiser and water reducing agent which imparts extremely high workability when added to a concrete mix or a cementitious grout. Being a highly effective deflocculating agent it disperses cement paste into its primary particles significantly increasing the flow characteristics of the paste.

Benefits

- Enables concrete to achieve high compaction with minimal or no vibration or tamping.
- Increases flow characteristics of concrete to assist with difficult pours.
- Permits significant reduction in water content of normal workability concrete with consequent reduction in water/cement ratio to produce higher early and ultimate strengths.

Addition

The optimum addition rate of ADOFLOW EXTRA is best determined after preliminary trials with the actual concrete under consideration. As a guide for carrying out trials an addition rate of 0.5 litres to 1.5 litres per 100 kilos Portland cement is recommended. Where high early and ultimate strength concrete is required, necessitating a steep reduction in water/cement ratio, the addition rate of ADOFLOW EXTRA may be increased up to 2.0 litres per 100 kilos Portland cement.

Mixing

ADOFLOW EXTRA is best added during the mixing cycle preferably at the same time as the water. Alternatively it may be added to a normal concrete mix just prior to the pour allowing for a further mixing cycle of at least 2 minutes.

Typical Comparisons

The following data is typical of what can be expected when comparing a concrete mix with the inclusion of ADOFLOW EXTRA to a control mix.

High Workability Self Compacting Concrete

- Aggregate/Cement Ratio 5.2:1
- W/C Ratio - Control Mix 0.58
- W/C Ratio - Test Mix 0.58

ADOFLOW EXTRA - Test Mix 1.0 litre per 100 kg OPC

- Slump - Control Mix 50 mm
- Slump - Test Mix Collapse

Compressive Strength - Test Mix:

- 7 days: 102 % of control
- 28 days: 103 % of control

High Early & Ultimate Strength Concrete

- Aggregate/Cement Ratio 5.2:1
- W/C Ratio - Control Mix 0.58
- W/C Ratio - Test Mix 0.47

ADOFLOW EXTRA - Test Mix 1.25 litre per 100 kg OPC

- Slump - Control Mix 50 mm
- Slump - Test Mix 50 mm

Compressive Strength - Test Mix

- 1 day: 180 % of control
- 7 days: 144 % of control
- 28 days: 135 % of control

Storage & Shelf Life

Store at temperatures above freezing but not above 28° C in dry condition and under cover. Should freezing occur, completely thaw material and then mix thoroughly before use. In these circumstances shelf life is indefinite.

Specification Clause

ADOFLOW EXTRA manufactured by ADOMAST Building Chemicals Ltd shall be added to the concrete mix in accordance with the manufacturers recommendation.

Health & Safety

ADOFLOW EXTRA is non-hazardous in normal use. If splashes should affect the eyes bathe immediately with copious quantities of clean water and then immediately seek medical advice. Reference should be made to the separate Health and Safety literature

ABCD 394 ISSUE: 4
ISSUED: JAN 1997



Data Sheet**MH501.GBR****1. Identification of the Substance and Company**

Product name: **Elkem Microsilica** [®]

Address/Phone No.: **Elkem ASA,
Materials
P.O.Box 8126 Vaagsbygd
N-4602 Kristiansand S., Norway
Telephone: + 47 38 01 75 00
Telefax: + 47 38 01 49 70**

Contact person: **Tore Danielssen**

Emergency Phone No.: **Not applicable**

2. Composition/Information on Ingredients

Synonyms: **Microsilica, Silica powder, Amorphous silica,
Silicon dioxide powder, condensed SiO₂-fume, Silica fume.**

CAS No.: **69012-64-2**

EINECS No.: **273-761-1**

HAZARDOUS INGREDIENT(S): **None**

Symbol: **None**

R and S Phrases: **None**

Constituents (analysis):	Weight%
Silicon dioxide (SiO ₂) amorphous	85-98
Iron oxide (Fe ₂ O ₃)	max.3.0
Aluminium oxide (Al ₂ O ₃)	max.1.5
Calcium oxide (CaO)	max.0.7
Magnesium oxide (MgO)	max.2.0
Sodium oxide (Na ₂ O)	max.1.0
Potassium oxide (K ₂ O)	max.3.0
Carbon (C)	max.3.0



C/S/B	Y13
Revised January 1993	

Sikadur 31

Thixotropic epoxy adhesive

Technical Data Sheet

Description

Sikadur 31 is a two component system, both components being thixotropic and containing fillers. The resin component is white and the hardener component black, ultimately producing a grey colour when mixed.

USES

Sikadur 31 is free of solvents.

Sikadur 31 will bond and fill virtually all building materials.

Sikadur 31 can be used for example to bond the following materials:

Concrete	Metals	Non-siliconised ceramics (slip bricks)
Asbestos	Stoneware	Cast asphalt
Wood	Glass	Polyester and epoxy components

Sikadur 31 resists the attack of a wide range of chemicals, solvents, etc.

Sikadur 31 is supplied in two grades: Normal and Rapid, and can be used in wet/damp or dry condition (no standing water), so enabling it to be used in most conditions within a temperature range of 0°C to 30°C. For structural strengthening please contact Sika's Specialist Engineering Division, for the appropriate materials and specification.

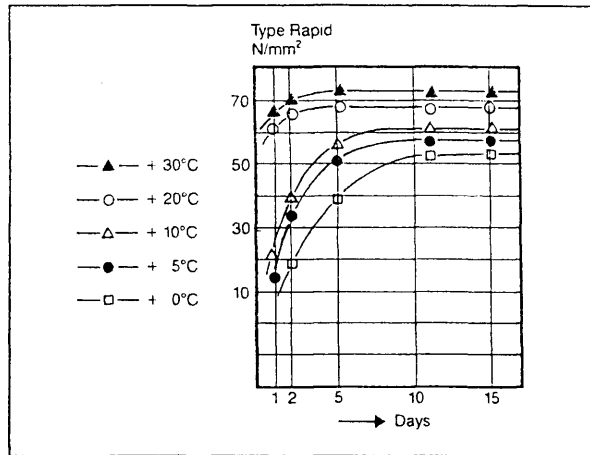
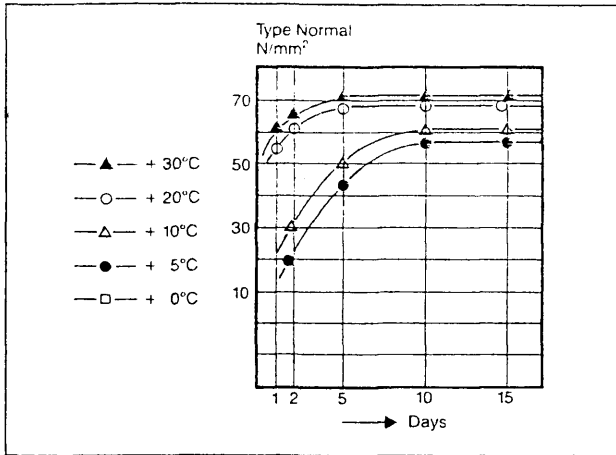
ADVANTAGES

- ★ Colour coded components for thorough mixing
- ★ Thixotropic – can be used on vertical and horizontal surfaces
- ★ Outstanding adhesion – bonds to virtually all building surfaces
- ★ Moisture tolerant – work can be carried out even in damp or wet conditions
- ★ Rapid grade available for use at temperatures down to 0°C
- ★ Sikadur 31 is approved for contact with potable water (WFBS No. 92 06505)
- ★ High resistance to water absorption and creep

TECHNICAL DATA†

Grade	Normal	Rapid
Colour	Grey	Grey
Density	1.5 kg/litre	1.5 kg/litre
Pot life	30°C 20 mins 20°C 40 mins 10°C 1½ hours 5°C 3½ hours 0°C –	– 10 mins 30 mins 1 hour 1¼ hours
Tack Free	12 hours (at 20°C) 8 hours (20°C)	
Shrinkage	Negligible	
Tensile strength*	14.8 N/mm ²	
Flexural strength*	36 N/mm ²	
Compressive strength	70–90 N/mm ²	
Shear strength	in excess of 21 N/mm ² (3,000 psi)	
E. Modulus	7-7.5 × 10 ⁴ kg/cm ²	
Storage life (minimum)	12 months in original containers at 5°C to 25°C	
Application ranges	Rapid 0°C to 15°C Normal 5°C to 30°C	
*Tested to B.S. 6319 (20°C cure)		
Adhesion	(DIN 53232) to concrete: approx 3.5–4.5 N/mm ² to grit blasted steel: approx 14 N/mm ² (BS 6319: Part 4) Slant/Shear Test Sikadur 31 : 54 N/mm ²	
†Typical values		

Guide to Compressive Strength Development (dependent on temperature)



SURFACE PREPARATION

All surfaces must be clean, sound and free from any dust, ice, oils, grease or other surface contaminants.

Concrete/Mortar Brickwork: Mechanically abrade the surface with a needle gun, mechanical wire brush, sandblast or grind. All surface laitence must be removed. Cement and concrete should be at least 4 weeks old.

Metals: Remove any paints, oils, grease, rust and oxide films by grit blasting. Where required apply one coat of **Friazinc R** or **Icosit EG1** as a primer/travel coat (refer to separate technical information sheet). **Sikadur 31** may be applied after approximately 8 hours. Note: In the event of extended waiting times, the surface of the **Friazinc R** or **Icosit EG1** should be thoroughly cleaned with fresh water.

Plastic components (epoxy, polyester), abrade and rinse with **Sikadur Cleaner**.

APPLICATION

Mix all of Part A (white resin) with all of Part B (black hardener) until an even grey colour is obtained. Mix well using a spatula or low speed drill and paddle.

Apply by trowel, serrated spreader, spatula or stiff brush (minimum thickness 1mm, maximum thickness per layer 30mm). Work the **Sikadur 31** well into the substrate, especially if the substrate is damp.

Bond any subsequent materials onto the **Sikadur 31** whilst it is still tacky.

Clean all tools, equipment with **Sikadur Cleaner** (flammable) whilst the resin is still soft. Hardened **Sikadur 31** can only be removed mechanically. **Do not part mix packs of Sikadur 31.**

Consumption guide (does not allow for surface texture and wastage)

1kg = approx	41 cubic inches or 666cc
Thickness of Sikadur 31	Kg/m ² approx
2mm	3.0
4mm	6.0
10mm	15.0

PACKAGING

- Sikadur 31 Normal:** 1kg and 5kg
- Sikadur 31 Rapid:** 1kg and 5kg
- Sikadur Cleaner:** 5 litres and 25 litres and 200 litres (flammable).

Handling Precautions

Sika products are generally harmless provided that certain precautions normally taken when handling chemicals are observed. The materials must not, for instance, be allowed to come in contact with foodstuffs or food utensils, and measures should also be taken to prevent the uncured materials from coming in contact with the skin, since people with particularly sensitive skin may be affected. The use of protective clothing, goggles, barrier creams and rubber gloves is required. The skin should be thoroughly cleansed at the end of each working period either by washing with soap and warm water or by using a resin-removing cream – the use of powerful solvents is to be avoided. Disposable paper towels – not cloth towels – should be used to dry the skin. Adequate ventilation of the working area is recommended. In case of accidental eye or mouth contact, flush with water – consult a doctor immediately. A leaflet "A Guide to the Safe Handling and Use of Sika Products" is available and we strongly advise that it is read prior to the use of Sika Products. Sika products should be stored in sealed containers away from the reach of children.

Important note

The information given in this data sheet is based on many years experience and is correct to the best of our knowledge. However, since the use of our products in accordance with the instructions given, and their success in application is dependent on a number of factors, we can only be responsible for the quality of our product at the time of despatch. Should any doubt arise about specification or application, our technical service department should be contacted immediately. As the information given herein is of general nature, we cannot assume any responsibility. Success will always depend on the peculiarities of the individual case. We also refer to our standard conditions of sale. Pack sizes, colours and price group may be subject to change at the discretion of Sika Limited. Please contact our Sales Office for up to date information. Sika data sheets are regularly updated and reprinted, customers are therefore advised to check that they are in possession of the current edition.

Please consult our technical sales department for further information.



Sika Limited

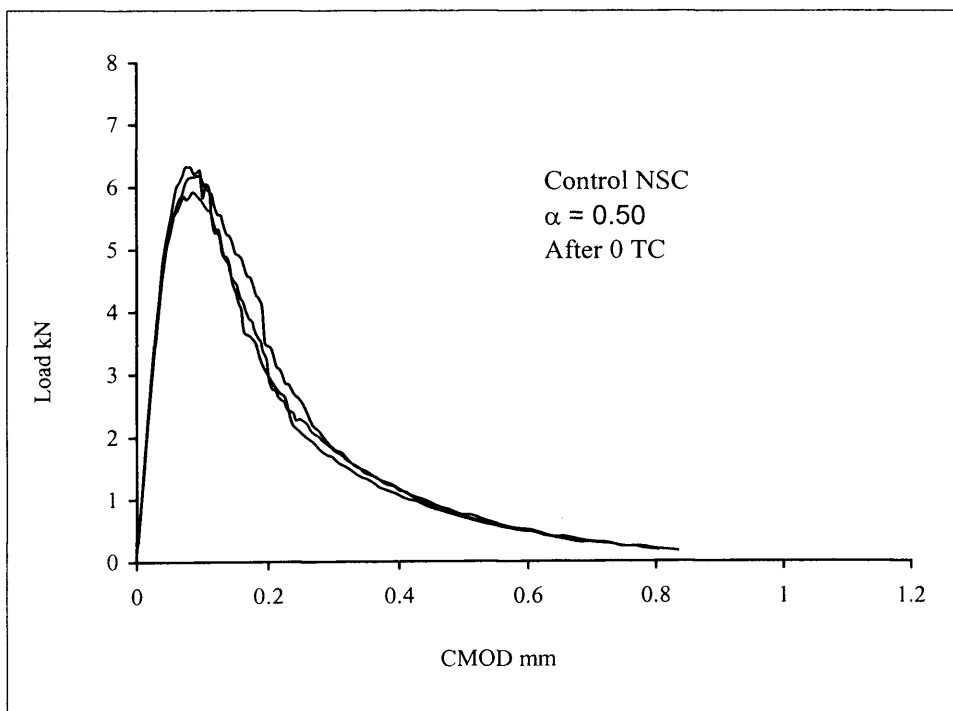
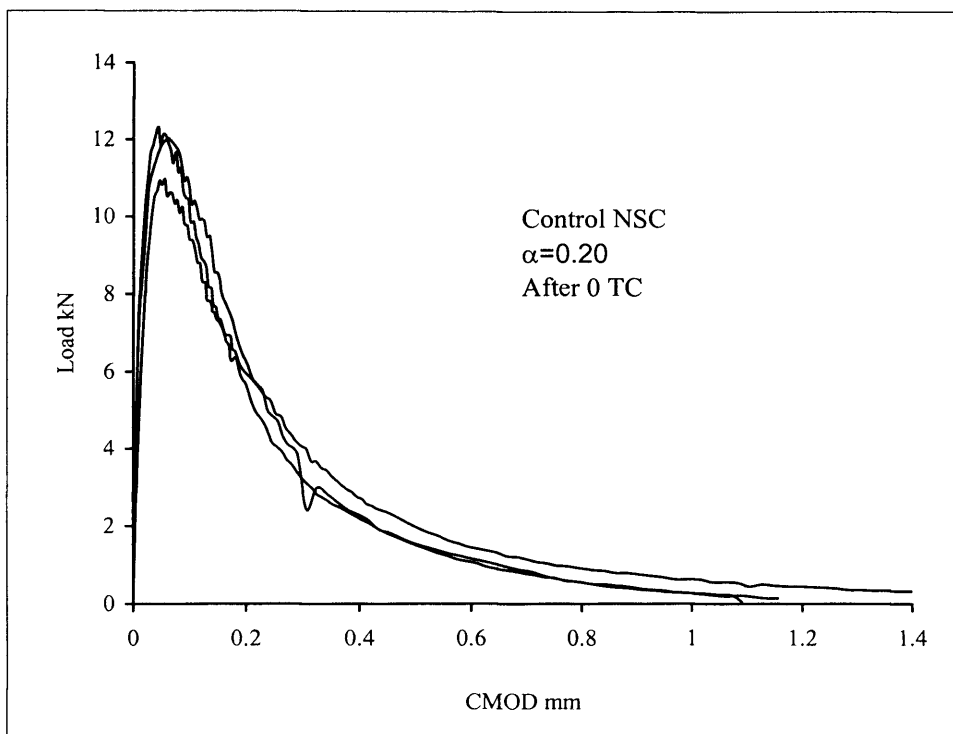
Watchmead, Welwyn Garden City, Hertfordshire, AL7 1BQ Fax: 0707 329129

Telephone: 0707 329241

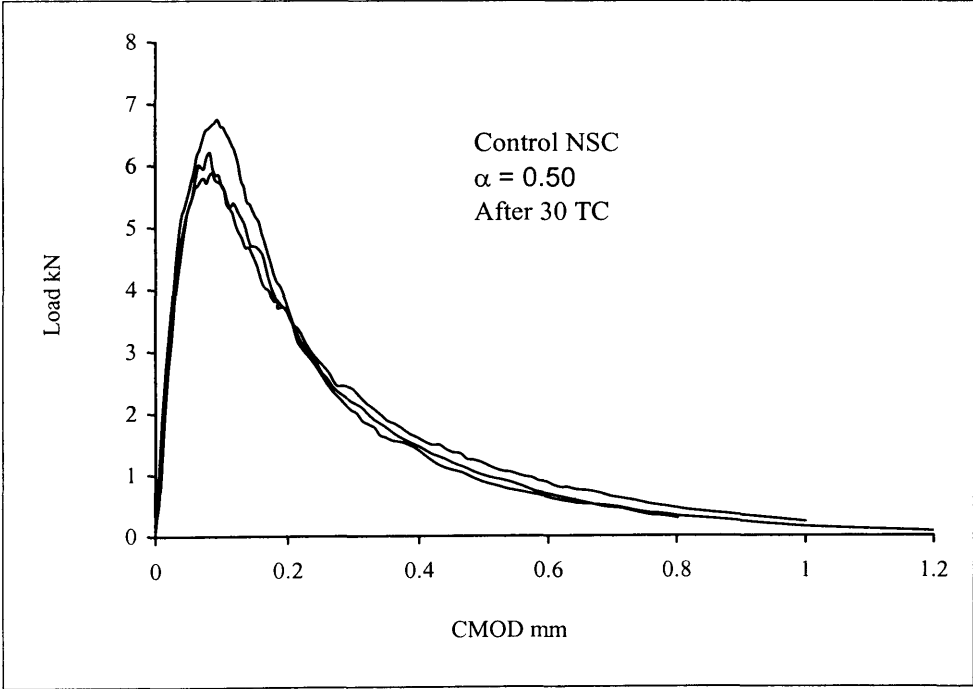
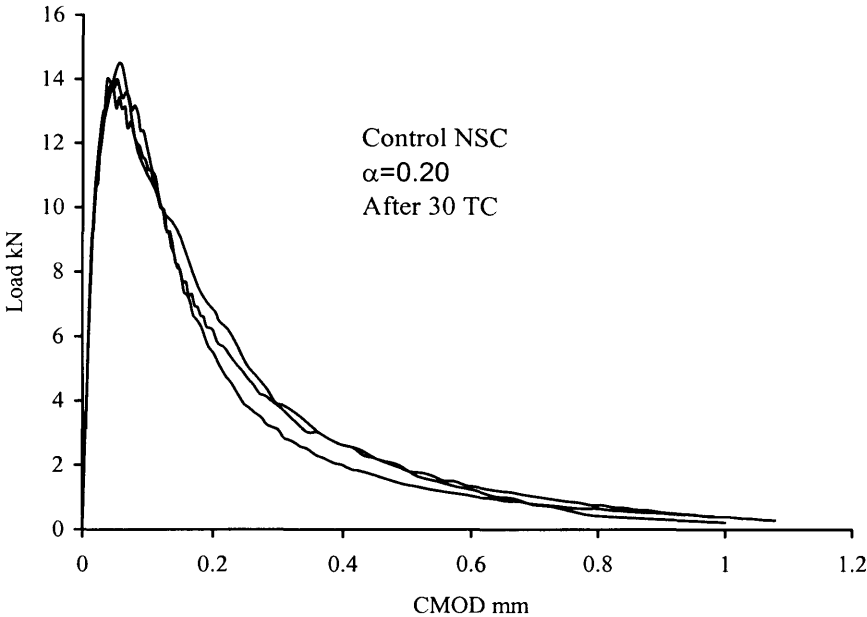
Appendix B

*Load-CMOD curves for control and
CARDIFRC[®] bonded specimens*

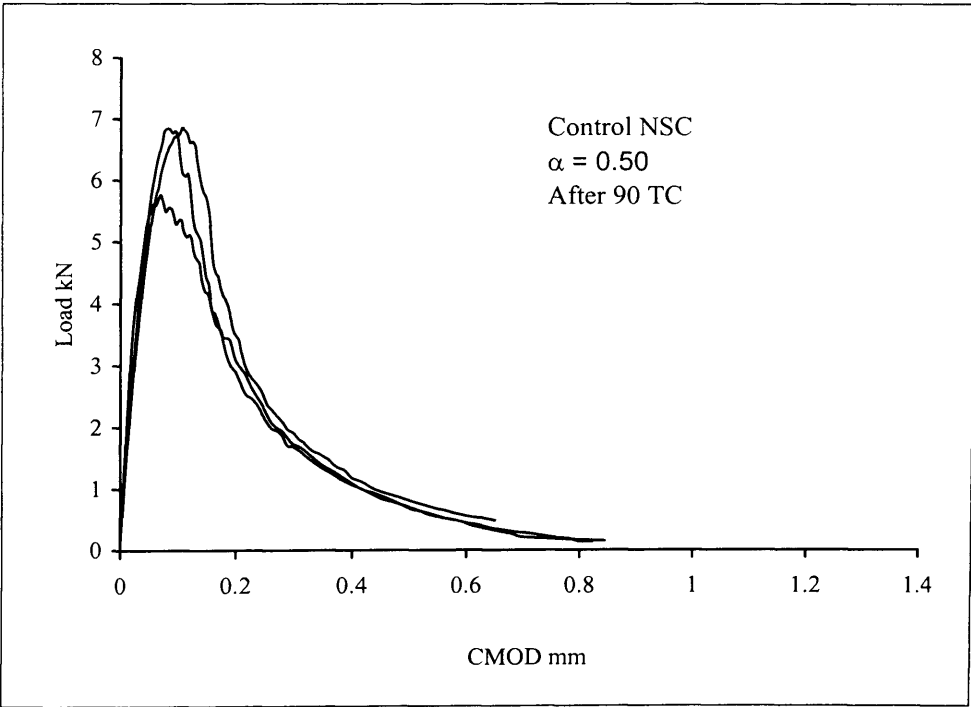
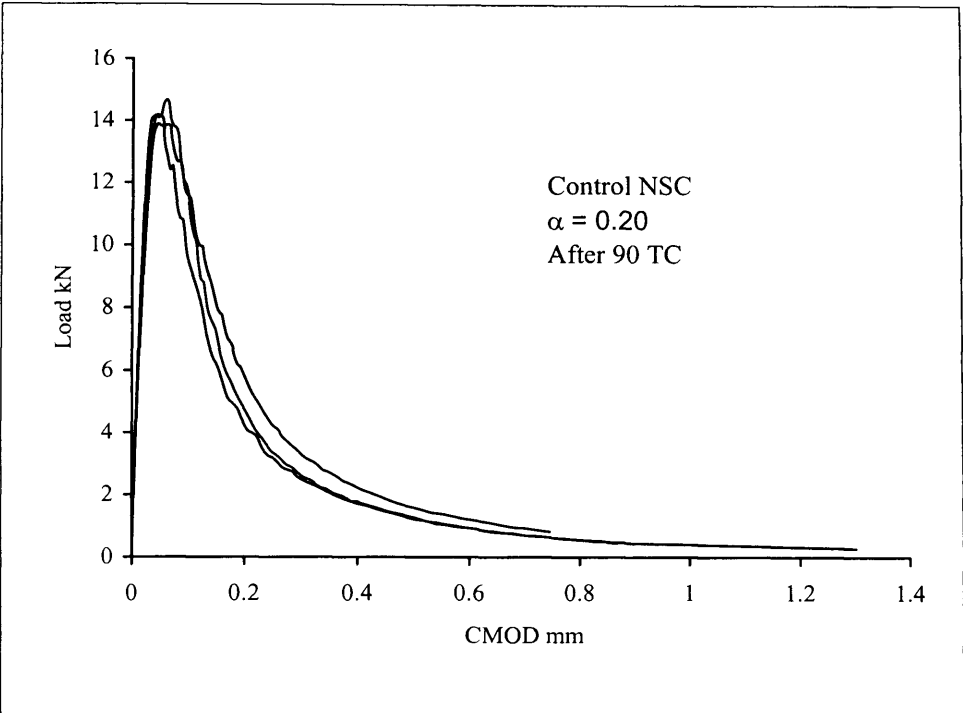
Appendix B: Load-CMOD curves for control and bonded specimens after thermal cycling



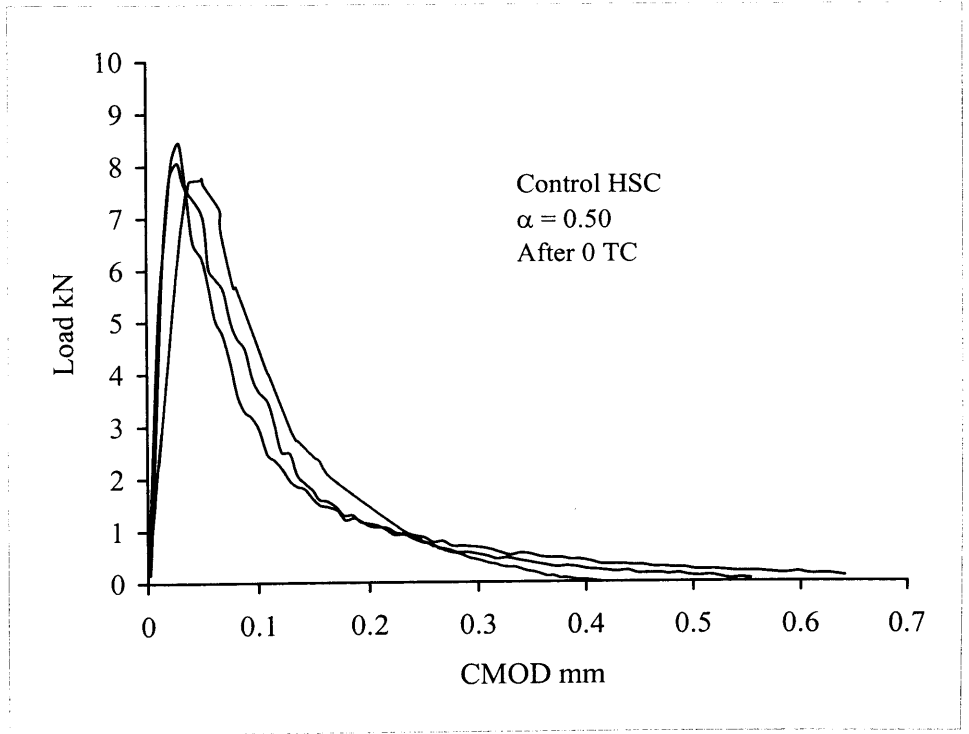
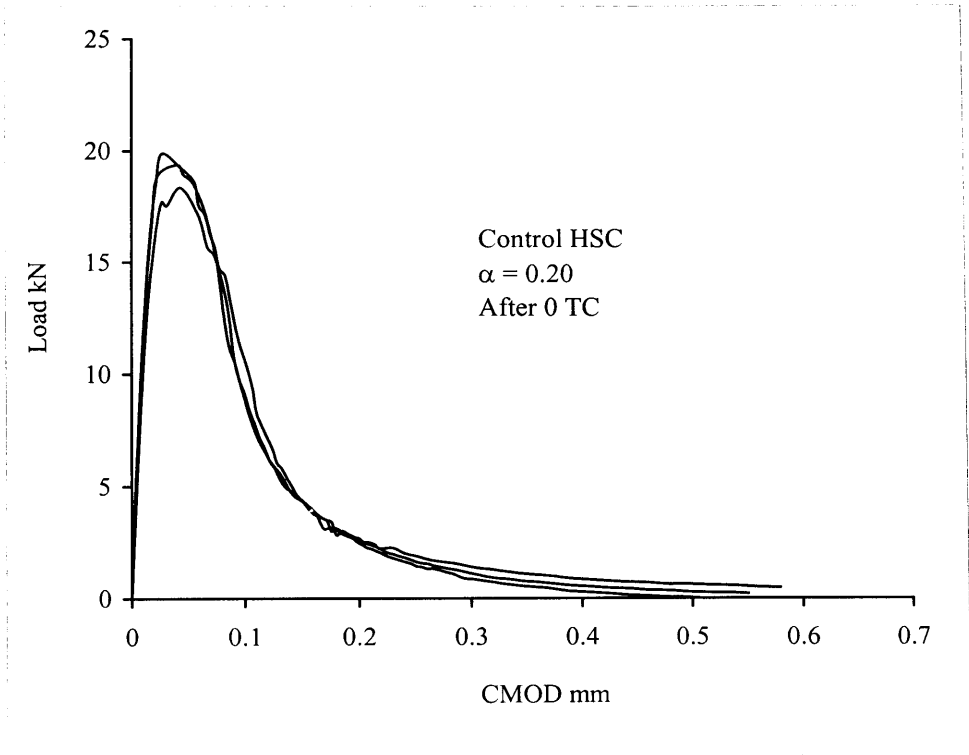
Appendix B: Load-CMOD curves for control and bonded specimens after thermal cycling



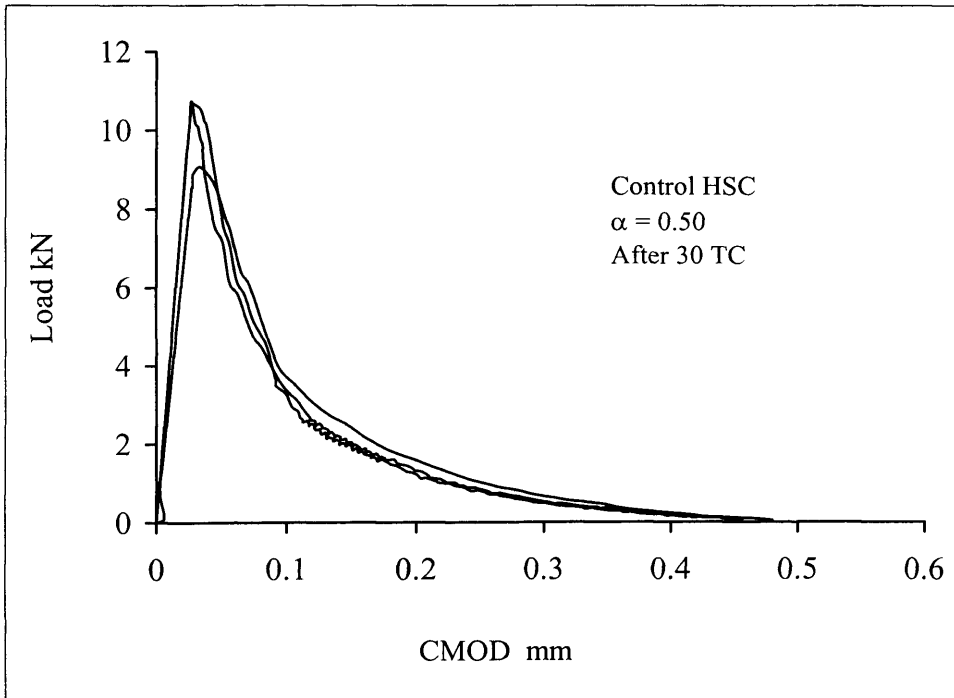
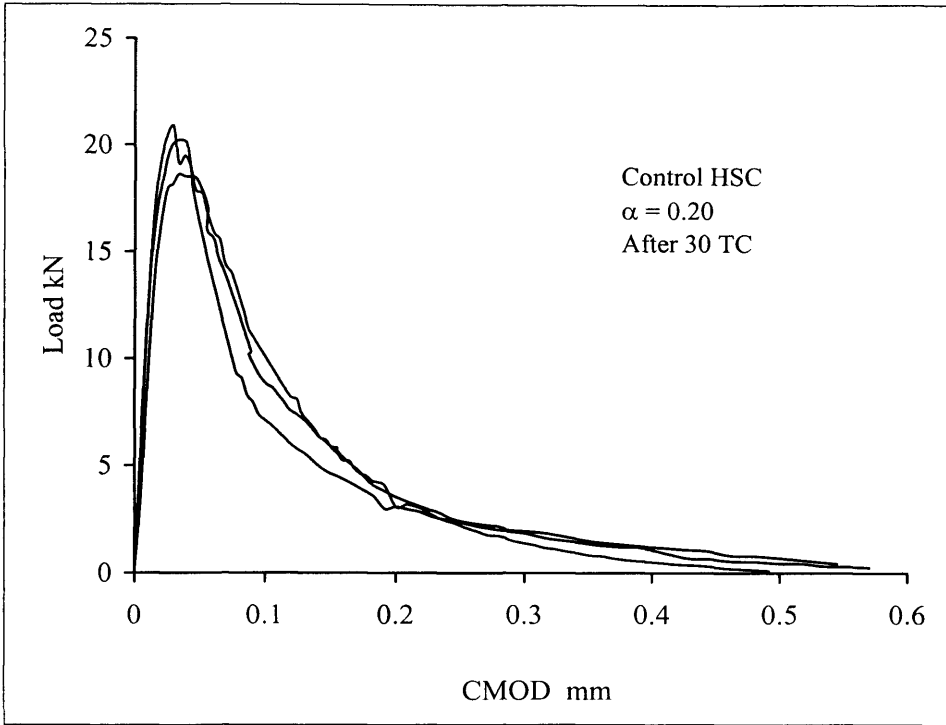
Appendix B: Load-CMOD curves for control and bonded specimens after thermal cycling



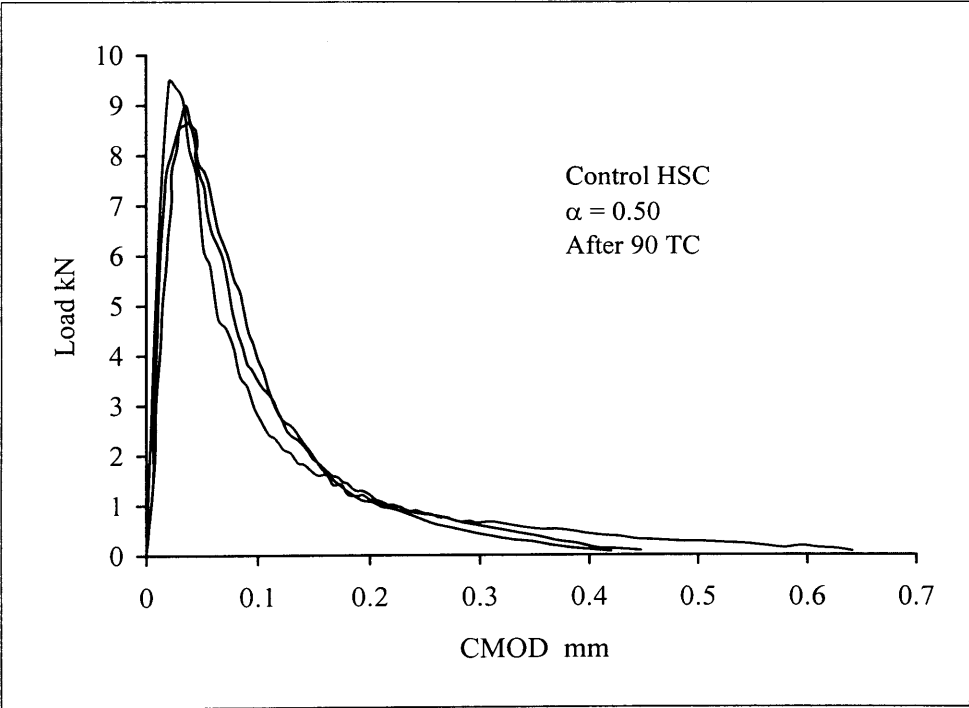
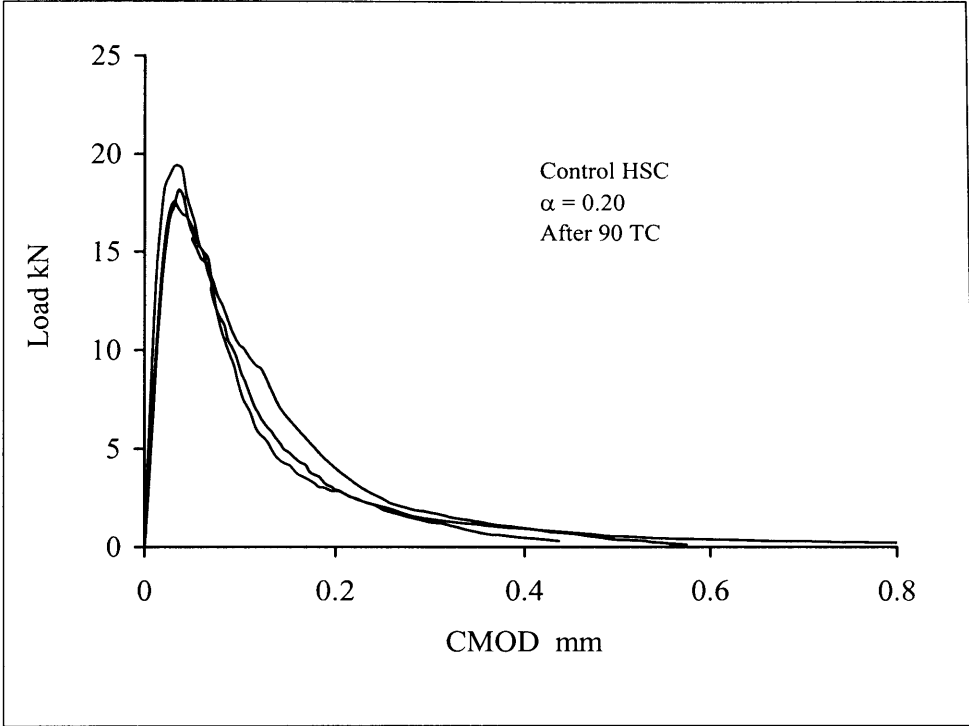
Appendix B: Load-CMOD curves for control and bonded specimens after thermal cycling



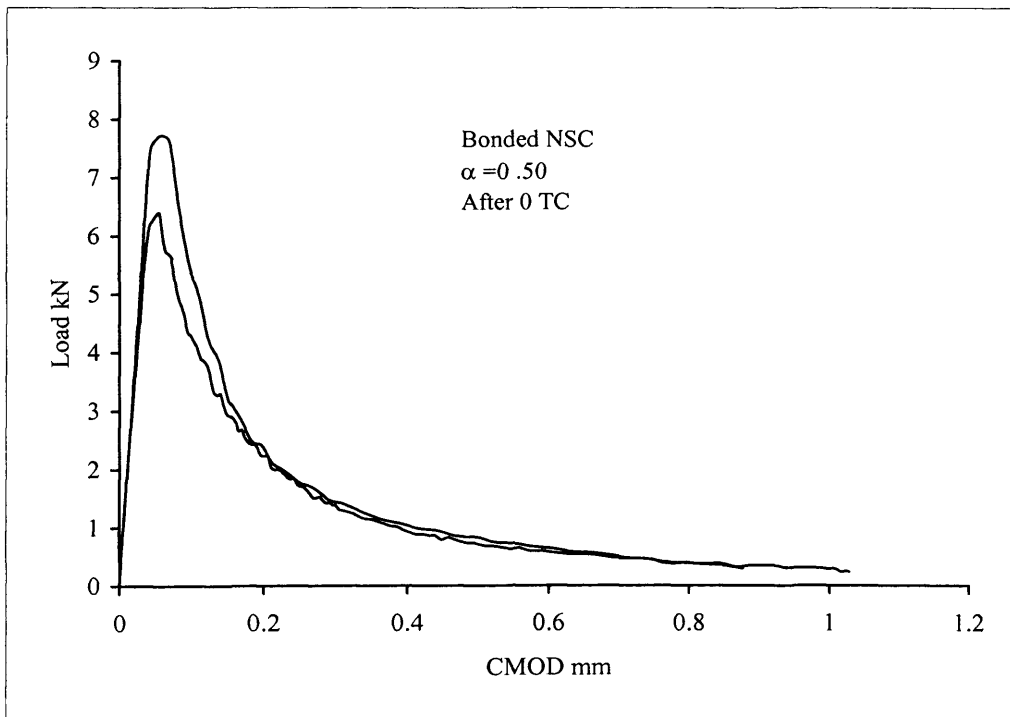
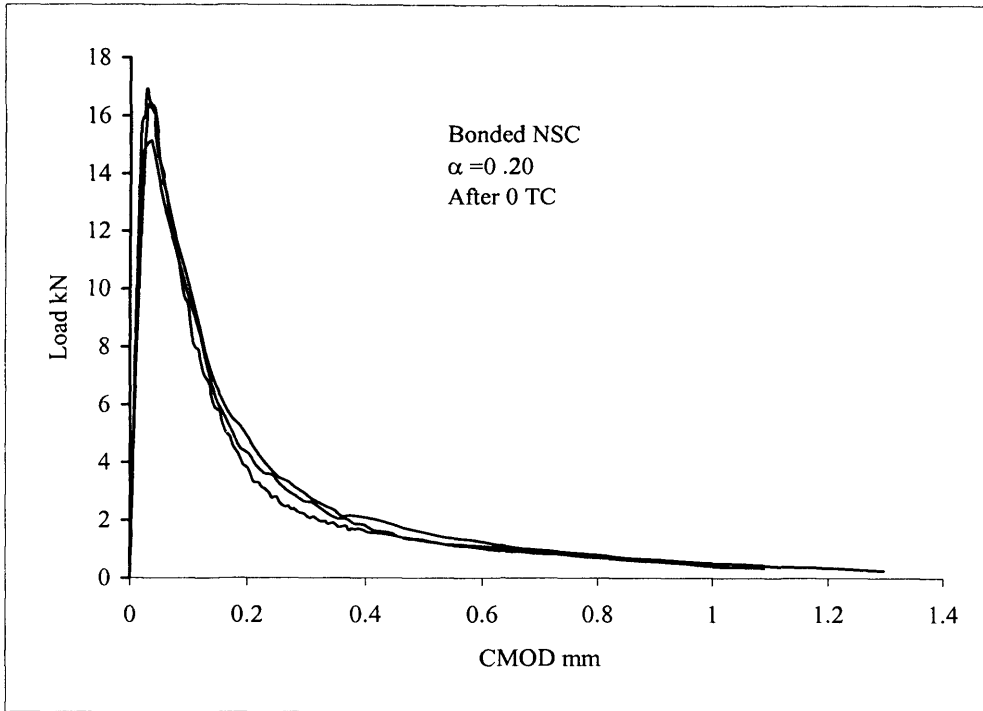
Appendix B: Load-CMOD curves for control and bonded specimens after thermal cycling



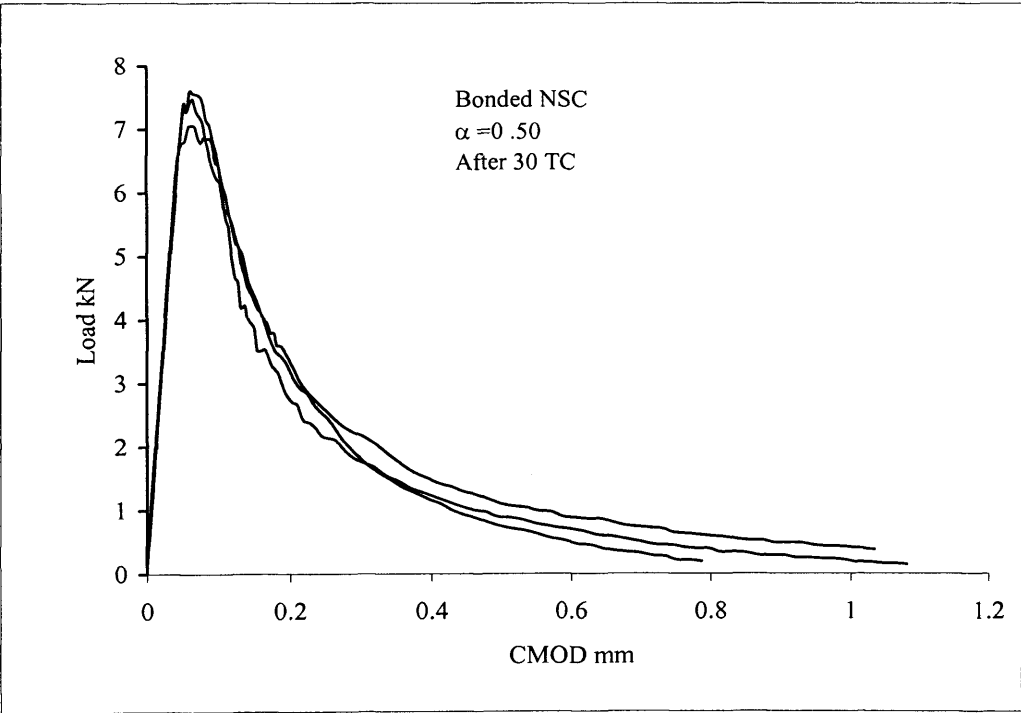
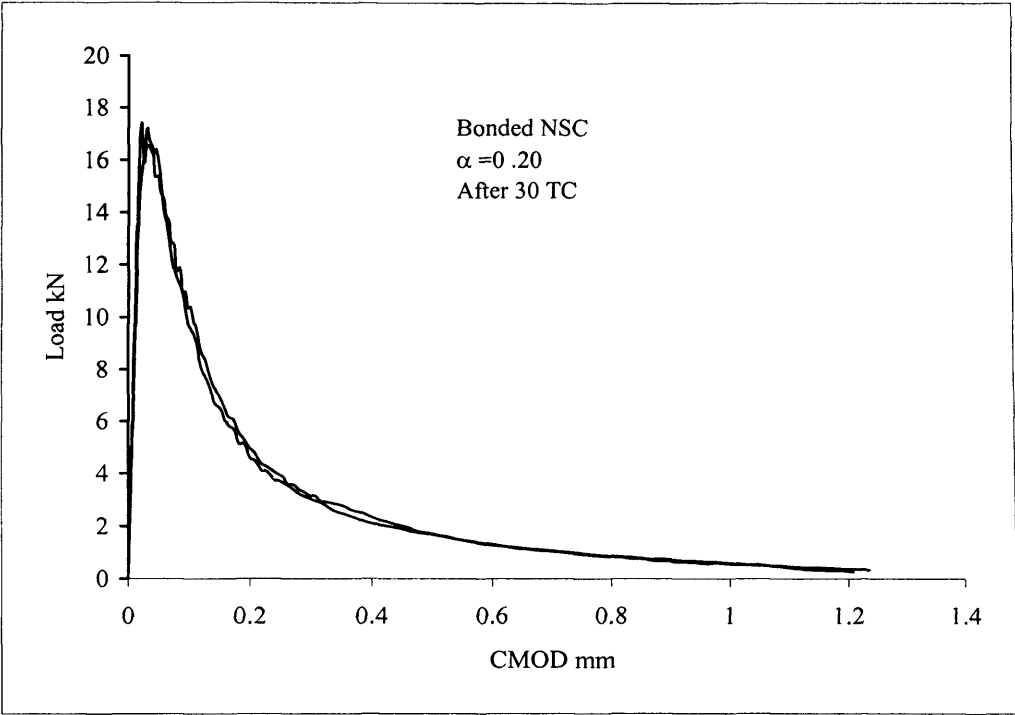
Appendix B: Load-CMOD curves for control and bonded specimens after thermal cycling



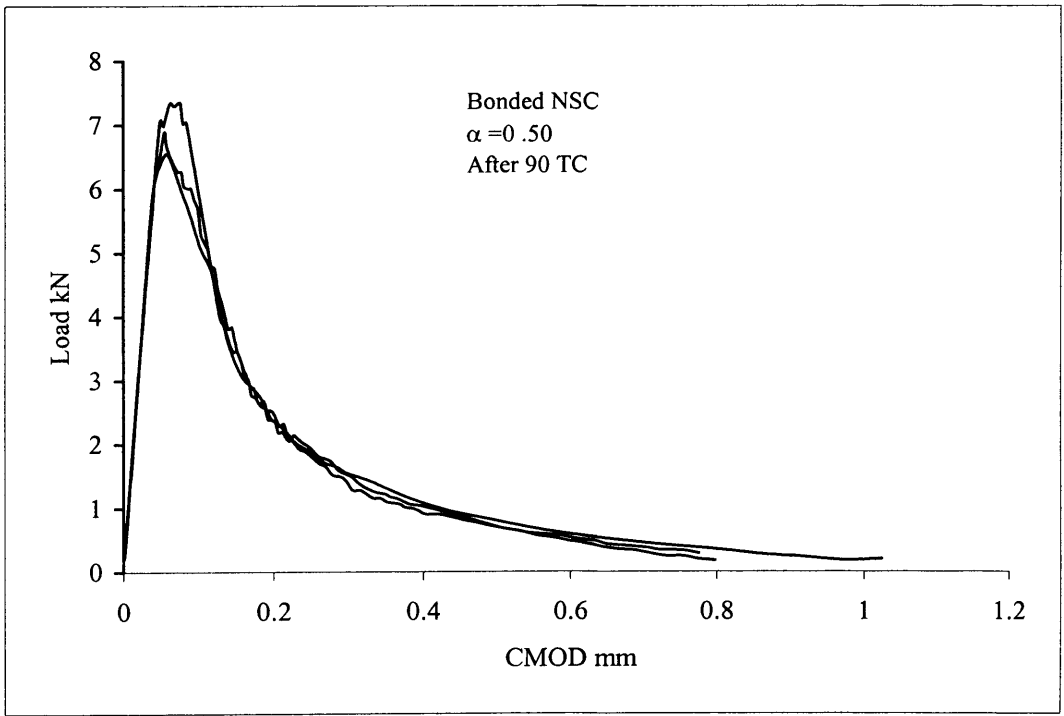
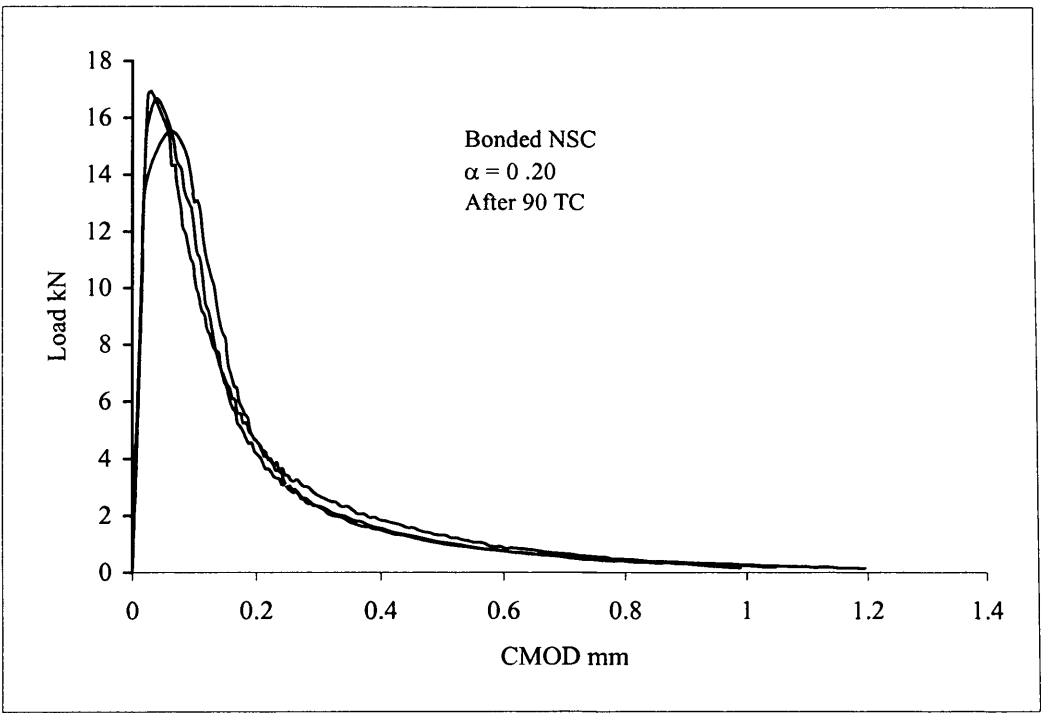
Appendix B: Load-CMOD curves for control and bonded specimens after thermal cycling



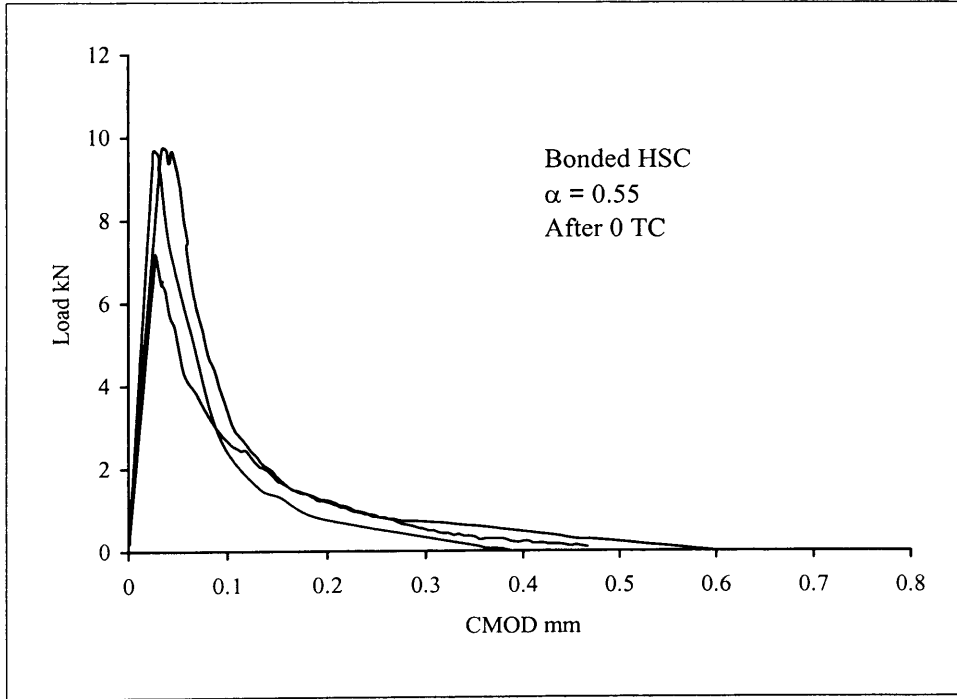
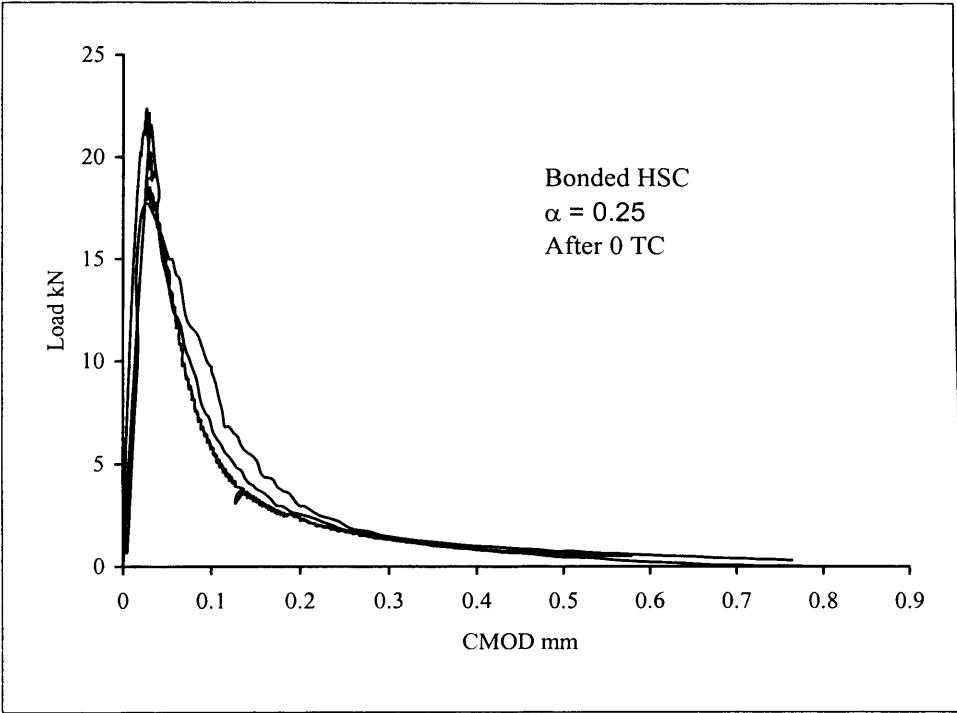
Appendix B: Load-CMOD curves for control and bonded specimens after thermal cycling



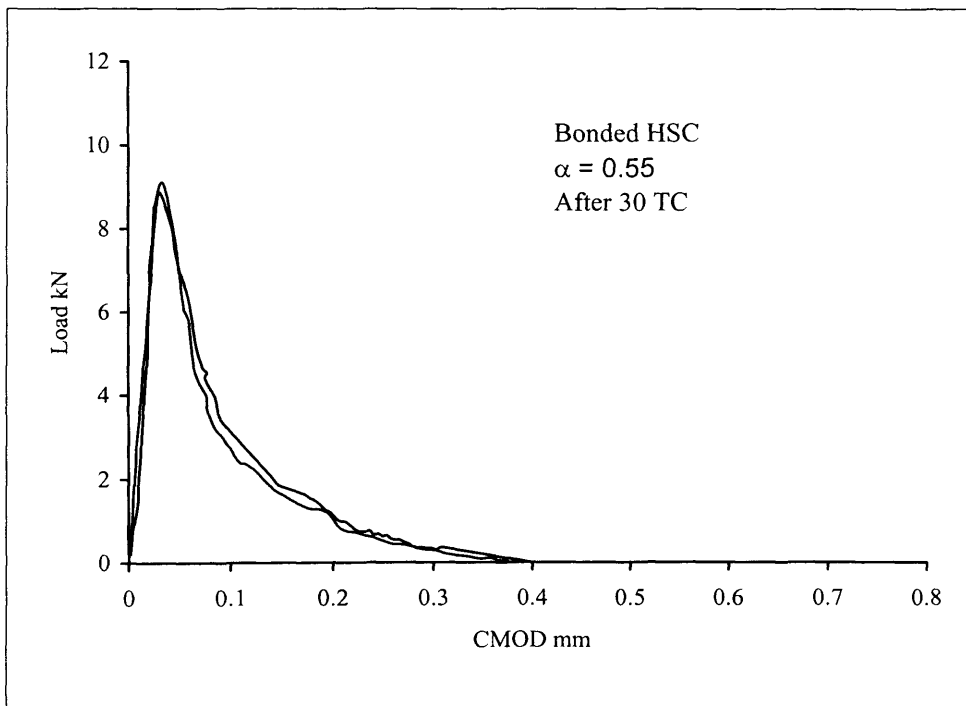
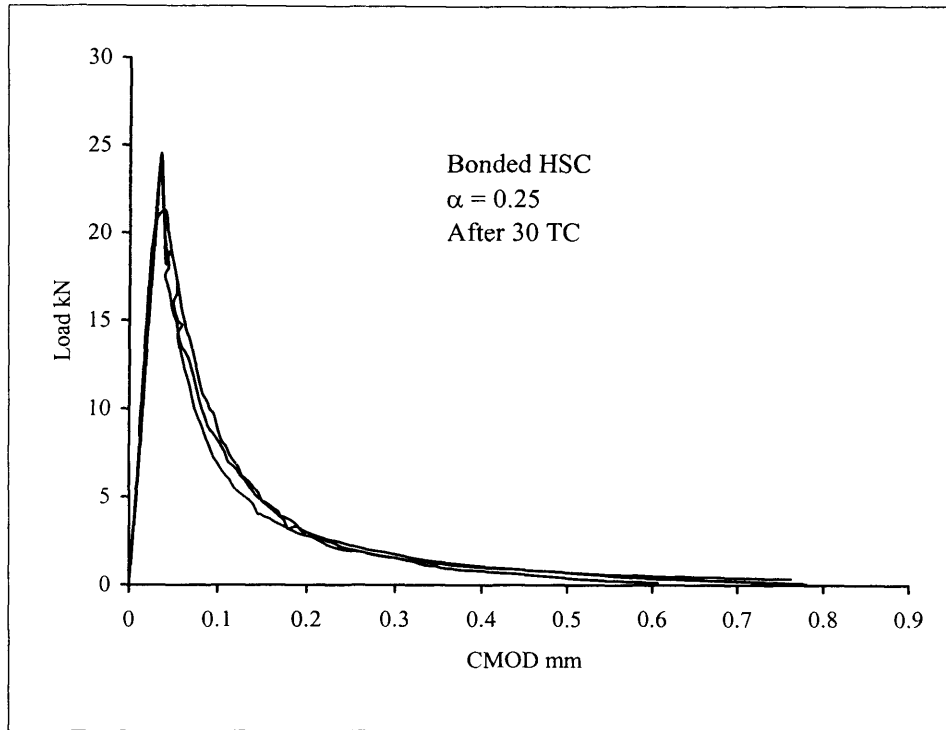
Appendix B: Load-CMOD curves for control and bonded specimens after thermal cycling



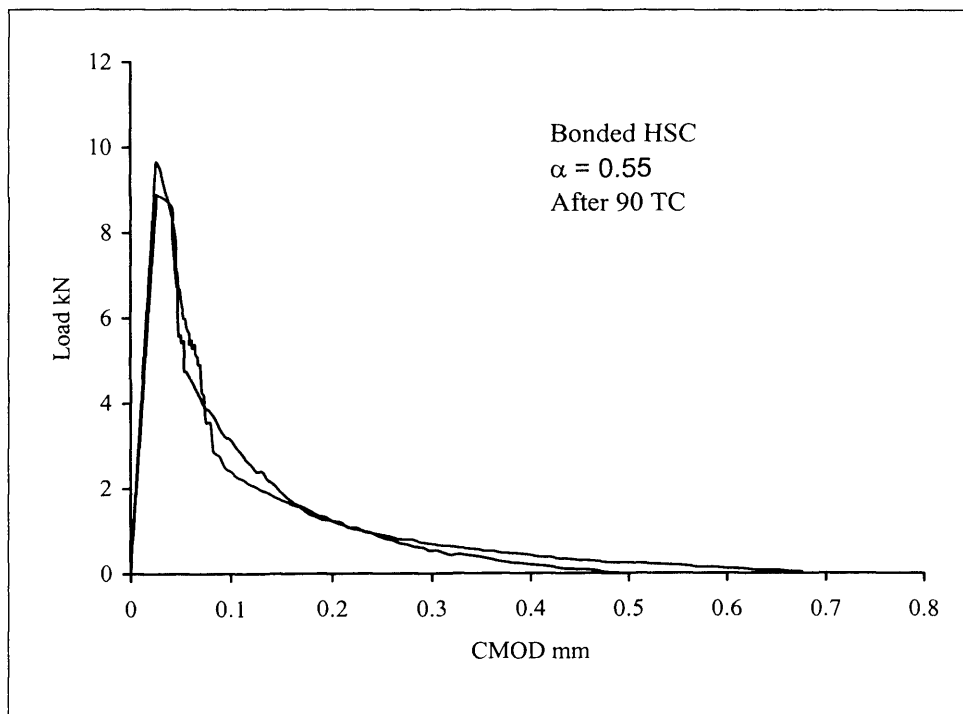
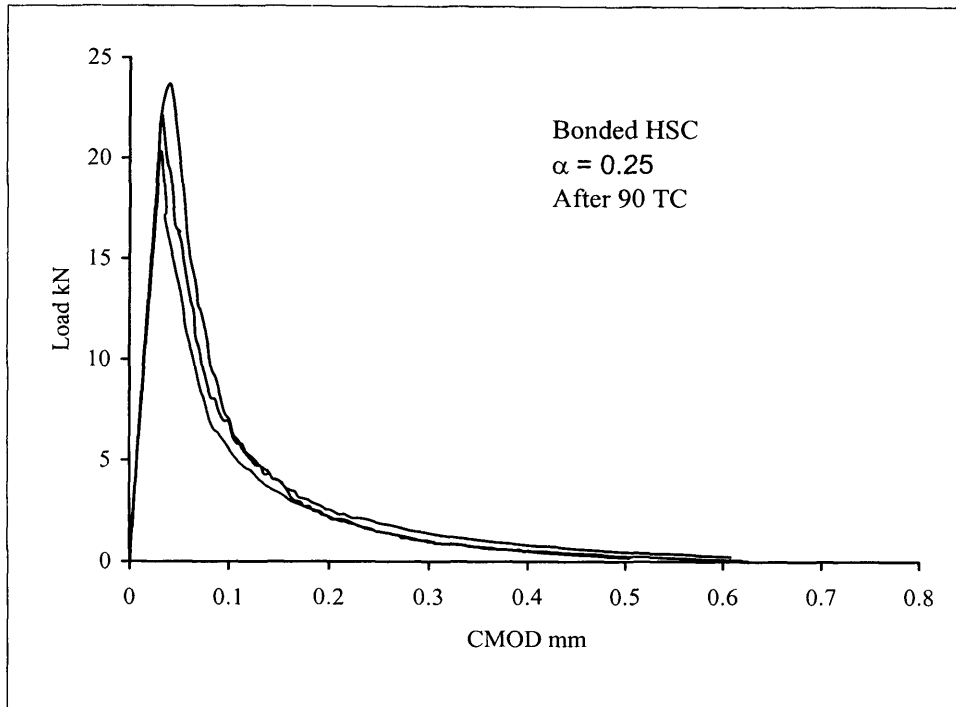
Appendix B: Load-CMOD curves for control and bonded specimens after thermal cycling



Appendix B: Load-CMOD curves for control and bonded specimens after thermal cycling

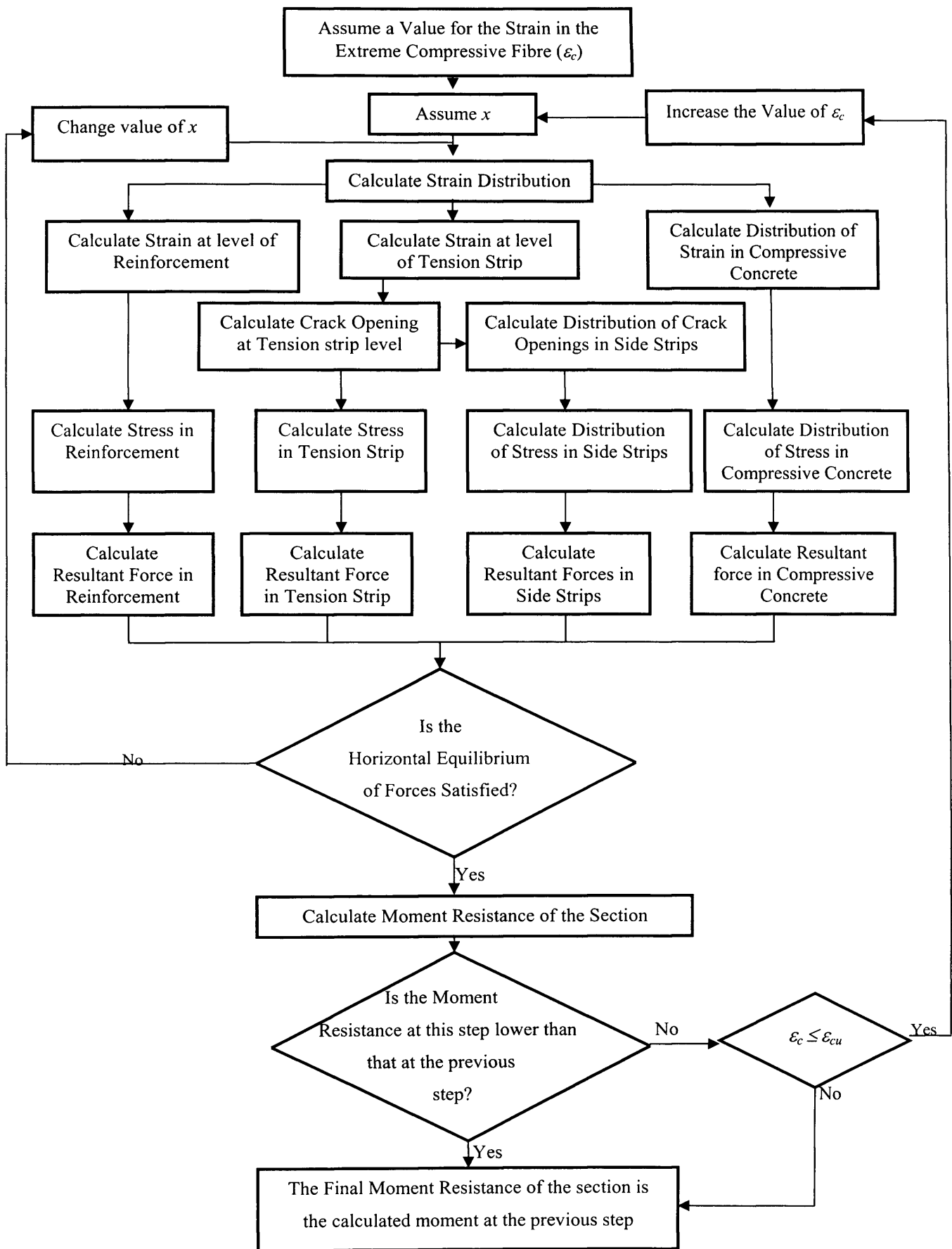


Appendix B: Load-CMOD curves for control and bonded specimens after thermal cycling

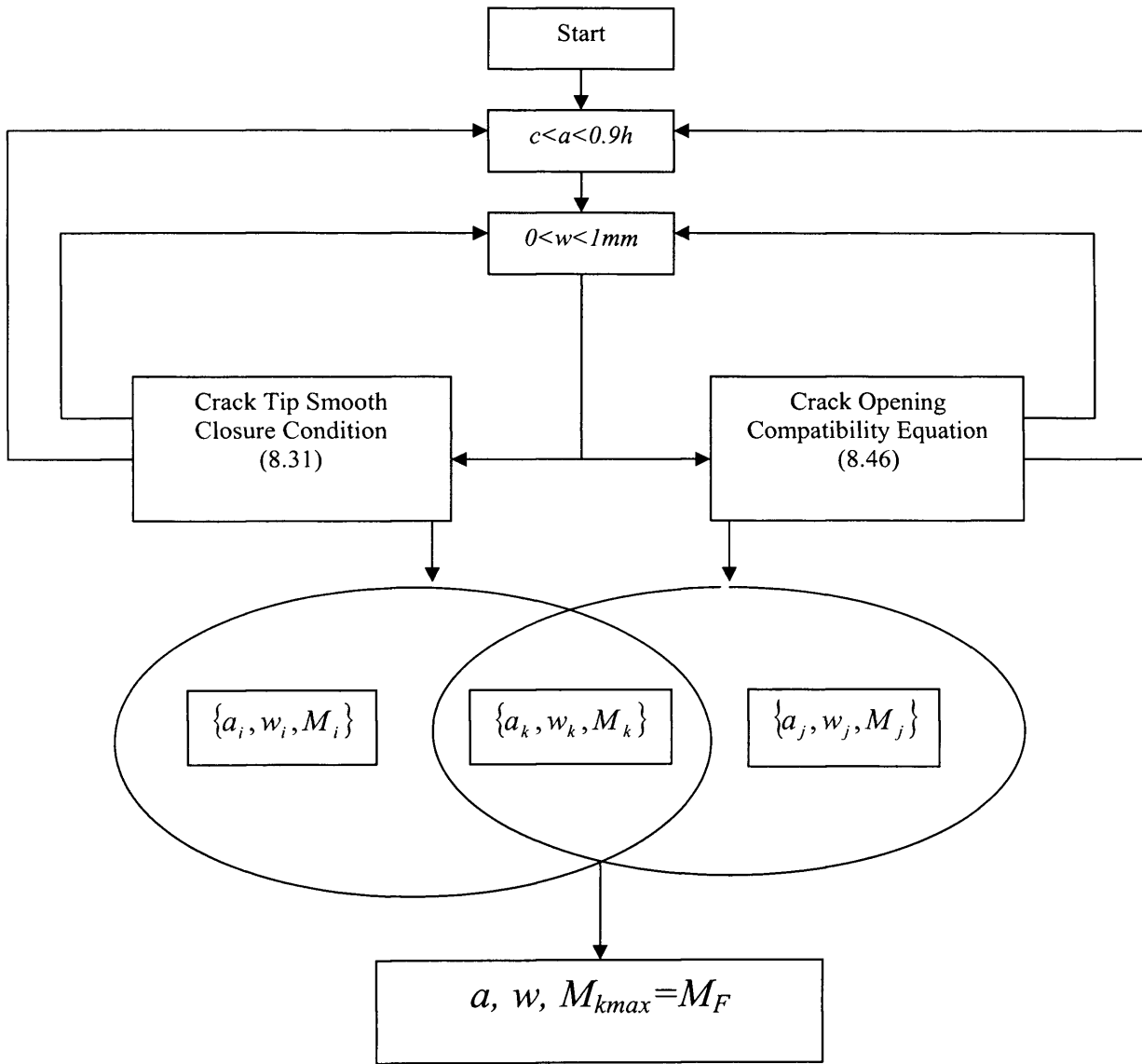


Appendix C

Computer programmes



Flowchart of the programme for calculating the moment resistance of the beams using the classical theory method (After Alae and Karihaloo, 2003a)



(b)

Flowchart of the programme for calculating the moment resistance of the beams using the fracture mechanics method (After Alaei and Karihaloo, 2003b)

Solution of the stress intensity factor equation (8.31) for the beams retrofitted with one plate.

```

CLS
COLOR 15, 1
pi = 3.141592

PRINT
PRINT "*****"
PRINT "          CALCULATION OF RESISTANT MOMENT OF A CONCRETE BEAM          "
PRINT "          STRENGTHENED BY ONE CARDIFRC® STRIP                          "
PRINT "
PRINT "          Using the concept of FRACTURE MECHANICS
PRINT "
PRINT "*****"
PRINT
PRINT

INPUT "Enter input file name:                ", I$
INPUT "Enter the first output file name :    ", o$

OPEN I$ FOR INPUT AS #1
OPEN o$ FOR OUTPUT AS #2

LINE INPUT #1, N$
LINE INPUT #1, N$
INPUT #1, b, h, c, Ec

LINE INPUT #1, N$
LINE INPUT #1, N$
LINE INPUT #1, N$
LINE INPUT #1, N$
LINE INPUT #1, N$
INPUT #1, Ass, fy, Es

LINE INPUT #1, N$
LINE INPUT #1, N$
LINE INPUT #1, N$
LINE INPUT #1, N$
LINE INPUT #1, N$
INPUT #1, t, fctm, Ef, wc

Ec = Ec * 1000
Es = Es * 1000
Ef = Ef * 1000                                'GPa to MPa

'INPUT "a="; a                                'a is the depth of crack
'INPUT "w="; w                                'w is the opening of crack at the bottom of
beam

PRINT #2,
PRINT #2, "
***** *
PRINT #2, "          *   CALCULATION OF RESISTANT MOMENT OF A CONCRETE BEAM *"
PRINT #2, "          *   STRENGTHENED BY one CARDIFRC® STRIP *"
PRINT #2, "          *   Using the concept of FRACTURE MECHANIC *"
PRINT #2, "
*****"
PRINT #2,
PRINT #2,
PRINT #2,

PRINT #2, "          -----"
PRINT #2, "          INPUT DATA *"
PRINT #2, "          -----"
PRINT #2, "          Width of beam, * b (mm) :"; b

```

Appendix C: Computer programmes

```

PRINT #2, "          Height of beam,                               h(mm):"; h
PRINT #2, "          Distance between rebar and the bottom of beam, c(mm):"; c
PRINT #2, "          Modulus of elestisity of concrete,          Ec(MPa):"; Ec

PRINT #2, "          -----"
PRINT #2, "          Cross sectional area of rebars,                    As(mm^2):"; Ass
PRINT #2, "          Yield stress of steel,                            fy(MPa):"; fy
PRINT #2, "          Modulus of elestisity of steel,                    Es(MPa):"; Es

PRINT #2, "          -----"
PRINT #2, "          Thickness of tension HPFRC strip,                  t(mm):"; t
PRINT #2, "          Tensile strength of HPFRC,                        fctm(MPa):"; fctm
PRINT #2, "          Modulus of Elasticityof HPFRC,                    Ef(MPa):"; Ef
PRINT #2, "          Maximum crack opening of HPFRC,                    wc(mm):"; wc
PRINT #2,
PRINT #2,

PRINT #2,
PRINT #2, "
*****"
PRINT #2, "          *                                                    *"
PRINT #2, "          *                      RESULTS                          *"
PRINT #2, "          *                                                    *"
PRINT #2, "
*****"
FOR a = c + 2 TO 130 STEP 2

PRINT #2,
PRINT #2,
PRINT #2,
PRINT #2, "          *****"
PRINT #2, "          *          a = ";
PRINT #2, USING "###.#          *"; a
PRINT #2, "          ***** "
PRINT #2,
PRINT #2, "          "
PRINT #2, "          _____"
PRINT #2, "          w          M-tot          M-c          M-s          M-p "
PRINT #2, "          (mm)          (kNm)          (kNm)          (kNm)          (kNm) "
PRINT #2, "          _____"

ksi = a / h
FOR w = 0 TO 1 STEP .01

  ym = 6 * ksi ^ .5 * (1.99 + .83 * ksi - .31 * ksi ^ 2 + .14 * ksi ^ 3) /
  ((1 - ksi) ^ 1.5 * (1 + 3 * ksi))

  ' _____ STEEL BAR _____
  Bta = c / h

  ws = (1 - Bta / ksi) * w

  AA = 4000          'Effective area of concrete

  ffs = 4.8 * 11876.5 * ws / (AA ^ .25)          'stress in steel

  IF ffs > fy THEN
    ffs = fy
  END IF

  Fs = Ass * ffs

  Fls = ((1.3 - .3 * (Bta / ksi) ^ 1.5) / (1 - (Bta / ksi) ^ 2) ^ .5 + .83 -
  1.76 * Bta / ksi) * (1 - (1 - Bta / ksi) * ksi)

  Funcs = ((3.52 * (1 - Bta / ksi) / (1 - ksi) ^ 1.5 - (4.35 - 5.28 * Bta /
  ksi) / (1 - ksi) ^ .5) + Fls) * 2 / (pi * ksi) ^ .5

```

Appendix C: Computer programmes

```

' _____RETROFITTING PLATE BONDED ON THE TENSION FACE_____
wte = (1 - t / (2 * h * ksi)) * w

IF 0 < wte AND wte < 6.5 THEN
  ppp = 3.069107E-03 * wte ^ 7 - .078952 * wte ^ 6 + .822382 * wte ^ 5
- 4.420119 * wte ^ 4 + 12.797151# * wte ^ 3 - 18.105342# * wte ^ 2 +
5.732789 * wte + 12.894413#

  ELSEIF wc <= wte THEN
    ppp = 0

  END IF

N = t / (2 * h)

FFp = ((1.3 - .3 * (N / ksi) ^ 1.5) / (1 - (N / ksi) ^ 2) ^ .5 + .83 -
1.76 * N / ksi) * (1 - (1 - N / ksi) * ksi)

Funcp = ((3.52 * (1 - N / ksi) / (1 - ksi) ^ 1.5 - (4.35 - 5.28 * N / ksi)
/ (1 - ksi) ^ .5) + FFp) * 2 / (pi * ksi) ^ .5

' _____CONCRETE IN TENSION_____

Int1 = 0

FOR ys = t / h TO .999 * ksi STEP ksi / 1000
  wy = (1 - ys / ksi) * w

  IF wy < .019 THEN                                     'cracked (1st part)
    dppc = (-.85 * 4.01 * wy / .0195 + 3.5)

    ELSEIF wy < .128 THEN
      dppc = (.15 * 4.01 * (wy - .128) / (.019 - .128)) 'cracked (2nd part)

    ELSE                                               'cracked (without any
stress
      dppc = 0                                       'transformation)
    END IF

    Flc = ((1.3 - .3 * (ys / ksi) ^ 1.5) / (1 - (ys / ksi) ^ 2) ^ .5 + .83 -
1.76 * ys / ksi) * (1 - (1 - ys / ksi) * ksi)

    dFunc = ((3.52 * (1 - ys / ksi) / (1 - ksi) ^ 1.5 - (4.35 - 5.28 * ys /
ksi) / (1 - ksi) ^ .5) + Flc) * 2 / (pi * ksi) ^ .5

    Int1 = Int1 + dFunc * dppc * ksi / 1000

  NEXT ys

' _____

M = h ^ 1.5 * b * (h ^ .5 * Int1 + ppp * Funcp * (t / h ^ .5) + Fs * Funcs /
(h ^ .5 * b)) / ym
Mc = h ^ 2 * b * Int1 / ym
Ms = h * Fs * Funcs / ym
Mp = h * b * ppp * Funcp * t / ym

PRINT #2, USING "    ##.##    ##.##    ##.##    ##.##
##.## "; w; M / 1000000; Mc / 1000000; Ms / 1000000; Mp / 1000000

NEXT w
NEXT a

```

Solution of the crack opening compatibility equation (8.46) for the beams retrofitted with one plate.

```

CLS
COLOR 15, 1
pi = 3.141592

PRINT
PRINT "*****"
PRINT "          CALCULATION OF RESISTANT MOMENT OF A CONCRETE BEAM          "
PRINT "          STRENGTHENED BY one CARDIFRC® STRIP                          "
PRINT "          "
PRINT "          Using the concept of FRACTURE MECHANIC                          "
PRINT "*****"
PRINT
PRINT

INPUT "Enter input file name:                ", i$
INPUT "Enter the first output file name :      ", o$

OPEN i$ FOR INPUT AS #1
OPEN o$ FOR OUTPUT AS #2

LINE INPUT #1, n$
LINE INPUT #1, n$
INPUT #1, B, h, c, E

LINE INPUT #1, n$
LINE INPUT #1, n$
LINE INPUT #1, n$
LINE INPUT #1, n$
LINE INPUT #1, n$
INPUT #1, Ass, fy, Es

LINE INPUT #1, n$
LINE INPUT #1, n$
LINE INPUT #1, n$
LINE INPUT #1, n$
LINE INPUT #1, n$
INPUT #1, t, fctm, Ef, wc

Ec = Ec * 1000
Es = Es * 1000
Ef = Ef * 1000                                'GPa to MPa

PRINT #2,
PRINT #2, "
*****"
PRINT #2, "          * CALCULATION OF RESISTANT MOMENT OF A CONCRETE BEAM *"
PRINT #2, "          *          STRENGTHENED BY one CARDIFRC® STRIP          *"
PRINT #2, "          *          Using the concept of FRACTURE MECHANIC          *"
PRINT #2, "
*****"
PRINT #2,
PRINT #2,
PRINT #2,

PRINT #2, "          -----"
PRINT #2, "                                INPUT DATA                                "
PRINT #2, "          -----"

PRINT #2, "          Width of beam,                b (mm):"; B
PRINT #2, "          Height of beam,                h (mm):"; h
PRINT #2, "          Distance between rebar and the bottom of beam, c (mm):"; c
PRINT #2, "          Modulus of elasticity of concrete, Ec (MPa):"; E

```

Appendix C: Computer programmes

```

PRINT #2, " -----"
PRINT #2, " Cross sectional area of rebars, As(mm^2):"; Ass
PRINT #2, " Yield stress of steel, fy(MPa):"; fy
PRINT #2, " Modulus of elasticity of steel, Es(MPa):"; Es
PRINT #2, " -----"
PRINT #2, " Thickness of tension HPFRC strip, t(mm):"; t
PRINT #2, " Tensile strength of CARDIFRC, fctm(MPa):"; fctm
PRINT #2, " Modulus of Elasticity of HPFRC, Ef(MPa):"; Ef
PRINT #2, " Maximum crack opening of HPFRC, wc(mm):"; wc
PRINT #2,
PRINT #2,
PRINT #2, "
*****"
PRINT #2, " * * "
PRINT #2, " * RESULTS * "
PRINT #2, " * * "
PRINT #2, " *****"

PRINT #2,
PRINT #2, "
-----"
PRINT #2, " a w M "
PRINT #2, " (mm) (mm) (kNm) "
PRINT #2, "
-----"

'%%%%%%%%%%
INPUT "Enter output file of K: " , ii$

OPEN ii$ FOR INPUT AS #3

FOR j = 1 TO 33
LINE INPUT #3, n$
NEXT j

FOR n = 1 TO 50

FOR j = 1 TO 4
LINE INPUT #3, n$
NEXT j

LINE INPUT #3, m1$
B$ = MID$(m1$, 37, 5)
a = VAL(B$)

FOR j = 1 TO 6
LINE INPUT #3, n$
NEXT j

FOR iii = 1 TO 101

LINE INPUT #3, l1$

B$ = MID$(l1$, 5, 4)
c$ = MID$(l1$, 18, 5)

w = VAL(B$)
Mk = VAL(c$)
Mk = Mk * 1000000
'%%%%%%%%%%

```

Appendix C: Computer programmes

```
'  
_____STEEL BAR_____  
Bta = c / h  
ksi = a / h  
ws = (1 - Bta / ksi) * w  
  
aaa = 4000 'Effective area of concrete  
  
ffs = 4.8 * 11876.5 * ws / (aaa ^ .25) 'stress in steel  
  
IF ffs > fy THEN  
ffs = fy  
END IF  
  
Fs = Ass * ffs  
  
'_____RETROFITTING PLATE_____  
  
wte = (1 - t / (2 * h * ksi)) * w  
  
IF 0 < wte AND wte < 6.5 THEN  
ppp = 3.069107E-03 * wte ^ 7 - .078952 * wte ^ 6 + .822382 * wte ^ 5 -  
4.420119 * wte ^ 4 + 12.797151# * wte ^ 3 - 18.105342# * wte ^ 2 + 5.732789  
* wte + 12.894413#  
  
ELSEIF wc < wte THEN  
ppp = 0  
  
END IF  
  
'  
_____  
  
Intm = 0  
Ints = 0  
Intp = 0  
Intc = 0  
Intcc = 0  
  
del = (ksi - Bta) / 1000  
  
FOR x = Bta + del TO ksi STEP del  
  
Ym = 6 * x ^ .5 * (1.99 + .83 * x - .31 * x ^ 2 + .14 * x ^ 3) / ((1 - x) ^  
1.5 * (1 + 3 * x))  
  
F1 = ((1.3 - .3 * (Bta / x) ^ 1.5) / (1 - (Bta / x) ^ 2) ^ .5 + .83 - 1.76 *  
Bta / x) * (1 - (1 - Bta / x) * x)  
  
Yp = (2 / (pi * x) ^ .5) * (3.52 * (1 - Bta / x) / (1 - x) ^ 1.5 - (4.35 -  
5.28 * Bta / x) / (1 - x) ^ .5 + F1)  
  
YmYp = Yp * Ym * del  
Intm = Intm + YmYp  
  
Yp2 = Yp ^ 2 * del  
  
Ints = Ints + Yp2  
  
q = t / (2 * h)  
  
FFp = ((1.3 - .3 * (q / x) ^ 1.5) / (1 - (q / x) ^ 2) ^ .5 + .83 - 1.76 * q  
/ x) * (1 - (1 - q / x) * x)  
  
F2 = (2 / (pi * ksi) ^ .5) * ((3.52 * (1 - q / x) / (1 - x) ^ 1.5 - (4.35 -  
5.28 * q / x) / (1 - x) ^ .5) + FFp)  
  
F3 = F2 * Yp * del
```

Appendix C: Computer programmes

Intp = Intp + F3
NEXT x

' _____ CONCRETE INTENSION _____

FOR ys = t / h TO .999 * ksi STEP ksi / 1000

Intcc = 0

wy = (1 - ys / ksi) * w

IF wy < .019 THEN 'cracked (1st part)

dppc = (-.85 * 4.01 * wy / .0195 + 4.01)

ELSEIF .019 < wy AND wy < .128 THEN

dppc = (.15 * 4.01 * (wy - .128) / (.019 - .128)) 'cracked (2nd part)

ELSE 'cracked (without any

stress

dppc = 0 'transformation)

END IF

BS = ys

IF ys < Bta THEN

BS = Bta

END IF

dell = (ksi - BS) / 100

FOR x = BS + dell TO ksi STEP dell

Ym = 6 * x ^ .5 * (1.99 + .83 * x - .31 * x ^ 2 + .14 * x ^ 3) / ((1 - x) ^ 1.5 * (1 + 3 * x))

' _____ Y(x,Bta) _____

F4 = ((1.3 - .3 * (Bta / x) ^ 1.5) / (1 - (Bta / x) ^ 2) ^ .5 + .83 - 1.76 * Bta / x) * (1 - (1 - Bta / x) * x)

F5 = (2 / (pi * x) ^ .5) * ((3.52 * (1 - Bta / x) / (1 - x) ^ 1.5 - (4.35 - 5.28 * Bta / x) / (1 - x) ^ .5) + F4)

' _____ Y(x,ys) _____

F6 = ((1.3 - .3 * (ys / x) ^ 1.5) / (1 - (ys / x) ^ 2) ^ .5 + .83 - 1.76 * ys / x) * (1 - (1 - ys / x) * x)

F7 = (2 / (pi * x) ^ .5) * ((3.52 * (1 - ys / x) / (1 - x) ^ 1.5 - (4.35 - 5.28 * ys / x) / (1 - x) ^ .5) + F6)

F8 = F5 * F7 * dell

'

Intcc = Intcc + F8

NEXT x

F9 = 2 * h * dppc * Intcc * ksi / (1000 * E) ' ksi/1000 =dys

Intc = Intc + F9

NEXT ys

M = h * B * E * (ws + 2 * Fs * Ints / (B * E) + 2 * ppp * t * Intp / E + Intc) / (Intm * 2)

Appendix C: Computer programmes

```
Ms = h * Fs * Ints / Intm
Mp = h * B * ppp * t * Intp / Intm

Mws = h * B * E * ws / (2 * Intm)

Mc = h * B * E * Intc / (2 * Intm)

IF ABS(M - Mk) < 100000 THEN

  PRINT #2, USING "          ###.#          #.##          ##.##"
"; a; w; M / 1000000
  END IF

  NEXT iii

NEXT n
```

Solution of the stress intensity factor equation (8.31) for the beams retrofitted with three plates.

```

CLS
COLOR 15, 1
pi = 3.141592

PRINT
PRINT "*****"
PRINT "          CALCULATION OF RESISTANT MOMENT OF A CONCRETE BEAM          "
PRINT "          STRENGTHENED BY THREE CARDIFRC® STRIPS                      "
PRINT "          Using the concept of FRACTURE MECHANIC                        "
PRINT "*****"
PRINT
PRINT

INPUT "Enter input file name:                ", i$
INPUT "Enter the first output file name :    ", o$

OPEN i$ FOR INPUT AS #1
OPEN o$ FOR OUTPUT AS #2

LINE INPUT #1, N$
LINE INPUT #1, N$
INPUT #1, b, h, c, Ec

LINE INPUT #1, N$
LINE INPUT #1, N$
LINE INPUT #1, N$
LINE INPUT #1, N$
LINE INPUT #1, N$
INPUT #1, Ass, fy, Es

LINE INPUT #1, N$
LINE INPUT #1, N$
LINE INPUT #1, N$
LINE INPUT #1, N$
LINE INPUT #1, N$
INPUT #1, t, fctm, Ef, wc

Ec = Ec * 1000
Es = Es * 1000
Ef = Ef * 1000                                'GPa to MPa

'INPUT "a="; a                                'a is the depth of crack
'INPUT "w="; w                                'w is the opening of crack at the bottom of
beam

PRINT #2,
PRINT #2, "
*****"
PRINT #2, "          *          CALCULATION OF RESISTANT MOMENT OF A CONCRETE BEAM          *"
PRINT #2, "          *          STRENGTHENED BY THREE CARDIFRC® STRIPS                      *"
PRINT #2, "          *          Using the concept of FRACTURE MECHANIC                        *"
PRINT #2, "
*****"
PRINT #2,
PRINT #2,
PRINT #2,

PRINT #2, "          -----"
PRINT #2, "          INPUT DATA          "
PRINT #2, "          -----"

PRINT #2, "          Width of beam,          b(mm):"; b
PRINT #2, "          Height of beam,         h(mm):"; h

```

Appendix C: Computer programmes

```

PRINT #2, "      Distance between rebar and the bottom of beam, c(mm):"; c
PRINT #2, "      Modulus of elestisity of concrete,          Ec(MPa):"; Ec

PRINT #2, "      -----"
PRINT #2, "      Cross sectional area of rebars,          As(mm^2):"; Ass
PRINT #2, "      Yield stress of steel,          fy(MPa):"; fy
PRINT #2, "      Modulus of elestisity of steel,        Es(MPa):"; Es

PRINT #2, "      -----"
PRINT #2, "      Thickness of tension HPFRC strip,          t(mm):"; t
PRINT #2, "      Tensile strength of HPFRC,          fctm(MPa):"; fctm
PRINT #2, "      Modulus of Elasticityof HPFRC,        Ef(MPa):"; Ef
PRINT #2, "      Maximum crack opening of HPFRC,        wc(mm):"; wc
PRINT #2,
PRINT #2,
PRINT #2, "
*****"
PRINT #2, "      *                               * "
PRINT #2, "      *                               * "
PRINT #2, "      *                               * "
PRINT #2, "      *                               * "
*****"

FOR a = c + 2 TO 130 STEP 2

PRINT #2,
PRINT #2,
PRINT #2,
PRINT #2, "      *****"
PRINT #2, "      *          a = ";
PRINT #2, USING "###.#      *"; a
PRINT #2, "      ***** "
PRINT #2,
PRINT #2, "      "

PRINT #2, "      w      M-tot      M-c      M-s      M-p      M-sp"
PRINT #2, "      (mm)      (kNm)      (kNm)      (kNm)      (kNm)      (kNm) "
PRINT #2, "      "

ksl = a / h
FOR w = 0 TO 1 STEP .01

  Ym = 6 * ksl ^ .5 * (1.99 + .83 * ksl - .31 * ksl ^ 2 + .14 * ksl ^ 3) /
  ((1 - ksl) ^ 1.5 * (1 + 3 * ksl))

  '-----STEELBAR-----

  Bta = c / h

  ws = (1 - Bta / ksl) * w

  AA = 4000          'Effective area of concrete

  ffs = 4.8 * 11876.5 * ws / (AA ^ .25)      'stress in steel

  IF ffs > fy THEN
    ffs = fy
  END IF

  Fs = Ass * ffs

  Fls = ((1.3 - .3 * (Bta / ksl) ^ 1.5) / (1 - (Bta / ksl) ^ 2) ^ .5 + .83 -
  1.76 * Bta / ksl) * (1 - (1 - Bta / ksl) * ksl)

```

Appendix C: Computer programmes

```

Funcs = (3.52 * (1 - Bta / ksi) / (1 - ksi) ^ 1.5 - (4.35 - 5.28 * Bta /
ksi) / (1 - ksi) ^ .5 + Fls) * 2 / (pi * ksi) ^ .5

' _____ RETROFITTING PLATE BONDED ON THE TENSION FACE _____

wte = (1 - t / (2 * h * ksi)) * w

IF 0 < wte AND wte < 6.5 THEN
    ppp = 3.069107E-03 * wte ^ 7 - .078952 * wte ^ 6 + .822382 * wte ^ 5
- 4.420119 * wte ^ 4 + 12.797151# * wte ^ 3 - 18.105342# * wte ^ 2 +
5.732789 * wte + 12.894413#

    ELSEIF wc < wte THEN
        ppp = 0

    END IF

N = t / (2 * h)

FFp = ((1.3 - .3 * (N / ksi) ^ 1.5) / (1 - (N / ksi) ^ 2) ^ .5 + .83 -
1.76 * N / ksi) * (1 - (1 - N / ksi) * ksi)

Funcp = (3.52 * (1 - N / ksi) / (1 - ksi) ^ 1.5 - (4.35 - 5.28 * N / ksi)
/ (1 - ksi) ^ .5 + FFp) * 2 / (pi * ksi) ^ .5

' _____ CONCRETE IN TENSION _____
Int1 = 0

FOR ys = t / h TO .999 * ksi STEP ksi / 1000

wy = (1 - ys / ksi) * w

IF wy < .019 THEN                                     'cracked (1st part)

    dppc = (-.85 * 4.01 * wy / .0195 + 4.01)

    ELSEIF wy < .128 THEN
        dppc = (.15 * 4.01 * (wy - .128) / (.0195 - .128)) 'cracked (2nd
part)

    ELSE                                               'cracked (without any
stress                                               'transformation)
        dppc = 0

    END IF

Flc = ((1.3 - .3 * (ys / ksi) ^ 1.5) / (1 - (ys / ksi) ^ 2) ^ .5 + .83 -
1.76 * ys / ksi) * (1 - (1 - ys / ksi) * ksi)

dFunc = (3.52 * (1 - ys / ksi) / (1 - ksi) ^ 1.5 - (4.35 - 5.28 * ys /
ksi) / (1 - ksi) ^ .5 + Flc) * 2 / (pi * ksi) ^ .5

Int1 = Int1 + dFunc * dppc * ksi / 1000

NEXT ys

' _____ RETROFITTING PLATES BONDED ON THE SIDES _____

Int2 = 0

FOR ys = 0 TO .999 * ksi STEP ksi / 1000

IF ys > (100 / h) THEN                                'limitation of the height of the side plate
    GOTO 2
END IF

```

Appendix C: Computer programmes

```
wy = (1 - ys / ksi) * w

IF 0 < wy AND wy < 6.5 THEN
  dpsp = 3.069107E-03 * wy ^ 7 - .078952 * wy ^ 6 + .822382 * wy ^ 5 -
4.420119 * wy ^ 4 + 12.797151# * wy ^ 3 - 18.105342# * wy ^ 2 + 5.732789 *
wy + 12.894413#

  ELSEIF wc < wy THEN
    dpsp = 0

  END IF

  Flsp = ((1.3 - .3 * (ys / ksi) ^ 1.5) / (1 - (ys / ksi) ^ 2) ^ .5 + .83 -
1.76 * ys / ksi) * (1 - (1 - ys / ksi) * ksi)

  dFuncsp = (3.52 * (1 - ys / ksi) / (1 - ksi) ^ 1.5 - (4.35 - 5.28 * ys /
ksi) / (1 - ksi) ^ .5 + Flsp) * 2 / (pi * ksi) ^ .5

  Int2 = Int2 + dFuncsp * dpsp * ksi / 1000

NEXT ys
'


---


2 M = h ^ 1.5 * b * (h ^ .5 * Int1 + 2 * h ^ .5 * t * (Int2 / b) + ppp *
Funcp * (t / h ^ .5) + Fs * Funcs / (h ^ .5 * b)) / Ym
  Mc = h ^ 2 * b * Int1 / Ym
  Ms = h * Fs * Funcs / Ym
  Mp = h * b * ppp * Funcp * t / Ym
  Msp = 2 * h ^ 2 * t * Int2 / Ym

PRINT #2, USING "    ##      ##.##      ##.##      ##.##
##.##      ##.## "; w; M / 1000000; Mc / 1000000; Ms / 1000000; Mp /
1000000; Msp / 1000000

NEXT w
NEXT a
```

Solution of the crack opening compatibility equation (8.46) for the beams retrofitted with three plates.

```

CLS
COLOR 15, 1
pi = 3.141592

PRINT
PRINT "*****"
PRINT "          CALCULATION OF RESISTANT MOMENT OF A CONCRETE BEAM          "
PRINT "          STRENGTHENED BY THREE CARDIFRC® STRIPS                    "
PRINT "          Using the concept of FRACTURE MECHANIC                      "
PRINT "*****"
PRINT
PRINT

INPUT "Enter input file name:                ", i$
INPUT "Enter the first output file name :    ", o$

OPEN i$ FOR INPUT AS #1
OPEN o$ FOR OUTPUT AS #2

LINE INPUT #1, n$
LINE INPUT #1, n$
INPUT #1, B, h, c, E

LINE INPUT #1, n$
LINE INPUT #1, n$
LINE INPUT #1, n$
LINE INPUT #1, n$
LINE INPUT #1, n$
INPUT #1, Ass, fy, Es

LINE INPUT #1, n$
LINE INPUT #1, n$
LINE INPUT #1, n$
LINE INPUT #1, n$
LINE INPUT #1, n$
INPUT #1, t, fctm, Ef, wc

Ec = Ec * 1000
Es = Es * 1000
Ef = Ef * 1000                                'GPa to MPa

PRINT #2,
PRINT #2, "
*****"
PRINT #2, "          *          CALCULATION OF RESISTANT MOMENT OF A CONCRETE BEAM          *"
PRINT #2, "          *          STRENGTHENED BY THREE CARDIFRC® STRIPS                    *"
PRINT #2, "          *          Using the concept of FRACTURE MECHANIC                      *"
PRINT #2, "
*****"
PRINT #2,
PRINT #2,
PRINT #2,

PRINT #2, "          -----"
PRINT #2, "                                INPUT DATA"
PRINT #2, "          -----"

PRINT #2, "          Width of beam,                                b(mm) :"; B
PRINT #2, "          Height of beam,                               h(mm) :"; h
PRINT #2, "          Distance between rebar and the bottom of beam, c(mm) :"; c

```

Appendix C: Computer programmes

```

PRINT #2, "          Modulus of elestisity of concrete,          Ec(MPa):"; E
PRINT #2, "          -----"
PRINT #2, "          Cross sectional area of rebars,          As(mm^2):"; Ass
PRINT #2, "          Yield stress of steel,          fy(MPa):"; fy
PRINT #2, "          Modulus of elestisity of steel,          Es(MPa):"; Es

PRINT #2, "          -----"
PRINT #2, "          Thickness of tension HPFRC strip,          t(mm):"; t
PRINT #2, "          Tensile strength of HPFRC,          fctm(MPa):"; fctm
PRINT #2, "          Modulus of Elasticityof HPFRC,          Ef(MPa):"; Ef
PRINT #2, "          Maximum crack opening of HPFRC,          wc(mm):"; ;
wc
PRINT #2,
PRINT #2,

PRINT #2,
PRINT #2, "
*****"
PRINT #2, "          *                                     *"
PRINT #2, "          *                               RESULTS                               *"
PRINT #2, "          *                                     *"
PRINT #2, "
*****"

PRINT #2,
PRINT #2, "
-----"
PRINT #2, "          a          w          M"
PRINT #2, "          (mm)          (mm)          (kNm) "
PRINT #2, "
-----"

'%%%%%%%%%%

INPUT "Enter output file of K:          ", ii$

OPEN ii$ FOR INPUT AS #3

FOR j = 1 TO 33
  LINE INPUT #3, n$
NEXT j

FOR n = 1 TO 50

  FOR j = 1 TO 4
    LINE INPUT #3, n$
  NEXT j

  LINE INPUT #3, m1$
  B$ = MID$(m1$, 37, 5)
  a = VAL(B$)

  FOR j = 1 TO 6
    LINE INPUT #3, n$
  NEXT j

  FOR iii = 1 TO 101

    LINE INPUT #3, l1$

    B$ = MID$(l1$, 5, 4)
    c$ = MID$(l1$, 18, 5)

    w = VAL(B$)
    Mk = VAL(c$)
    Mk = Mk * 1000000

```

Appendix C: Computer programmes

```

'%%%%%%%%%%%%%%%%%%%%%%%%%%%%%%%%%%%%%%%%%%%%%%%%%%%%%%%%%%%%%%%%%%%%%%%%%%
'
'                                     STEEL BAR
'
Bta = c / h
ksi = a / h
ws = (1 - Bta / ksi) * w
aaa = 4000
ffs = 4.8 * 11876.5 * ws / (aaa ^ .25)
'Effective area of concrete
'stress in steel

IF ffs > fy THEN
ffs = fy
END IF

Fs = Ass * ffs
'
'                                     RETROFITTING PLATE
'

wte = (1 - t / (2 * h * ksi)) * w

IF 0 < wte AND wte < 6.5 THEN
ppp = 3.069107E-03 * wte ^ 7 - .078952 * wte ^ 6 + .822382 * wte ^ 5
- 4.420119 * wte ^ 4 + 12.797151# * wte ^ 3 - 18.105342# * wte ^ 2 +
5.732789 * wte + 12.894413#

ELSEIF wc < wte THEN
ppp = 0

END IF

'
'
Intm = 0
Ints = 0
Intp = 0
Intc = 0
Intcc = 0
Intspp = 0
Intsp = 0

del = (ksi - Bta) / 1000

FOR x = Bta + del TO ksi STEP del

Ym = 6 * x ^ .5 * (1.99 + .83 * x - .31 * x ^ 2 + .14 * x ^ 3) / ((1 - x)
^ 1.5 * (1 + 3 * x))

F1 = ((1.3 - .3 * (Bta / x) ^ 1.5) / (1 - (Bta / x) ^ 2) ^ .5 + .83 - 1.76
* Bta / x) * (1 - (1 - Bta / x) * x)

Yp = 2 / (pi * x) ^ .5 * (3.52 * (1 - Bta / x) / (1 - x) ^ 1.5 - (4.35 -
5.28 * Bta / x) / (1 - x) ^ .5 + F1)

YmYp = Yp * Ym * del

Intm = Intm + YmYp

Yp2 = Yp ^ 2 * del

Ints = Ints + Yp2

q = t / (2 * h)

FFp = ((1.3 - .3 * (q / x) ^ 1.5) / (1 - (q / x) ^ 2) ^ .5 + .83 - 1.76 *
q / x) * (1 - (1 - q / x) * x)

F2 = (3.52 * (1 - q / x) / (1 - x) ^ 1.5 - (4.35 - 5.28 * q / x) / (1 - x)
^ .5) + FFp

F3 = F2 * 2 / (pi * ksi) ^ .5

```


Appendix C: Computer programmes

```

F4 = F3 * Yp * del

Intp = Intp + F4

NEXT x

' _____ CONCRETE IN TENSION _____
FOR ys = t / h TO .999 * ksi STEP ksi / 1000

Intcc = 0

wy = (1 - ys / ksi) * w

IF wy < .019 THEN                                     'cracked (1st part)

    dppc = (-.85 * 4.01 * wy / .0195 + 3.5)

    ELSEIF wy < .128 THEN
part) dppc = (.15 * 4.01 * (wy - .128) / (.0195 - .128)) 'cracked (2nd

    ELSE                                             'cracked (without any
stress dppc = 0                                     'transformation)

    END IF
    BS = ys
    IF ys < Bta THEN
    BS = Bta
    END IF

    dell = (ksi - BS) / 100

    FOR x = BS + dell TO ksi STEP dell

    Ym = 6 * x ^ .5 * (1.99 + .83 * x - .31 * x ^ 2 + .14 * x ^ 3) / ((1 - x)
^ 1.5 * (1 + 3 * x))

' _____ Y(x,Bta) _____
F5 = ((1.3 - .3 * (Bta / x) ^ 1.5) / (1 - (Bta / x) ^ 2) ^ .5 + .83 - 1.76 *
Bta / x) * (1 - (1 - Bta / x) * x)

F6 = (3.52 * (1 - Bta / x) / (1 - x) ^ 1.5 - (4.35 - 5.28 * Bta / x) / (1 -
x) ^ .5 + F5)

F7 = F6 * 2 / (pi * x) ^ .5
' _____ Y(x, ys) _____
F8 = ((1.3 - .3 * (ys / x) ^ 1.5) / (1 - (ys / x) ^ 2) ^ .5 + .83 - 1.76 *
ys / x) * (1 - (1 - ys / x) * x)

F9 = (3.52 * (1 - ys / x) / (1 - x) ^ 1.5 - (4.35 - 5.28 * ys / x) / (1 - x)
^ .5 + F8)

F10 = F9 * 2 / (pi * x) ^ .5

F11 = F10 * F7 * dell
' _____
Intcc = Intcc + F11

NEXT x

F12 = 2 * h * dppc * Intcc * ksi / (1000 * E)          ' ksi/1000 =dy

Intc = Intc + F12

```

Appendix C: Computer programmes

NEXT ys

' _____ SIDE PLATE IN TENSION _____

FOR ys = 0 TO .999 * ksi STEP ksi / 1000

IF ys > (100 / h) THEN 'limitation of the height of the side plate
GOTO 2
END IF

Intspp = 0

wy = (1 - ys / ksi) * w

IF 0 < wy AND wy < 6.5 THEN

dpsp = 3.069107E-03 * wy ^ 7 - .078952 * wy ^ 6 + .822382 * wy ^ 5 -
4.420119 * wy ^ 4 + 12.797151# * wy ^ 3 - 18.105342# * wy ^ 2 + 5.732789 *
wy + 12.894413#

ELSEIF wc < wy THEN
dpsp = 0

END IF

BS = ys

IF ys < Bta THEN

BS = Bta

END IF

dell = (ksi - BS) / 100

FOR x = BS + dell TO ksi STEP dell

Ym = 6 * x ^ .5 * (1.99 + .83 * x - .31 * x ^ 2 + .14 * x ^ 3) / ((1 - x) ^
1.5 * (1 + 3 * x))

' _____ Y(x, Bta) _____
F5 = ((1.3 - .3 * (Bta / x) ^ 1.5) / (1 - (Bta / x) ^ 2) ^ .5 + .83 - 1.76 *
Bta / x) * (1 - (1 - Bta / x) * x)

F6 = (3.52 * (1 - Bta / x) / (1 - x) ^ 1.5 - (4.35 - 5.28 * Bta / x) / (1 -
x) ^ .5 + F5)

F7 = F6 * 2 / (pi * x) ^ .5

' _____ Y(x, ys) _____

F8 = ((1.3 - .3 * (ys / x) ^ 1.5) / (1 - (ys / x) ^ 2) ^ .5 + .83 - 1.76 *
ys / x) * (1 - (1 - ys / x) * x)

F9 = (3.52 * (1 - ys / x) / (1 - x) ^ 1.5 - (4.35 - 5.28 * ys / x) / (1 - x)
^ .5 + F8)

F10 = F9 * 2 / (pi * x) ^ .5

F11 = F10 * F7 * dell

' _____

Intspp = Intspp + F11

NEXT x

F12 = 4 * dpsp * h * t * Intspp * ksi / (1000 * E * B) ' ksi/1000 =dys

Intsp = Intsp + F12

NEXT ys



Appendix C: Computer programmes

```
2 M = h * B * E * (ws + 2 * Fs * Ints / (B * E) + 2 * ppp * t * Intp / E +  
Intc + Intsp) / (Intm * 2)
```

```
Ms = h * Fs * Ints / Intm
```

```
Mp = h * B * ppp * t * Intp / Intm
```

```
Mws = h * B * E * ws / (2 * Intm)
```

```
Mc = h * B * E * Intc / (2 * Intm)
```

```
Msp = h * B * E * Intsp / (2 * Intm)
```

```
IF ABS(M - Mk) < 100000 THEN
```

```
    PRINT #2, USING "          ###.#          #.##          ##.##  
"; a; w; (M + Mk) / 2000000  
    END IF
```

```
    NEXT iii
```

```
NEXT n
```